TREE-NUREG-1173
for U.S. Nuclear Regulatory Commission

EXPERIMENT DATA REPORT IFA-226 POSTIRRADIATION EXAMINATION

September 1977

EG&G Idaho, Inc.

IDAHO NATIONAL ENGINEERING LABORATORY

ENERGY RESEARCH AND DEVELOPMENT ADMINISTRATION

IDAHO OPERATIONS OFFICE UNDER CONTRACT EY-76-C-07-1570

DISCLAIMER

Available from
National Technical Information Service
U.S. Department of Commerce
5285 Port Royal Road
Springfield, Virginia 22161
Price: Printed Copy $~~10.00~~; Microfiche $3.00
11.00

"The NRC will make available data tapes and operational computer codes on research programs dealing with postulated loss-of-coolant accidents in light water reactors. Persons requesting this information must reimburse the NRC contractors for their expenses in preparing copies of the data tapes and the operational computer codes. Requests should be submitted to the Research Applications Branch, Office of Nuclear Regulatory Research, Nuclear Regulatory Commission, Washington, D.C. 20555."

TREE-NUREG-1173

EXPERIMENT DATA REPORT IFA-226 POSTIRRADIATION EXAMINATION

Approved:

Niels Hansen, Head of Metallurgy Department
Risø National Laboratory.

P. E. MacDonald, Manager
Experiment Specification and Analysis

J. G. Crocker, Manager
Thermal Fuels Behavior Division

Stougaard Jensen/København

TREE-NUREG-1173

Distributed Under Category:
NRC-3
Water Reactor Safety Research
Fuel Behavior

EXPERIMENT DATA REPORT

IFA-226 POSTIRRADIATION

EXAMINATION

C. Bagger, H. Carlsen, J. Domanus,

H. Hougaard, E. Larsen

and N. Larsen

Prepared by

Risø National Laboratory

Roskilde - Denmark

Prepared for

EG&G Idaho, Inc.

September 1977

PREPARED FOR THE
U.S. NUCLEAR REGULATORY COMMISSION
AND
ENERGY RESEARCH AND DEVELOPMENT ADMINISTRATION
IDAHO OPERATIONS OFFICE
UNDER CONTRACT NO. EY-76-C-07-1570

FOREWORD

Fuel rod behavior studies are being conducted by the Thermal Fuels Behavior Program at the Idaho National Engineering Laboratory. This program is conducted by EG&G Idaho, Inc., as part of the Nuclear Regulatory Commission's (NRC) Water Reactor Safety Research Fuel Behavior Program[a]. Experimental data for verification of analytical models developed to predict the behavior of light water nuclear fuel rods under normal and postulated accident conditions are being obtained from a variety of in-reactor experiments. Some of these experiments are being conducted in the Halden Boiling Water Reactor (HBWR), located in Halden, Norway, under the NRC's participation in the Organization for Economic Cooperation and Development Halden Reactor Project.

One such experiment was instrumented fuel Assembly 226 (IFA-226) irradiated in the HBWR from November 1971 through September 1975. IFA-226 contained twelve, mixed plutonium-uranium oxide fuel rods arranged in two, six-rod clusters. The assembly was designed to study fuel-cladding mechanical interaction, fuel thermal response, and fission gas release as a function of fuel density, initial fuel-to-cladding gap, rod power, and burnup. Data were obtained from fuel rod centerline thermocouples, fission gas pressure transducers, and cladding elongation sensors.

An important part of any irradiation test is a thorough postirradiation examination (PIE). This report was prepared by the Risø National Laboratory of the Danish Atomic Energy Commission and contains the results of the PIE of the IFA-226 test rods conducted by Risø for EG&G Idaho, Inc.

[a] United States Nuclear Regulatory Commission, Reactor Safety Research Program, A Description of Current and Planned Reactor Safety Research Sponsored by the Nuclear Regulatory Commission's Division of Reactor Safety Research, NUREG-75/058 (June 1975).

Results of both nondestructive and destructive examinations are presented. The PIE indicated that one fuel rod failed during service as a result of internal hydriding of the end plug. Circumferential cladding ridges resulting from fuel-cladding interaction were present on all of the rods, with the largest ridges present on the rod with the smallest initial fuel-to-cladding gap. No incipient fuel rod failures were detected. Maximum fuel centerline temperatures estimated from fuel grain growth were in general agreement with the results from fuel rod thermocouples. Fuel density for high burnup samples decreased several percent during irradiation.

P. E. MacDonald, Manager
Experiment Specification
and Analysis
Thermal Fuels Behavior Program
EG&G Idaho, Inc.

CONTENTS

Page

1. INTRODUCTION

This report presents the results obtained from the post-irradiation examination of IFA-226 performed in the Hot Cells at the Risø National Laboratory, Denmark.

The instrumented fuel assembly IFA-226 was designed, fabricated, and initially irradiated in the Halden Boiling Water Reactor (HBWR) by Nuclear Fuel Services, Inc., (NFS) of Rockville, Maryland, USA. In 1974 the assembly and all its existing data were acquired from NFS by the USNRC. The continued use and management of the assembly are being directed by the EG & G under the participation of the USNRC in the OECD Halden Reactor Project.

Irradiation of IFA-226 began on 24.11.1971 and terminated on 20.9.1975. At that time it had obtained a calculated average burn-up of approx. 30,000 MWd/t MeO_2. For the last two months, the assembly was operated with one failed fuel rod.

After 7 months' cooling in the reactor pond at Halden, the complete assembly, including the shroud tube, was transferred to the Risø National Laboratory for post-irradiation examination according to a contract between the USNRC and Risø.

The purpose of the IFA-226 experiment was to study the effects of:

- pellet/cladding mechanical interaction,
- fuel centre-line temperature,
- rod internal pressure

as a function of:

- initial pellet-to-clad gap,
- fuel density,
- fuel power,
- burn-up

on UO_2-PuO_2 fuel.

The extent of the post-irradiation examination is shown in Table 1.

2. ASSEMBLY AND ROD DATA

The instrumented fuel assembly IFA-226 consisted of a vertically stacked train of two clusters of six fuel rods each. Each cluster was about 915 mm in length and 70 mm in diameter. The rods within each cluster were arranged in a hexagonal lattice. A diagram of IFA-226 is presented in Fig. 1 [1], and a schematic diagram of each of the four types of test rod within the assembly is shown in Fig. 2 [1].

The test assembly was cooled by natural circulation of heavy water. When the assembly was operating at high, steady-state power levels, the nominal inlet flow rate of the coolant was about 2 l/s, and the coolant inlet temperature was about 237°C. The nominal coolant pressure and the saturation temperature was $3.45 \cdot 10^6$ N/m^2 and 240°C, respectively.

The fuel was fabricated from recycled plutonium oxide powder, which was mechanically mixed with depleted (0.20 wt% ^{235}U) uranium-oxide powder. This mixed oxide material (9.5 wt% PuO_2) was pressed, sintered and ground into pellet and clad with Zircaloy-4. The final pellet and rod dimensions, except for length, are typical of those of pressurized water reactor reload fuel. The fuel rod data are shown in Table 2.

All fabrication data are given in [1].

3. NON-DESTRUCTIVE EXAMINATION

3.1. Reception and Dismantling

At reception the shroud tube had some ovality at the end where it was cut at Halden, and it was slightly bent. The deviation from a straight line was about 10 mm in the middle of the shroud tube.

The shroud tube was cut just below the lower end of the lower rods, but because of its deformation it was impossible to remove it from the fuel bundle. It was, therefore, necessary to recut the shroud tube between the upper and the lower bundle of rods. Even then, the shroud could not be removed and subsequently it was milled longitudinally.

Figures 3 and 4 show the fuel bundle after removal of the shroud tube.

The spacer springs were removed and all the rods except AK-11 could easily be removed from the spacers.

Rod AK-11 was failed at the upper end. The rod expansion at the failure location was so severe that it was necessary to cut the spacer twice before the rod could be removed.

Figures 5 and 6 show, respectively, the failure before and after the rod was released from the spacer.

3.2. Visual Inspection

In general, the rods appeared light grey in colour. The most pronounced features were spacer marks and visible welding zones, as shown in Figures 7-12. The spacer marks varied from the light one shown in Fig. 8 to the heaviest one shown in Fig. 11.

3.3. Length Measurements

The length of the rods was measured relative to a standard length with a dial gauge (±0.01 mm).

The measured length was from the top end-plug shoulder to the bottom end (outmost point) of the rod. The rods were rotated, and l_{max} and l_{min} were found. The results are shown in Table 3.

3.4. Bow Measurements

Each rod was rested on two fix points, one at the end, the other near the mid-point of the rod. The rod was rotated, and the maximum and the minimum vertical positions of the free end were measured; the principle is seen in Fig. 13. Assuming a circular shape of the rod, the rod deflection is found as one fourth of the difference between the two readings. Both ends of each rod were measured. The circular shape of the rods seems reasonable; the results with this assumption will probably give upper limits to the deflection.

The results are shown in table 4.

3.5. Profilometry and Eddy Current Testing

Profilometry was performed on all 12 rods. The measurements were performed along 6 generating lines. The probe set up for

profilometry has sapphire rods of 1 mm dia., coupled to a differential transformer, and the contact pressure of the sapphires is 35 pond. The differential transformer is calibrated against polished stainless steel normals before each rod measurement. The accuracy of the set-up has been determined on polished stainless steel to be 0.5 - 1µm. The measurements were made digitally at locations 0.3 mm apart and recorded on magnetic tape.

Eddy current testing was performed on the rods when possible; as the technique adopted at Risø utilizes an encircling coil, rods with end plugs of a diameter larger than the rod itself could not give significant measuring results.

The results for each rod are given in the following and summarized in table 5.

Rod AA-1, fig. 14 Mean OD unchanged.

Some ridge-like diameter patterns are observed. The ridge locations coincide with locations of pellet interfaces. The ridges are never rotationally symmetric.

Two diameter variations at the bottom are noticable. On the 150° generating line at the top of pellet no. 2 from the bottom, the diameter change is rather large, 60 µm, and not symmetrical. Further, it extends over a length of 15 mm.

On the 60°, the 90° and the 120° generating lines at the location of the large interpellet distance of about 2 mm, 86 mm from the bottom datum,*) a small (15 - 20 µm) diameter increase is observed. It does not resemble ridging and might suggest a weak spot in the cladding.

In the area 460 - 580 mm from the datum plane a region with diameter variations (80 - 90 µm) is observed. The general picture might indicate that this is the result of external mechanical damage to the rod. However, the distance between the diameter peaks corresponds to the pellet lengths.

Eddy current measurements could not be made on the rod because of the end plug diameters.

Rod AB-2, fig. 15.

The average diameter of rod AB-2 seems a little larger than the pre-irradiation average. However, variations along the individual generating lines show that the rod has an ovality of

*) For the definition of datum see Fig. 2.

40 µm in some places. The rod was measured after piercing at the plenum end, the result of which is clearly shown. A slight tendency to ridge formation is observed, the ridge height being only of the order of 5 µm.

Rod AC-3, Fig. 16.

An increase of about 15 µm in clad diameter is observed. Like rod 2, a slight tendency to ridge formation is noted with ridge heights of 2.5 - 5 µm. The rod was measured after piercing at the plenum end, the effect of which is clearly shown.

Rod AD-4, fig. 17.

No diameter change compared to the pre-irradiation diameter; however, the plenum end appears to have an average diameter that is about 10 µm greater than the average diameter of the rest of the same generating line. The largest degree of ovality, 30 µm, is observed in the area 50 mm - 250 mm from the bottom. Like rods 2 and 3, a slight tendency to ridge formation is noted, the ridge height being of the order of 2.5 µm.

Rod AE-5, fig. 18.

A general increase of about 15 - 20 µm is observed on all generating lines compared to the pre-irradiation diameter. Ridging is observed for the first pellets containing the TC. At 170 - 270 mm on the 90° trace, an increase in diameter of 10 - 15 µm is observed. This is probably due to deposition of corrosion products in the reactor.

Rod AG-6, fig. 19.

No changes are noted in the average diameter as a result of irradiation. The ridging is very pronounced, with a max. ridge height of 15 - 18 µm. At the hotter end, the beginning of ridging resulting from pellet cracks is even observed.

Rod AH-7, fig. 20.

No average diameter can be given, as it varies along the axis of the rod. With respect to the plenum, the average diameter varies between 10.690 and 10.705 mm. Regarding the pellet stack, the diameter - excluding the ridges - follows the same pattern as shown in the gross scan curve, from 10.72 at the hotter end down to 10.69 mm at the colder end. The ridges are superimposed on these diameters and have a max. height of 30 µm. Both primary and secondary ridging are seen. The eddy current trace (fig. 26) gave no evidence of the existence of major cladding defects, although the presence of ridging to the

extent observed would to some degree mask such defect signals.

Rod AJ-8, fig. 21.

No average diameter can be given as for rod No. 7. The average diameter at the plenum is 10.68 mm. The average diameter of the rod varies axially along the fuel stack from 10.68 mm at the hotter end of the stack to 10.67 mm at the colder end of the stack following the trend of the power profile. The ridges superimposed on this trace have a maximum height of 30 µm. The primary ridging is very clear, with secondary ridging at the hotter end. The eddy current trace (fig. 27) does not indicate major cladding effects.

Rod AO-9, fig. 22.

The average diameter is unchanged as compared to the pre-irradiation diameter. Minor ridging is observed with max. ridge heights of 2.5 - 5 µm. At 112 mm from the bottom a decrease in diameter of about 20 µm is observed. Eddy current testing (fig. 28) indicates this position to be the only one on the rod where there might be a major cladding defect.

Rod AM-10, fig. 23.

When disregarding the ridges, the average diameter is unaffected by irradiation. Primary ridging is found along almost the whole fuel stack, while secondary ridging is only observed in a couple of cases. Maximum ridge height, 30 µm. Eddy current (fig. 29) shows an irregularity at a distance of about 175 mm from the bottom end. Nothing unusual is seen on the diameter traces at this location.

Rod AK-11, fig. 24.

The failed rod No. 11 shows a diameter increase of 10 - 20 µm as a result of irradiation; this explains why ridging in this 96% TD pellet rod is not as pronounced as in rod 10. Max. ridge heights, 2.5 - 5 µm. A number of defects are noted along the rod, primarily at positions 50, 70, 130, 150, 185, 215, 405, 417, 590 and 640 mm from the bottom. These positions are verified by the ECT (fig. 30) and are probably secondary hydriding and cracks.

Rod B5-12, fig. 25.

The average diameter in the plenum area is unchanged, but an ovality of 30 µm has developed. The average diameter of the remainder of the rod has decreased by about 20 µm. Primary ridging is observed with ridge heights of 15 - 20 µm.

3.6. Gamma Scanning

3.6.1. Experimental and Results

Gamma scanning was performed on all rods except B5-12.

Scanning was performed with a nominally 0.5 mm tungsten collimator slit giving an effective slit width of 0.54 mm. The rods were run past the slit by a step-motor with a speed of 1.2 mm/min. averaged over a run and a stop period. The radiation of the rod was detected by a nitrogen-cooled Ge/Li crystal. After proper amplification, the output was tranferred to a series of single-channel analysers connected in parallel. Each of the isotopes ^{106}Ru/Rh, ^{137}Cs, ^{95}Zr/Nb and ^{144}Ce/Pr, at energies 512 keV, 662 keV, 756-765 keV and 696 keV, were registered by two single-channel analysers, the first set on the photo-peak, the second on the background before the peak. The gross activity was registered by one single-channel analyser. The output of each single-channel analyser was transferred to a CAMAC scaler that was read and erased by a computer for every 0.5 mm of rod passing the collimator.

Table 6 gives the relevant information about the isotopes recorded in the scanning.

Table 7 gives the form factors calculated from the curves. Local peaks are neglected in the calculation.

From the integration of the individual gamma scans given in table 8, the relative power of the rods is calculated based on different isotopes (table 9).

In table 10 the length of the post-irradiation fuel stack obtained from the gamma scanning is given together with the pre--irradiation length.

3.6.2. Rod Support Influence on the Curves

Small deviations from the expected isotope distribution are seen axially for all the rods. The deviations are positive on the gross curves, and negative on the isotope curves. The positions are given in table 11. The deviations were given great consideration, as they seemed inexplicable from a fabrication and irradiation point of view. Earlier scanning practice with analogue recording has never revealed similar features. Had they existed, they would have been masked by the statistical variations in the isotope decay. It may be concluded that these

deviations originate from the supports for the rods during the scanning operations.

The supports are made of brass, 25 mm long with steel rollers. Approximately 10% of the rod volume will be shielded by approx. 4 mm of brass. The influence upon the isotope scans should be almost negligible, as confirmed by the curves for the single isotopes, but an unexpectedly large influence due to the radiation scattered by the brass is seen on the gross curves. The influence on the total counts in the gross scanning curves is about 0.3%, which does not give rise to corrections of earlier tables. The influence upon other curves is much less.

3.6.3. Comments on results

When comparing the form factors originating from ^{137}Cs, valid for the irradiation as a whole, and ^{95}Zr, valid for the last few months of the irradiation, it is observed that the burn-up profile becomes flatter. This is to be expected because of the overall enrichment changes as a function of burning and build-up of Pu.

The presence of central thermocouples, especially in rods AA-1 and AE-5 at the hot ends, is reflected both in the form factors and in the calculated power distribution between the rods.

The form factors, as well as the relative power distribution among the rods, obtained from ^{106}Ru and ^{144}Ce are not readily explained. It appears that both fission product migration and neutron capture in fission products are required for a suitable explanation.

3.7. Neutron Radiography

3.7.1. Experimental

Neutron radiography was performed by the transfer method, using a 0.1 mm thick Dysprosium imaging foil and Agfa-Gevaert double-coated Structurix D4 X-ray film.

The rods were radiographed at two perpendicular projections step by step on 12 cm long foils with sufficient overlapping. The end-plug of rod 11 was additionally neutron-radiographed at 0^{o}, 120^{o} and 240^{o} on a single-coated Kodak SR film.

Radiography was carried out at the reactor DR 1 by simul-

taneous use of two 10 x 10 cm beam holes with intensities of 1.8×10^6 and 1.4×10^6 n/($cm^2 \cdot s$), respectively. To obtain equal exposures, the exposure times were 25 and 30 min,respectively.

3.7.2. Results

Rod AA-1.

Cracks were seen in almost all pellets. One pellet with more extensive transversal cracks is shown in fig. 42.

No longitudinal cracks were observed. Chips were broken off a few of the pellets. A chip from pellet No. 15 from the top end had entered the pellet-to-pellet gap. One larger pellet-to-pellet gap was seen close to the end of the thermocouple, see fig. 43.

Rod AB-2.

Several of the pellets had extensive cracks, fig. 44. Longitudinal cracks were also found, fig. 45, some of them extending through several pellets, fig. 46.

Rod AC-3.

Three pellets from the top of the fuel column were extensively cracked, fig. 47. The general appearance is seen in fig. 48. A small central void is seen in the bottom pellets (max. flux region), fig. 49.

Hydrides were observed in the end-plug shown in fig. 50.

Rod AD-4.

Randomly distributed cracks of minor intensities were observed. The pellet-to-pellet gap was highly enlarged, fig. 51. A slight gap between the spring sleeve and the cladding was seen at the 90° projection, fig. 52, but not at the 0° projection.

Rod AE-5.

Most of the pellets had randomly distributed cracks. Several corner chips were observed; some of these in the pellet-to-pellet gap as shown in fig. 53.

Rod AG-6.

The pellets were nearly unaffected by the irradiation, as can be seen in fig. 54.

Rod AH-7.

Transversal cracks were observed in all pellets. The dishings were almost filled up at the upper end of the rod, fig. 55.

Rod AJ-8.

Cracks were observed on all pellets except the bottom one. The dishings were almost filled up at the upper end of the rod, fig. 56.

Rod AO-9.

All pellets contained cracks, mostly transverse. The dishings were almost filled up, fig. 57. A wide gap between pellets 5 and 6 from the top end is shown in fig. 58. Chips are observed in the gap and a central void had formed close to the end of the thermocouple. The central void extends up to 200 mm from the top of the fuel column.

Rod AM-10.

Transverse cracks were observed on all pellets except the bottom one. Only few, small longitudinal cracks were seen.

Rod AK-11.

Only few, mostly transverse, cracks were observed.

Hydrides were observed in connection with the cracked end-plug, fig. 59.

Rod B5-12.

All pellets contained cracks, mostly transverse, fig. 60a.

General remarks

In general, the dishings were more closed towards the hotter end of the rods. Chips were only observed in pellet-to-pellet gaps, never in the pellet-to-clad gap and no fuel-cladding interaction was revealed.

No hydriding of the cladding was observed with the exception of the end-plug in rod AC-3 and in connection with the failed end plug in rod AK-11.

4. DESTRUCTIVE EXAMINATION

4.1. Piercing and Fission Gas Analysis

4.1.1. Experimental

The rods were pierced in the plenum area close to the top end-plug. The piercing area was sealed by an O-ring, and a mechanical penetration was made. The fission and filler gasses were extracted, and their volume determined. The accuracy of the determination of the amount of the extracted gas is 1.5%, corresponding to one standard deviation.

After completed extraction, the rod was backfilled with helium at a pressure of 1 ata. The helium was extracted and the free volume of the rod hereby measured. As the dead volume of the piercing head is less than 0.5 cm^3, the accuracy of the freevolume determination is better than 2.0%, corresponding to one standard deviation.

The pressure in the rods (in Hot-Cell condition) was calculated on this basis. The accuracy of this is better than 2.5%, corresponding to one standard deviation.

Gas from each rod was filled into glass bulbs, which were used for mass-spectrometric analysis and for gas-chromatography. Through mass-spectrometric analysis, the relative distribution of H_2, He, N_2 + CO, O_2, Ar, CO_2, CH_4 and isotopes of Kr and Xe was found. The ratio between N_2 and CO was determined by gas--chromatography.

4.1.2. Results

The amount and composition of the extracted gas are shown in tables 12 and 13. Neither CO nor CH_4 was found in any sample. Results from AC-3 are excluded because of equipment failure, and from AK-11 because this pin was failed and therefore not examined. Where two numbers appear in the tables, two samples were analysed. The difference in two such analysis results is probably mainly caused be the fact that the samples from the extracted gas were taken during the extraction, and not from the total gas volume combined after extraction.

Table 14 shows the amount of extracted fission gas (Kr + Xe), the gas release per cent, the free volume of the rods and

the pressure in the rods. The fission gas release is calculated from a gas production equal to 0.3×10^{-4} $cm^3/(\frac{MWd}{tMeO_2} \times$ gram $MeO_2)$ at 0^oC and 760 mm Hg [2].

The burn-up figures required for the calculation of the fission gas production are average figures calculated from destructive isotope analysis and ^{137}Cs scans.

For rods subjected to destructive isotope analysis, the burn-up found was set proportional to the ^{137}Cs activity at the corresponding axial position, from which it follows that the average activity of the rod is proportional to the average burn-up.

For rods not subjected to destructive isotope analysis, the burn-up value was based upon the figure obtained for rod AA-1, multiplied by the ratio of the average ^{137}Cs activities between the rod in question and rod AA-1.

For rod B5-12, neither isotope analysis nor gamma scanning was requested. The burn-up was chosen as the average burn-up of the remaining rods in the lower cluster.

4.1.3. Comments on Individual Rods

Rod AA-1: High H_2-content.

Rod AB-2: High H_2- and N_2-content; very small content of O_2 excludes inleak of air during piercing.

Rod AD-4: No remarks.

Rod AE-5: High N_2-content; very small content of O_2 excludes inleak of air during piercing.
Total absence of He seems unexplainable; unusually low gas content.

Rod AG-6: High N_2 and O_2 contents indicate inleak of air during piercing.
Unusually high He-content.

Rod AH-7: No remarks.

Rod AJ-8: No remarks.

Rod AO-9: No remarks.

Rod AM-10: No remarks.

Rod B5-12: Unusually high He-content.

4.2. Metallography, Ceramography and Autoradiography

4.2.1. Sample Locations

Rods AA-1, AE-5, AH-7, AO-9 and AK-11 were examined. The sample position in these rods is shown in fig. 60b and table 15.

4.2.2. Preparation of Samples

The samples were prepared and examined according to the following scheme:

- cutting
- vacuum impregnation with araldite
- mounting in araldite
- grinding on 600 grit SiC-paper
- polishing with 7 µm diamond
- fuel attack polishing in Al_2O_3 + CrO_3
- cladding attack polishing in CrO_3 + HF
- examination in microscope (polished)
- fuel etching in H_2SO_4 + H_2O_2
- cladding etching in lactic acid + HNO_3 + HF
- examination in microscope (etched)

4.2.3. α-Autoradiography Technique

A Kodak film, type CA 80-15, was loaded on the sample and exposed for ~ 5 s. The film was developed by a standard procedure.

4.2.4. β/γ-Autoradiography Technique

A Kodak film, type 2, high resolution, was loaded on the sample and exposed for 3 - 4 min. The film was developed by a standard procedure.

4.2.5. General Observations

1) The fuel contains two classes of pore; the normal, small pores and some very large ones, about 80 µm in diameter. The latter are randomly distributed (from fabrication) - see e.g. fig. 62.

2) The fuel appears inhomogeneous. There are several examples of larger or smaller areas that have a pore distri-

bution very different from their surroundings - see e.g. figs. 169 and 255.

3) The α- and β/γ- autoradiographs generally show a very finegrained structure with an increased radiation intensity towards the surface of the fuel - see e.g. fig. 63. A skew radiation intensity is seen in several samples, probably indicating a skew flux profile in the reactor - see e.g. figs. 230-233.

4) The hydrides in the cladding are circumferentially orientated, except in rod AK-11, where radial hydrides are found (the cracked rod).

5) The measurements of the oxide layer thickness on the inner and the outer surface of the cladding, the cladding and gap thickness, the estimated hydride content in the cladding, the extent of fuel restructuring, and an estimated fuel centerline temperature are shown in table 16.

The hydride content is estimated from the micrographs. The estimate of the fuel centerline temperature is regarded as very rough. The basis for this estimate is the fraction of the fuel with columnar grains. A model [3] for this type of grain growth (for pure UO_2) gives the centerline temperature.

Figure 61 gives a survey of the samples (excl. sample Nos. AK-11-2-1 and AK-11-6-1).

Figures 62-264 show for each sample (with a few exceptions):

- a macrophotograph of the polished sample
- α- and β/γ-autoradiographs in the same magnification as the macro, in polished and in etched condition
- a radius of the sample in polished and in etched condition (not always the same area)
- diverse macro- and micrographs, including pictures for quantitative metallographic analysis.

4.2.6. Remarks on Individual Samples

Sample AA-1-1, fig. 62-77

No remarks.

Sample AE-5-1, fig. 78-90

No remarks.

Sample AH-7-1, fig. 91-103

Metallic inclusions are observed in an area with large fuel grains - fig. 102. The latter contain some small black "needles" of unknown composition. A grey zone - fig. 103 - is observed between fuel and cladding oxide; it looks like fuel.

Sample AO-9-1, fig. 104-116

A very broad grey zone, as in sample 7-1, is observed - figs. 115-116. Metallic inclusions and pores are often seen in the columnar grains - fig. 114. No traces from TC are observed.

Sample AO-9-2A, fig. 117-127

A reasonable explanation of the appearance of the centre void could be that, as a result of the large pellet/pellet gap, observed in the neutron radiograph fig. 58, some evaporation has occurred from the hotter surroundings with a corresponding condensation at the end-section. This implies that the large pellet/pellet gap was present while the rod was in the reactor.

The black shadow seen in the β/γ-autoradiographs - figs. 120-121, and the sharply defined missing fuel in the etched α-autoradiograph - fig. 119 are the result of an underlying trace of an erroneous cutting.

In the β/γ-autoradiographs - figs. 120-121 - are seen 3 distinct zones of different radiation intensity along a radius. The fuel is apparently depleted in β/γ-emitting elements near the centre. The columnar grains apparently have subgrain boundaries with small pores - fig. 126.

Sample AO-9-5A, fig. 128-142

The marks in the cladding surface are made for orientation of the sample.

The section contains a secondary fuel crack - fig. 128. Three zones in the β/γ-autoradiographs - fig. 131-132 - are seen, as in sample 9-2A. Notice the area with very small pores in fig. 140.

Sample AK-11-1, fig. 143-157

This is the cracked end-plug.

Along the sides of the widest crack in the outer ring, the grain size in the outer two-thirds is larger than elsewhere - fig. 156.

These large grains, the small grains along the inner surface of the plug, and a few other randomly distributed grains show some twin or Widmanstätten structure. The smaller and thinner ring contains some cracks, fig. 157. The hydride content and orientation are shown in figs. 144-149.

Sample AK-11-2-A, fig. 158-178

This section contains only destroyed TC-fragments, mainly in cracks - figs. 169-170. Severe cladding attack is seen in figs. 165, 166, 174, 175 and 176.

Some radial hydrides in the cladding are seen in fig. 171.

Between the fuel and the cladding are seen two layers, the inner one being more or less curved and separated from the outer one by small pores; the phases look like ZrO_2 - fig. 178.

There are many white, sometimes sponge-like strings, in the cladding. Near the inner surface of the cladding these strings appear to condense to some hard phase - figs. 172 and 173. In fig. 173 this hard phase lies in the same plane as the fuel, while the cladding lies at a lower level; the boundary between the hard phase and the cladding appears as a black zone; actually this zone is just a slope lying in shadow. The origin and composition of this strange phase are unknown.

Sample AK-11-2-1, fig. 179-194

This shows a cladding failure - figs. 192, 193 and 194; notice an oxide layer on the crack surface in fig. 192. There are small fuel-cladding interactions in two other places - fig. 190. The section contains only destroyed TC-fragments, mainly in cracks - figs. 186 and 187. There are layers between the fuel and the cladding as seen in sample 11-2-A - see here fig. 191. Some Pu-concentrations are observed - figs. 188-189.

Sample AK-11-3, fig. 195-210

The black spot in the cladding is a fault in preparation and can be ignored.

This section contains destroyed TC-fragments only, mainly

in cracks - fig. 209-210. Some small fuel-cladding interactions are observed - fig. 207. There are layers between the fuel and the cladding as in sample 11-2-A.

Sample AK-11-6-A, fig. 211-228

This shows a cladding failure - figs. 218-219. There are white strings in the cladding, and layers between fuel and cladding, cf. sample 11-2-A. A few radial hydrides are observed - fig. 225. There are several Pu-concentrations - fig. 224.

Sample AK-11-6-1, fig. 229-241

During preparation, cracks were observed in the cladding; however, no cracks were visible in the final stage of microscopy. Further grinding did not reveal any cracks, indicating that the failed zone had been removed during preparation. There are layers between fuel and cladding, as in sample 11-2-A, fig. 241. Some Pu-concentrations are observed, fig. 237.

Sample AK-11-7, fig. 242-264

This shows a cladding failure - figs. 249, 250, 263 and 264. Small interactions are seen - figs. 259-260. At two other positions - apart from the failure position - there are zones with hydride concentration or radial hydrides - figs. 257-258. There are layers between fuel and cladding as in sample 11-2-A. Some Pu-concentrations are observed - fig. 256.

4.3. Quantitative Metallography

The purpose of this examination was to obtain an estimate of the size and distribution of the smaller pores in the fuel. The examination was performed on selected areas of the samples already used for ceramography.

The fuel samples contained a certain number of pores of approximately 80 µm in diameter (from fabrication); these are not included in the present examination (see figures from the ceramography examination).

The areas were selected outside fuel cracks and represent different fuel densities, but they have a uniform density within the individual areas.

The exaimination was performed using Leitz equipment. Positive photographs at 400 times magnification with a high degree of contrast were used.

Pore sizes were classified in 21 classes, the lowest comprising pores with a diameter < 0.5 μm (the greatest sensitivity obtainable), the interval 0.5 to 8.5 μm being in steps of 1 μm and the interval 8.5 to 32.5 μm into steps of 2 μm.

The average diameter and the total pore area were calculated for each sample. The results are shown in table 17 and 18.

4.4. Fuel Density Determination

The density of the fuel was measured by immersion in water containing 10 mg detergent (catanac) per liter.

The size of each sample was approx. one pellet. However, a smaller amount of fuel adhered to the cladding after defuelling, and in all five cases some of the fuel was sampled as coarse powder.

The results are shown in table 19.

According to [1], the pre-irradiation density in the table is equivalent to the density by immersion. All mass measurements were performed on an analytical balance, ± 0.01 mg, the water temperature was measured within 0.2°C. The contribution to the overall uncertainty from these density measurements is negligible compared with the uncertainty due to the powdered samples, because it was necessary to remove the powder before the determinations. The relatively small decrease in density of the sample from rod AO-9 may reflect this feature, because this sample had the highest powder content (approximately 50%).

4.5. Isotope Analysis of Fuel

Isotope fuel analysis was carried out on diluted fuel solutions along three lines as determinations of:

1) Uranium and plutonium isotopes;
2) ^{148}neodymium;
3) ^{238}plutonium, ^{241}americium, ^{242}curium, and ^{244}curium.

4.5.1. Cutting and Dissolution Procedure

Each specimen was cut at the pre-determined position, having a length corresponding to a pellet length, and the specimen was stored in a polyethylene container. Before dissolution, the pellet was extracted from the piece of cladding and crushed in disposable equipment. The small pieces of fuel were weighed in their container, whereafter the fuel was transferred to the dissolution flask, and the empty container reweighed. The fuel was dissolved in 50 ml of concentrated nitric acid. The dissolution took an average of 72 hours. The solution was transferred quantitatively to a weighed polyethylene bottle, and subsequently made up to about 100 g with washing liquids, 8 M HNO_3, and reweighed. After homogeneisation by magnetic stirring, a weighed aliquot (about 0.7 g) was diluted with 500.0 g 8 M HNO_3. This solution, containing 0.14-0.21 mg fuel pr. g, was used as the working solution for the three lines of analysis.

4.5.2. Uranium and Plutonium Determination

The isotope composition and the concentrations of U and Pu were determined by mass spectrometry and isotopic dilution mass spectrometry, respectively. U and Pu were fixed on a Dowex (1 x 8) ion exchanger column in a 8 M HNO_3 solution. Fission products, americium, curium, and excess uranium, were removed by washing with 8 M HNO_3. Finally, U and Pu were removed by washing with 0.35 M HNO_3 and ^{233}U, ^{234}U, ^{235}U, ^{236}U ^{238}U, ^{239}Pu, ^{240}Pu, ^{241}Pu, and ^{242}Pu were determined by mass spectrometry. Spiking was performed with ^{233}U and ^{242}Pu obtained from ORNL, calibrated against natural uranium and a ^{239}Pu standard (NBS). In the case of spiked samples, the plutonium spike and the plutonium in the sample were adjusted to the same oxidation level prior to the ion exchange by an oxidation/reduction procedure using sodium nitrite and hydroxylammonium chloride.

In most cases, three separations without spike and two separations with spike were sufficient to give satisfactory results. The separation procedure is described in [5].

Mass spectrometric measurements were performed on a mass spectrometer, MAT CH-4, using rhenium double filaments. A

minimum of ten runs for each separation formed the basis for the calculation.

4.5.3. Neodymium Determination

Determination of ^{148}Nd was carried out by isotopic dilution mass spectrometry, using ^{150}Nd as spike.

The sample was loaded on an ion exchange column, Dowex (1 x 4), in a methanol - 0.04 M nitric acid solution. The lanthanides were successively eluted by a methanol - 0.0032 M nitric acid solution. The procedure is described in [6], although some small modifications were made. The separated Nd solution was determined mass spectrometrically on a MAT CH-4 mass spectrometer using rhenium double filaments. The masses of the neodymium isotopes were analysed from a minimum of ten runs. The mass range 140-152 was measured before and after the ten runs. The absence of masses 140 and 152 was used as an indication of satisfactory separation of neodymium from cerium and samarium, respectively. The mass spectrometry results were corrected for contamination with natural neodymium. Double determinations were performed both on unspiked and spiked samples.

4.5.4. Alpha Spectrometry

Alpha spectrometry was carried out to determine the concentration of the isotopes ^{238}Pu, ^{241}Am, ^{242}Cm, and ^{244}Cm.

From 5 to 10 drops of the working solution were placed on a 20 mm diameter disc made of polished stainless steel. The disc was dried under a infrared lamp and heated to 800°C on an electric burner. After cooling, the disc was transferred to a vacuum chamber, where it was placed under a silicon crystal with an active area corresponding to the disc area. The alpha radiation was analysed by a ND multichannel analyser, utilizing 1000 channels for the energy range between 4.8 and 6.3 MeV. The FWHM of the crystal was approximately 20 keV.

The evaluation of the spectrum to determine the amounts of ^{238}Pu + ^{241}Am, ^{244}Cm, and ^{242}Cm, relative to the sum of ^{239}Pu and ^{240}Pu, was performed using the method described in [7].

The analysis was repeated using a solution from which americium and curium were removed by ion exchange (the same procedure as described in 4.5.2). This analysis gave the amount of ^{238}Pu relative to the sum of ^{239}Pu and ^{240}Pu.

From these two alpha spectrometry determinations, and from the mass spectrometric determinations of $^{239}Pu/^{240}Pu$ and $^{239}Pu/^{238}U$ were calculated the amounts of ^{238}Pu, ^{241}Am, ^{242}Cm and ^{244}Cm relative to ^{238}U at the moment of analysis.

4.5.5. Decay Corrections

The following isotopes were corrected for accumulation and/or disappearance during the period between shut-down of the reactor and the time of analysis:

^{234}U
^{238}Pu
^{241}Pu
^{241}Am
^{242}Cm
^{244}Cm

^{234}U was corrected according to:

$$^{238}Pu \xrightarrow{\alpha} {}^{234}U$$

^{238}Pu was corrected according to the scheme:

$$^{242}Cm \xrightarrow{\alpha} {}^{238}Pu \xrightarrow{\alpha} {}^{234}U$$

taking into account the fact that some ^{238}Pu was formed by the decay of ^{242}Cm and that the ^{238}Pu decayed to ^{234}U.

^{241}Pu was corrected according to the event:

$$^{241}Pu \xrightarrow{\alpha} {}^{241}Am$$

^{241}Am was corrected according to the scheme:

$$^{241}Pu \xrightarrow{\beta} {}^{241}Am \xrightarrow{\alpha} {}^{237}Np$$

taking into account the formation of ^{241}Am from beta decay of ^{241}Pu and the alpha decay of ^{241}Am.

^{242}Cm and ^{244}Cm were corrected according to:

$^{242}Cm \xrightarrow{\alpha} {}^{238}Pu$

$^{244}Cm \xrightarrow{\alpha} {}^{240}Pu.$

4.5.6. Results

Six fuel samples were analysed according to the procedures described above. The results are shown in table 20; cutting positions are included in the table and in fig. 60b.

The isotope values (except the values for g ^{238}U per g fuel) are the ratios between the number of atoms and the number of ^{238}U atoms. Decay corrections are performed so that the results are valid at the time of fuel discharge (20 September 1975).

BU (A/O) is the per cent of all initial heavy metal atoms that have fissioned, i.e. equal to % FIMA. The burn-up results are calculated using 0.0170 as the fission yield of ^{148}Nd. The factor $8.3 \cdot 10^3$ can be used to convert BU (A/O) to MWd/t MeO_2, i.e. a BU (A/O) value of 1 is equal to 8,300 MWd/t MeO_2.

The accuracy on the burn-up results is 1-3% determined from the precision on the double determinations, and on our experience with the standard solutions involved.

The results from the alpha spectrometrical part of the analysis, and especially the determinations of ^{241}Am and ^{244}Cm, have an estimated uncertainty of up to 15% (only single determinations were performed). This high uncertainty is primarily due to energy degradation and to the resulting overlap of the alpha peaks, a problem usually encountered in alpha spectrometry.

5. DISCUSSION

5.1. General Behaviour

The rods appeared normal both visually and dimensionally regarding length and bow. The length had increased less than 0.2%, and the bow was negligible in relation to the rod length.

Four rods showed an increase in average diameter of 10-15 µm (AB-2, AC-3, AE-5 and AK-11). No explanation can be given; it is, however, noticeable that the fission gas analyses for two

of the rods, AB-2 and AE-5, showed the presence of a fairly large amount of N_2; no gas analyses are available for rod AC-3, as the piercing of this rod failed, or for AK-11 that failed in the reactor. No other rods showed noticeable amounts of N_2 in the plenum gas.

5.2. Burn-up

The results from the isotope fuel analysis seem reasonable when comparing the figures mutually and when comparing them with the gamma scans. There is one exception, however. The burn-up results for sample AO-9-3 may be about 4.5% too high, as seen from the isotope correlation technique and from gamma scans.

The figure below shows the correlation between the atomic ratio ^{240}Pu /^{239}Pu and BU (A/O) determined by the ^{148}Nd method. Assuming a linear correlation,

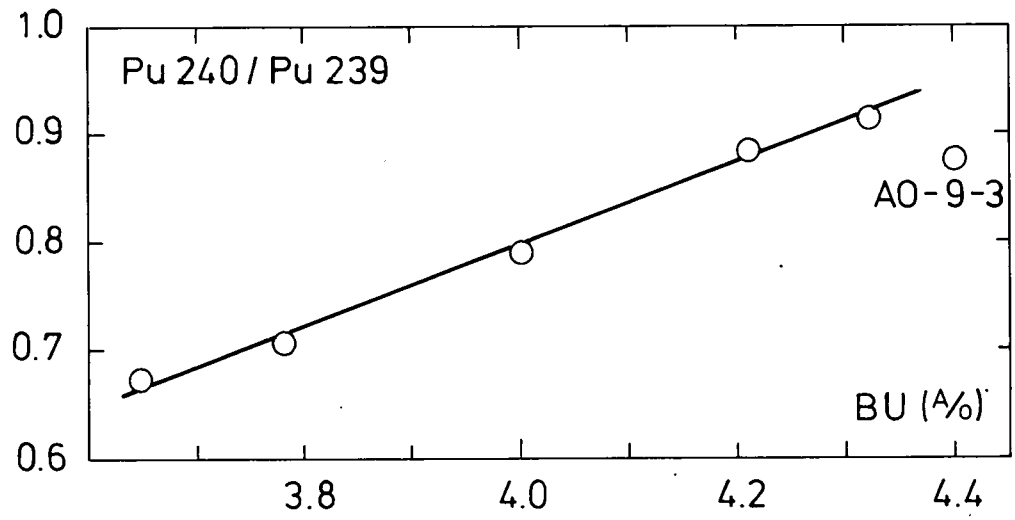

it is seen that the $^{240}Pu/^{239}Pu$ ratio for sample AO-9-3 corresponds to a Bu equal to 4.2 A/O; other correlations indicate a similar BU for this sample. Furthermore, this BU-value is to be expected from the ^{137}Cs gamma scan on rod AO-9, using the BU-value for sample AO-9-6 as a calibration point.

5.3. Fuel Behaviour

From the distribution of Cs as obtained from gamma scanning, the relative distribution of temperature between the fuel rods was estimated. Special features at TC-bores and TC failure locations were neglected. The estimate gives for the upper cluster:

$T_{AG-6} < T_{AD-4} < T_{AA-1} = T_{AB-2} = T_{AC-3} < T_{AE-5}$

T_{AA-1} being about 1600°C, and for the lower cluster:

$T_{AK-11} < T_{AH-7} < T_{AJ-8} = T_{AM-10} < T_{AO-9}$

T_{AH-7} being about 1600°C.

It should be noted that rod AK-11 failed, therefore the principles for comparison may not be applicable in this case.

These estimates are in good agreement with the estimates obtained from ceramography (table 16), except for rod AK-11.

From the figure below it may be concluded that the fission gas release increases with increasing pellet density.

Increasing the gap apparently increases the gas release at high BU, whereas an unexpected decrease is observed at the low BU; this observation may, however, be insignificant as it is based on very few results from a release process that is known to give highly scattered results.

The gas release is clearly higher for the lower cluster as compared to the upper cluster.

The isotope ratios (table 13) are fairly constant for the upper and for the lower cluster rods. The ratios differ in the two clusters, as expected.

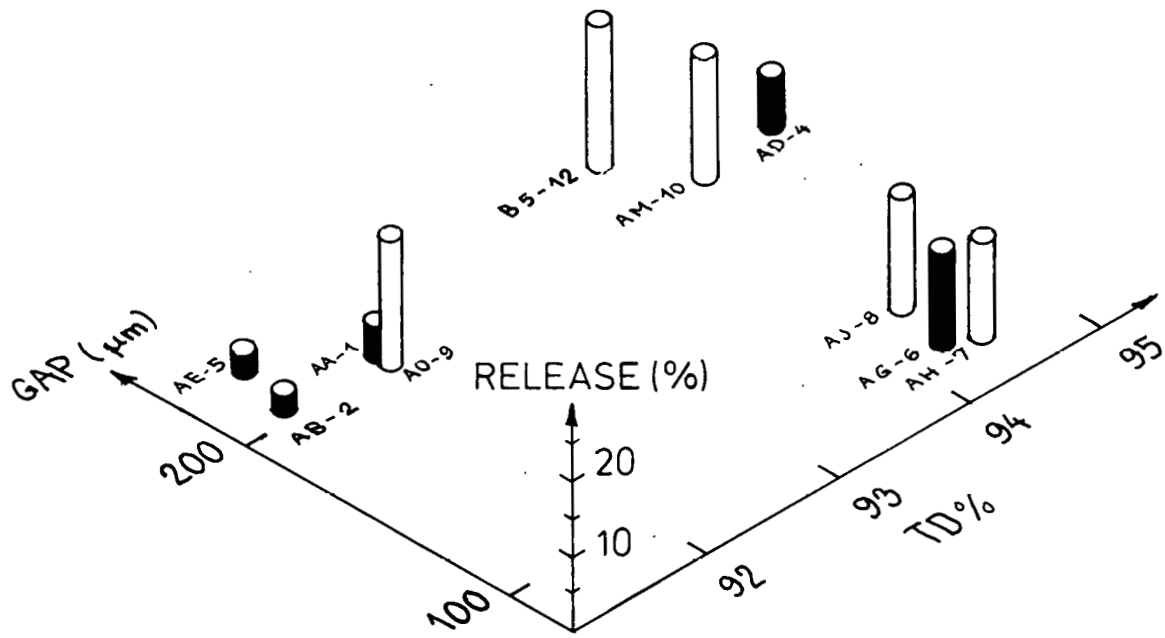

● ~ 23000 MWd/t MeO_2, O ~ 30000 MWd/t MeO_2

It is evident from the ceramographic examination that the fuel density varies quite considerably within a single sample; nevertheless, samples for quantitative metallography could be selected from homogeneous areas. To obtain a more detailed picture of the pore size distribution, different porosity areas were chosen for the examination. The results suggest that the pore size distribution is independent of the fuel density. Most of the pores were below 4 µm in diameter with an average of about 2 µm. In samples from rod AK-11, some almost pore-free areas are observed. The derived theoretical density of the examined areas is included in table 18.

The measured pellet densities are all lower than pre-irradiation densities, which might be expected as all the samples are taken from positions with a burn-up of 30000 MWd/t MeO_2 or more.

5.4. Pellet-clad Interaction, PCI

Variations in initial fuel density caused little, if any PCI at an average BU of 23100 MWd/t MeO_2 in rods having an initial gap of 210 µm (rods AA-1, AB-2, AC-3 and AD-4 with initial densities 92.06, 91.5, 90.6 and 95.1% TD, respectively). With the same gap at an average BU of 30800 MWd/t MeO_2, higher initial density (rod AM-10, 94.5% TD) caused a larger extent of PCI (compared to rod AO-9, 92.1% TD). In none of the rods in question was any decrease in cladding diameter observed; it is therefore assumed that the observed PCI is solely a function of swelling of the fuel.

The bottom ends of rods AA-1, AB-2, AC-3 and AD-4, having a BU of app. 30000 MWd/t MeO_2, resemble rod AO-9 in cladding behaviour, indicating that the closure of the 210 µm gap occurred close to 30000 MWd/t MeO_2.

The changes in the fuel stack length of the rods are in accordance with the PCI observations. The low density rods (AA-1, AB-2 and AC-3) have an overall fuel stack shortening of 4-5 mm, the higher density rod (AD-4) at the low BU level exhibited a fuel stack shortening of only 2 mm, whereas, at the high BU level, the low density rod AO-9 showed an increase in fuel stack length of about 1 mm and the stack of the high density rod AM-10 similarly increased 2.5 mm.

The influence of initial gap size on cladding behaviour was clearly demonstrated at 30800 MWd/t MeO_2. With an initial density of about 94.3% TD, rods AH-7 (90 µm gap), AJ-8 (140 µm gap), AM-10 (210 µm gap), and B5-12 (250 µm gap) produced ridging. Rod AH-7 produced primary as well as secondary ridging along the full stack length on a cladding that had had an average diameter increase that varied in accordance with the power profile. Rod AJ-8 produced primary ridging along the full stack length, with secondary ridging at the hot end. Also here a diameter increase varying in accordance with the power profile was observed. Rod AM-10 produced primary ridging, with a few randomly distributed secondary ridges, but the general diameter increase (seen in rods AH-7 and AJ-8) was absent. Rod B5-12 produced primary ridging only.

At 23100 MWd/t MeO_2, rods AD-4 and AG-6, having initial densities of 95.1% TD and 94.3% TD, respectively, exhibited a different cladding behaviour; rod AG-6 with an initial gap of 100 µm showed a pronounced ridging, while rod AD-4 (210 µm gap) only showed a slight tendency to ridging.

5.5. The Failed Rod AK-11

Rod AK-11, which failed a couple of months before the termination of irradiation, was severely hydrided. The failure is supposed to have initiated at the upper end-plug where a thermocouple passed through. The cable insulation material (Sauereisen), which is composed of water-glass and silicagel, is known to release some water at elevated temperature. Such water released at on-power conditions might have initiated hydriding of the end-plug, which, because of the corresponding increase of volume of the material, would have resulted in the cracking of the plug.

6. CONCLUSION

One out of the twelve rods failed (rod AK-11), presumably from reasons unconnected with fuel/clad design or irradiation conditions. This rod was found to have a leak and to be failed at the end-plug, while several (presumably secondary) failures were observed in it.

Ridging existed on all rods. The smallest initial gap caused the largest ridgings.

With the possible exception of rod AO-9 (EC-signal), no signs of potential failures were observed in spite of pellet--clad interaction.

In a few cases an increase in general diameter of up to 15 µm was observed and a decrease of 20 µm was measured in one case (rod B5-12).

The oxide formation and the hydride content in the cladding agrees with the actual burn-up as can be expected for water--reactor fuel rods.

The normal maximum fuel temperature estimated from ceramography was 1850-2000°C; samples from rod AO-9 have experienced a higher temperature, presumably caused by a TC-reaction or some fuel irregularity.

In the hottest areas of the fuel, the dishings were practically filled out.

The Pu was distributed homogeneously as a fine-grained structure.

The distribution of the pore size was found to be independent of the initial fuel density, with most of the pores below 4 µm in diameter.

The fuel density, measured only on samples in the high burn-up areas, showed a decrease of less than three per cent.

ACKNOWLEDGEMENTS

The authors gratefully acknowledge the participation of the staff members from the Metallurgy/Hot Cell Department, the Chemistry Department and the DR 1 Reactor. Especially the following persons are acknowledged: Frank Adrian, Susanne T. Andersen, Dennis Cooper, Knud Jensen, Palle V. Jensen, Claus Johansen, Preben B. Olesen, Ole Olsen, Kishore C. Sahoo and Torben R. Strauss.

Thanks are also due to J. Christensen, W.F. Domenico, P.E. MacDonald and W.J. Quapp for fruitful discussions during the examination.

REFERENCES

[1] ANCR-1270, NRC-3.
USNRC-OECD Halden Project Fuel Behaviour Test Programme. Experiment Data Report for Test Assemblies IFA-226 and IFA-239.
E.T. LAATS, P.E. MacDONALD, W.J. QUAPP, 1975.

[2] KFK 2057.
Spaltgasverhalten in Oxid-Brennelementen für Schnelle Brüter.
H. Zimmermann 1974.

[3] F.A. Nichols, J.Nucl.Mat. 22 (1967) p. 214-222.

[4] M.F.Ashby and R. Ebeling
Trans.Met.Soc. AIME, vol. 236, p. 1396 (1966).

[5] EUR 4638e, p. 106-108.

[6] TRG Report 1496. The Separation of Neodymium for the Determination of the Burn-up of Nuclear Fuels.
D.J. Savage, L. Drummond, 1967.

[7] B.A.R.C. - 824. Determination of Plutonium-238 in Plutonium by Alpha Spectrometry.
S.K. Aggaval et al., 1975.

Table 1

Extent of the post-irradiation examination

Rod	1 AA	2 AB	3 AC	4 AD	5 AE	6 AG	7 AH	8 AJ	9 AO	10 AM	11 AK	12 B5
Visual inspect.	x	x	x	x	x	x	x	x	x	x	x	%
Length measurem.						x	x	x		x		x
Bow measurement						x	x	x		x		x
Profilometry	x	x	x	x	x	x	x	x	x	x	x	x
Gamma scanning	x	x	x	x	x	x	x	x	x	x	x	
Eddy current testing							x	x	x	x	x	
Neutron radiography	x	x	x	x	x	x	x	x	x	x	x	x
Piercing	x	x	x	x	x	x	x	x	x	x	x	x
Metallography	x				x		x		x		x	
Autoradiography	x				x		x		x		x	
Quantitative metallography	x				x		x		x		x	
Fuel density	x				x		x		x		x	
Burn-up; isotope analysis	x				x		x		x		x	

Table 2

FUEL ROD DATA FOR IFA-226 (as fabricated, cf. [1])

	Rod	Danish ref. No.	Cladding[a]		Fuel[b]			Gap[d] (mm)	Instrumentation*
			OD (mm)	ID (mm)	Density[c] (%theoretical)	Diameter (mm)	Stack Length (mm)		
Upper Cluster	AA	1	10.69	9.51	92.06	9.30	653	0.21	FCT,PT
	AB	2	10.64	9.52	91.50	9.30	650	0.21	PT
	AC	3	10.66	9.51	90.58	9.30	650	0.21	PT
	AD	4	10.65	9.52	95.10	9.30	663	0.21	PT
	AE	5	10.68	9.51	91.64	9.26	655	0.25	FCT,PT
	AG	6	10.68	9.50	94.33	9.40	663	0.10	ES
Lower Cluster	AH	7	10.69	9.49	94.46	9.40	607	0.09	ES
	AJ	8	10.67	9.50	94.43	9.35	610	0.14	ES
	AK	11	10.66	9.51	95.94	9.31	607	0.20	FCT,ES
	AM	10	10.68	9.50	94.52	9.30	607	0.20	ES
	AO	9	10.66	9.52	92.11	9.30	615	0.21	FCT,ES
	B5	12	10.67	9.51	94.18	9.26	612	0.25	-

* FCT = Fuel Centerline Thermocouple, hole diameter = 1.73 mm

* PT = Pressure Transducer

* ES = Elongation Sensor

[a] All cladding made of zircaloy-4

[b] Fuel pellet length = 15.0 mm, Dish depth = 0.33 mm, Dish shoulder = 1.70 mm, Dish spherical radius = 6.79 mm

[c] The values listed here are measured geometric densities (that is, weight divided by volume). The density of a limited number of fuel samples was also measured by immersion techniques. The immersion (true) densities were found to be about 3/4% higher at all density levels.

[d] Backfill helium pressure = 1.01×10^4 N/m^2.

Table 3

Results of the length measurements.
The pre-irradiation length was specified to be 824 ± 0.5 mm

Rod	$l_{min.}$ (mm)	$l_{max.}$ (mm)	l_{mean} (mm)
AG-6	824.26	824.28	824.27
AH-7	825.22	825.25	825.24
AJ-8	824.97	825.02	825.00
AM-10	825.09	825.10	825.10
B5-12	825.12	825.17	825.15

Table 4

Results of the bow measurements

Rod	Max.bowing[a] (mm)
AG-6	.7
AH-7	.5
AJ-8	1.0
AM-10	1.2
B5-12	1.0

[a] The values are ± 0.1 mm

Table 5

Summary of the profilometry

Rod	As fab. gap (μm)	Changes in outer diameter	Ridging	Remarks
AA-1	210	NIL	Slight tendency	Ridging not rotationally symmetric
AB-2	210	10-15 μm increase	Slight tendency	Ovality max. 40 μm
AC-3	210	15 μm increase	Slight tendency; height 2.5-5 μm	-
AD-4	210	NIL	Slight tendency; height 2.5-5 μm	Ovality max. 30 μm
AE-5	250	15 μm increase	Only at TC pellets	-
AG-6	100	NIL	Pronounced; height 15-18 μm	Beginning of secondary ridging at hot end
AH-7	90	see text	Pronounced; height 30 μm	Secondary ridging all along the stack
AJ-8	140	see text	Pronounced; height 30 μm	Secondary ridging at hot end
AO-9	210	NIL	Slight tendency; height 2.5-5 μm	-
AM-10	200	NIL	Pronounced; height 30 μm	Few secondary ridges
AK-11	200	15 μm increase	Slight tendency; height 2.5-5 μm	Rod failed
B5-12	250	20 μm decrease	Pronounced; height 15-20 μm	Ovality max. 30 μm

Table 6

Data concerning isotopes registered in the gamma scanning

Isotope	Half-life	Fission yields %		
		^{235}U	^{239}Pu	^{241}Pu
^{106}Ru	368 d	0.4	4.4	6.08
^{137}Cs	30.6 y	6.18	6.48	6.49
^{95}Zr	64 d	6.47	5.8	4.78
^{144}Ce	284 d	5.40	3.79	4.09

Table 7

Form factors calculated from the respective isotope gamma scans

Rod \ Isotope	^{137}Cs	^{106}Ru	^{144}Ce	^{95}Zr	Gross
AA - 1	1.54	1.34	1.66	1.39	1.52
AB - 2	1.59	1.36	1.70	1.45	1.54
AC - 3	1.60	1.35	1.76	1.41	1.58
AD - 4	1.58	1.31	1.71	1.40	1.58
AE - 5	1.56	1.37	1.69	1.41	1.53
AG - 6	1.58	1.31	1.68	1.41	1.54
AH - 7	1.17	1.09	1.21	1.10	1.14
AJ - 8	1.16	1.10	1.21	1.11	1.12
AO - 9	1.17	1.08	1.20	1.11	1.16
AM - 10	1.16	1.11	1.20	1.10	1.14
AK - 11	1.12	1.10	1.20	1.10	1.16

Table 8

Total number of counts accumulated in the gamma scans. The results of the digital integration are given in total counts

Rod	Isotope	^{137}Cs 10^{-6}	^{106}Ru 10^{-6}	^{144}Ce 10^{-6}	^{95}Zr 10^{-6}	Gross 10^{-9}
AA - 1		31.28	34.93	6.30	40.12	1.459
AB - 2		32.91	36.02	6.99	44.66	1.545
AC - 3		32.97	36.37	6.98	45.91	1.554
AD - 4		32.76	36.41	6.96	47.31	1.551
AE - 5		30.50	34.44	6.08	39.80	1.451
AG - 6		33.28	35.92	7.02	46.55	1.568
AH - 7		45.05	41.89	10.13	52.17	2.135
AJ - 8		44.34	42.18	9.90	50.27	2.101
AO - 9		42.60	41.39	9.26	48.94	2.013
AM - 10		42.00	40.74	9.15	48.19	1.984
AK - 11		41.43	39.63	8.79	46.94	1.958

Table 9

Power distribution among the rods relative to rod AH-7, the distribution is based upon total number of counts (table 8)

Rod	Isotope	^{137}Cs	^{106}Ru	^{144}Ce	^{95}Zr	Gross
AA - 1		0.69	0.83	0.62	0.77	0.68
AB - 2		0.73	0.86	0.69	0.86	0.72
AC - 3		0.73	0.87	0.69	0.88	0.73
AD - 4		0.73	0.87	0.69	0.91	0.73
AE - 5		0.68	0.82	0.60	0.76	0.68
AG - 6		0.74	0.86	0.69	0.89	0.73
AH - 7		1.0	1.0	1.0	1.0	1.0
AJ - 8		0.98	1.01	0.98	0.96	0.98
AO - 9		0.95	0.99	0.91	0.94	0.94
AM - 10		0.93	0.97	0.90	0.92	0.93
AK - 11		0.92	0.95	0.87	0.90	0.92

Table 10

Determination of fuel stack length changes from gamma scanning

Rod	Post-irradiation stack length (mm)	Pre-irradiation stack length (mm)	Change in fuel stack length* (mm)
AA - 1	651.6	653.0	- 5
AB - 2	646.3	650.6	- 4
AC - 3	645.75	650.6	- 5
AD - 4	662.4	662.9	- 2
AE - 5	660.0	656.03	+ 1.5
AG - 6	655.3	662.6**	- 7.5**
AH - 7	611.1	606.6	+ 4.5
AJ - 8	611.2	608.4	+ 2.5
AO - 9	617.85	613.84	+ 1
AM - 10	609.0	606.12	+ 2.5
AK - 11	612.25	607.2	+ 5

* To give the change in fuel stack length, the post-irradiation fuel stack length was corrected as best possible for inter-pellet spaces obtained from neutron radiography.

** These figures should be taken with caution because all the calculations performed to obtain a verification of the stated pre-irradiation length failed. For rod AG-6, the "pellet position in fuel stack" sheet in the fabrication report indicates the presence of 43 pellets in the stack, but both gamma scanning and neutron radiography only showed 42 pellets. Two pellet numbers - 29 and 34 - are reported twice in the stack. Five pellets - 4, 14, 21, 20, 19 - are reported as originating from the loading pellets intended for rod AH-7, but they are also reported to be present in rod AH-7.

Table 11

Positions of rod supports during the individual scanning operations

Rod	Support positions*		
AA - 1	22-47		415-440
AB - 2	80-105		523-548
AC - 3	96-121		540-565
AD - 4		345-371	
AE - 5	173-198		570-595
AG - 6		317-342	
AH - 7	277-302		549-573
AJ - 8	276-301		547-572
AO - 9	295-320		551-576
AM - 10	277-302		547-572
AK - 11	184-209		581-606

*measured in mm from the datum/bottom end

Table 12

Results of fission gas analysis*

Rod	Extracted gas (cm^3)***	Σ Xe (%)	Σ Kr (%)	He (%)	H_2 (%)	N_2 (%)	O_2 (%)	Ar (%)	CO_2 (%)
AA-1	25.4	32.5 62.2	1.81 3.52	44.0 27.0	20.4 5.1	.83 1.4	.04 .08	.42 .69	-
AB-2	23.4	34.1 39.0	2.17 2.44	19.9 16.8	14.6 11.4	28.5 29.6	.11 .07	.61 .58	.01 .02
AD-4	39.6	60.4 61.4	3.88 3.80	35.0 34.1	0	.22 .22	.01 .02	.38 .37	.05 .08
AE-5	12.2	47.2 61.1	2.13 2.65	0	0	49.9 35.4	.10 .06	.74 .80	0
AG-6**	103.1	41.6	2.28	43.5	0	9.4	2.1	.59	.53
AH-7	71.0	71.1 70.1	4.01 3.95	23.3 24.2	.50 .43	.53 .64	.03 .04	.40 .41	.13 .26
AJ-8	85.4	73.3	3.88	21.6	0	.83	.02	.29	.19
AO-9	83.8	77.0 75.3	4.38 4.25	16.2 17.0	.47 .50	.95 1.24	.06 .08	.46 .47	.42 .47
AM-10	87.2	74.0	4.02	21.0	0	.66	.01	.29	.03
B5-12	116.4	62.8	3.38	32.8	0	.55	.02	.22	.06

*Two numbers refer to the results from two samples

**Presumably an inleak of air occurred during the piercing

***at $0^{\circ}C$ and 1 at.

Table 13

Mass spectrometric determinations of Xe- and Kr isotope ratios*

Rod	Xe isotopes				Kr isotopes			
	$\frac{Xe\ 130}{Xe\ 136}$	$\frac{Xe\ 131}{Xe\ 136}$	$\frac{Xe\ 132}{Xe\ 136}$	$\frac{Xe\ 134}{Xe\ 136}$	$\frac{Kr\ 83}{Kr\ 86}$	$\frac{Kr\ 84}{Kr\ 86}$	$\frac{Kr\ 85}{Kr\ 86}$	$\frac{\Sigma\ Xe}{\Sigma\ Kr}$ **
AA-1	0	.348	.533	.742	.361	.626	.131	18.0
	0	.344	.529	.740	.358	.624	.129	17.7
AB-2	0	.353	.540	.757	.362	.625	.131	15.7
	0	.354	.541	.759	.360	.626	.130	16.0
AD-4	.0025	.332	.521	.720	.359	.636	.128	15.6
	.0023	.333	.522	.718	.360	.640	.129	16.1
AE-5	0	.337	.519	.716	.360	.628	.136	22.2
	0	.332	.512	.711	.360	.628	.136	23.1
AG-6	0	.315	.498	.687	.350	.663	.124	18.2
AH-7	0	.269	.526	.670	.294	.693	.127	17.7
	0	.266	.523	.668	.294	.690	.127	17.7
AJ-8	0	.273	.528	.671	.295	.685	.124	18.9
AO-9	0	.275	.527	.673	.298	.692	.127	17.6
	0	.275	.527	.673	.298	.690	.127	17.7
AM-10	0	.275	.531	.677	.293	.691	.124	18.4
B5-12	0	.275	.530	.676	.298	.693	.126	18.6

*mean values of 10 determinations ** $\frac{\Sigma\ Xe}{\Sigma\ Kr}$ from table 12

Table 14

Piercing results

Rod	Extracted fission gas (cm^3)* (Kr+Xe)	Fission gas release (%)	Free volume of rod (cm^3)	Pressure in rods in Hot Cell condit. (ata)
AA-1	8.7 16.7	2.9 5.5	-	-
AB-2	8.5 9.7	2.7 3.1	14.9	1.7
AD-4	25.5 25.8	7.5 7.6	12.1	3.6
AE-5	6.0 7.8	2.0 2.6	13.3	1.0
AG-6	45.2	13.1	10.9	10.6
AH-7	53.3 52.6	13.6 13.4	14.5	5.4
AJ-8	65.9	15.7	15.0	6.4
AO-9	68.4 66.8	17.1 16.7	16.1	5.8
AM-10	68.0	17.3	15.5	6.3
B5-12	77.1	19.5	16.1	8.2

*at $0^{o}C$ and 1 ata.

Table 15

Sample positions for metallography/ceramography

Rod-sample	Position from datum/bottom end (mm)	Motivation for choice of sample position*
AA-1-1	79.1	TC, max. flux next to BU
AE-5-1	82.7	TC, max. flux - - -
AH-7-1	563.0	Max. flux - - -
AO-9-1	562.1	TC, max. flux
AO-9-2A	542.1-560.6	Anomaly from NR - - -
AO-9-5A	401.2-416.6	- - -
AK-11-1	825.0	Cracked end-plug
AK-11-2A	594.1	Max. flux, EC- and P-signal
AK-11-2-1	585.0	Max. flux, EC- and P-signal
AK-11-3	565.4	TC, max. flux - - -
AK-11-6A	415.9	EC- and P-signal
AK-11-6-1	399.3	EC- and P-signal
AK-11-7	130.8	P-signal

*TC - thermocouple, BU - burn-up sample, NR - neutron-radiography, EC - eddy current, P - profilometry

Table 16

Evaluation of ceramography and metallography

Rod-sample	Thickness of oxide on outer surface of cladding (μm)	Thickness of oxide on inner surface of cladding (μm)	Cladding thickness (μm)	Gap (μm)	Estimated hydride content (ppm)	Radial fraction of fuel with columnar grains	Outer radial fraction of fuel with equiaxed grains	Estimated fuel centre temperature (°C)
AA-1-1	0-14 discont.	4-7 cont.	555-560	29-67	50 surf. 80-90	0	.77	< 1600
AE-5-1	0-6 discont.	0-6 discont.	575-595	21-55	55-65	.36	.75	1850
AH-7-1	5-13 discont.	5-13 discont.	580-595	0	60-70	0	.72	< 1600
AO-9-1	5-20 cont.	0-10 discont.	560	24-48	40	.68	.86	2600
AO-9-2A	10 discont.	5 discont.	560	38	15	.62	.82	2350
AO-9-5A	12 discont.	10 discont.	555	38	35-40	.37	.68	1850
AK-11-2-A	5-9 discont.	4-26 cont.	570-590	0	50 surf. 90-100	.48	.71	2000
AK-11-2-1	0-14 discont.	11-18 discont.	580-590	0-10	50 surf. 90-100	.35	.66	1850
AK-11-3	0-14 discont.	10-14 cont.	575-585	0-20	30-40	.36	.72	1850
AK-11-6-A	4-11 discont.	10-16 discont.	570-580	10-15	40	0	.63	< 1600
AK-11-6-1	2-13 discont.	12-18 discont.	585-590	0-30	40	0	.67	< 1600
AK-11-7	6-11 discont.	0-9 discont.	570-580	0-30	60-75	0	.63	< 1600

Table 17

Data from quantitative metallography

Class midpoint (µm)	Number of pores	Number of pores	Number of pores	Number of pores	Number of pores	Number of pores
	Fig.69	Fig.70	Fig.71	Fig.72	Fig.87	Fig.88
< 0.5	44	26	48	29	32	34
1.5	35	33	42	36	25	26
2.5	16	23	25	36	12	13
3.5	5	5	15	16	9	9
4.5	10	2	3	10	10	5
5.5	4	2	4	3	5	6
6.4	8	1	1	2	5	6
7.4	6	1	0	2	4	5
8.8	5	0	0	0	15	2
10.4	2	0	0	2	0	5
≥12.4	0	0	0	2	1	1
	Fig.89	Fig.90	Fig.98	Fig.99	Fig.100	Fig.101
< 0.5	21	49	18	23	88	76
1.5	14	42	20	13	44	51
2.5	22	26	7	4	12	15
3.5	16	15	6	1	4	14
4.5	10	7	3	0	1	14
5.5	4	3	3	2	0	5
6.4	2	2	3	0	0	4
7.4	1	1	1	0	1	4
8.8	0	0	0	0	0	4
10.4	0	0	0	0	0	1
≥12.4	0	0	1	0	0	0
	Fig.111	Fig.112	Fig.125	Fig.135	Fig.136	Fig.137
< 0.5	12	342	224	28	78	361
1.5	19	145	175	22	74	27
2.5	7	46	4	22	35	0
3.5	3	19	0	12	9	0
4.5	7	5	0	9	7	1
5.5	5	1	0	6	0	0
6.4	2	4	0	5	0	0
7.4	3	1	0	5	0	0
8.8	5	0	0	2	0	0
10.4	0	0	0	0	0	0
≥12.4	1	1	0	0	0	0

Table 17 continued

Class midpoint (μm)	Number of pores	Number of pores	Number of pores	Number of pores	Number of pores	Number of pores
	Fig.138	Fig.167	Fig.168	Fig.203	Fig.202	Fig.204
< 0.5	317	38	65	98	120	64
1.5	171	34	9	34	67	63
2.5	12	12	2	7	25	22
3.5	3	4	0	2	8	9
4.5	2	3	0	1	3	14
5.5	0	2	0	0	1	3
6.4	2	0	0	0	3	2
7.4	1	0	0	0	0	0
8.8	1	0	0	0	0	1
10.4	1	0	0	0	0	1
≥12.4	0	0	0	0	0	0
	Fig.221	Fig.220	Fig.222	Fig.251	Fig.252	Fig.253
< 0.5	1	24	50	33	31	42
1.5	3	25	36	30	31	56
2.5	0	12	8	14	13	15
3.5	1	16	2	11	11	16
4.5	0	10	0	5	4	7
5.5	0	12	0	3	3	4
6.4	0	2	2	3	0	0
7.4	0	1	0	1	1	3
8.8	0	0	0	1	0	1
10.4	0	2	0	0	0	0
≥12.4	0	0	0	0	0	0
	Fig.254					
< 0.5	45					
1.5	39					
2.5	26					
3.5	5					
4.5	5					
5.5	9					
6.4	4					
7.4	4					
8.8	3					
10.4	0					
≥12.4	1					

Table 18

Evaluation of quantitative metallography

Rod-sample	Fig. No.	Position (fraction of radius from centre)	Avcrage pore diam-eter (μm)	Area of pores (%)	Theoretical density* TD (%)
AA 1-1	69	.13	2.7	23.3	68.9
	70	.55	1.8	5.4	94.2
	71	.89	1.7	7.2	91.9
	72	.98	2.5	14.9	81.7
AE 5-1	87	.09	3.3	26.3	67.0
	88	.17	3.1	22.6	66.8
	89	.60	2.5	7.3	92.9
	90	.94	1.9	8.1	91.2
AH 7-1	98	.06	2.3	10.0	86.1
	99	.55	1.3	1.7	97.9
	100	.68	1.1	3.5	95.7
	101	.98	2.1	20.0	72.0
AO 9-1	111	.64	3.3	15.8	80.2
	112	.96	1.1	16.6	75.8
AO 9-2A	125	.90	.9	4.4	95.8
AO 9-5A	135	.46	2.7	15.3	83.0
	136	.73	1.5	6.0	93.8
	137	.90	.6	1.9	98.4
	138	.96	1.0	15.1	79.9
AK 11-2	167	.70	1.5	4.1	95.5
	168	.78	.7	.6	99.4
AK 11-3	203	.72	.9	2.0	97.6
	202	.78	1.3	6.9	91.5
	204	.96	1.8	14.1	82.2
AK 11-6	221	.78	1.4	.2	99.8
	220	.87	2.8	13.0	85.5
	222	.98	1.2	2.9	96.4
AK 11-7	251	.09	2.0	7.2	91.3
	252	.43	1.8	5.4	93.9
	253	.72	1.9	11.0	86.8
	254	.98	2.3	14.5	80.7

* Calculated by the method given in [4]

Table 19

Fuel density

Rod-sample	Sample pos. from the datum/bottom end (a) (mm)	Post-irradiation density (b) (% TD)	Pre-irradiation density (c) (% TD)	Change in density (% TD)
AA-1-3	120.8 - 136.8	91.61	92.58	-1.0
AE-5-3	99.8 - 114.8	91.01	93.10	-2.1
AH-7-3	509.2 - 525.2	92.14	94.09	-2.0
AO-9-4	509.0 - 525.2	92.59	92.87	-0.3
AK-11-5	515.5 - 531.7	93.93	96.65	-2.7

(a) See also fig. 60b

(b) By immersion

(c) From [1], geometric + 0.75% on actual pellets

Table 20

Results of isotope analysis of fuel. The isotopes are relative to ^{238}U

Rod-sample		AA-1-2	AE-5-2	AH-7-2	AO-9-3	AO-9-6	AK-11-4
Sample position from the datum/bottom end (mm)		104.0-119.7	83.8-98.3	542.0-556.8	526.1-541.3	387.3-401.0	533.1-549.0
g ^{238}U/g fuel		0.786	0.784	0.784	0.772	0.770	0.778
U	^{234} (a)	$2.08 \cdot 10^{-5}$	$1.88 \cdot 10^{-5}$	$1.94 \cdot 10^{-5}$	$1.93 \cdot 10^{-5}$	$1.97 \cdot 10^{-5}$	$1.94 \cdot 10^{-5}$
	235	$1.36 \cdot 10^{-3}$	$1.31 \cdot 10^{-3}$	$1.22 \cdot 10^{-3}$	$1.16 \cdot 10^{-3}$	$1.22 \cdot 10^{-3}$	$1.15 \cdot 10^{-3}$
	236	$1.60 \cdot 10^{-4}$	$1.62 \cdot 10^{-4}$	$1.83 \cdot 10^{-4}$	$1.78 \cdot 10^{-4}$	$1.72 \cdot 10^{-4}$	$1.81 \cdot 10^{-4}$
Pu	^{238} (a)	$4.41 \cdot 10^{-4}$	$4.30 \cdot 10^{-4}$	$4.56 \cdot 10^{-4}$	$4.42 \cdot 10^{-4}$	$4.56 \cdot 10^{-4}$	$4.56 \cdot 10^{-4}$
	239	$3.63 \cdot 10^{-2}$	$3.56 \cdot 10^{-2}$	$2.89 \cdot 10^{-2}$	$2.91 \cdot 10^{-2}$	$3.20 \cdot 10^{-2}$	$2.71 \cdot 10^{-2}$
	240	$2.45 \cdot 10^{-2}$	$2.52 \cdot 10^{-2}$	$2.57 \cdot 10^{-2}$	$2.56 \cdot 10^{-2}$	$2.53 \cdot 10^{-2}$	$2.48 \cdot 10^{-2}$
	241	$5.47 \cdot 10^{-3}$	$5.66 \cdot 10^{-3}$	$5.97 \cdot 10^{-3}$	$5.92 \cdot 10^{-3}$	$6.08 \cdot 10^{-3}$	$5.80 \cdot 10^{-3}$
	242	$2.00 \cdot 10^{-3}$	$2.07 \cdot 10^{-3}$	$2.38 \cdot 10^{-3}$	$2.44 \cdot 10^{-3}$	$2.33 \cdot 10^{-3}$	$2.44 \cdot 10^{-3}$
Am	241 (a)	$6.98 \cdot 10^{-4}$	$6.61 \cdot 10^{-4}$	$9.70 \cdot 10^{-4}$	$8.70 \cdot 10^{-4}$	$5.46 \cdot 10^{-4}$	$6.54 \cdot 10^{-4}$
Cm	242 (a)	$7.39 \cdot 10^{-5}$	$7.54 \cdot 10^{-5}$	$7.70 \cdot 10^{-5}$	$9.33 \cdot 10^{-5}$	$8.00 \cdot 10^{-5}$	$8.63 \cdot 10^{-5}$
	244 (a)	$3.67 \cdot 10^{-5}$	$2.96 \cdot 10^{-5}$	$4.30 \cdot 10^{-5}$	$3.49 \cdot 10^{-5}$	$4.86 \cdot 10^{-5}$	$3.87 \cdot 10^{-5}$
Nd	148	$6.97 \cdot 10^{-4}$	$7.16 \cdot 10^{-4}$	$7.96 \cdot 10^{-4}$	$8.33 \cdot 10^{-4}$	$7.56 \cdot 10^{-4}$	$8.16 \cdot 10^{-4}$
Bu (A/O)		3.65	3.78	4.21	4.40	4.00	4.32

(a) Corrected to 20 September 1975

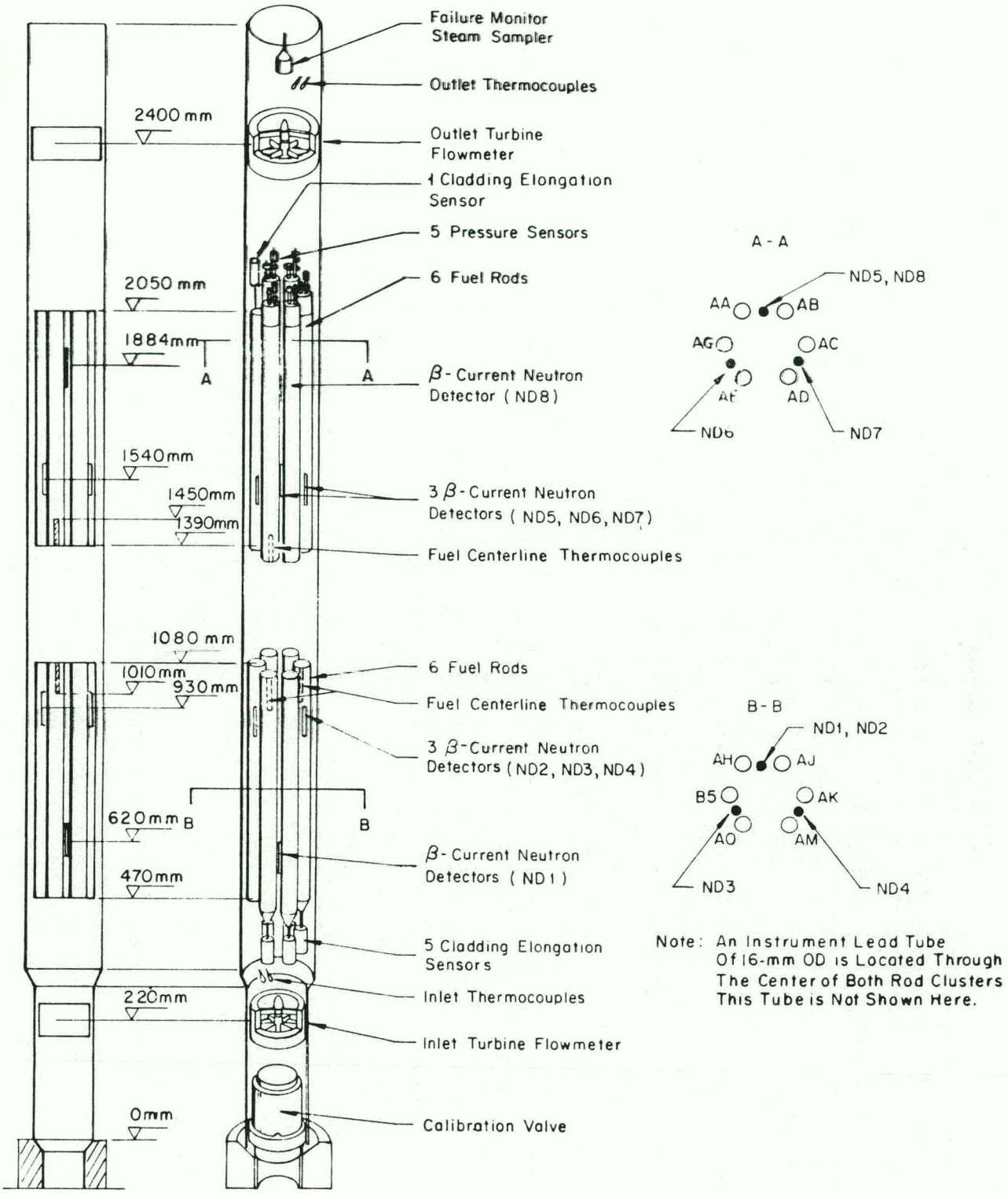

Fig. 1 Diagram of Instrumented Fuel Assembly 226.

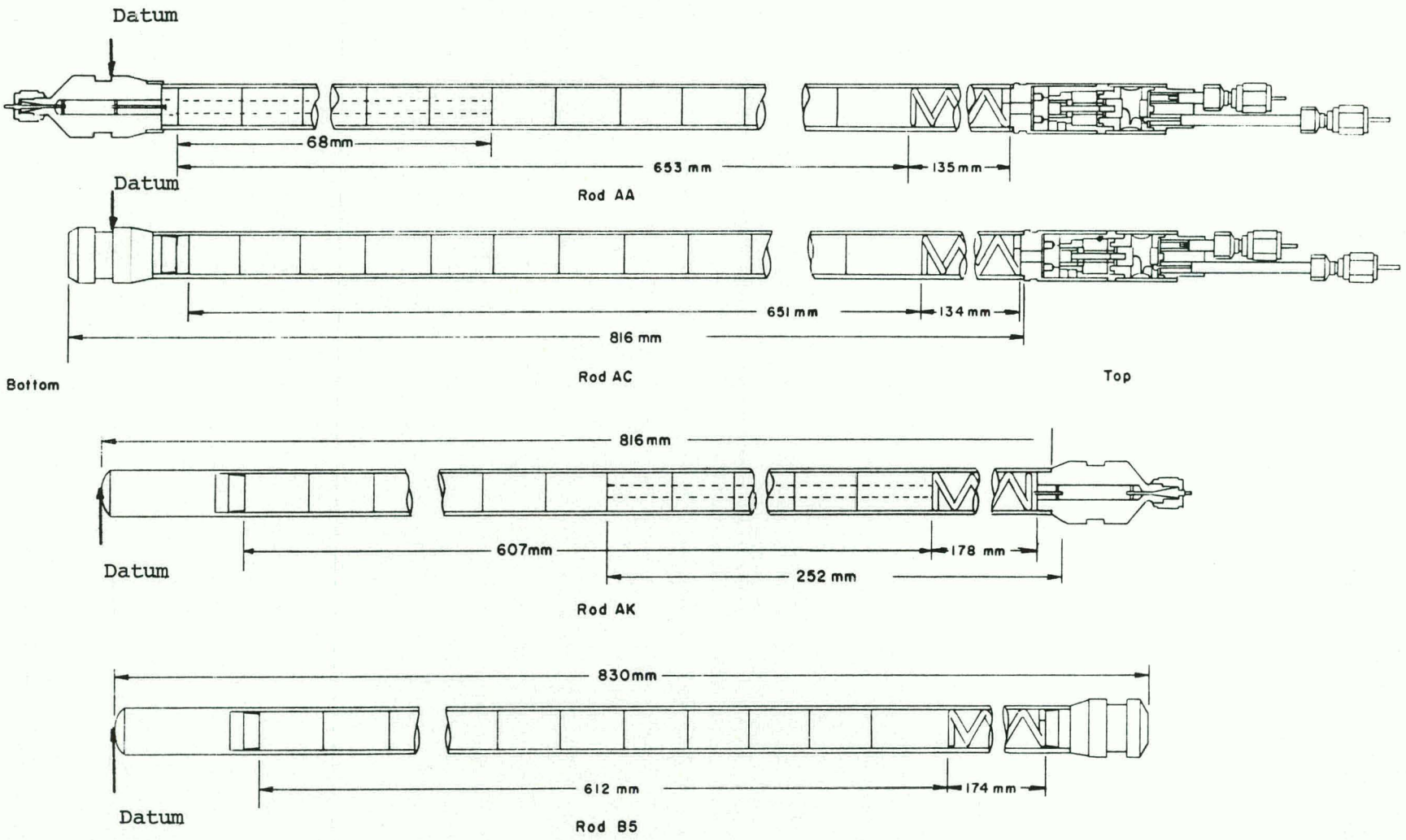

Fig. 2 Schematic diagram of four types of IFA-226 test rods.

The datum plane is defined for upper cluster rods as shown for rods AA and AC, for lower cluster rods as shown for rods AK and B5.

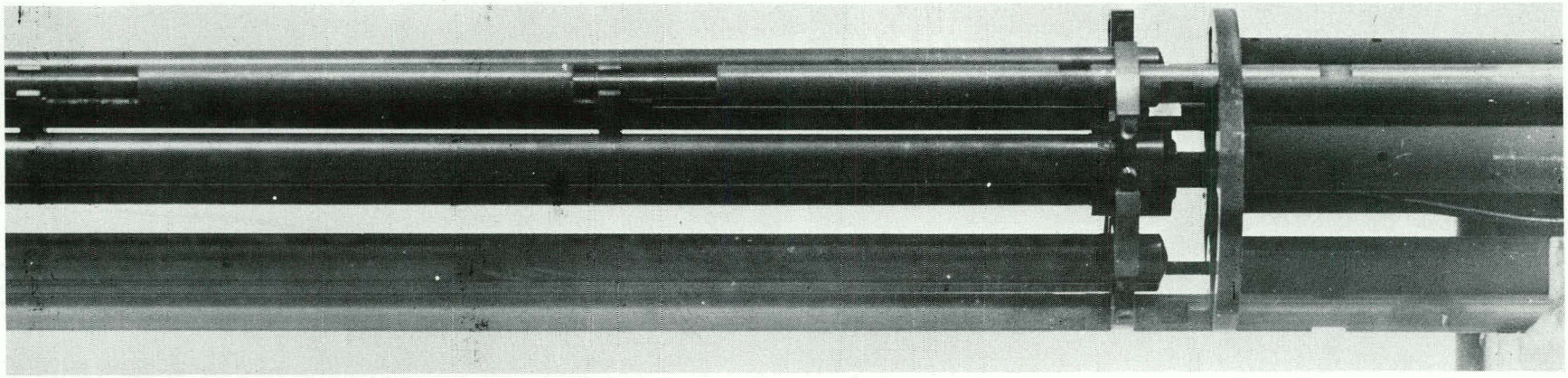

Fig. 3 Upper end of the fuel bundle, as received.

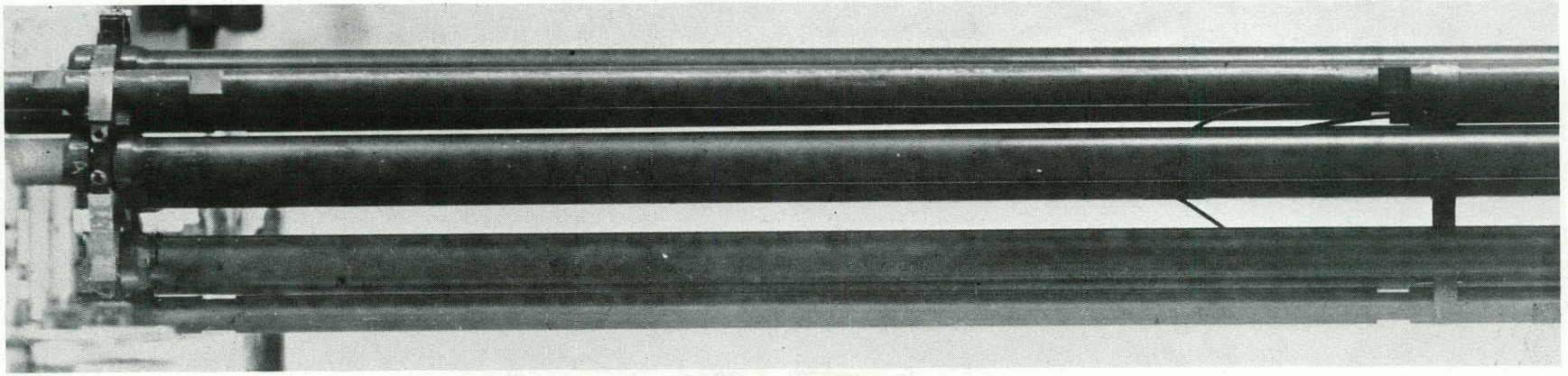

Fig. 4 Lower end of the fuel bundle, as received.

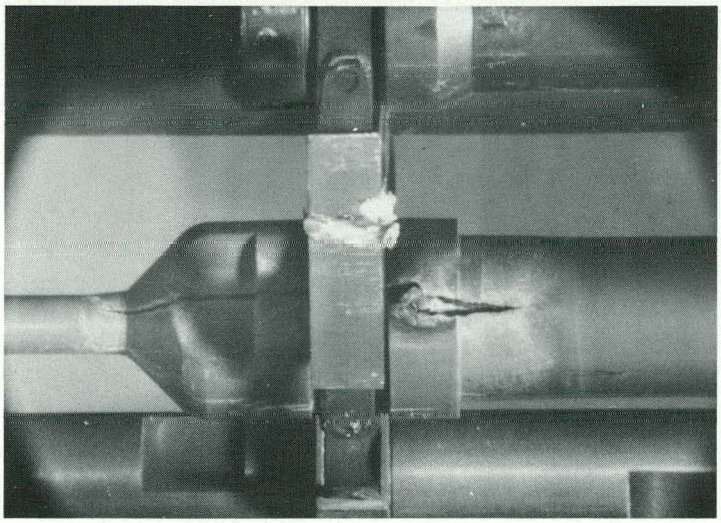

Fig. 5 Plenum end of rod AK-11 before removal from the spacer.

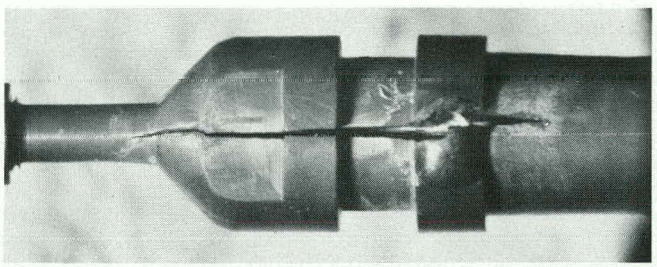

Fig. 6 Rod AK-11 after removal from the spacer.

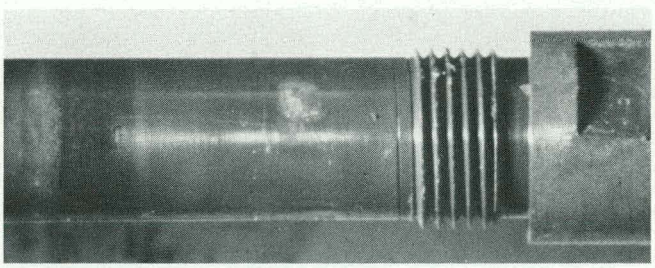

Fig. 7 Rod AA-1. Spacer mark and welding zone at the plenum end.

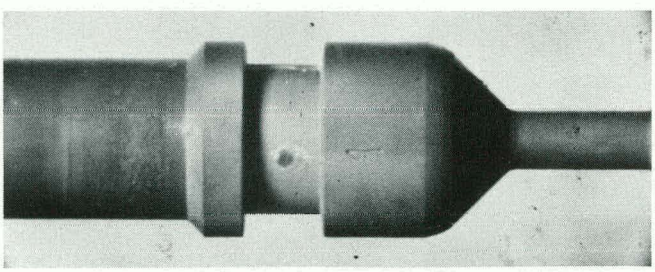

Fig. 8 Rod AA-1 Spacer mark at the lower end.

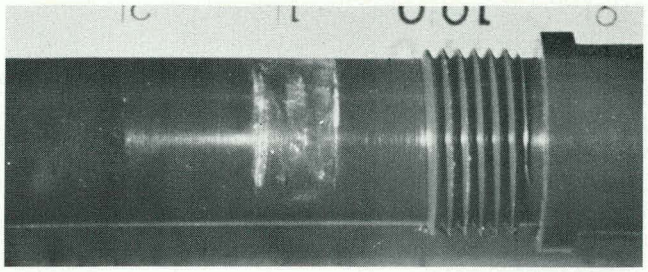

Fig. 9 Rod AB-2. Spacer mark at the plenum end.

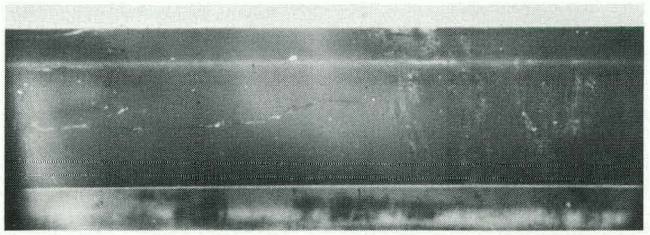

Fig. 1o Rod AB-2. Crack in the oxide layer 22o to 244 mm from the top end.

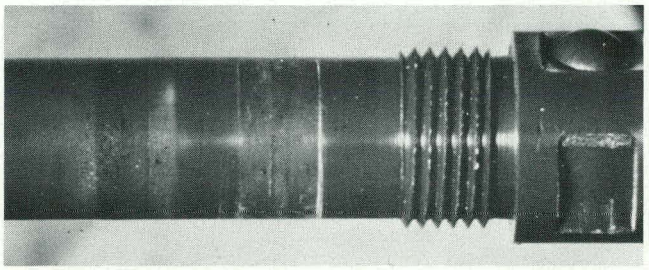

Fig. 11 Rod AD-4. Spacer mark and welding zone at the upper end.

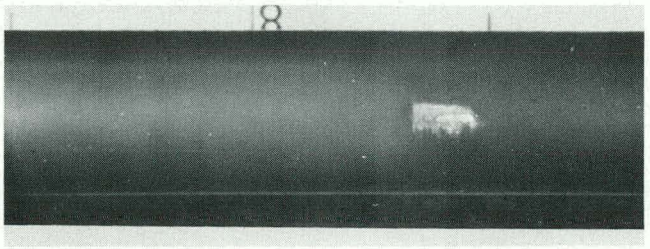

Fig. 12 Rod AH-8. Typical rod surface with a small handling mark.

Rod deflection ≡ Δ

Rod length = l

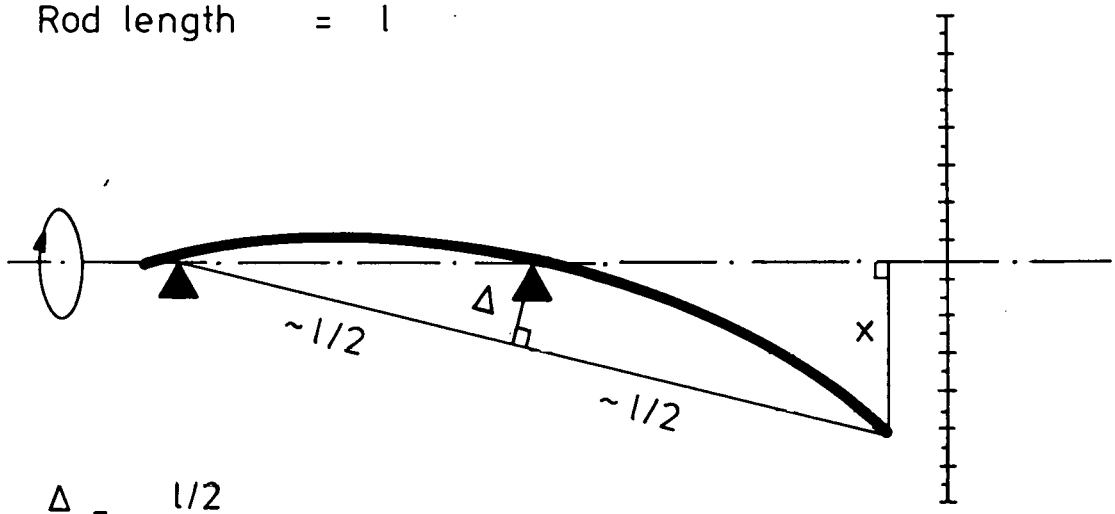

$$\frac{\Delta}{x} = \frac{l/2}{\sqrt{l^2 - x^2}}$$

$$l \gg x \Longrightarrow \Delta \simeq \frac{x}{2}$$

Fig. 13. Principle of bow measurements.

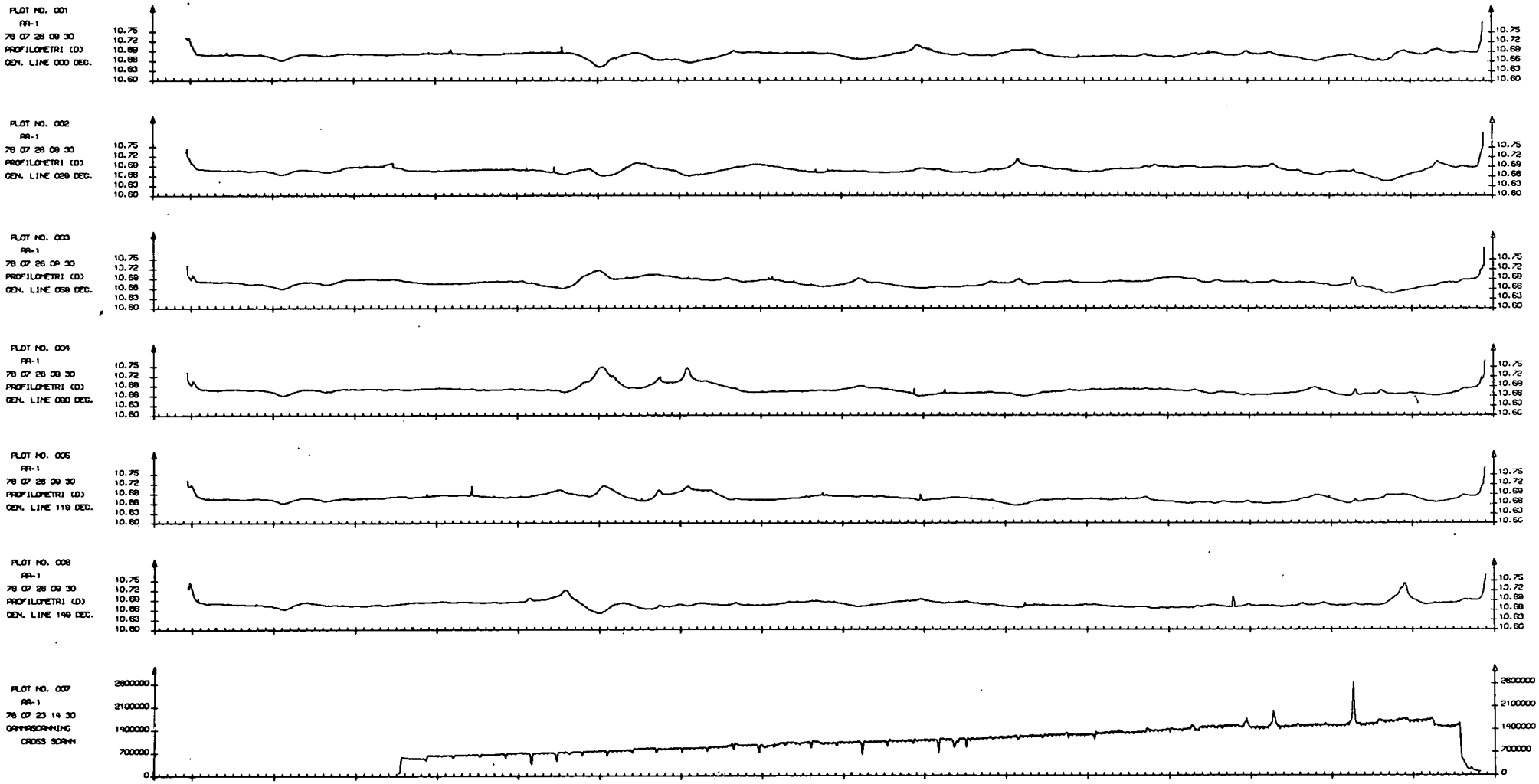

Fig. 14 Profilometry on rod AA-1, together with gross gamma scan.
Top to the left.
Each div. on axial scale equals 5 mm.

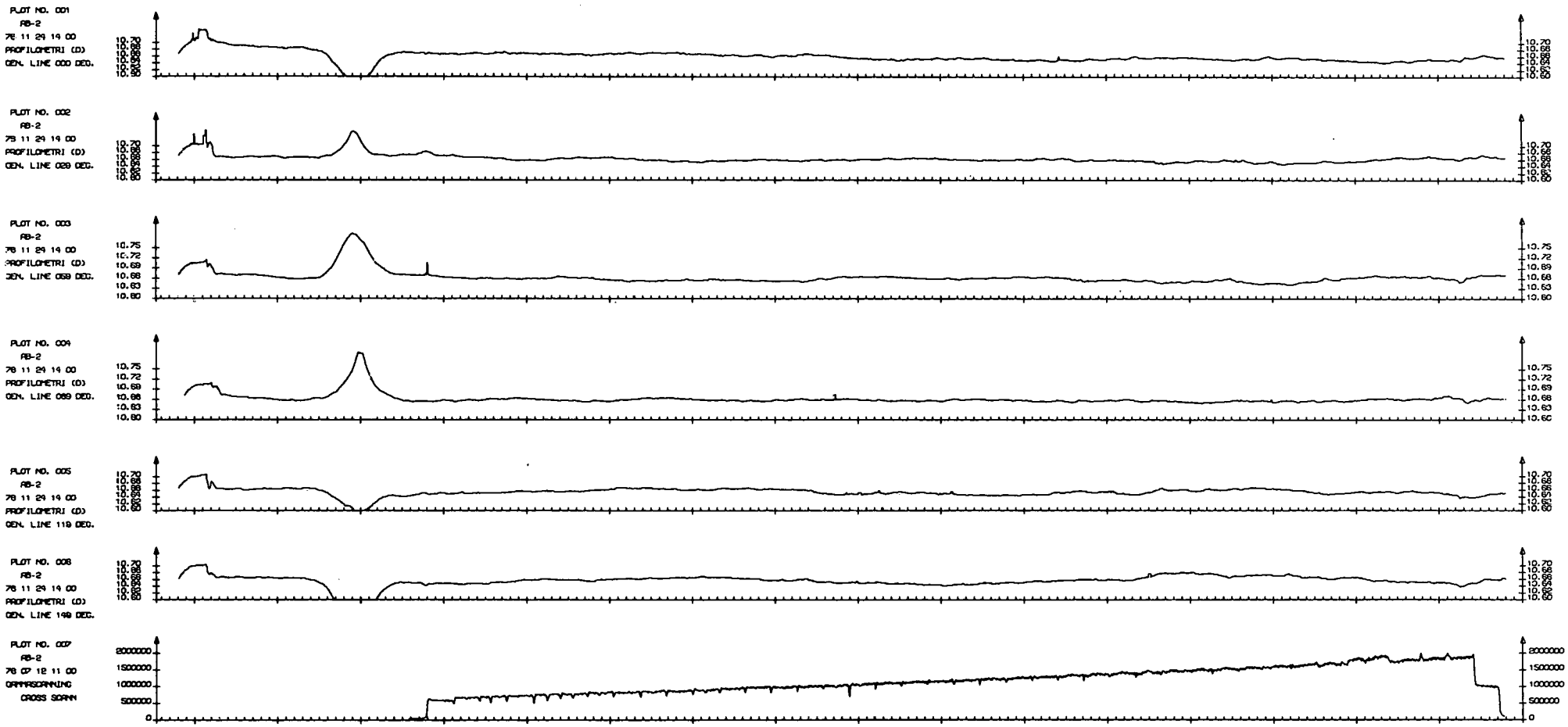

Fig. 15 Profilometry on rod AB-2, together with gross gamma scan.
Top to the left.
Each div. on axial scale equals 5 mm.

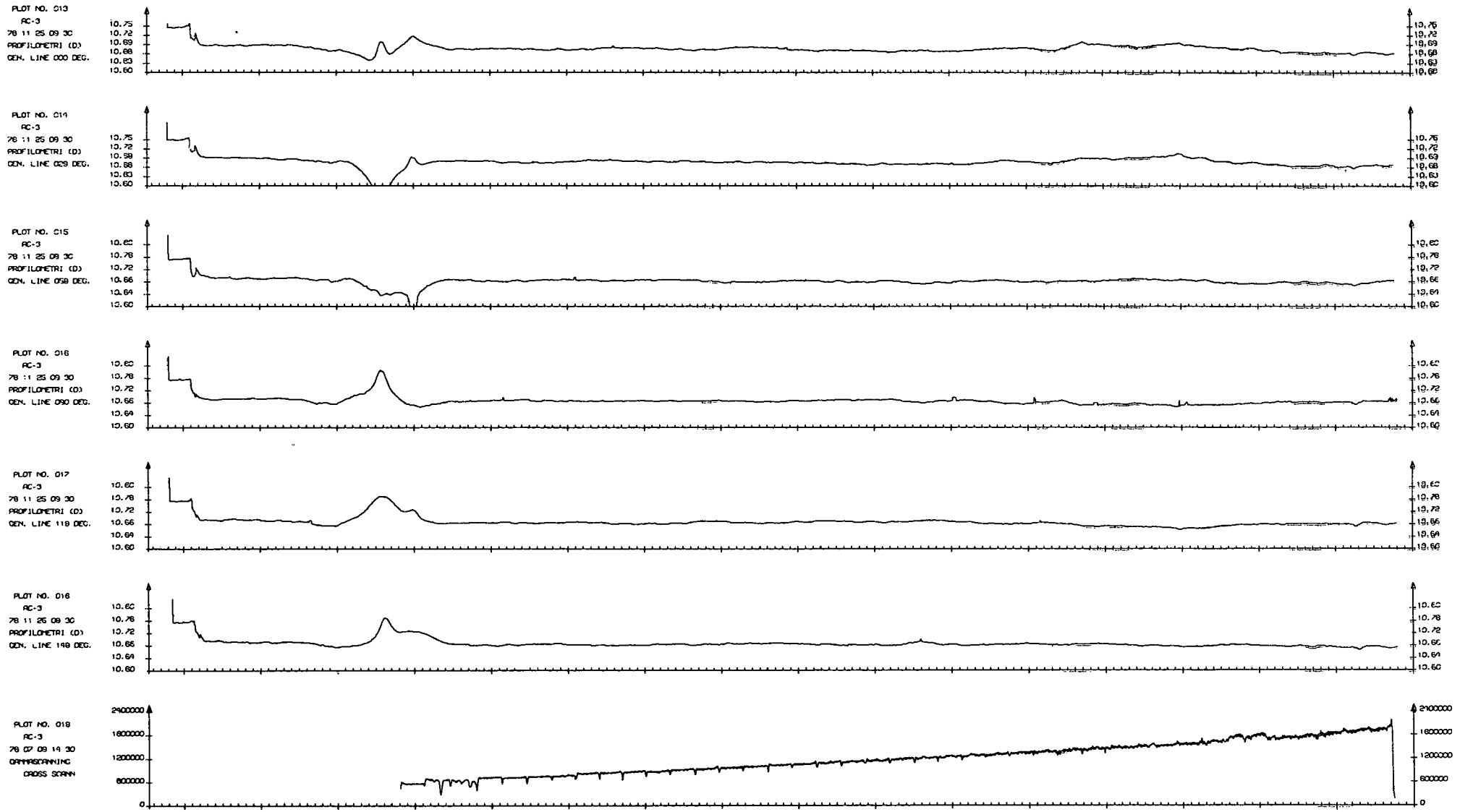

Fig. 16 Profilometry on rod AC-3, together with gross gamma scan.
Top to the left.
Each div. on axial scale equals 5 mm.

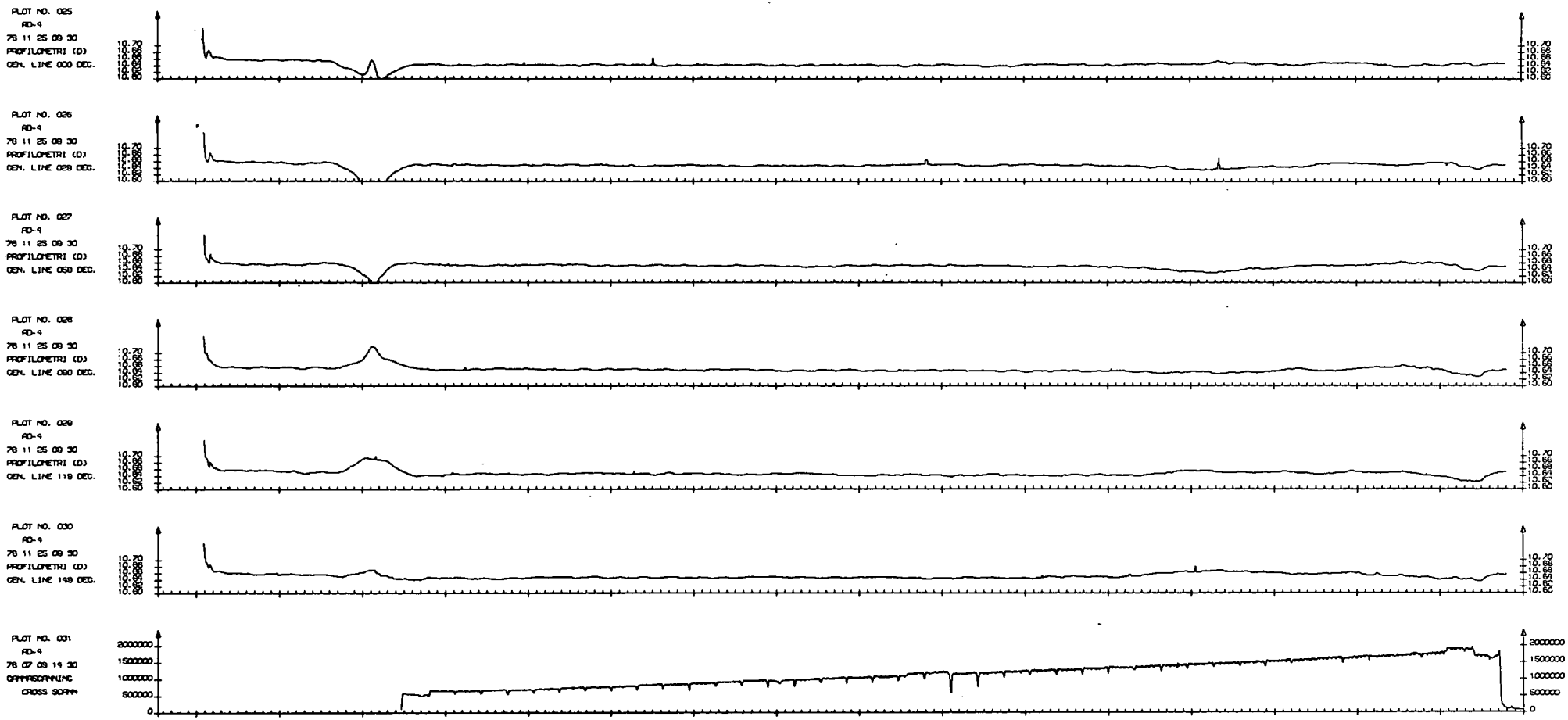

Fig. 17 Profilometry on rod AD-4, together with gross gamma scan.
Top to the left.
Each div. on axial scale equals 5 mm.

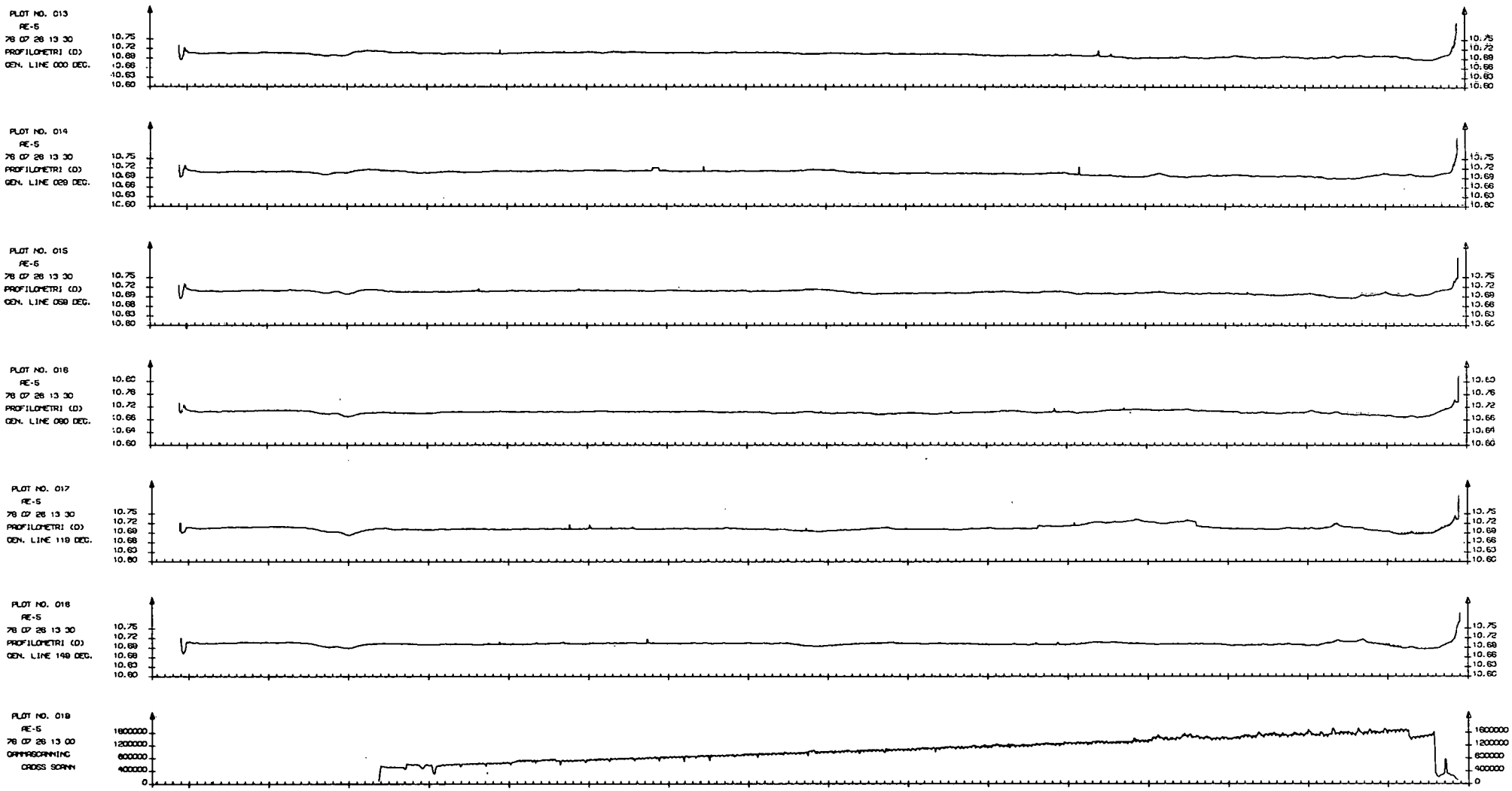

Fig. 18 Profilometry on rod AE-5, together with gross gamma scan.
Top to the left.
Each div. on axial scale equals 5 mm.

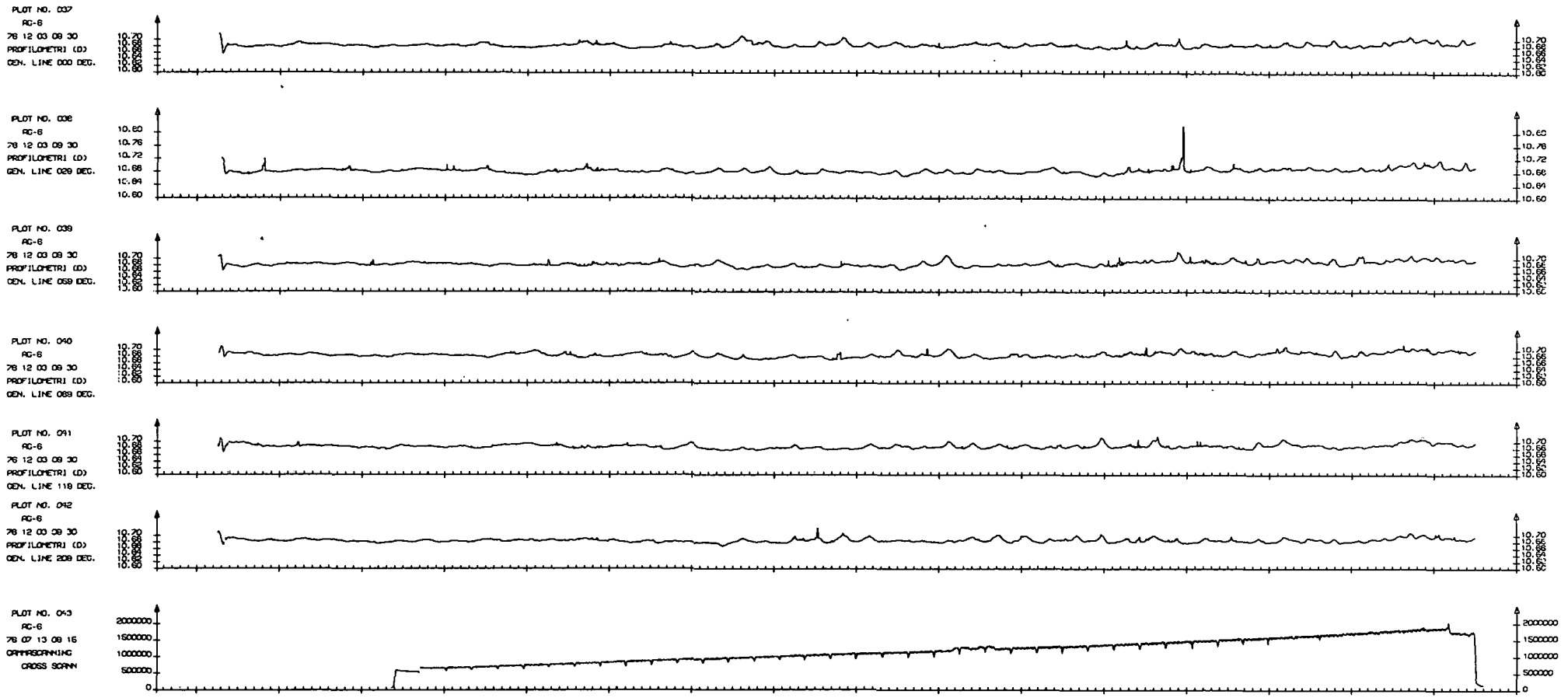

Fig. 19 Profilometry on rod AG-6, together with gross gamma scan.
Top to the left.
Each div. on axial scale equals 5 mm.

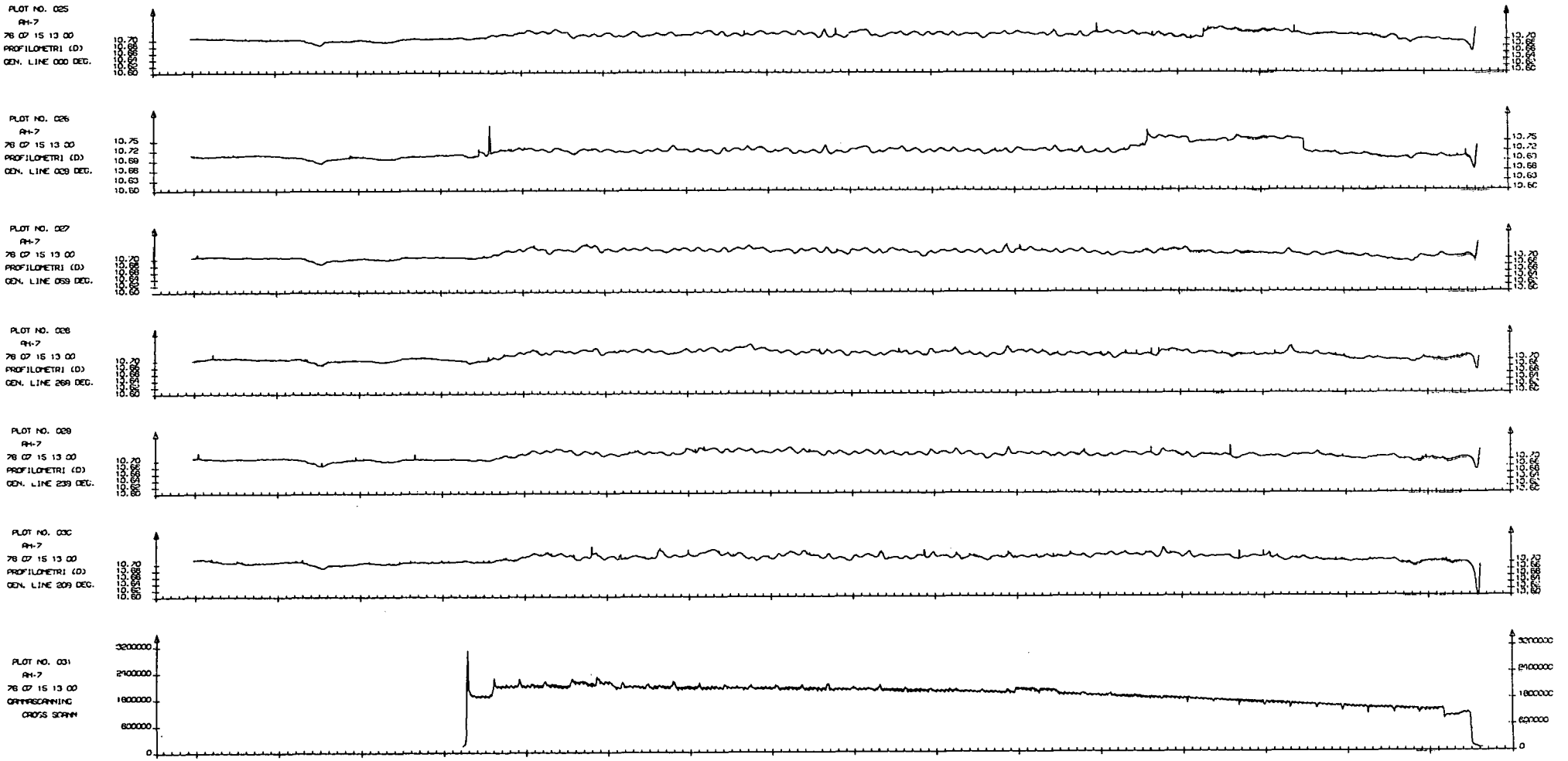

Fig. 2o Profilometry on rod AH-7, together with gross gamma scan.
Top to the left.
Each div. on axial scale equals 5 mm.

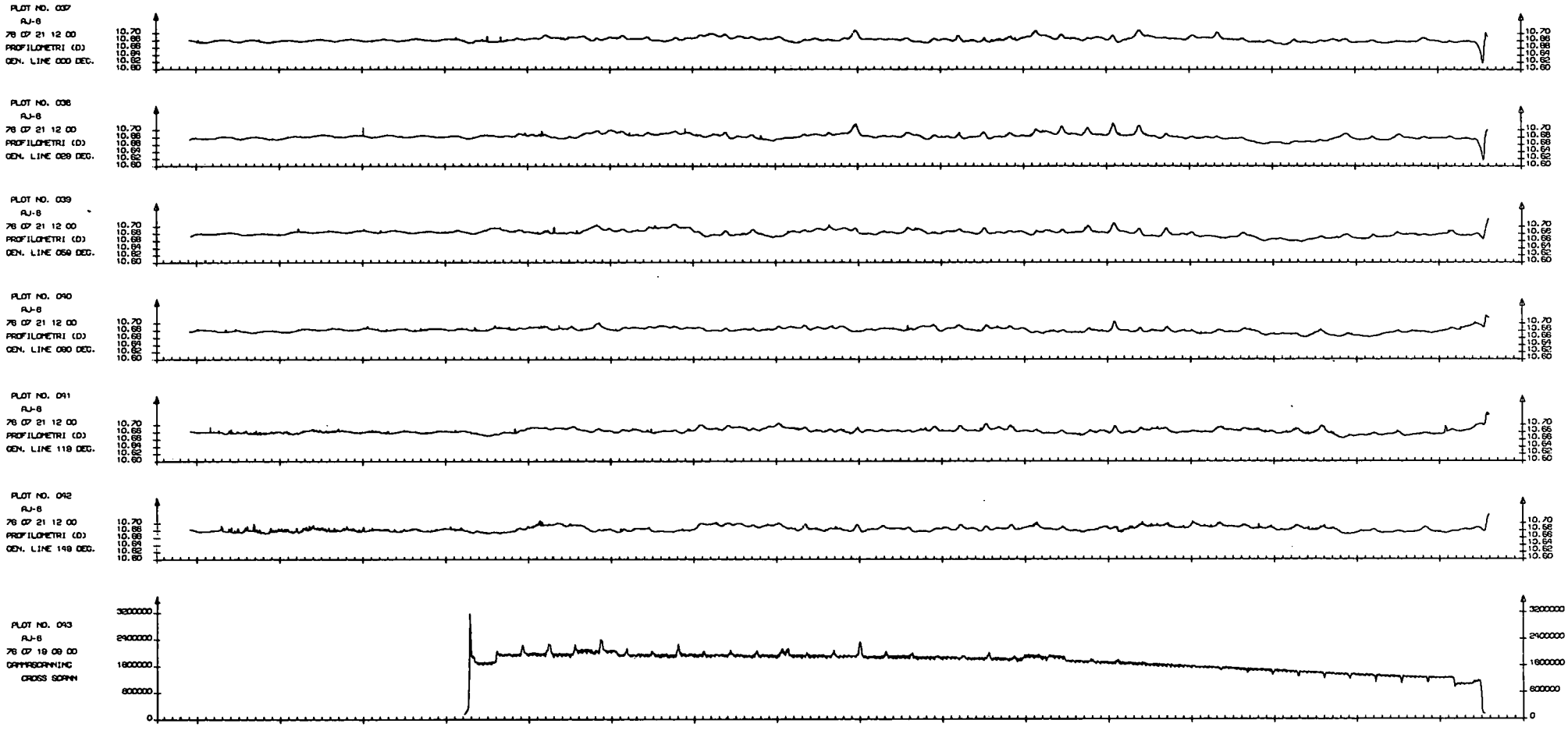

Fig. 21 Profilometry on rod AJ-8, together with gross gamma scan.
Top to the left.
Each div. on axial scale equals 5 mm.

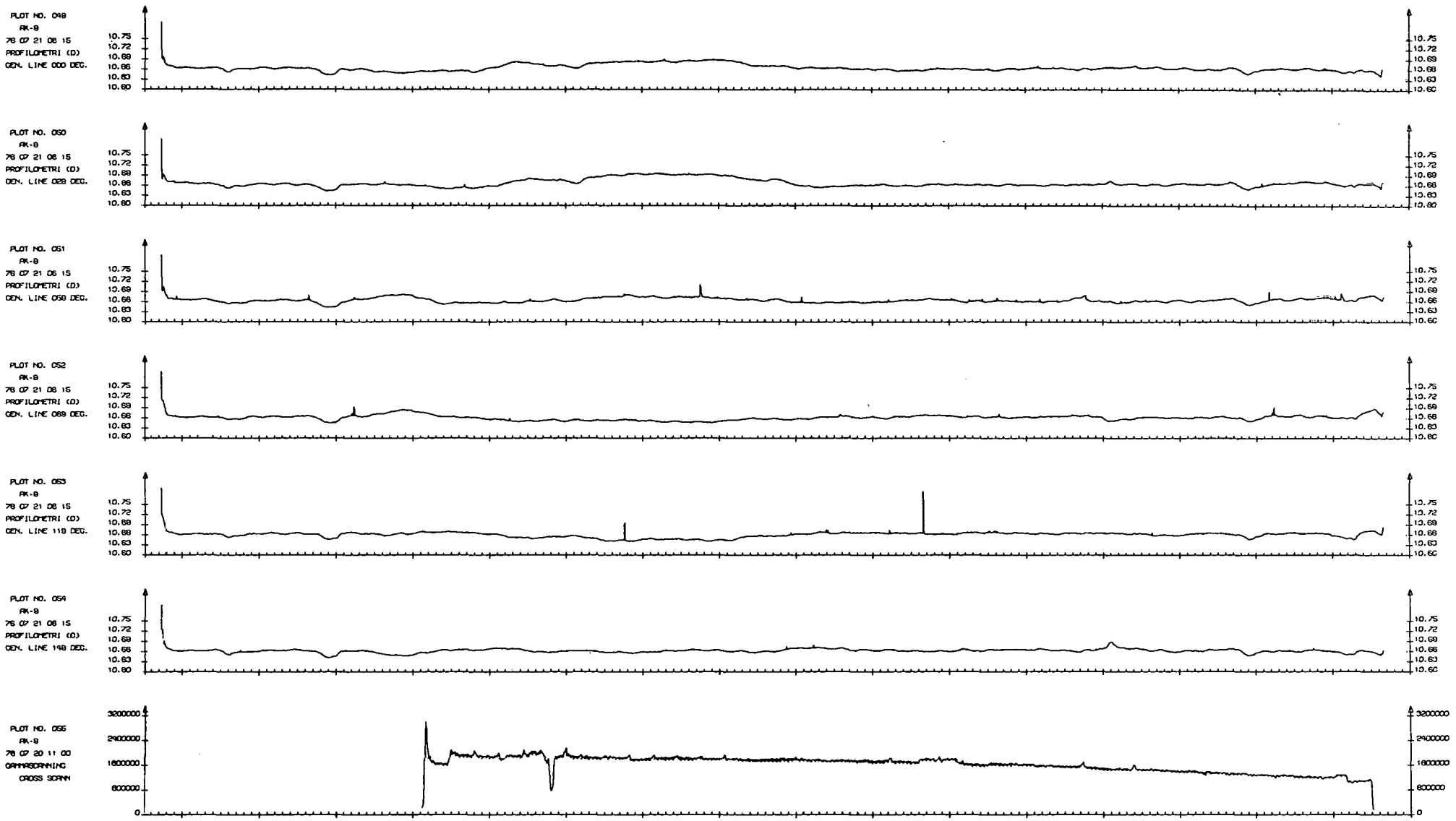

Fig. 22 Profilometry on rod AO-9, together with gross gamma scan.
Top to the left.
Each div. on axial scale equals 5 mm.

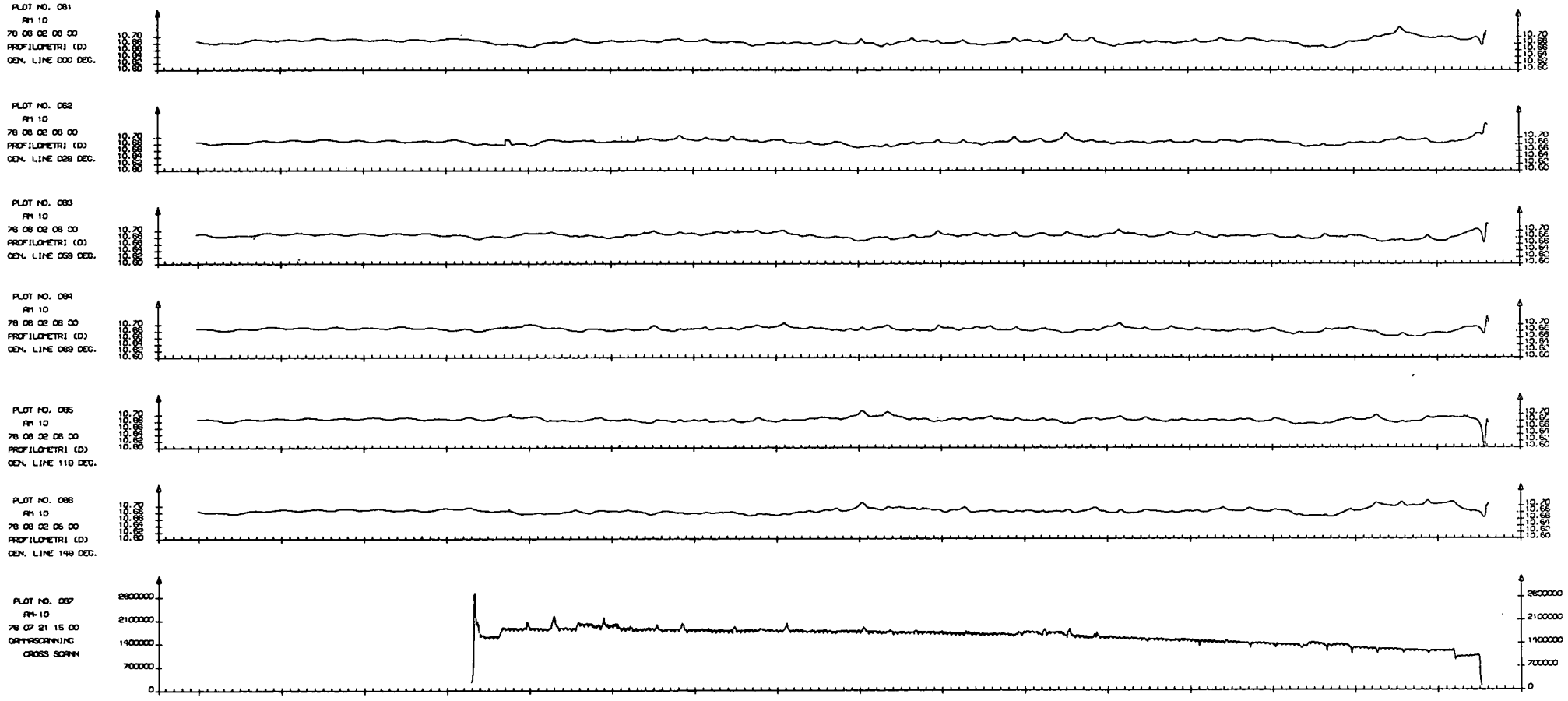

Fig. 23 Profilometry on rod AM-lo, together with gross gamma scan.
Top to the left.
Each div. on axial scale equals 5 mm.

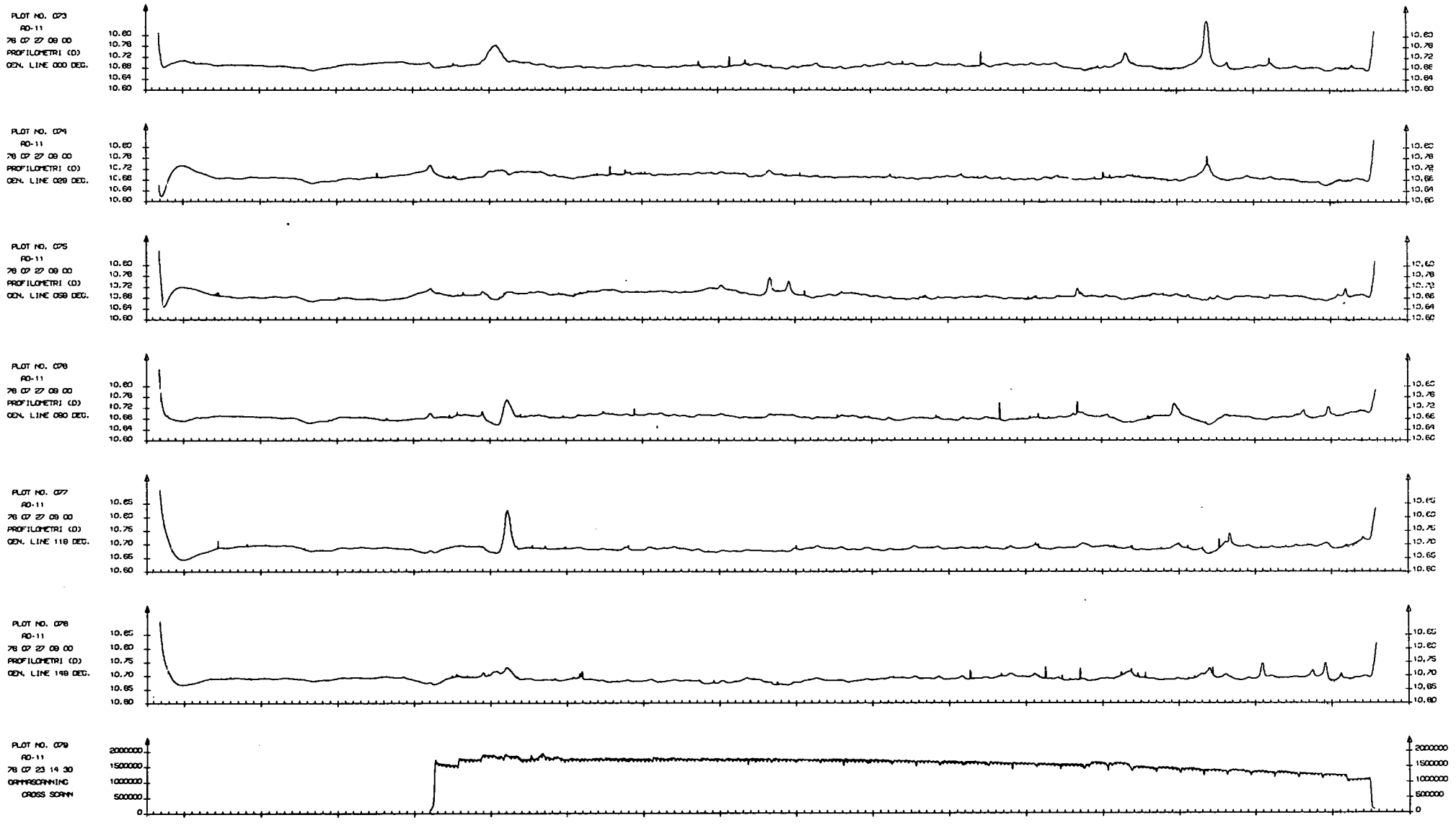

Fig. 24 Profilometry on rod AK-11, together with gross gamma scan.
Top to the left.
Each div. on axial scale equals 5 mm.

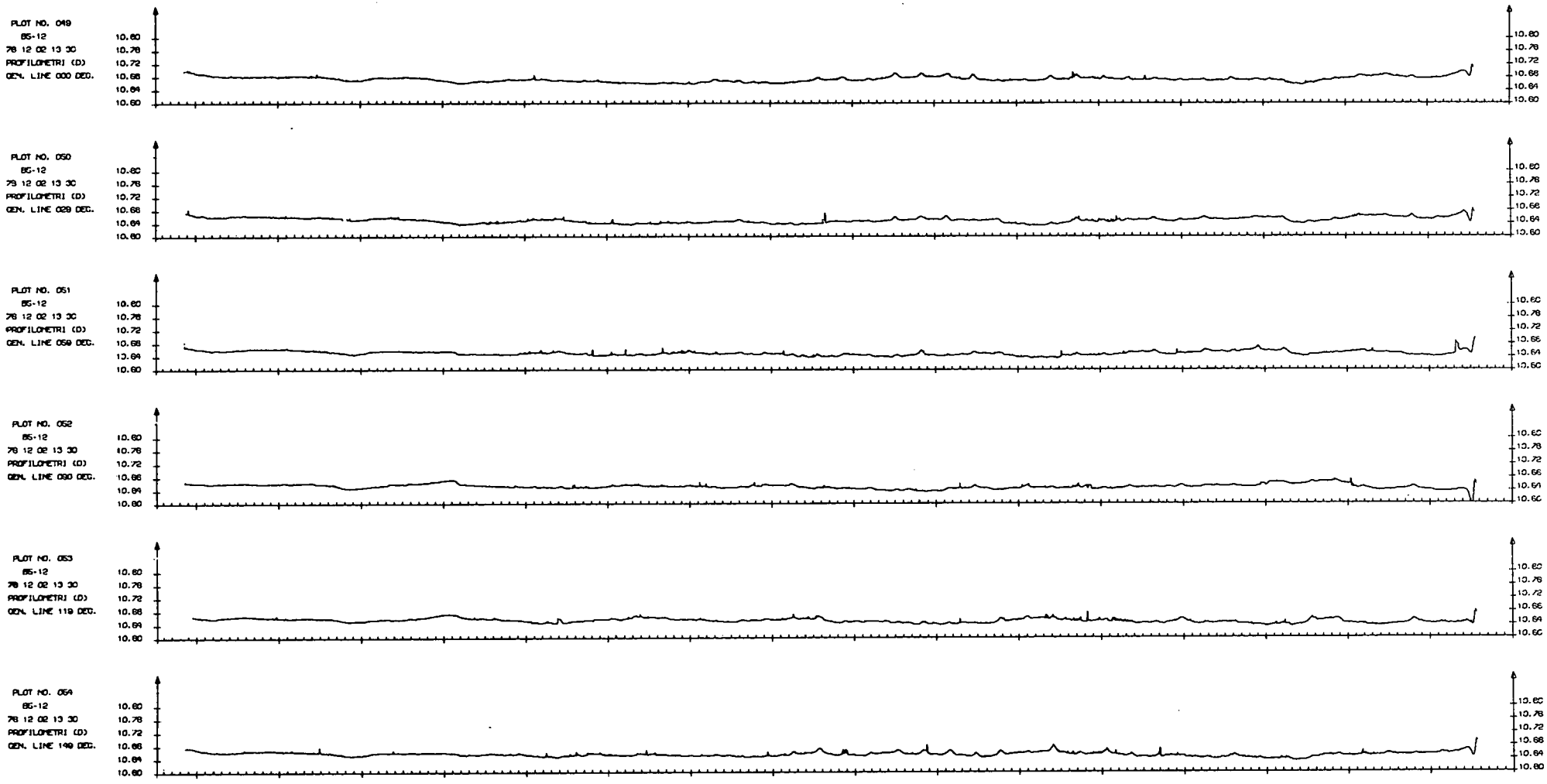

Fig. 25 Profilometry on rod B5-12, together with gross gamma scan. Top to the left.
Each div. on axial scale equals 5 mm.

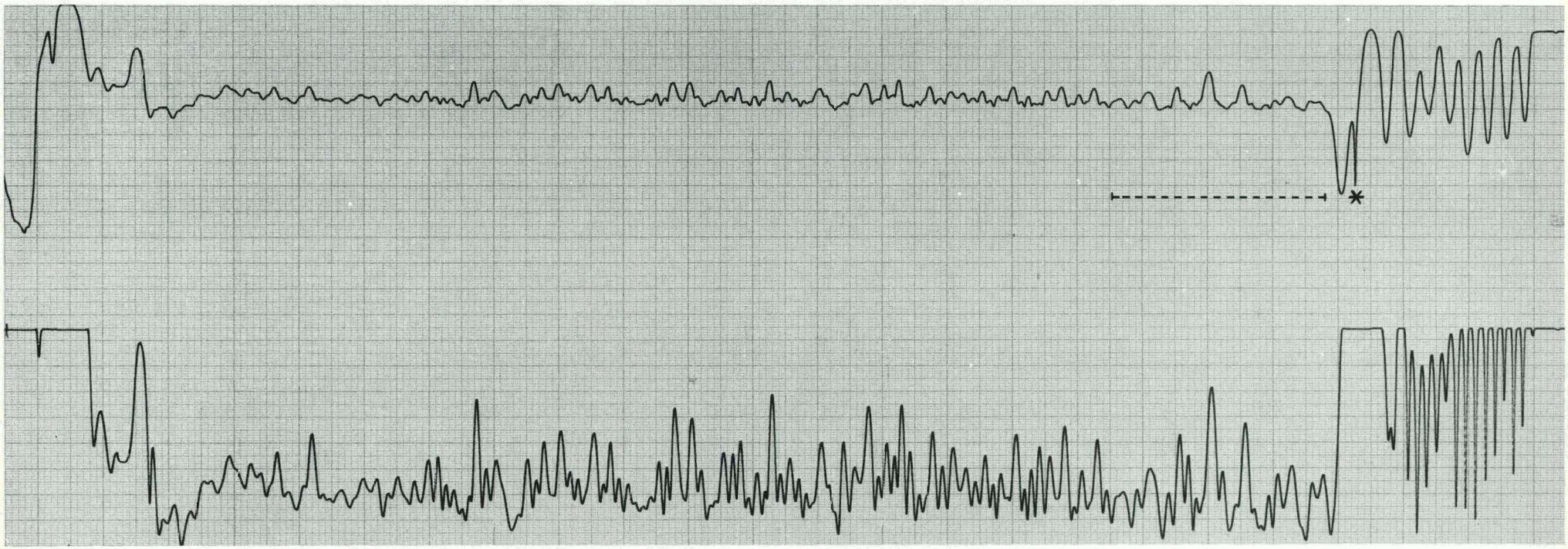

Fig. 26 Eddy current trace, rod AH-7.
Upper trace: phase curve.
Lower trace: amplitude curve
* Washer position
Length of broken line loo mm.
Top to the right.

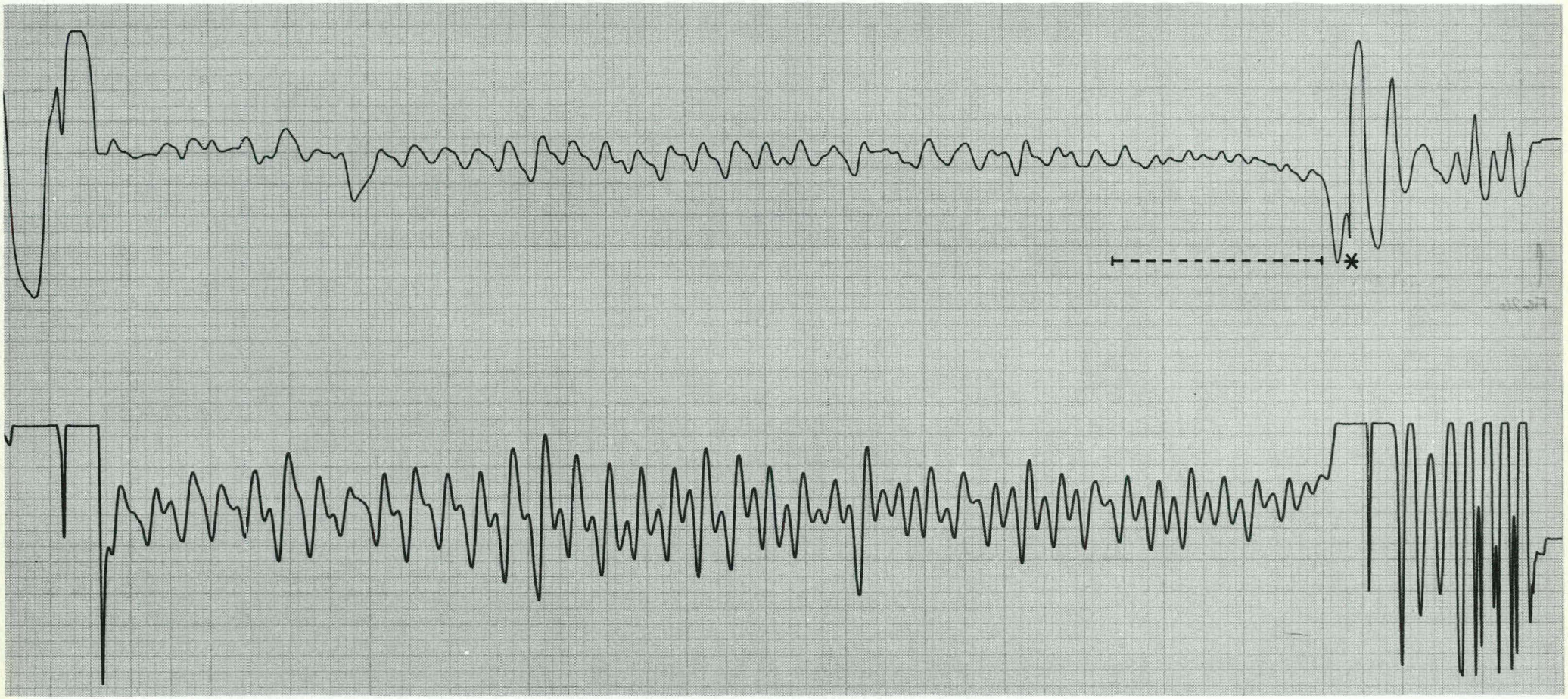

Fig. 27 Eddy current trace, rod AJ-8
Upper trace: phase curve
Lower trace: amplitude curve
* Washer position.
Length of broken line loo mm.
Top to the right.

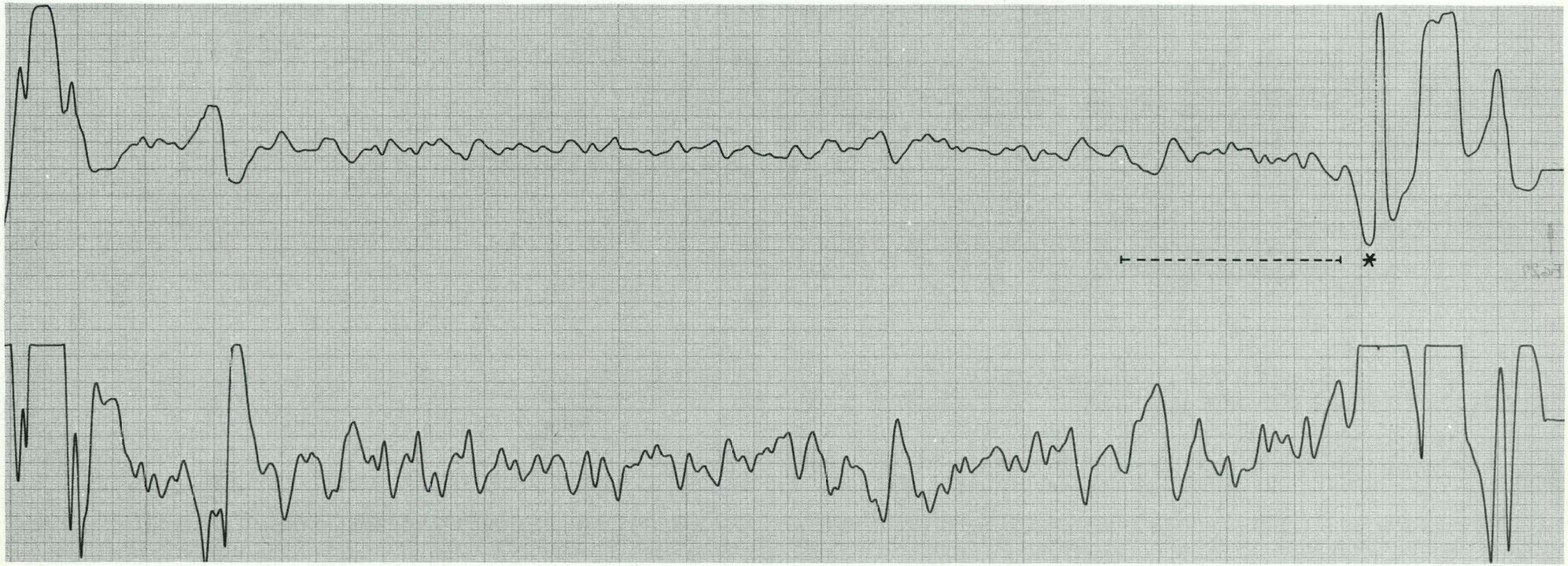

Fig. 28 Eddy current trace, rod AO-9
Upper trace: phase curve
Lower trace: amplitude curve
* Washer position.
Length of broken line loo mm.
Top to the right.

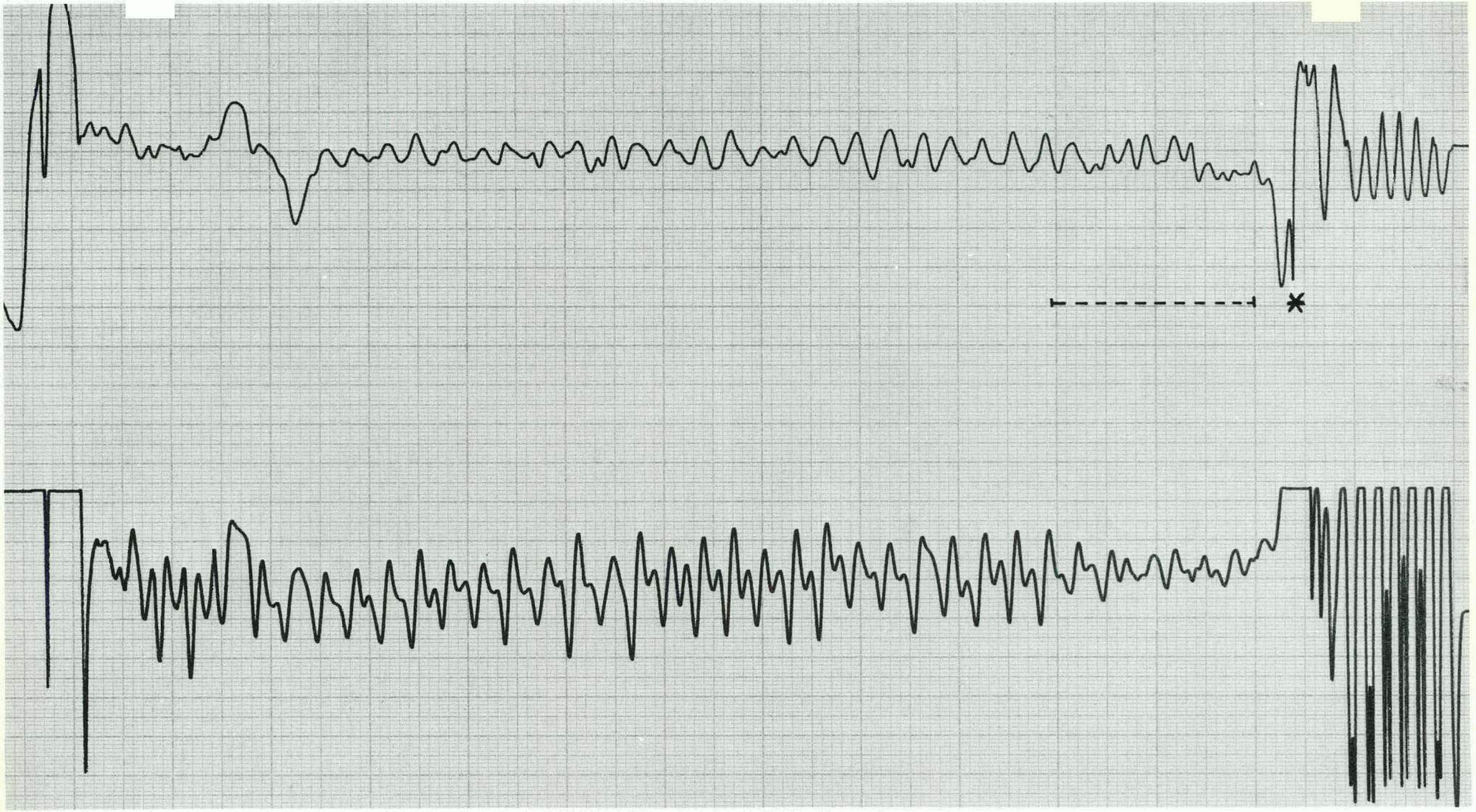

Fig. 29 Eddy current trace, rod AM-lo
Upper trace: phase curve
Lower trace: amplitude curve
× Washer position.
Length of broken line 1oo mm.
Top to the right.

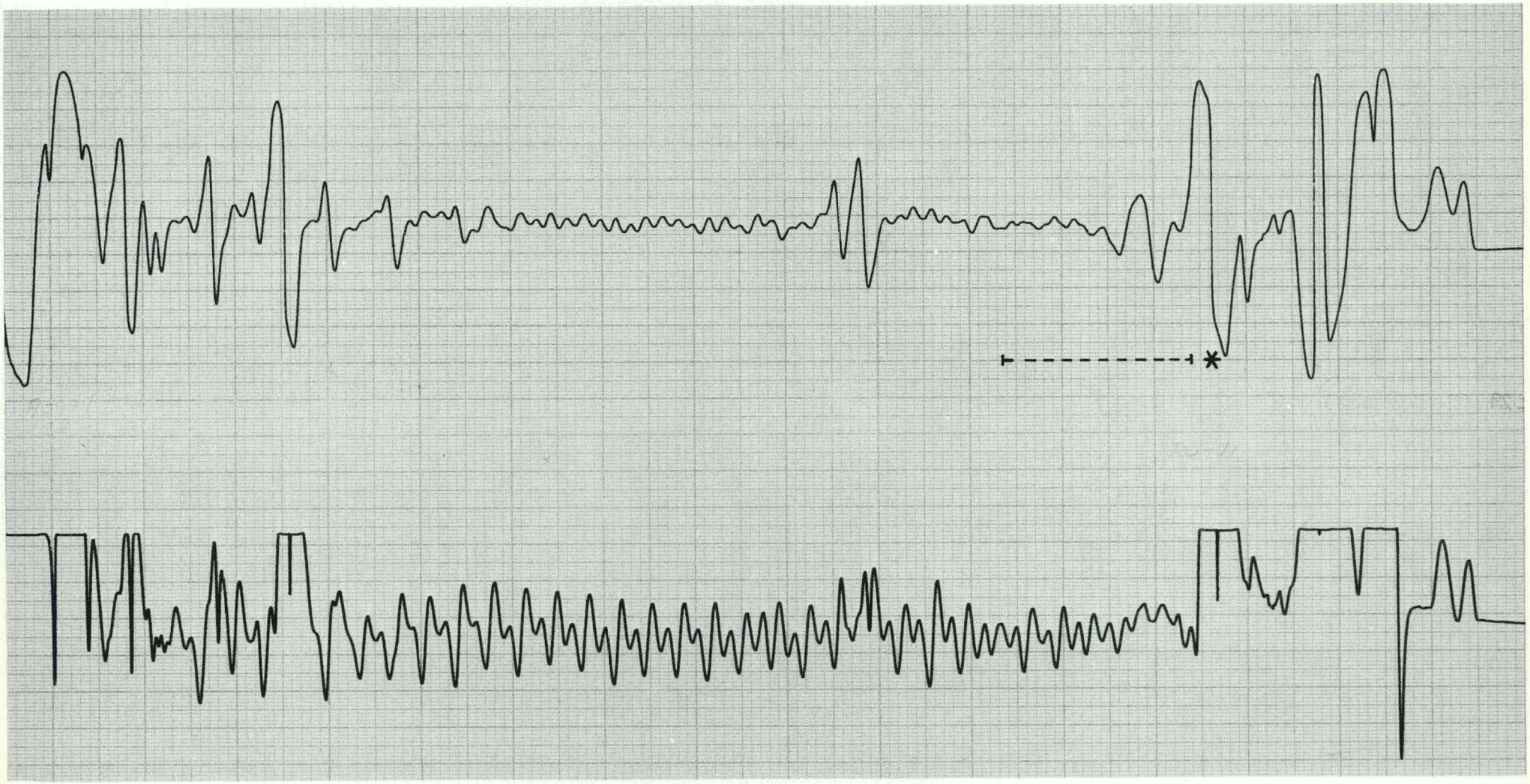

Fig. 30 Eddy current trace, rod AK-11
Upper trace: phase curve
Lower trace: amplitude curve
× Washer position.
Length of broken line loo mm.
Top to the right.

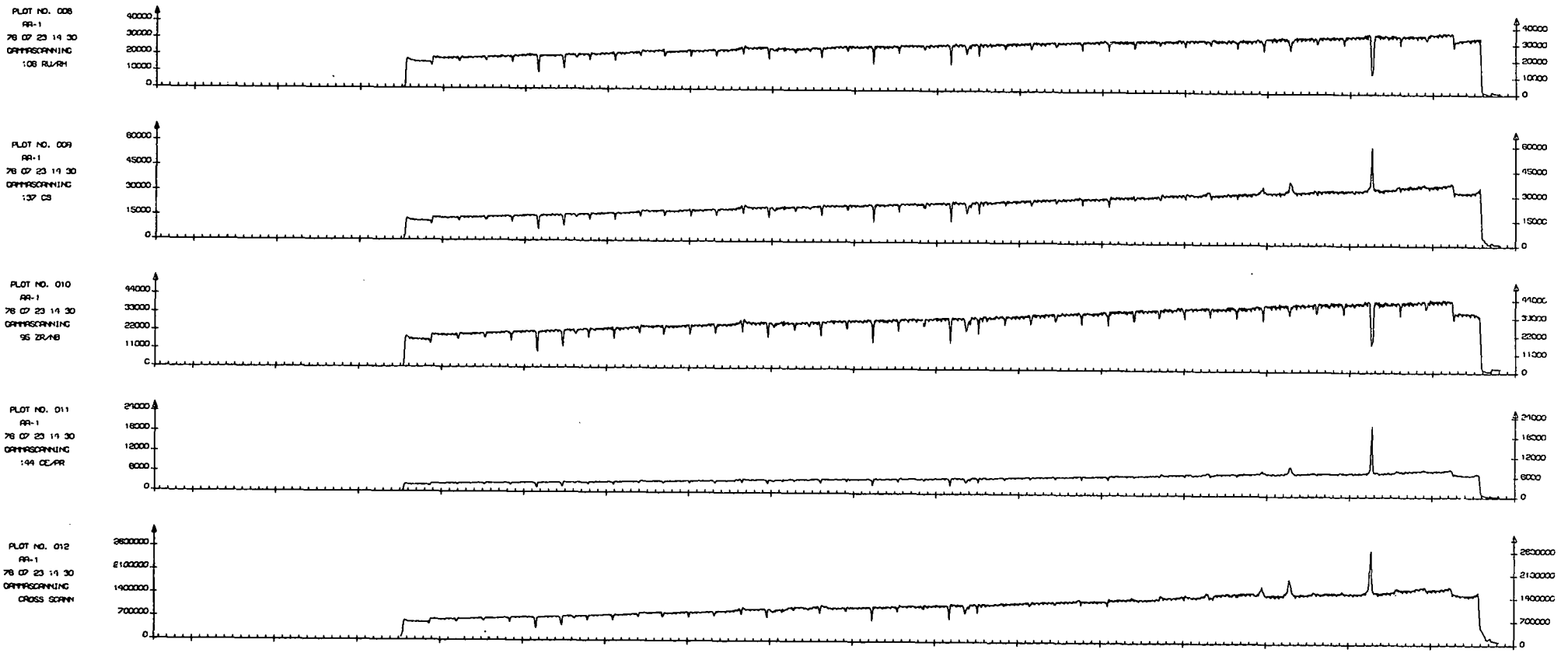

Fig. 31 Gamma scanning rod AA-1
Isotopes from top downwards
1o6 Ru/Rh, 137 CS, 95 Zr/Nb, 144Ce/Pr, gross scan.
Top to the left.
Each division on axial scale equals 5 mm.

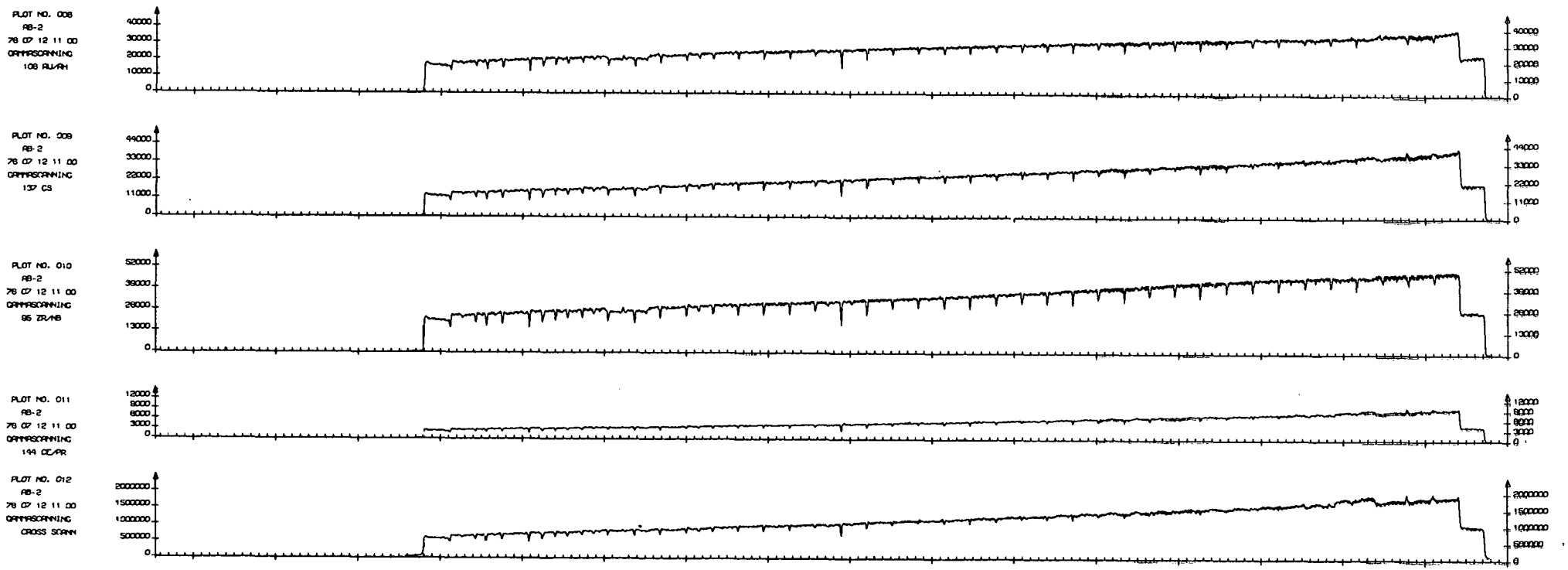

Fig. 32 Gamma scanning, rod AB-2
Isotopes from top downwards
106 Ru/Rh, 137 Cs, 95 Zr/Nb, 144 Ce/Pr, gross scan.
Top to the left.
Each division on axial scale equals 5 mm.

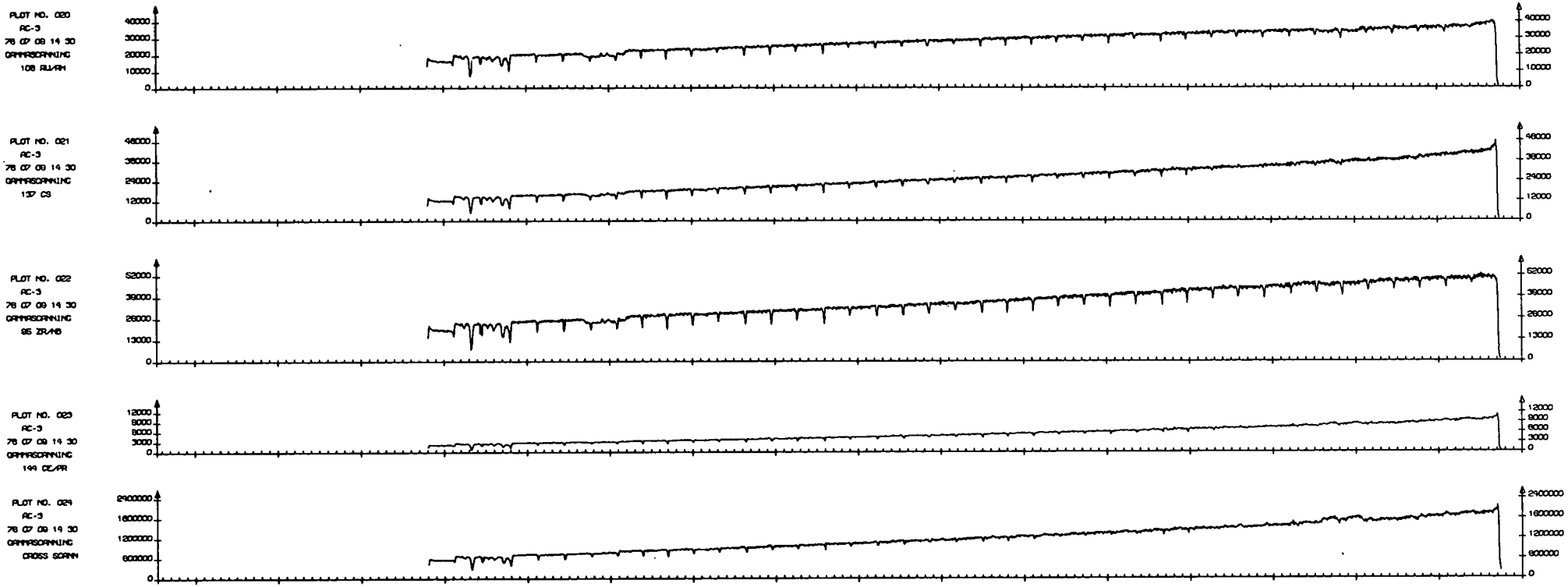

Fig. 33 Gamma scanning, rod AC-3
Isotopes from top downwards
lo6 Ru/Rh, 137 Cs, 95 Zr/Nb, 144 Ce/Pr, gross scan.
Top to the left.
Each division on axial scale equals 5 mm.

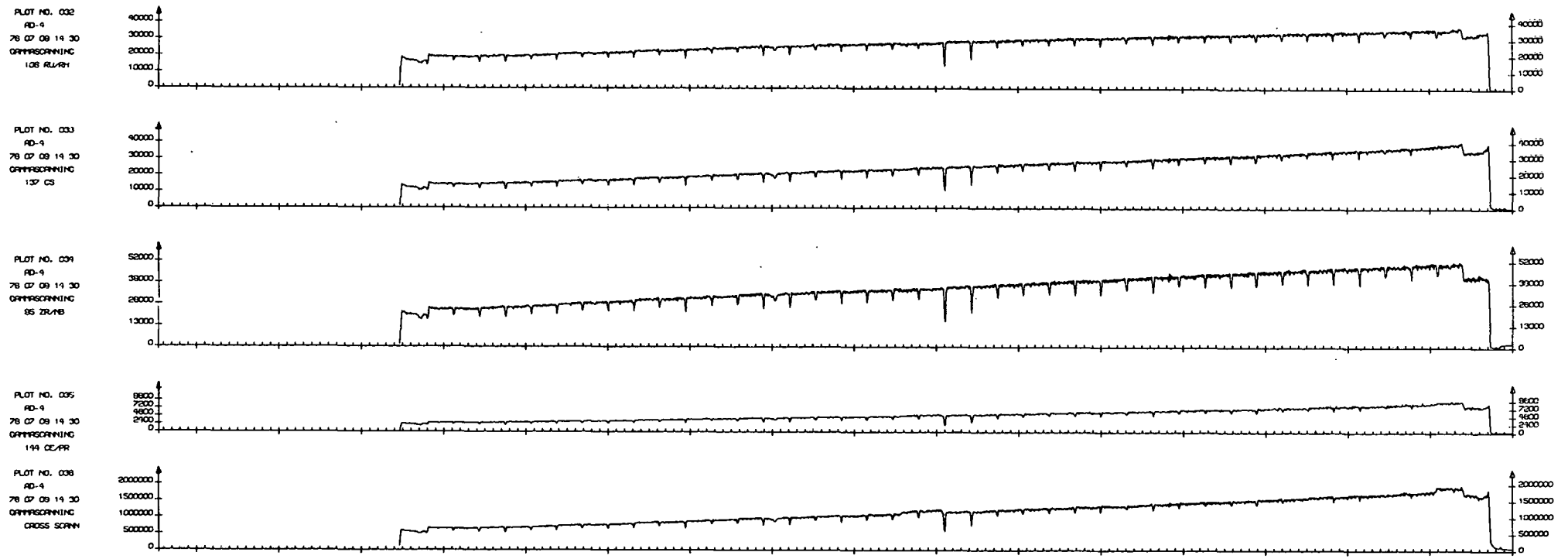

Fig. 34 Gamma Scanning, rod AD-4
Isotopes from top downwards.
1o6 Ru/Rh, 137 Cs, 95 Zr/Nb, 144 Ce/Pr, gross scan.
Top to the left.
Each division on axial scale equals 5 mm.

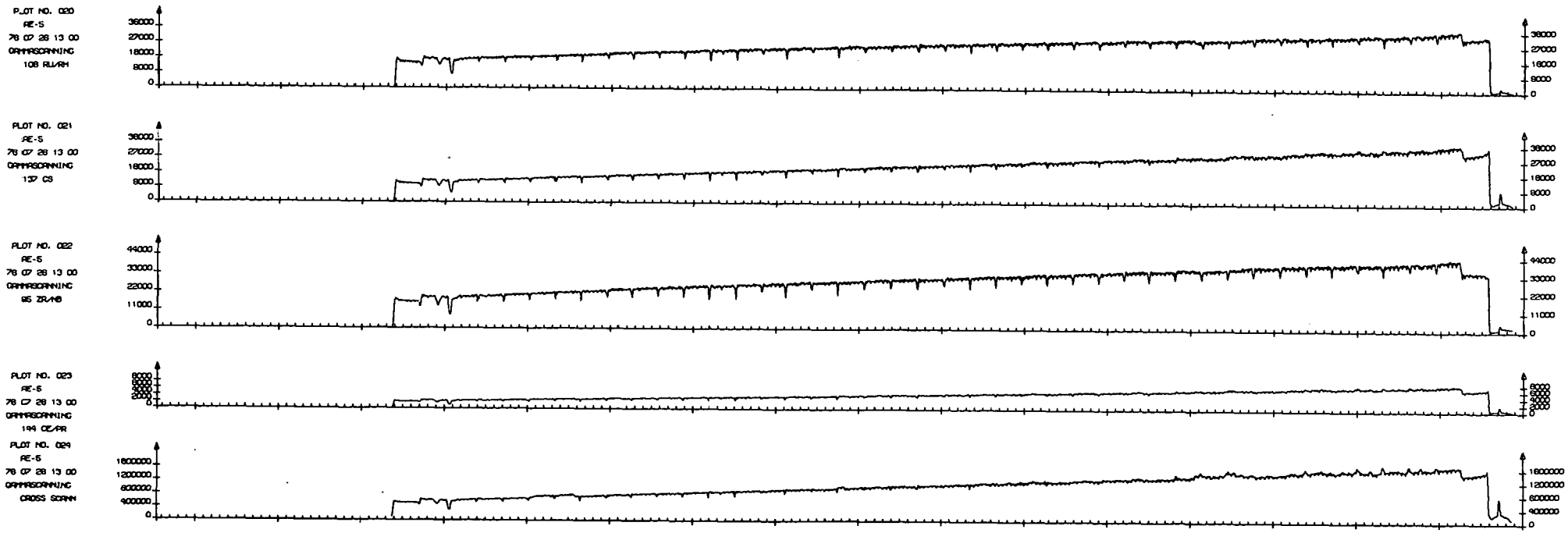

Fig. 35 Gamma scanning, rod AE-5
Isotopes from top downwards
1o6 Ru/Rh, 137 Cs, 95 Zr/Nb, 144 Ce/Pr, gross scan.
Top to the left.
Each division on axial scale equals 5 mm.

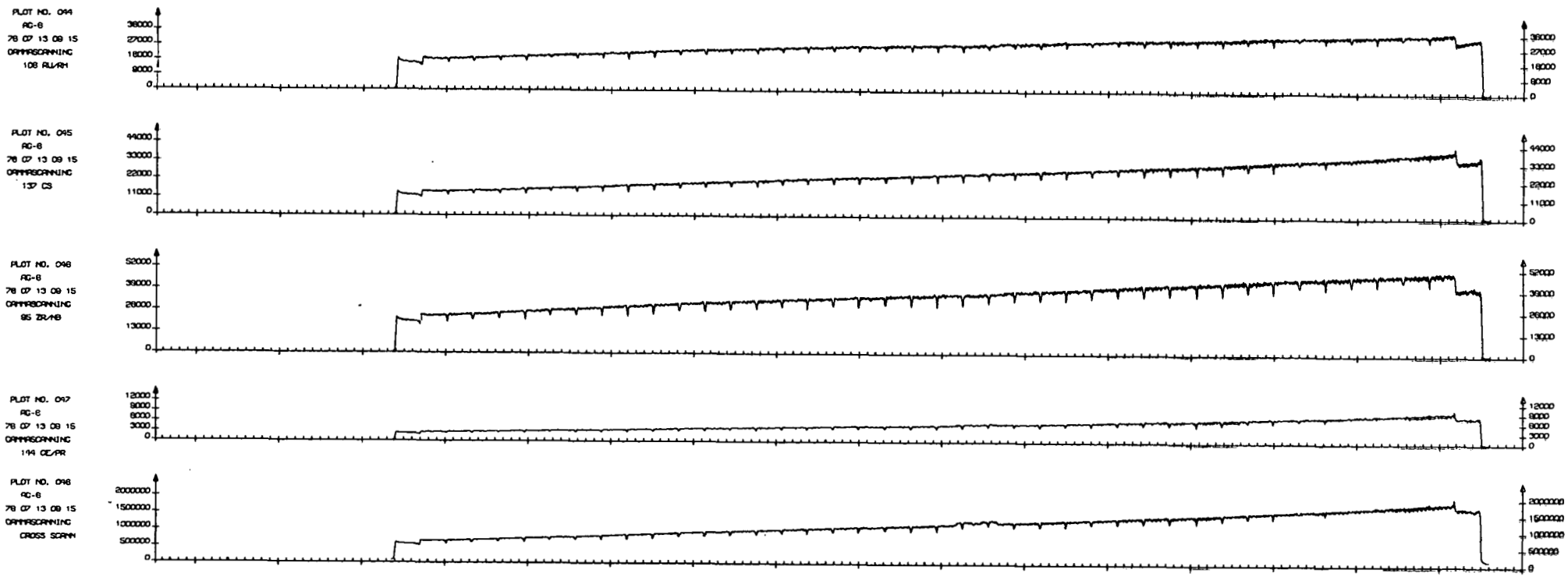

Fig. 36 Gamma Scanning, rod AG-6
Isotopes from top downwards
lo6 Ru/Rh, 137 Cs, 95 Zr/Nb, 144 Ce/Pr, gross scan.
Top to the left.
Each division on axial scale equals 5 mm.

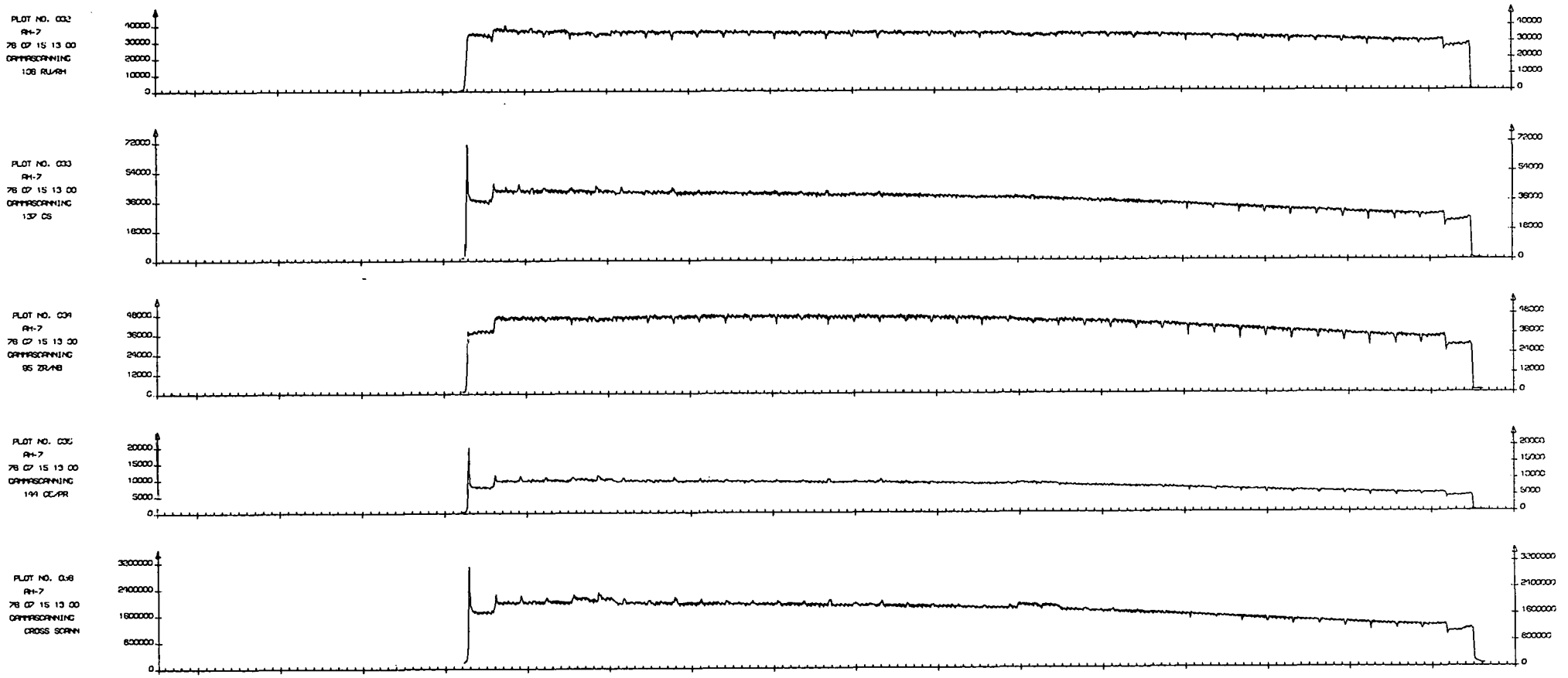

Fig. 37 Gamma scanning, rod AH-7
Isotopes from top downwards
1o6 Ru/Rh, 137 Cs, 95 Zr/Nb, 144 Ce/Pr, gross scan.
Top to the left.
Each division on axial scale equals 5 mm.

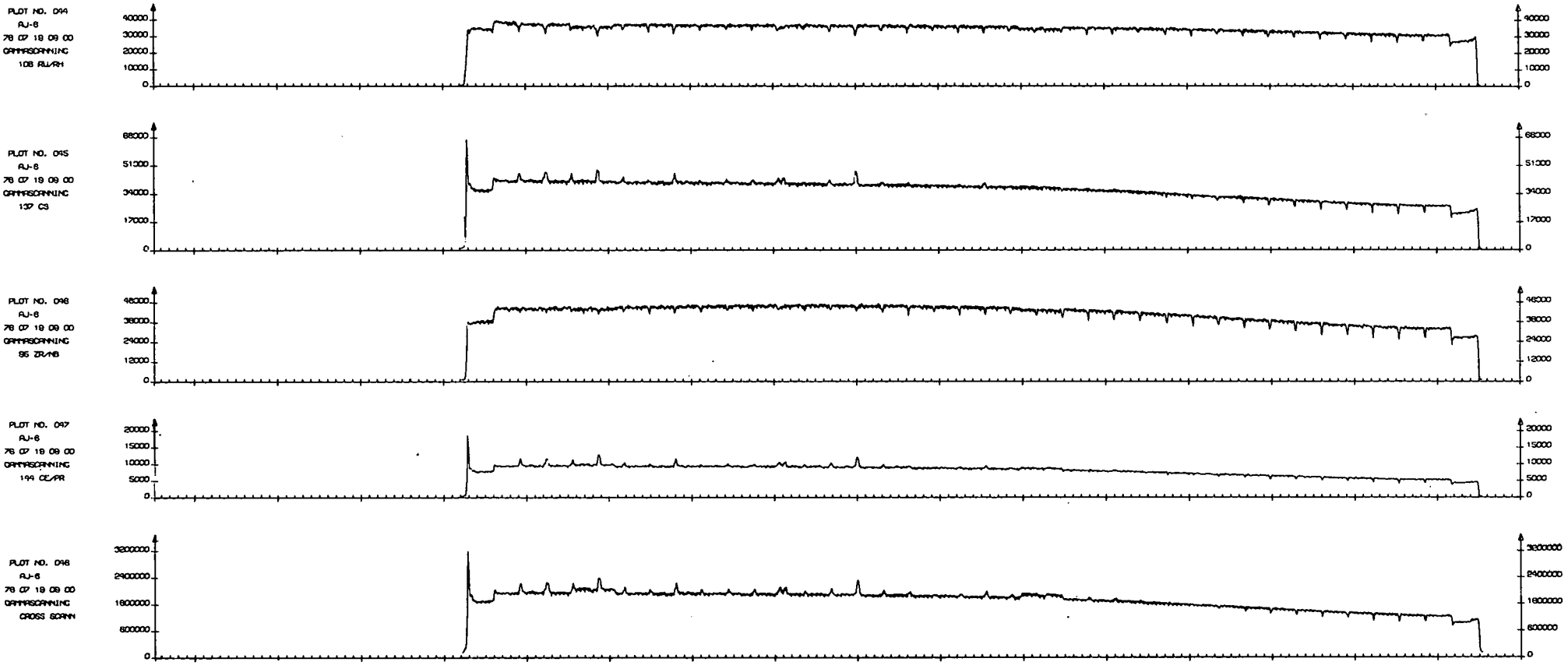

Fig. 38 Gamma scanning, rod AJ-8
Isotopes from top downwards
1o6 Ru/Rh, 137 Cs, 95 Zr/Nb, 144 Ce/Pr, gross scan.
Top to the left.
Each division on axial scale equals 5 mm.

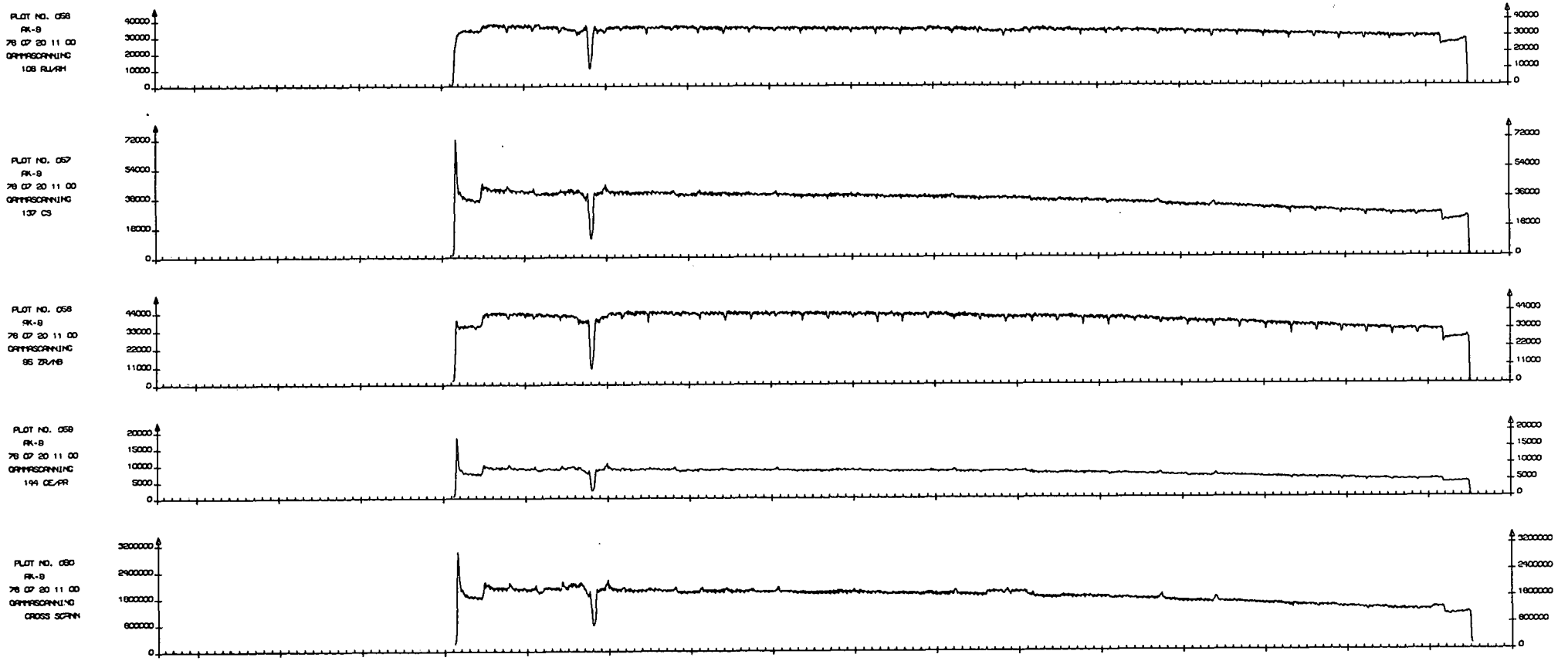

Fig. 39 Gamma scanning, rod AO-9
Isotopes from top downwards
1o6 Ru/Rh, 137 Cs, 95 Zr/Nb, 144 Ce/Pr, gross scan.
Top to the left.
Each division on axial scale equals 5 mm.

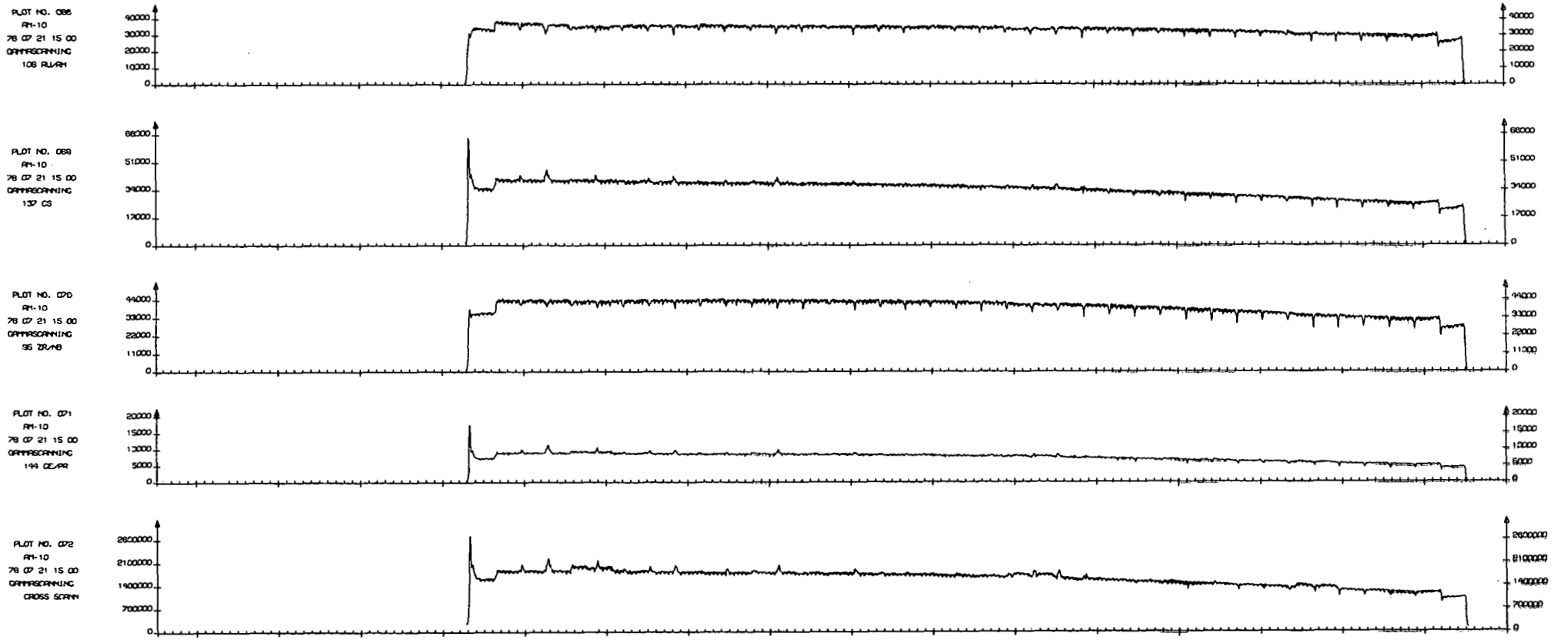

Fig. 40 Gamma scanning, rod AM-lo
Isotopes from top downwards
lo6 Ru/Rh, 137 Cs, 95 Zr/Nb, 144 Ce/Pr, gross scan.
Top to the left.
Each division on axial scale equals 5 mm.

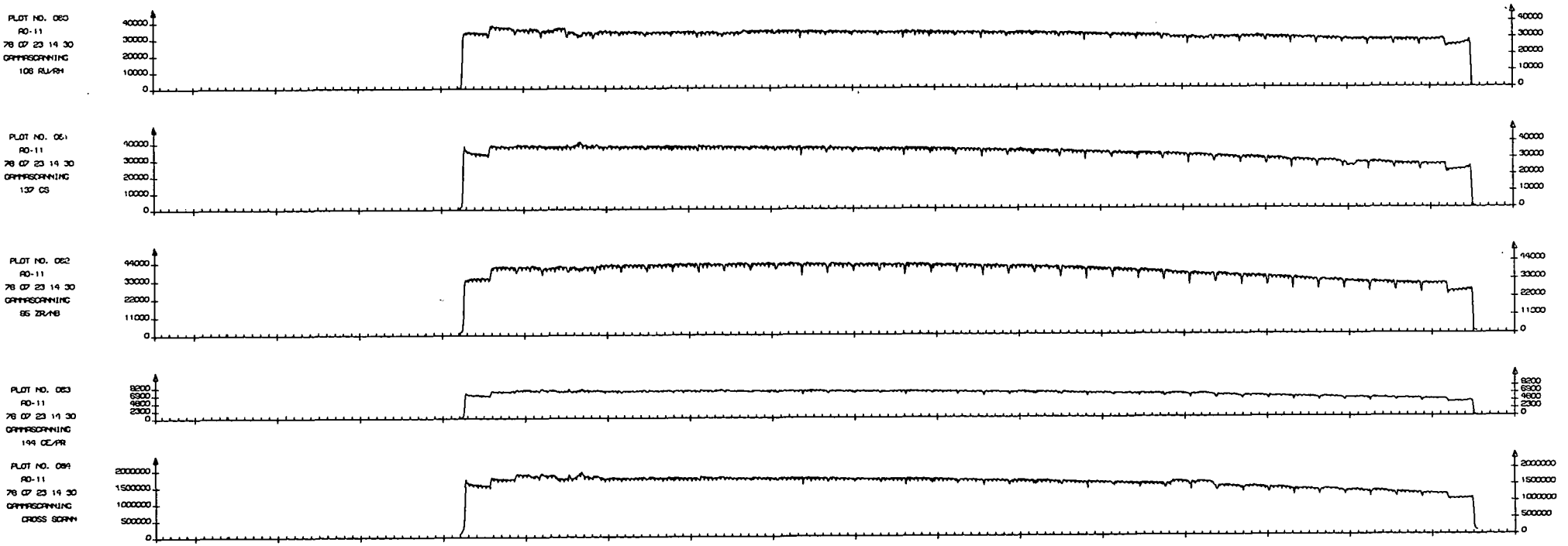

Fig. 41 Gamma scanning, rod AK-11
Isotopes from top downwards
1o6 Ru/Rh, 137 Cs, 95 Zr/Nb, 144 Ce/Pr, gross scan.
Top to the left.
Each division on axial scale equals 5 mm.

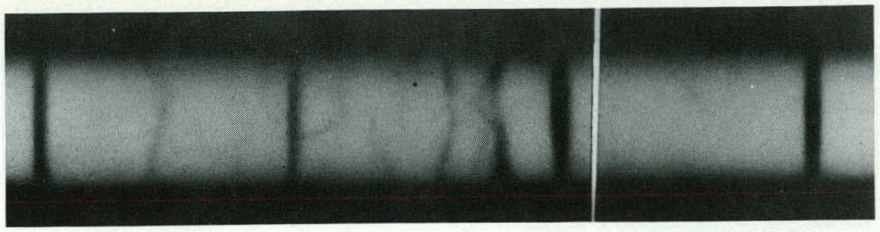

Fig. 42. Rod AA-1

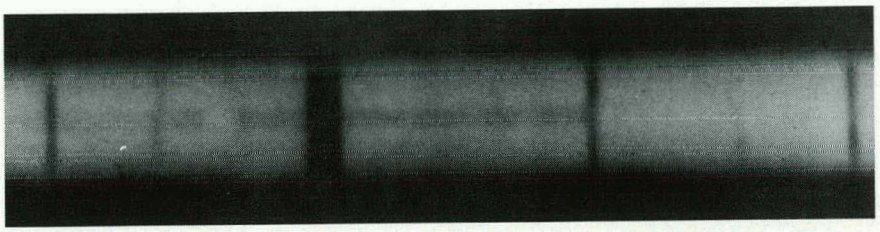

Fig. 43. Rod AA-1

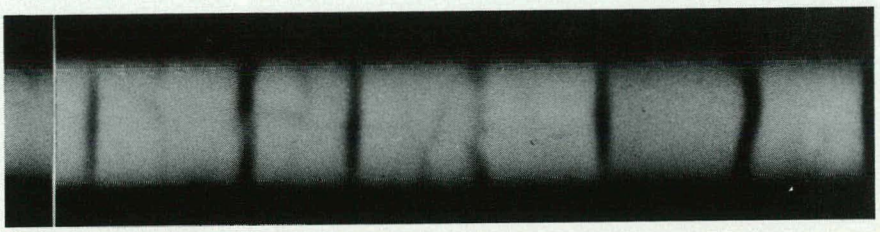

Fig. 44. Rod AB-2

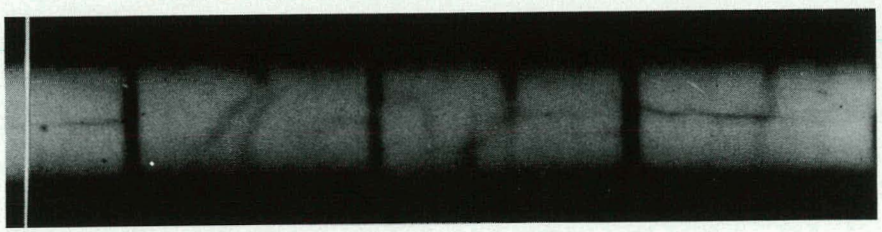

Fig. 45. Rod AB-2

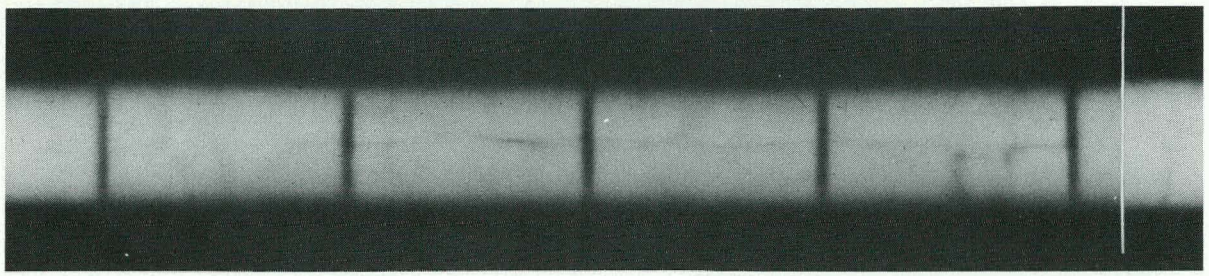

Fig. 46. Rod AB-2

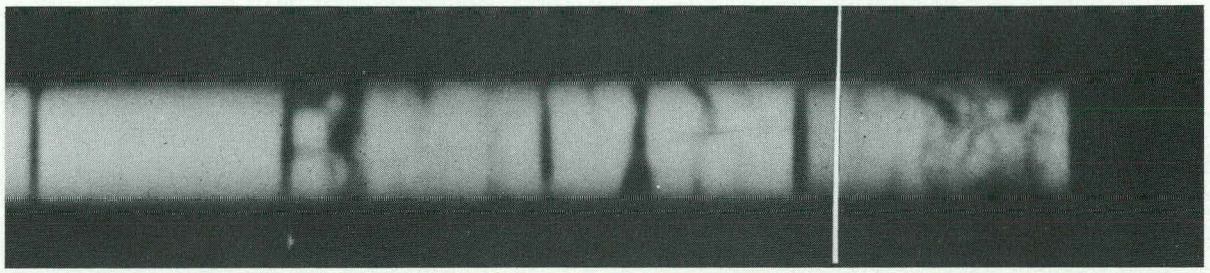

Fig. 47. Rod AC-3

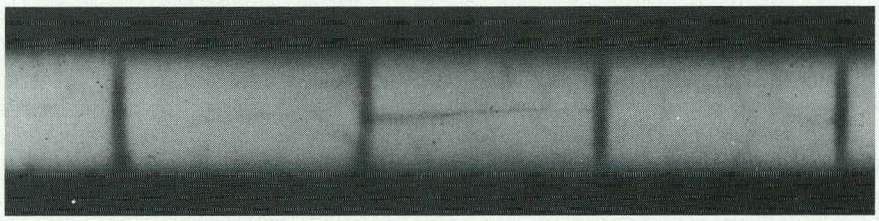

Fig. 48. Rod AC-3

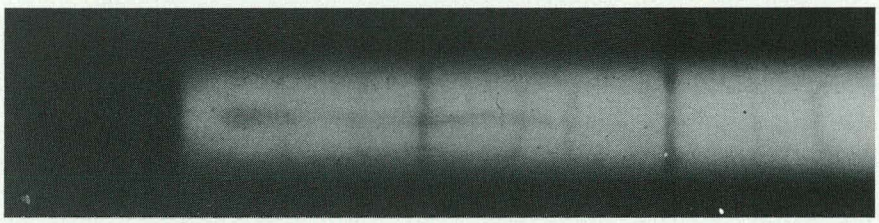

Fig. 49. Rod AC-3

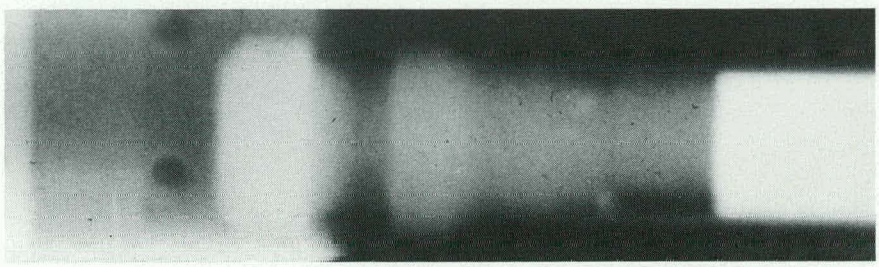

Fig. 50. Rod AC-3

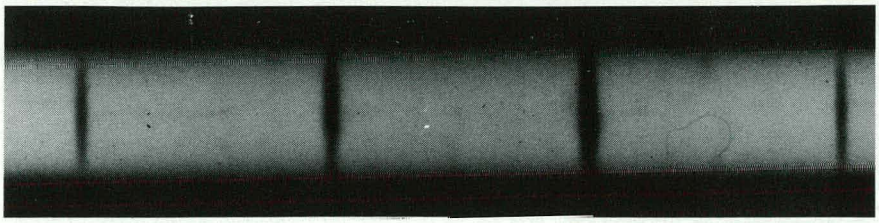

Fig. 51. Rod AD-4

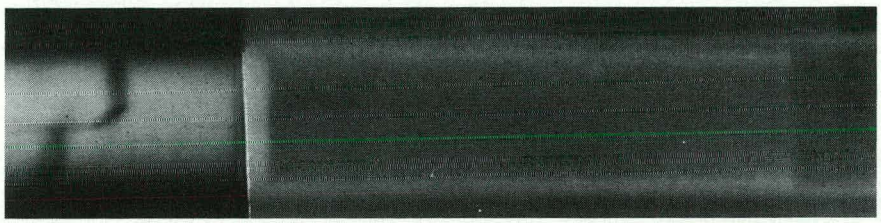

Fig. 52. Rod AD-4

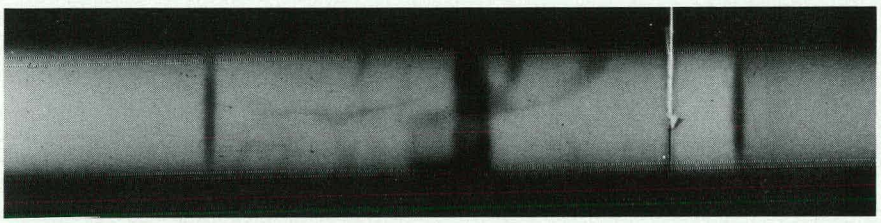

Fig. 53. Rod AE-5

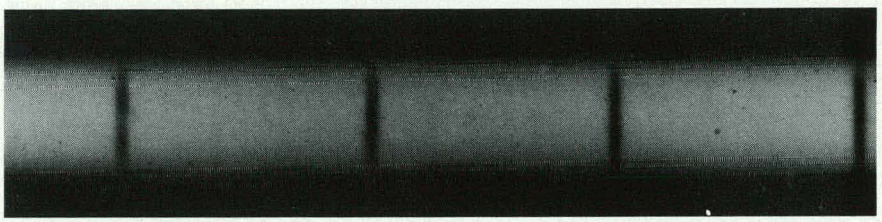

Fig. 54. Rod AG-6

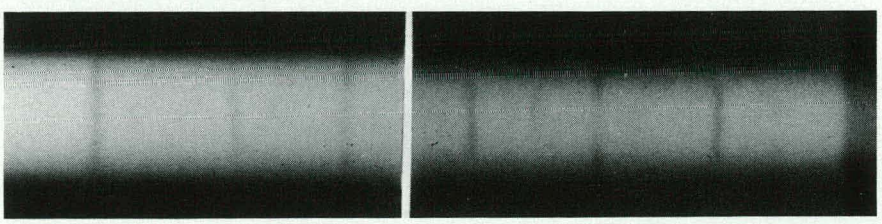

Fig. 55. Rod AH-7

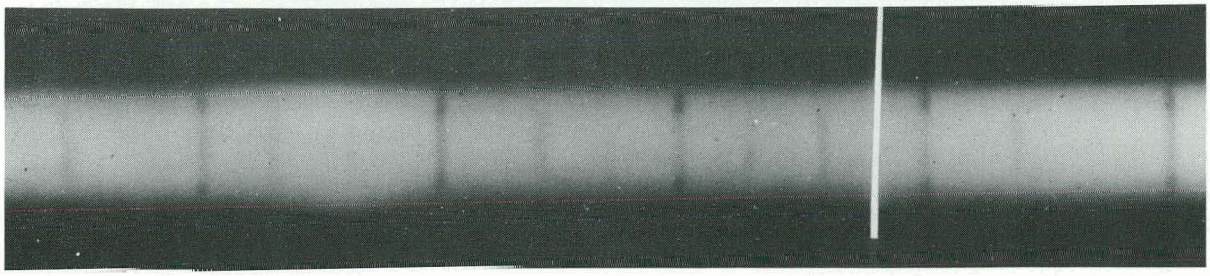

Fig. 56. Rod AJ-8

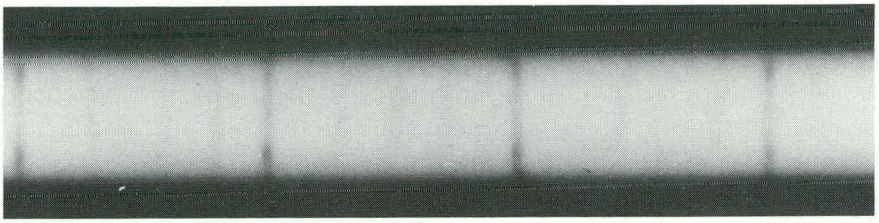

Fig. 57. Rod AO-9

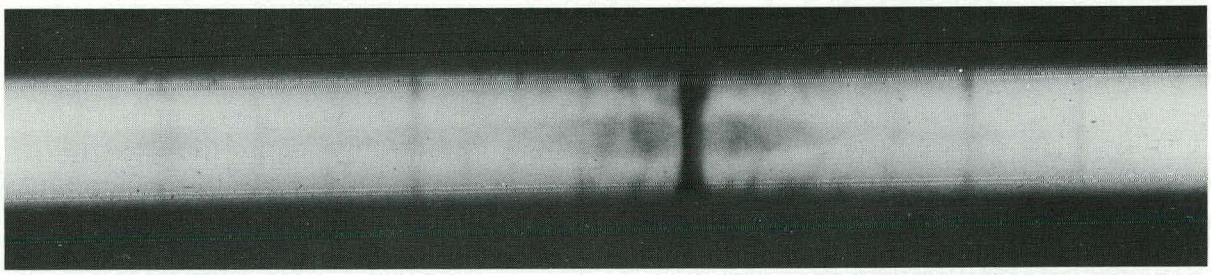

Fig. 58. Rod AO-9

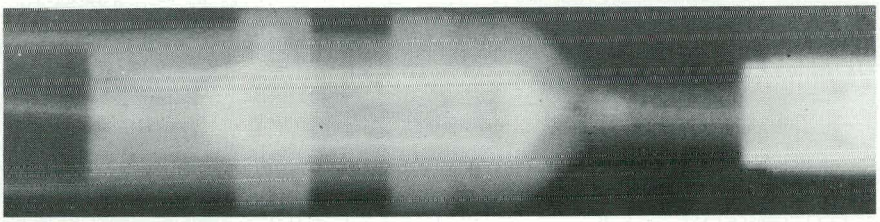

Fig. 59. Rod AK-11

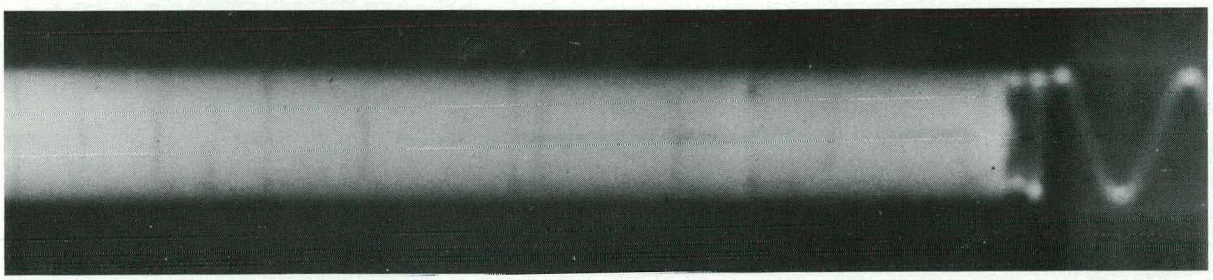

Fig. 60a Rod B5-12

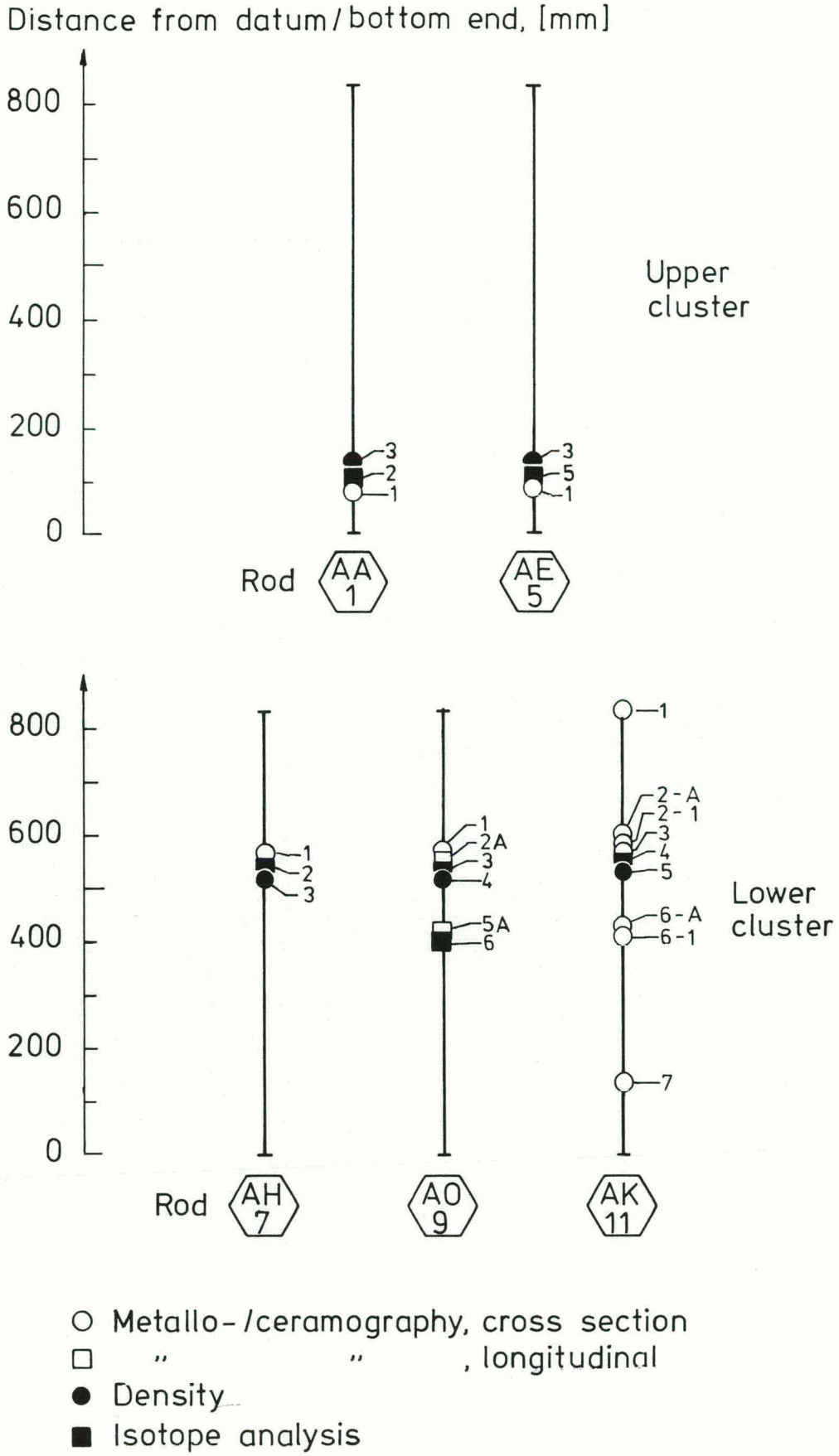

Fig. 6o b. Samples for destructive examination.

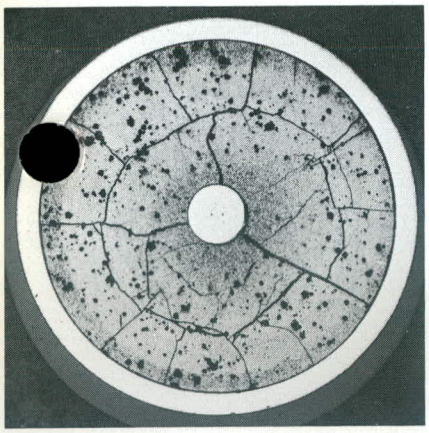

Sample 1-1

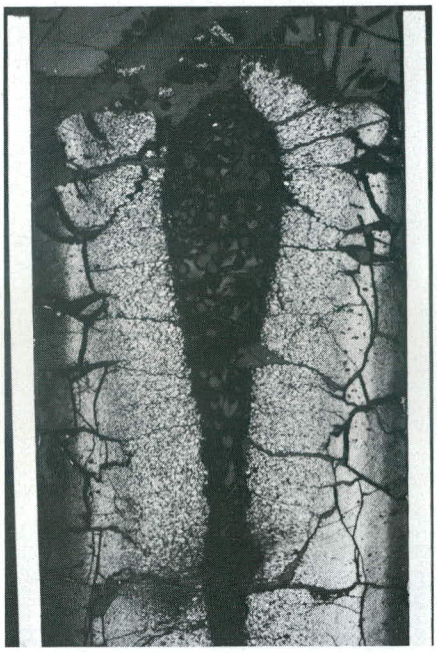

Sample 9-2A

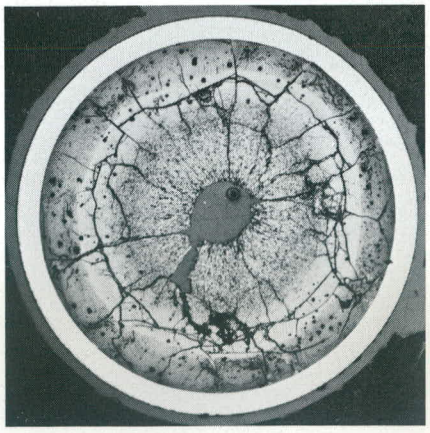

Sample 11-2

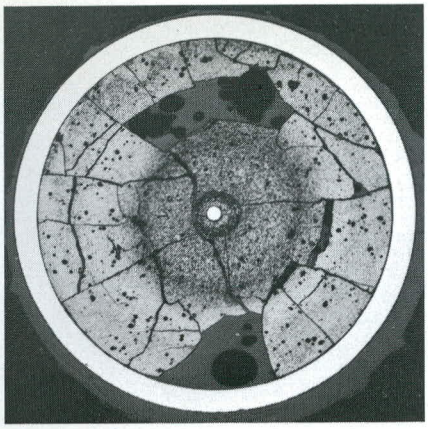

Sample 5-1

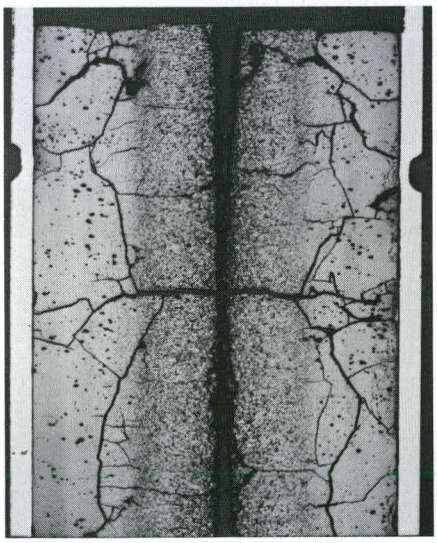

Sample 9-5A

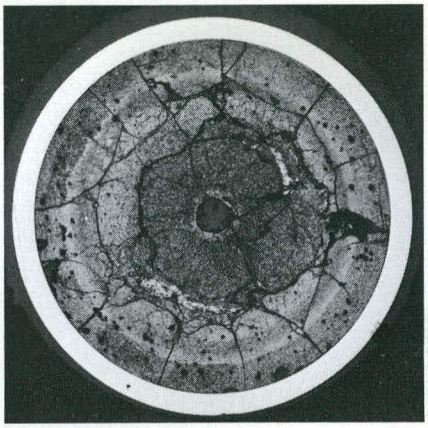

Sample 11-3

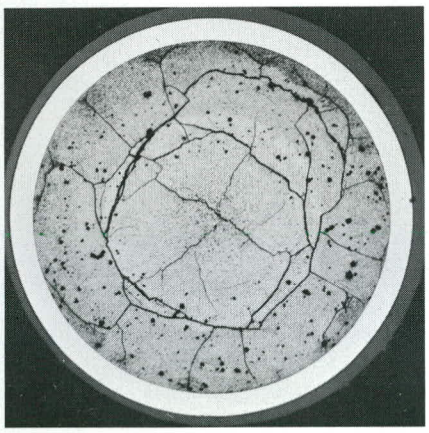

Sample 7-1

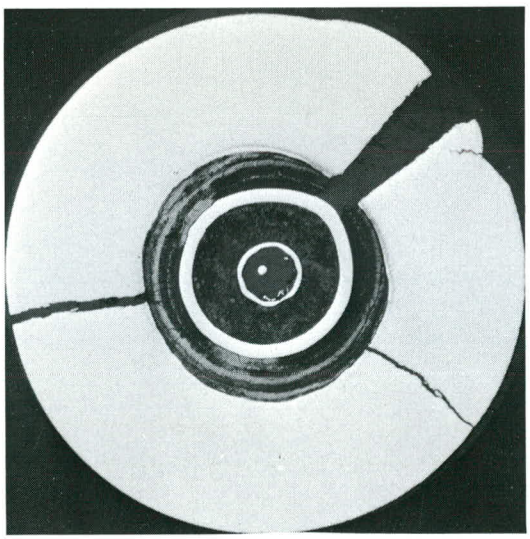

Sample 11-1

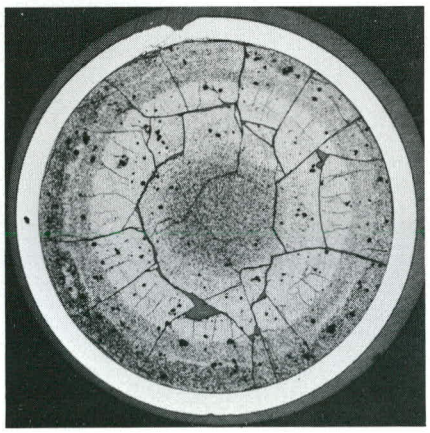

Sample 11-6

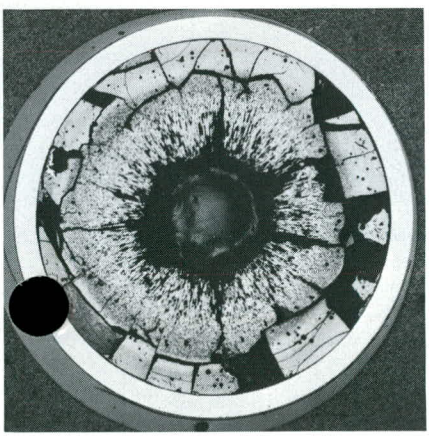

Sample 9-1

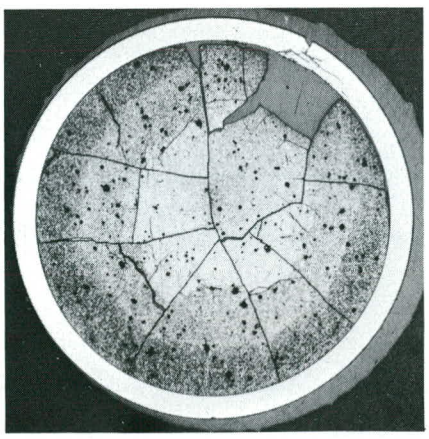

Sample 11-7

Fig. 61 Summary of met. samples (excl. 11-2-1 and 11-6-1)

Sample 1-1

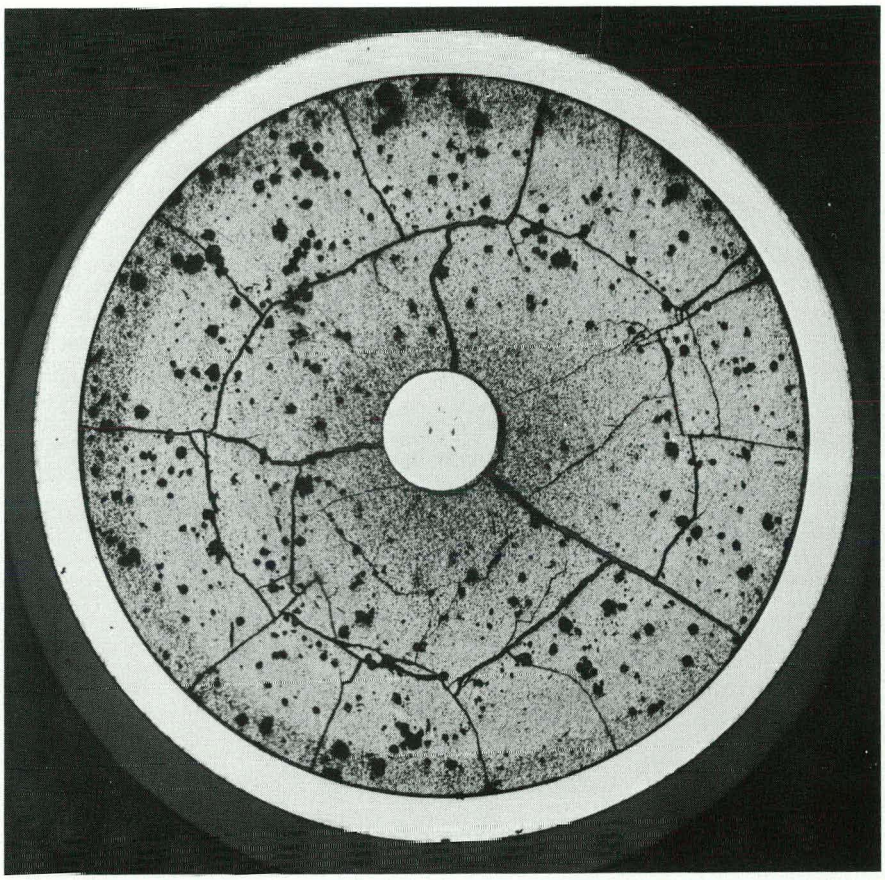

Fig. 62 X 10

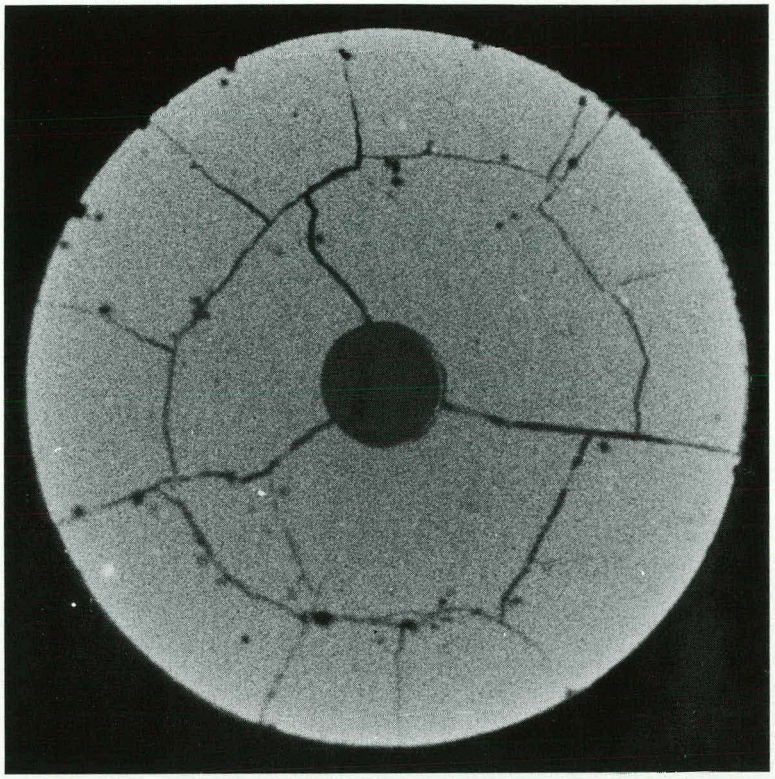

Fig. 63, α-auto., polished X 10

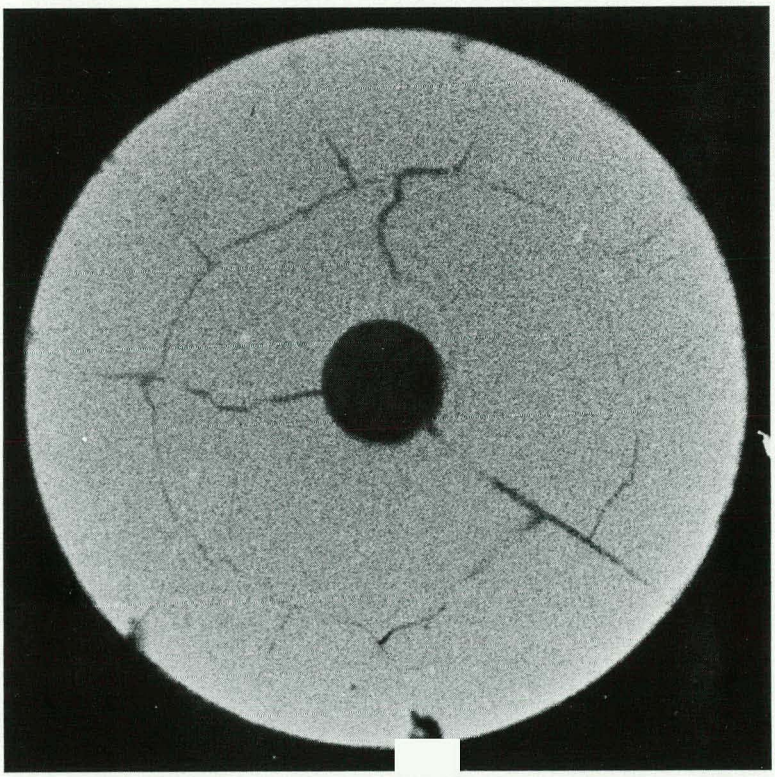

Fig. 64, α-auto., etched X 10

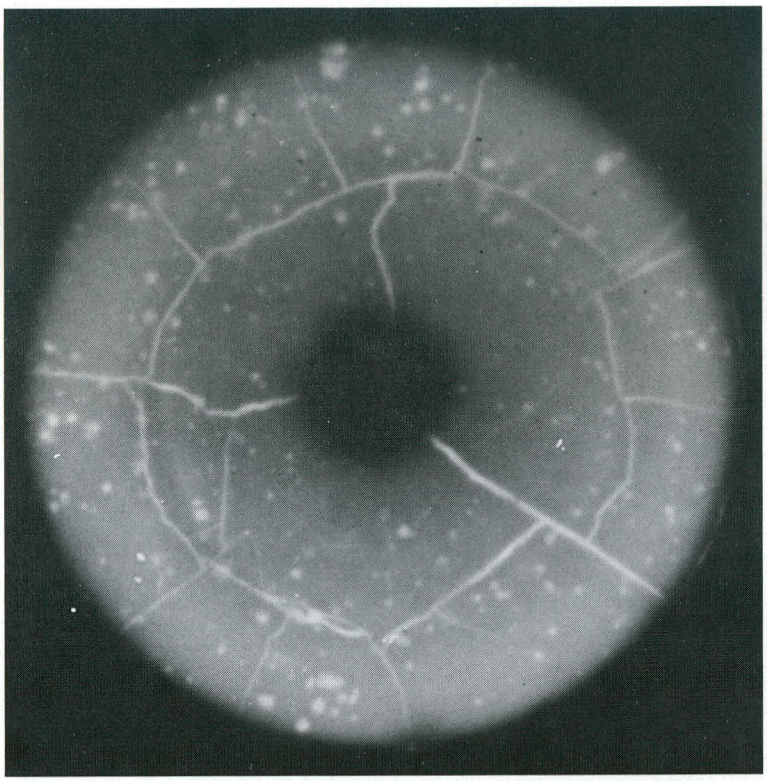

Fig. 65, β/γ-auto., polished X 10

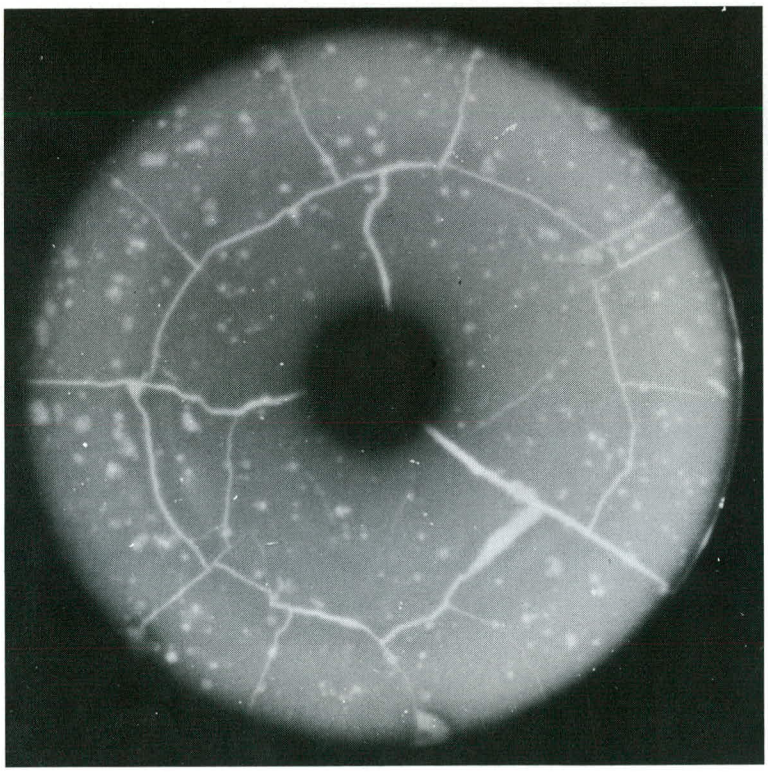

Fig. 66, β/γ-auto., etched X 10

Sample 1-1

Fig. 67, polished, X 30

Fig. 68, etched, X 30

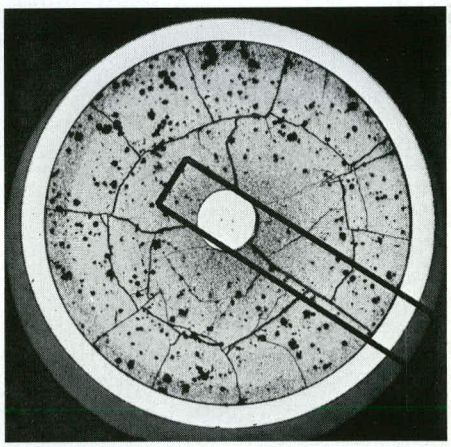

Fig. 67
Fig. 68

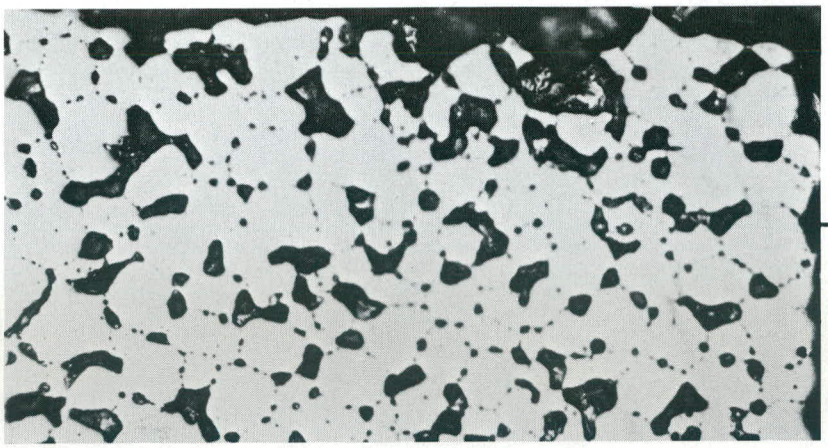

Fig. 69 Polished, X 4oo

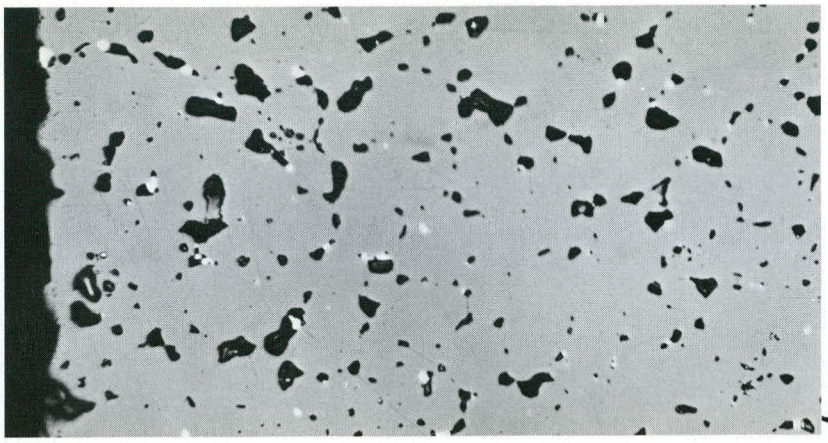

Fig. 7o Polished, X 4oo

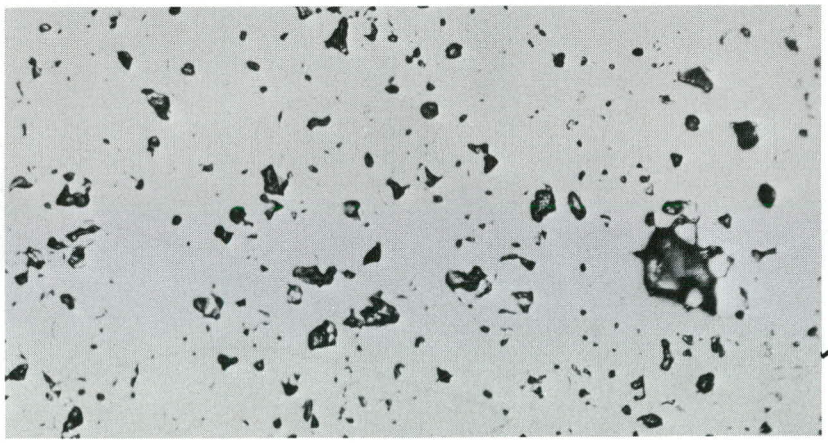

Fig. 71 Polished, X 4oo

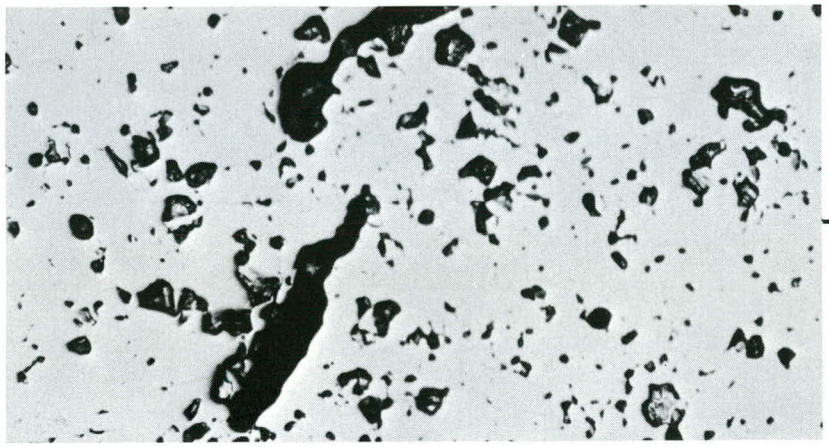

Fig. 72 Polished, X 4oo

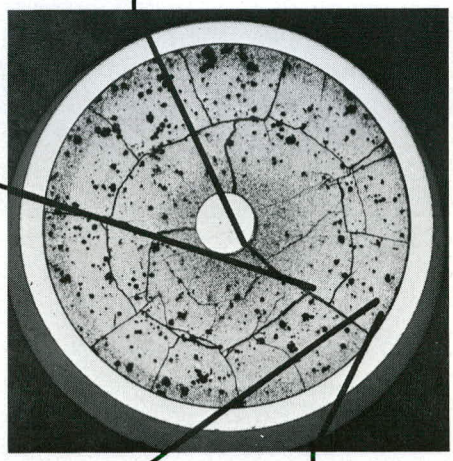

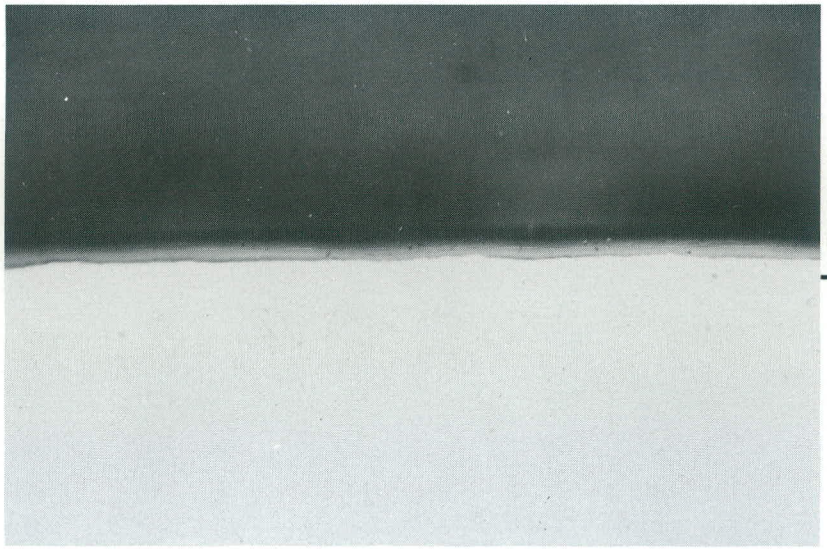

Fig. 73 Outer oxide layer, polished, X 4oo

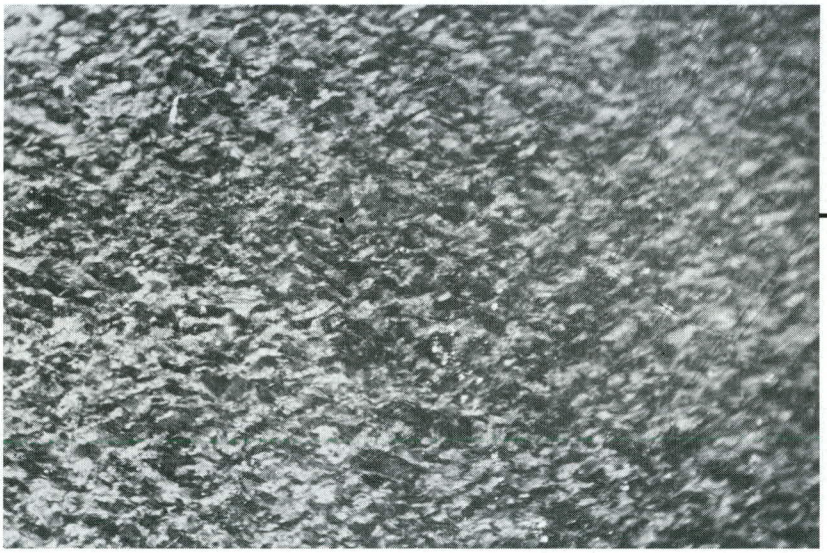

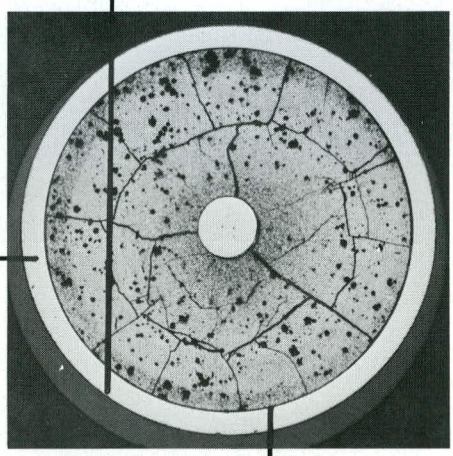

Fig. 74 Polished, pol. light, X 4oo

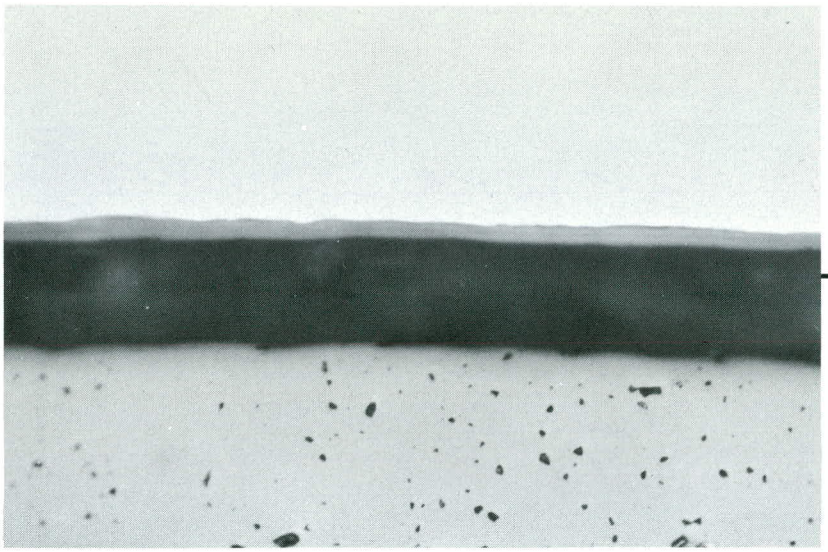

Fig. 75 Inner oxide layer, polished, X 4oo

Sample 1-1

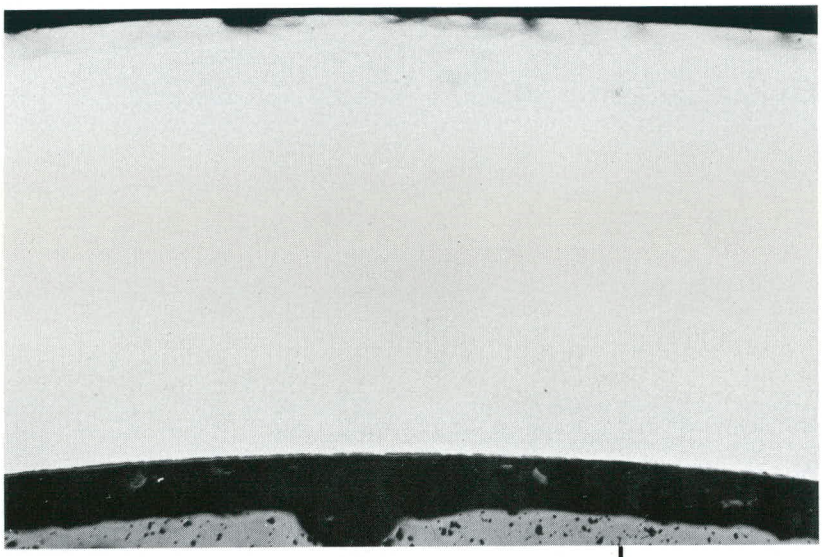

Fig. 76 Polished, X loo

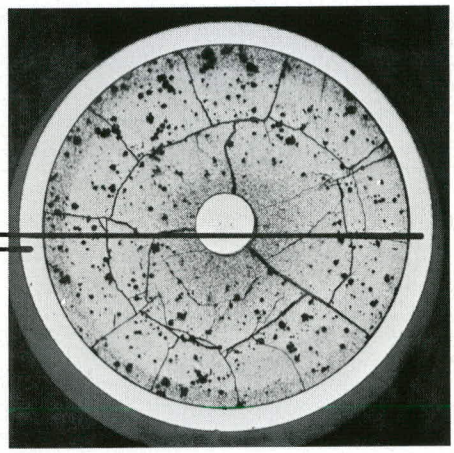

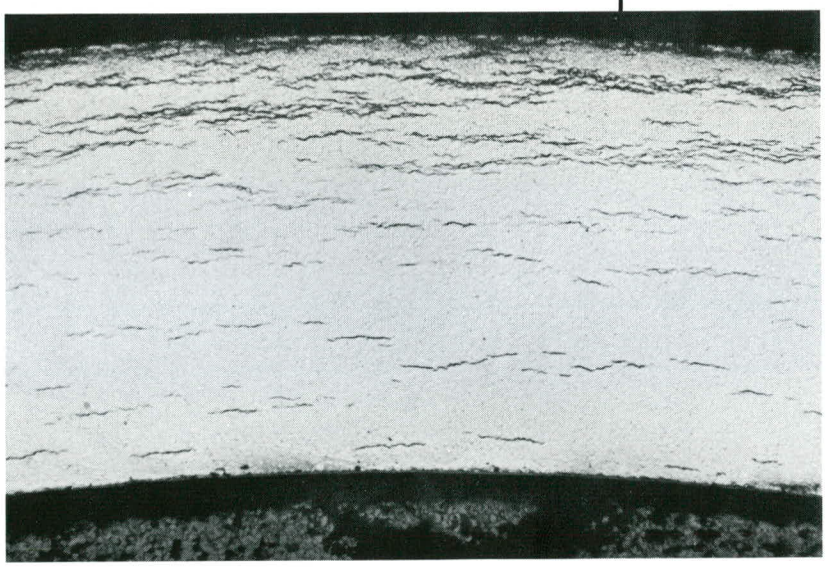

Fig. 77 Etched, X loo

Sample 5-1

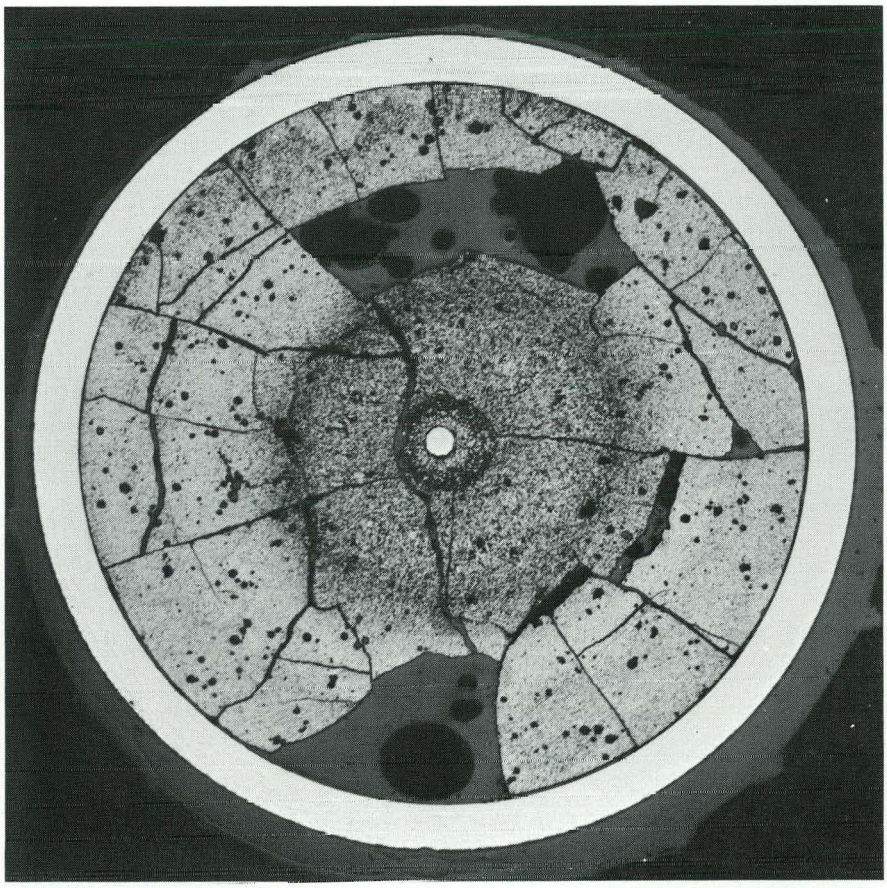

Fig. 78 X 10

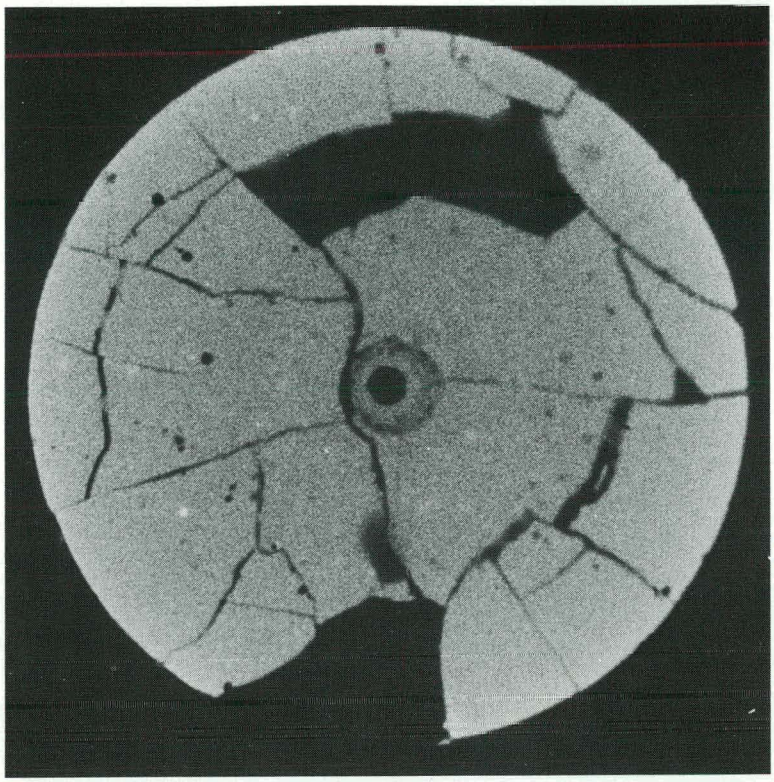

Fig. 79, α-auto., polished X 10

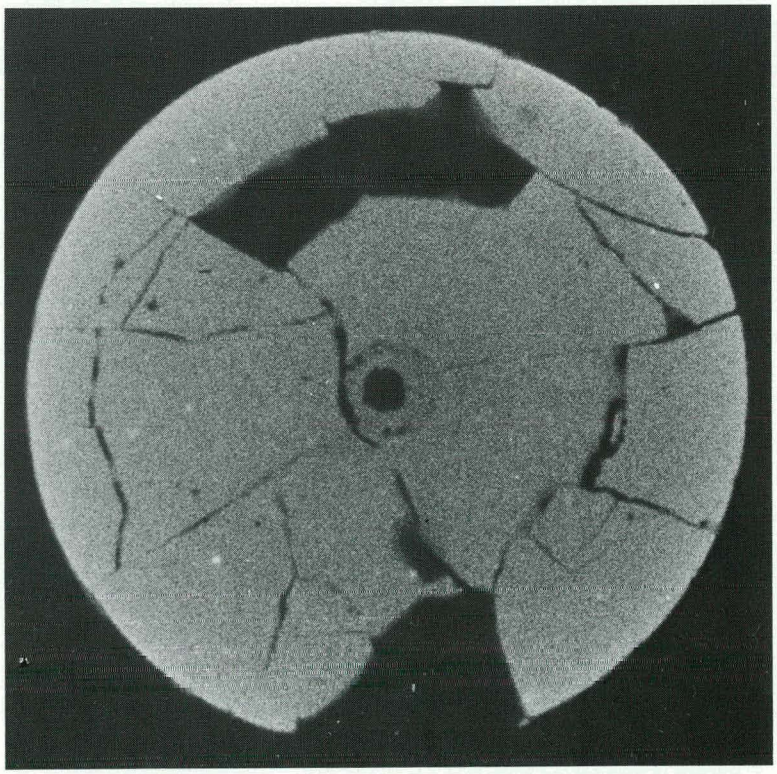

Fig. 80, α-auto., etched X 10

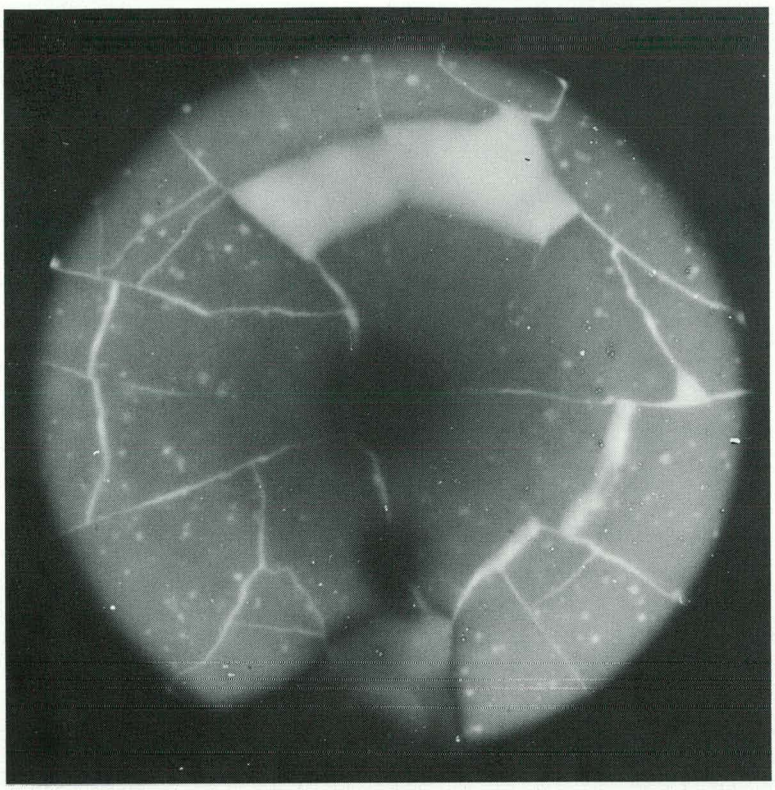

Fig. 81, β/γ-auto., polished X 10

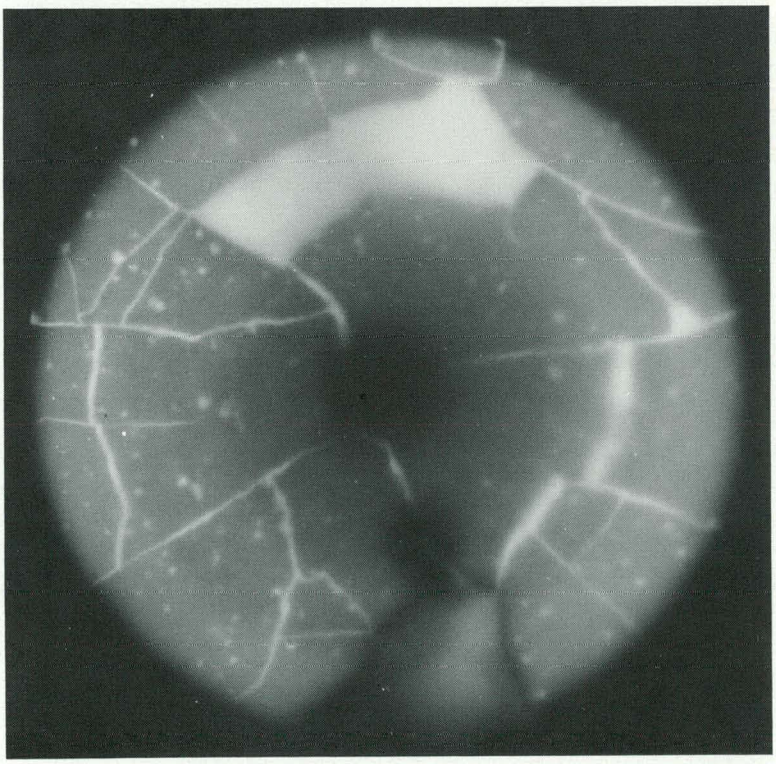

Fig. 82, β/γ-auto., etched X 10

Sample 5-1

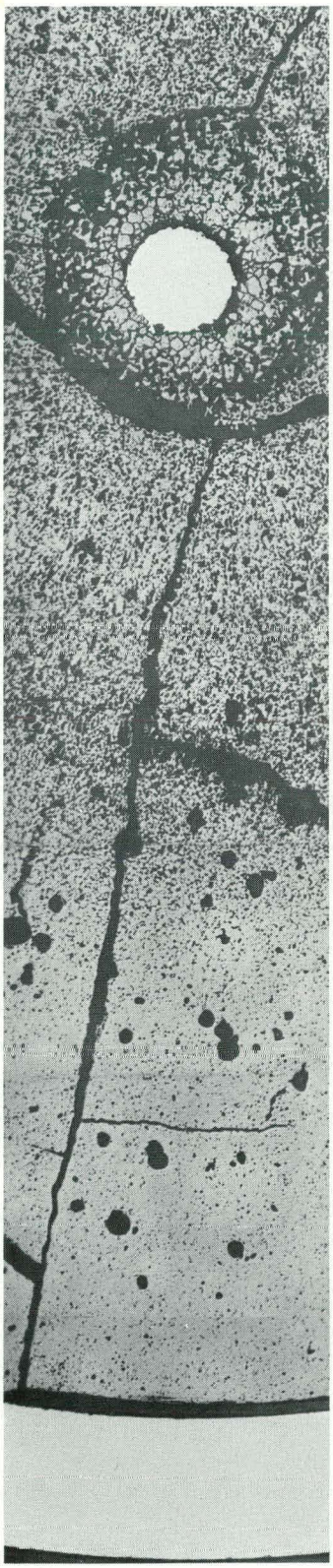

Fig. 83, polished, X 30

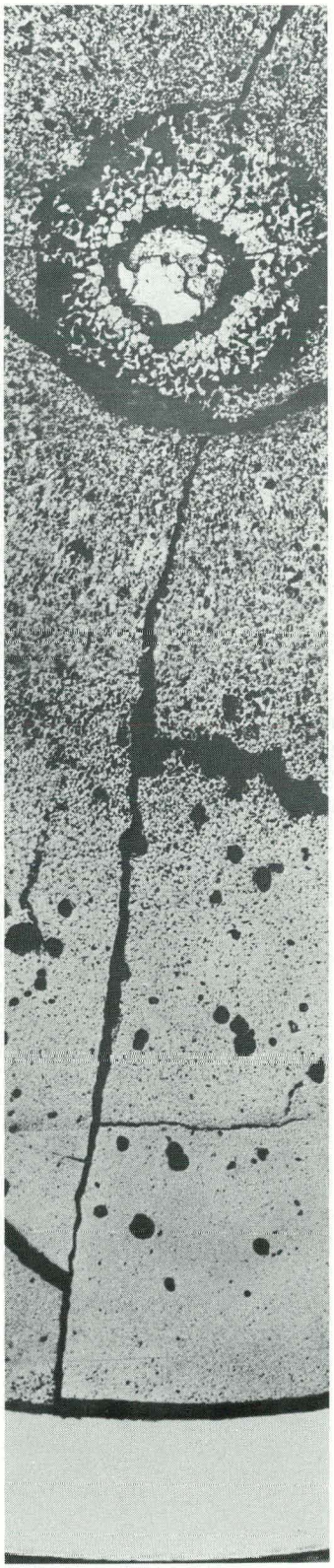

Fig. 84, etched, X 30

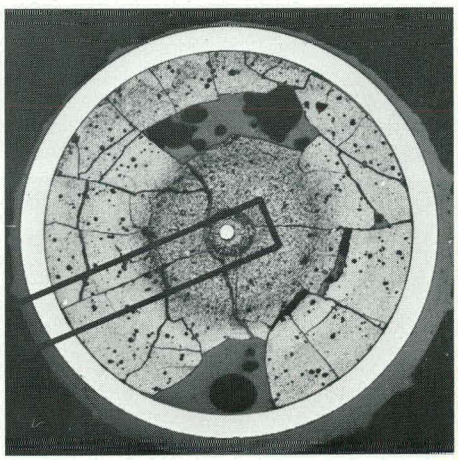

Fig. 83
Fig. 84

Sample 5-1

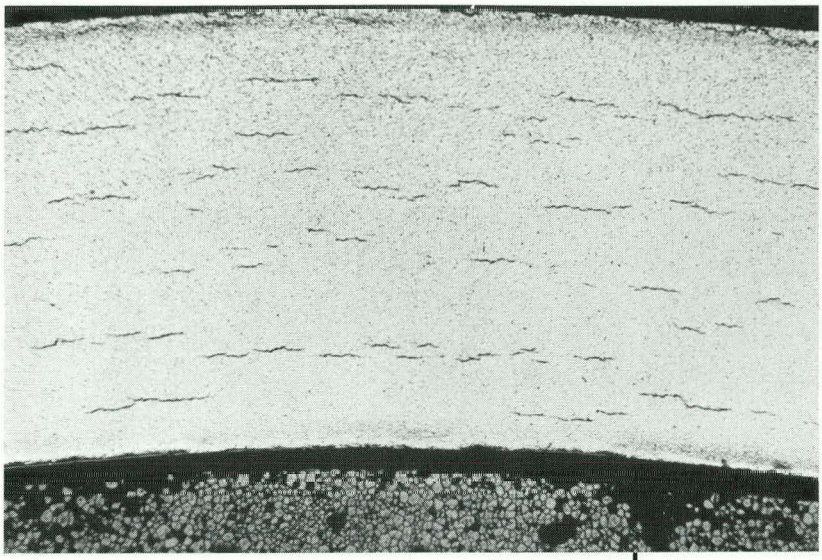

Fig. 85 Etched, X 1oo

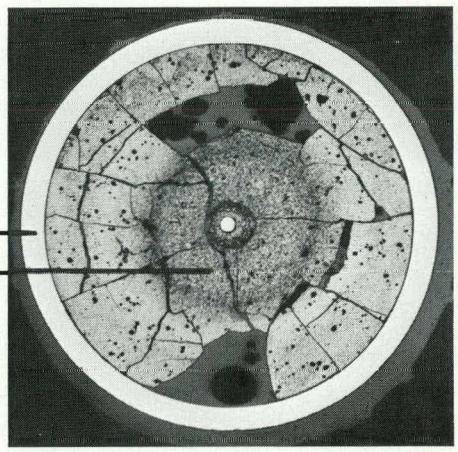

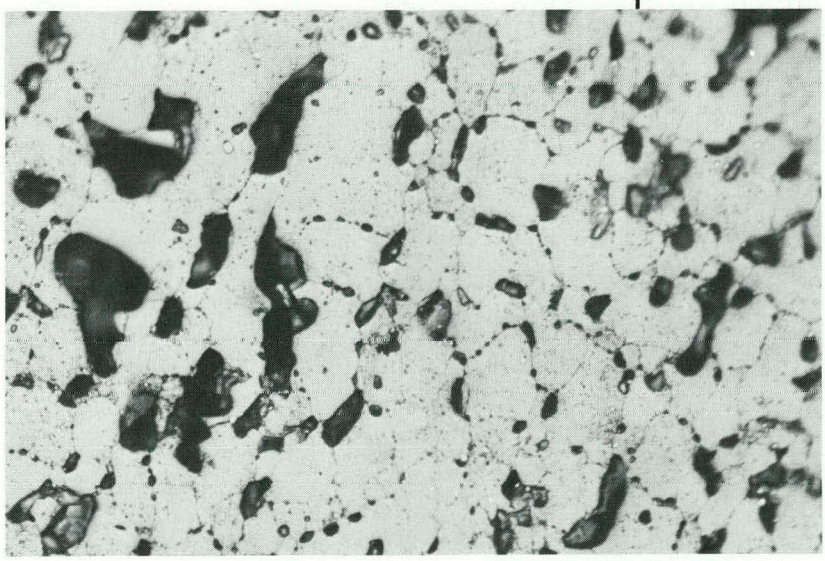

Fig. 86 Etched, X 4oo

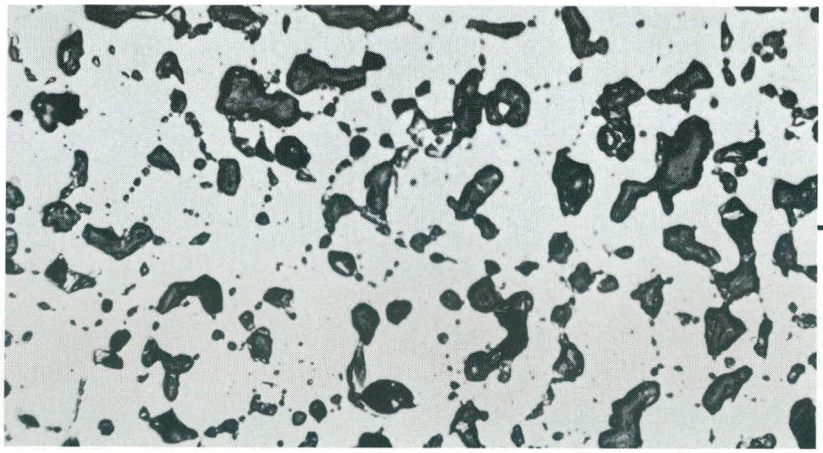

Fig. 87 Polished, X 4oo

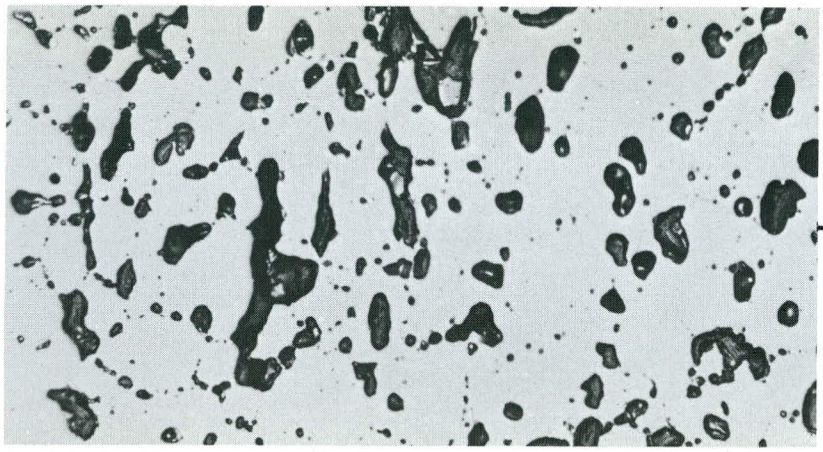

Fig. 88 Polished, X 4oo

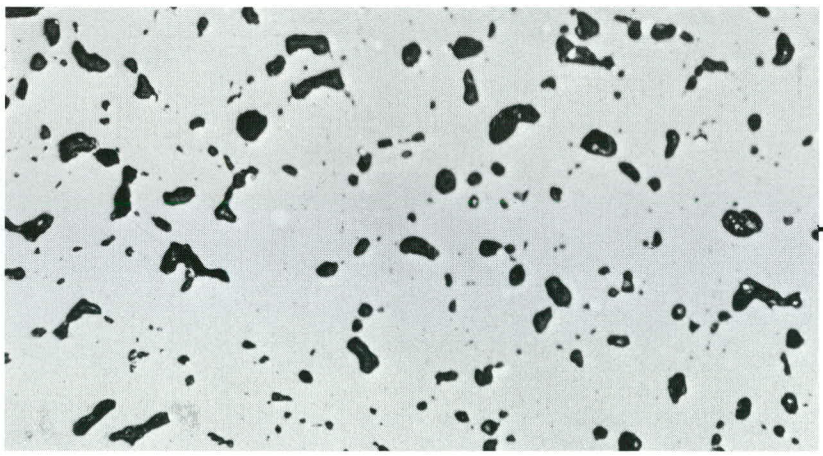

Fig. 89 Polished, X 4oo

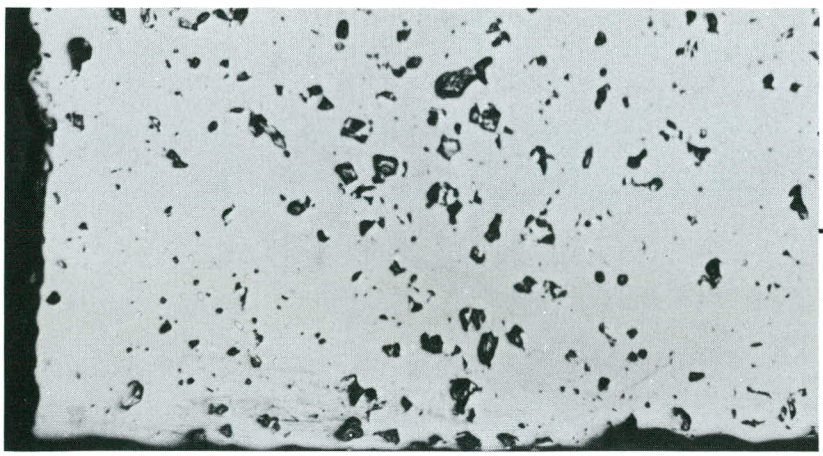

Fig. 9o Polished, X 4oo

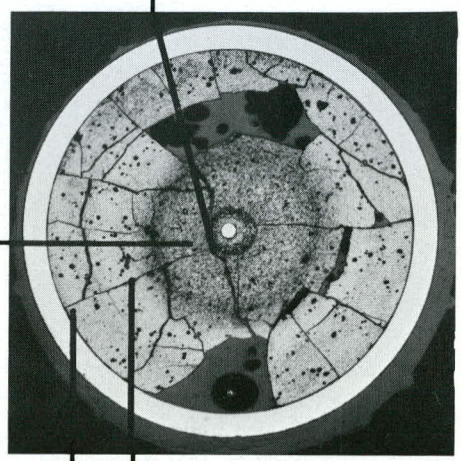

Sample 7-1

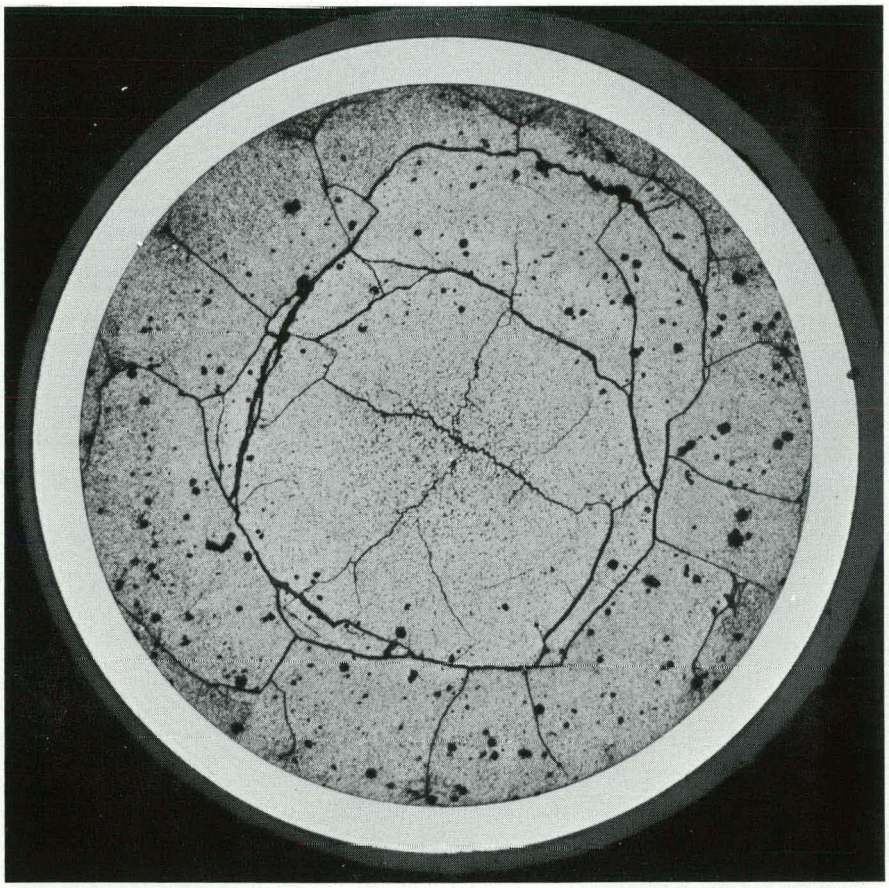

Fig. 91 X 10

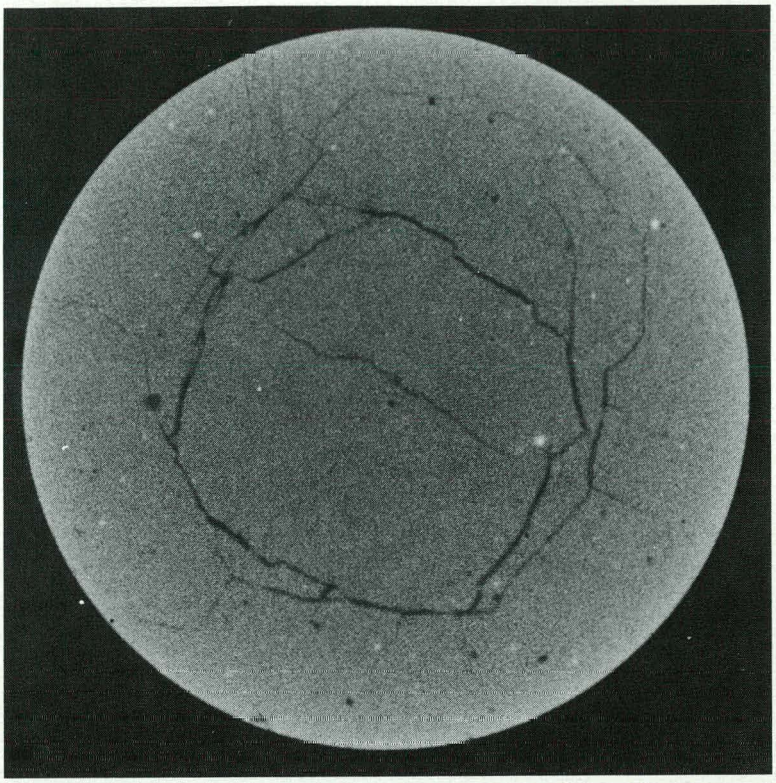

Fig. 92, α-auto., polished X 10

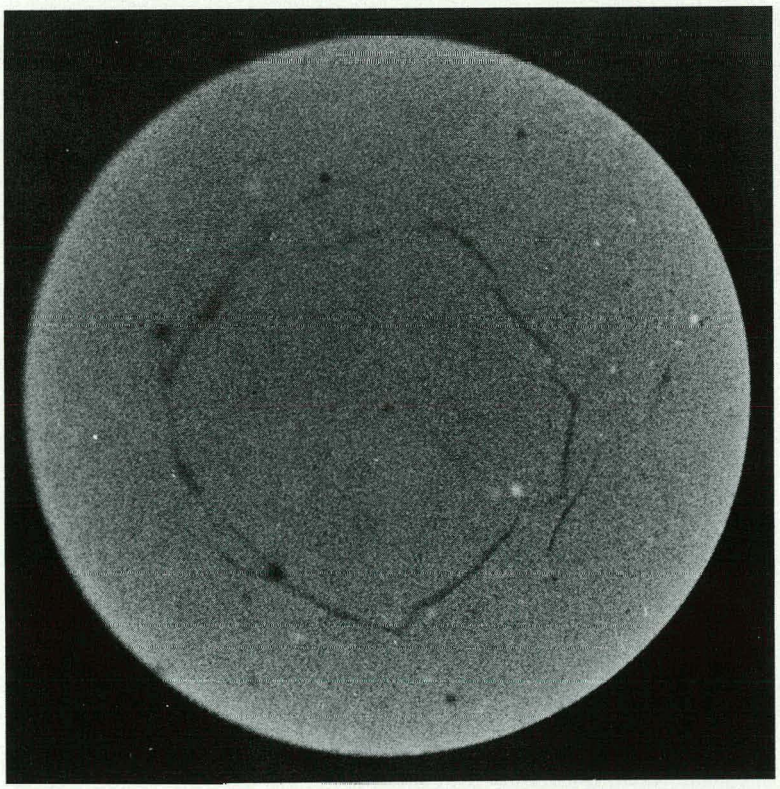

Fig. 93, α-auto., etched X 10

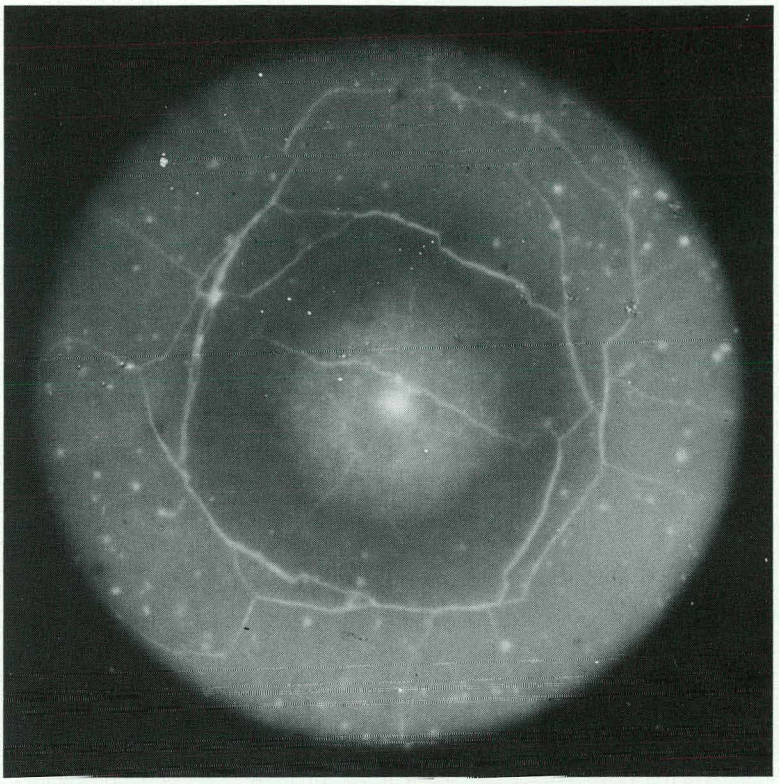

Fig. 94, β/γ-auto., polished X 10

Fig. 95, β/γ-auto., etched X 10

Sample 7-1

Fig. 96, polished, X 30

Fig. 97, etched, X 30

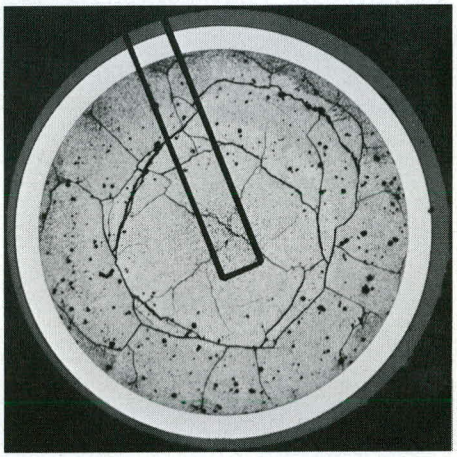

Fig. 96
Fig. 97

Sample 7-1

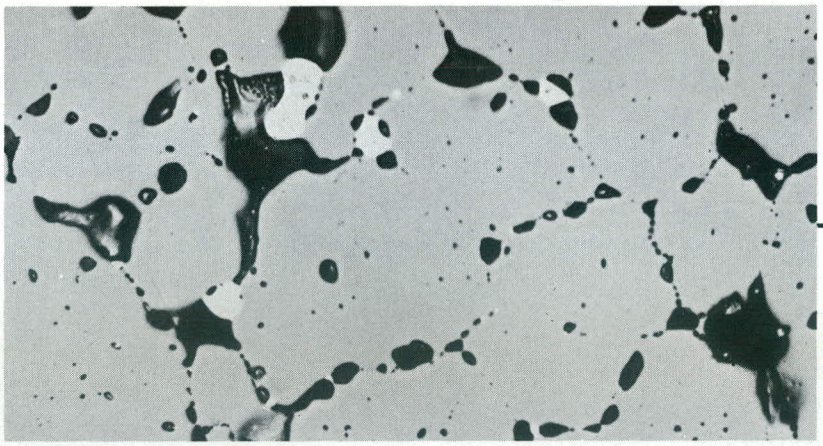

Fig. 98 Polished, X 4oo

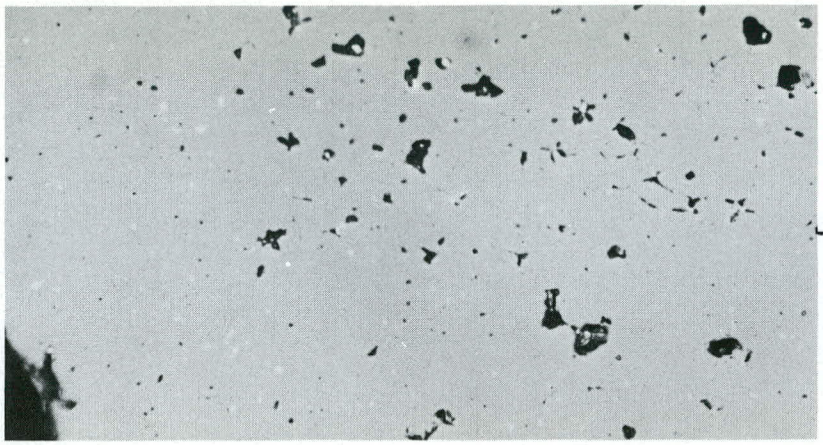

Fig. 99 Polished, X 4oo

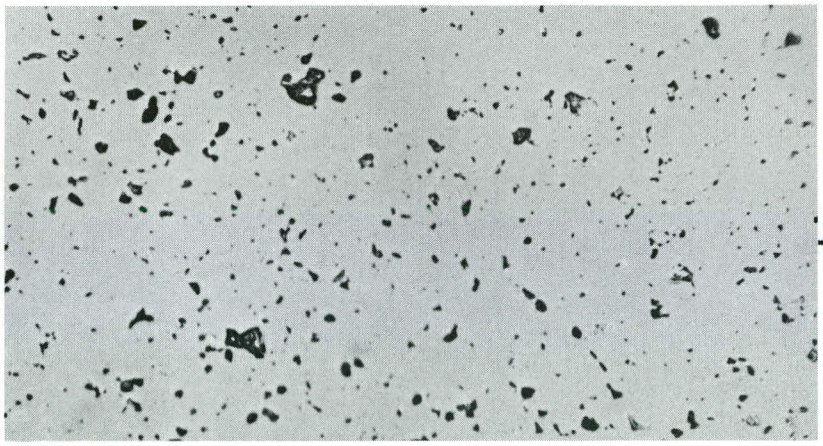

Fig. 1oo Polished, X 4oo

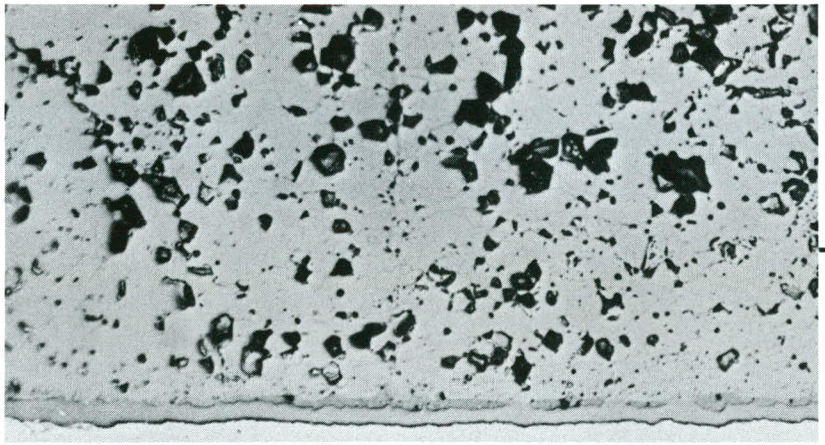

Fig. 1o1 Polished, X 4oo

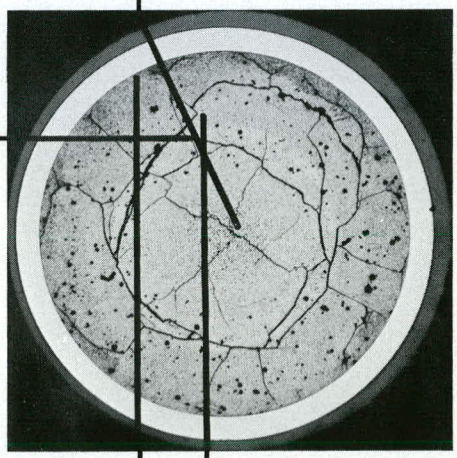

Sample 7-1

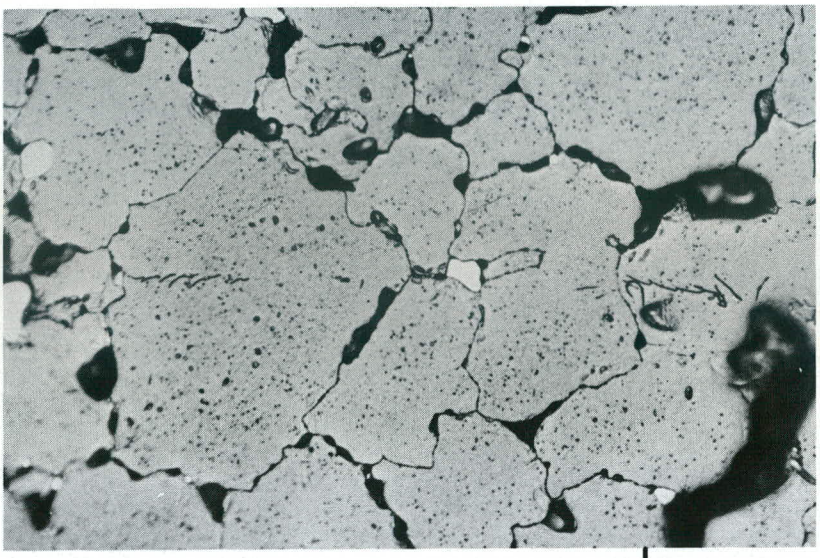

Fig. 102 Etched, X 400

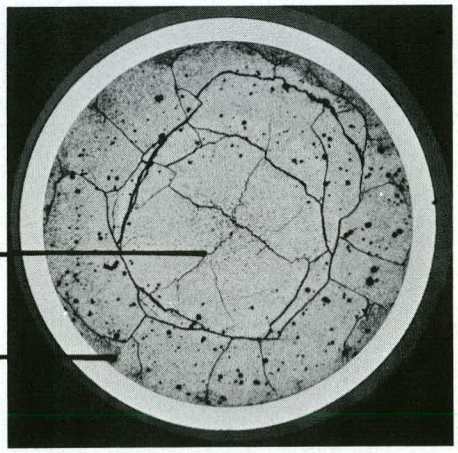

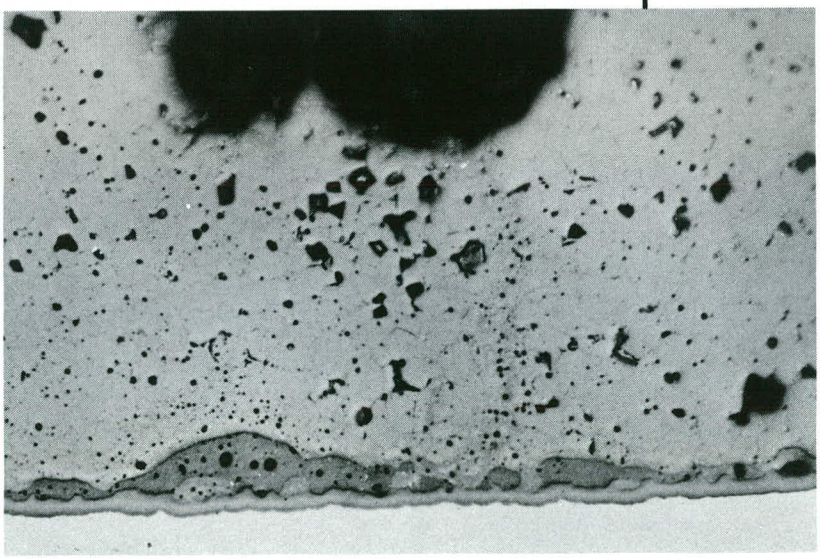

Fig. 103 Polished, X 400

Sample 9-1

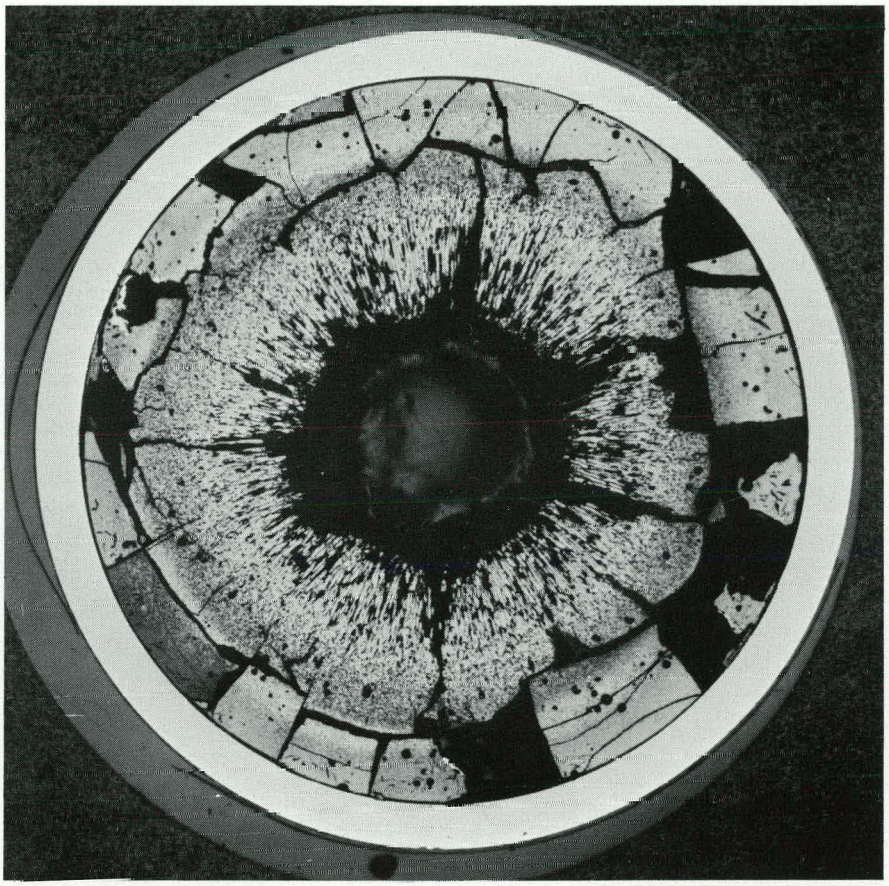

Fig. 104 X 10

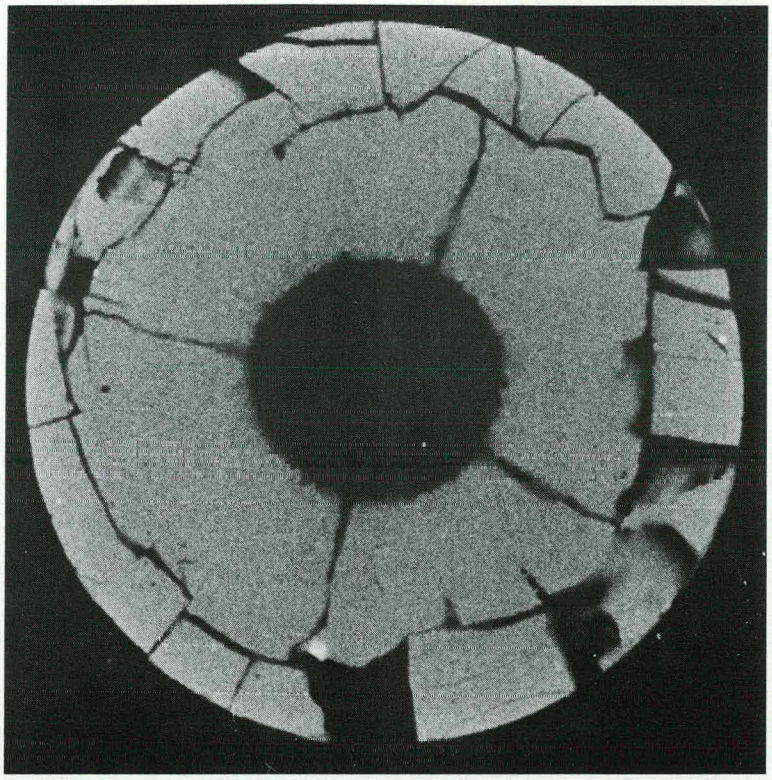

Fig. 105, α-auto., polished X 10

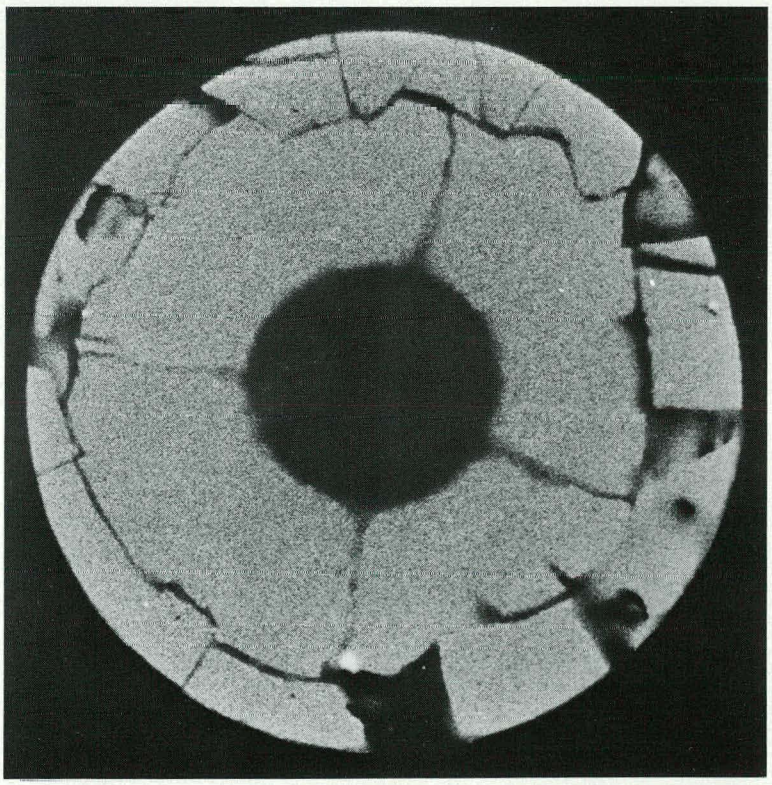

Fig. 106, α-auto., etched X 10

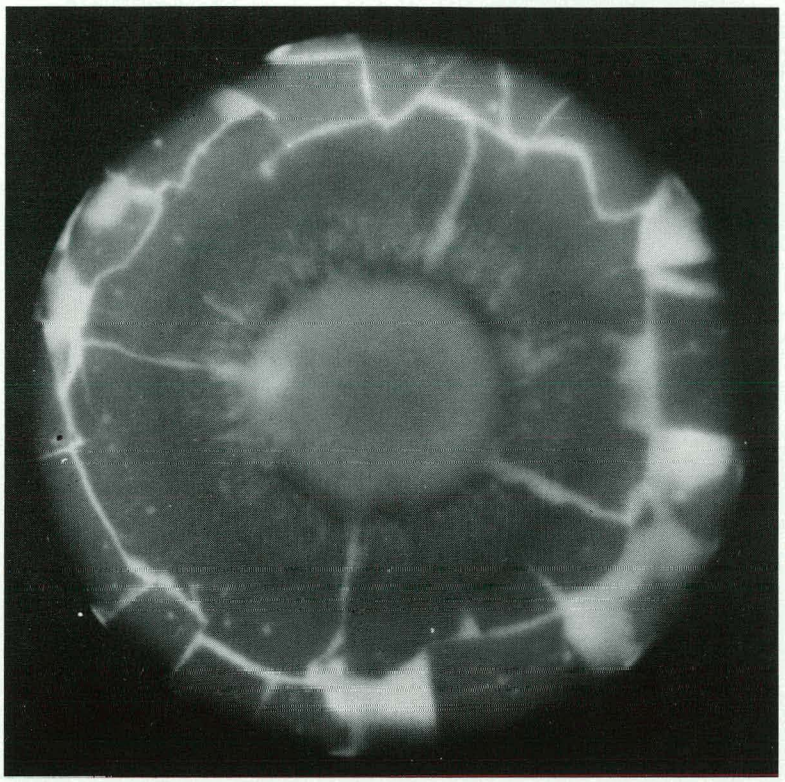

Fig. 107, β/γ-auto., polished X 10

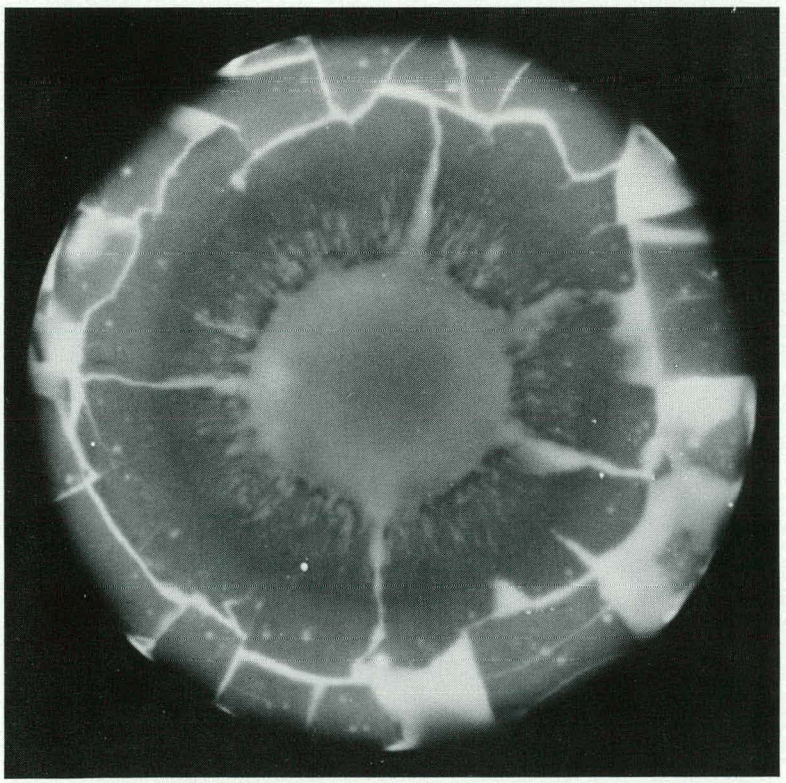

Fig. 108, β/γ-auto., etched X 10

Sample 9-1

Fig. 109, polished, X 30

Fig. 110, etched, X 30

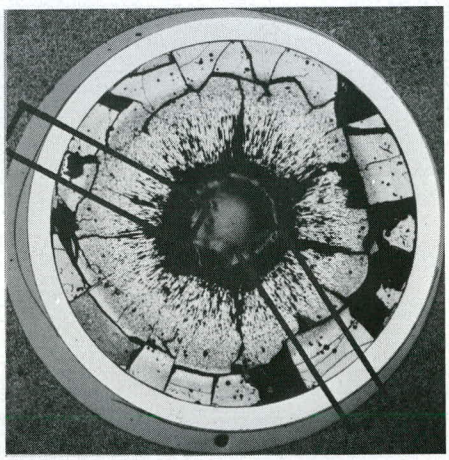

Fig. 109 Fig. 110

Sample 9-1

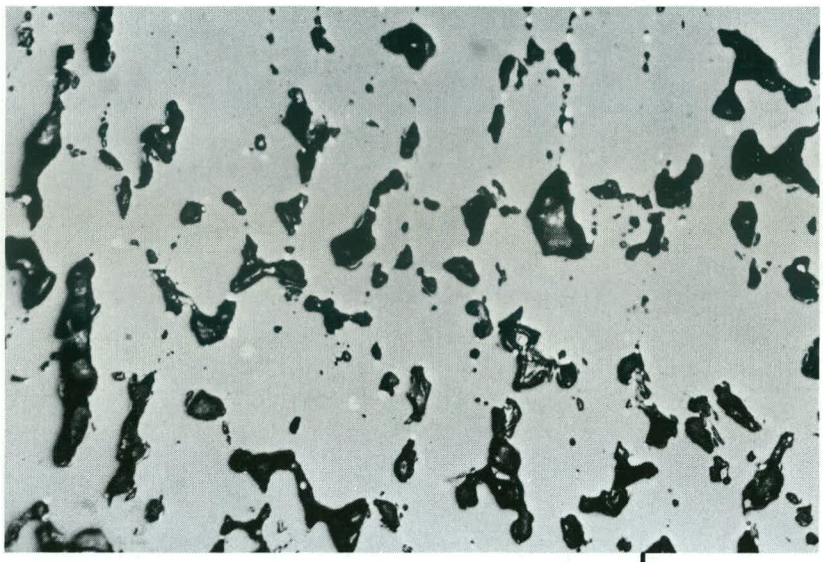

Fig. 111 Polished, X 4oo

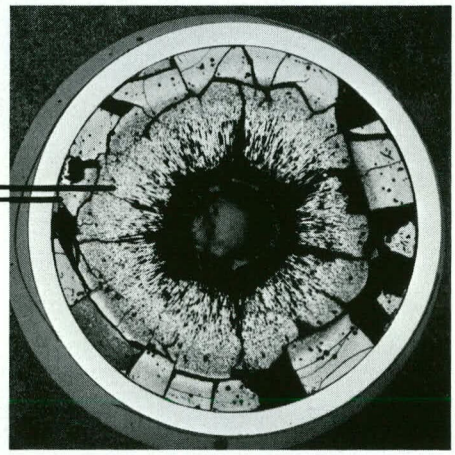

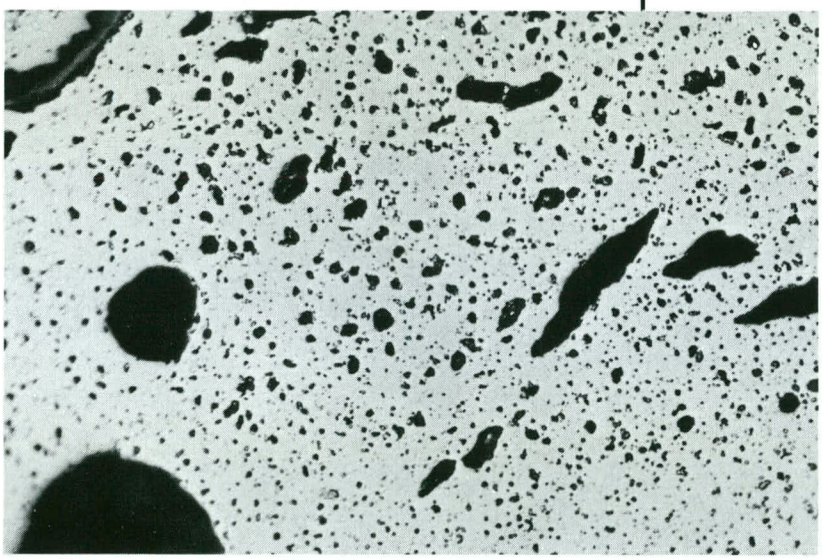

Fig. 112 Polished, X 4oo

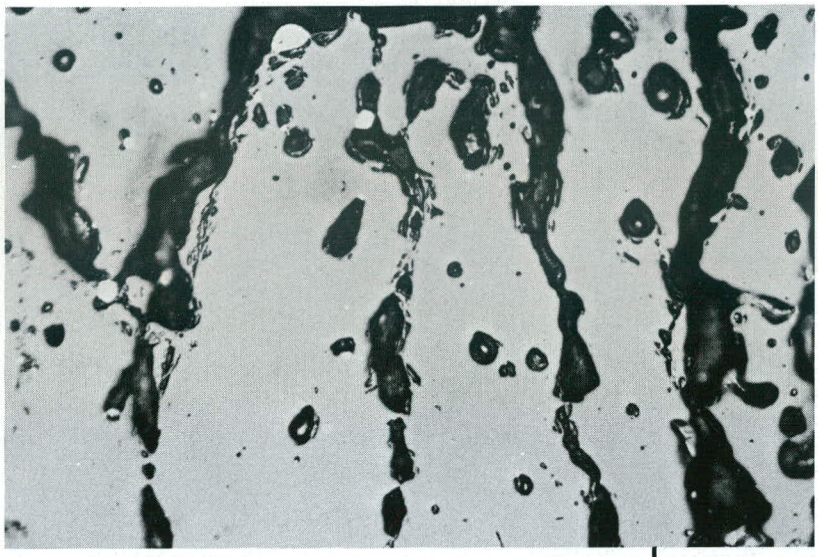

Fig. 113 Polished, X 4oo

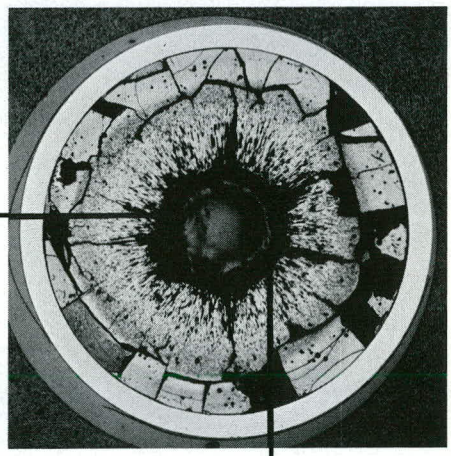

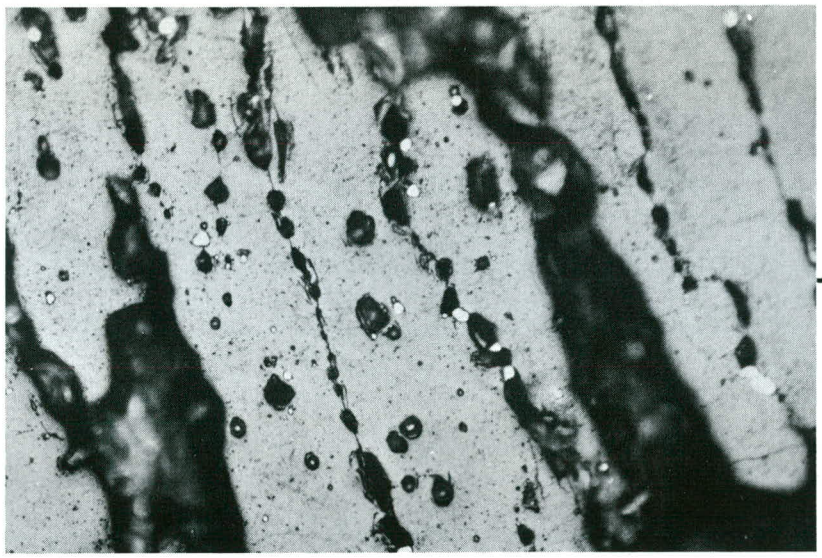

Fig 114 Etched, X 4oo

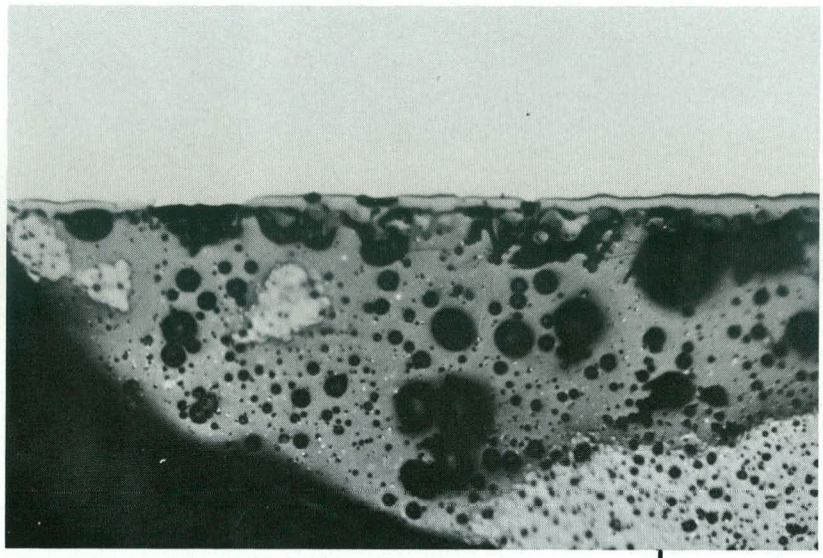

Fig. 115 Polished, X 4oo

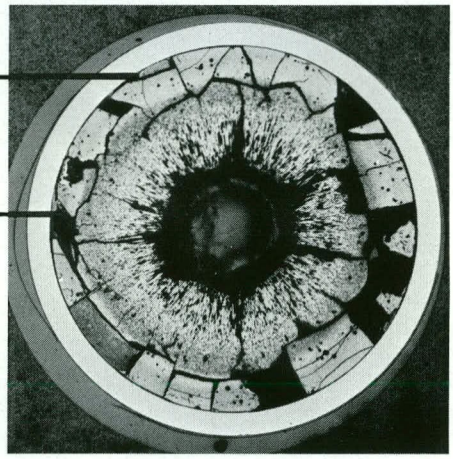

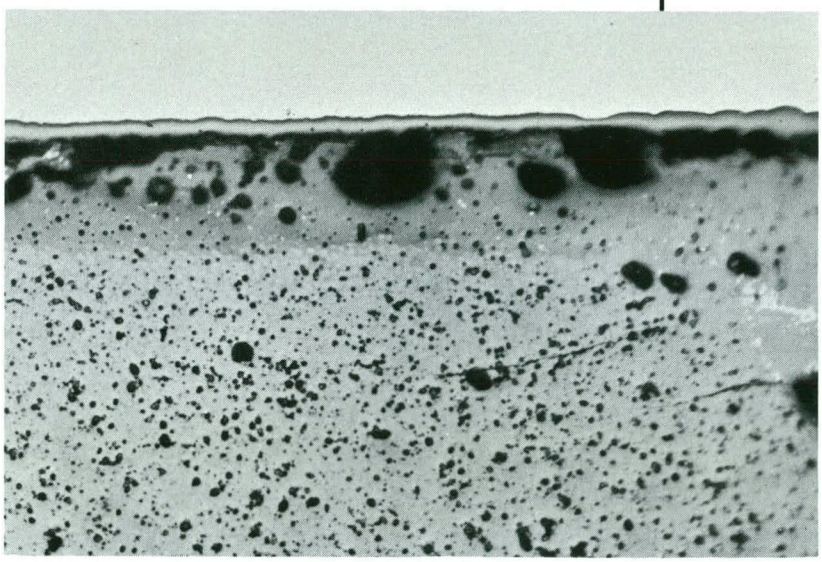

Fig. 116 Polished, X 4oo

Sample 9-2A

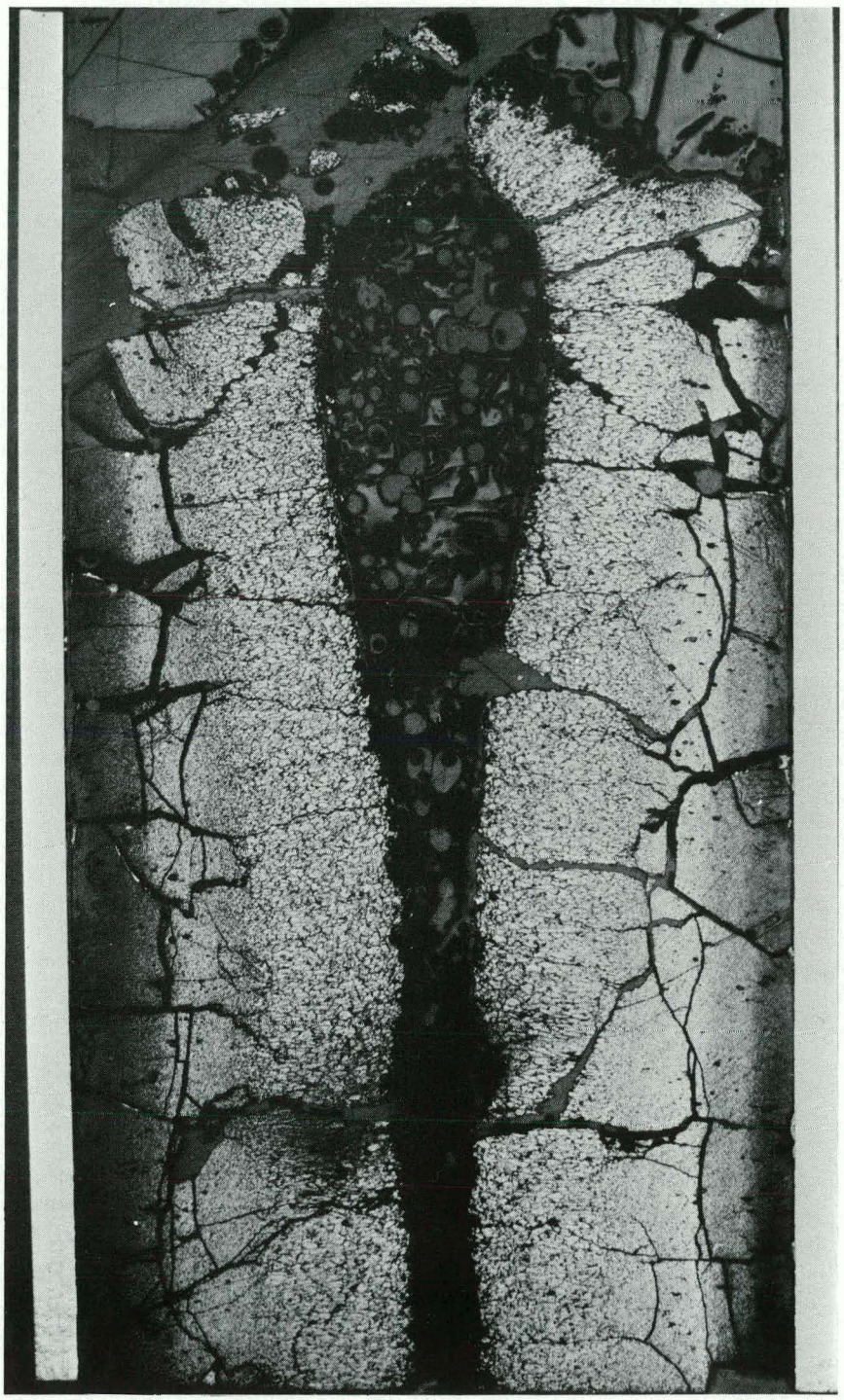

Fig. 117 X 10

Sample 9-2A

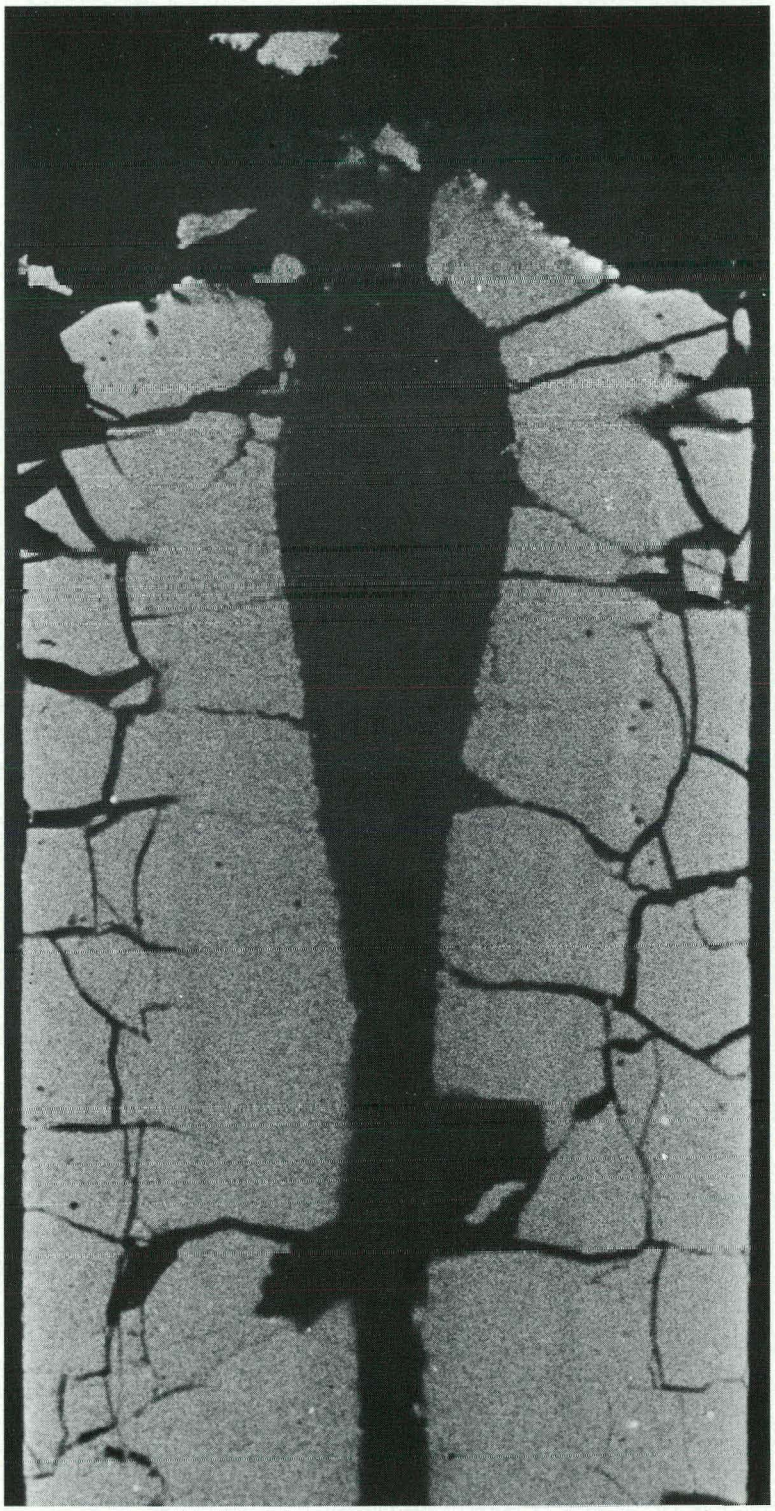

Fig. 118, α-auto., polished X 10

Sample 9-2A

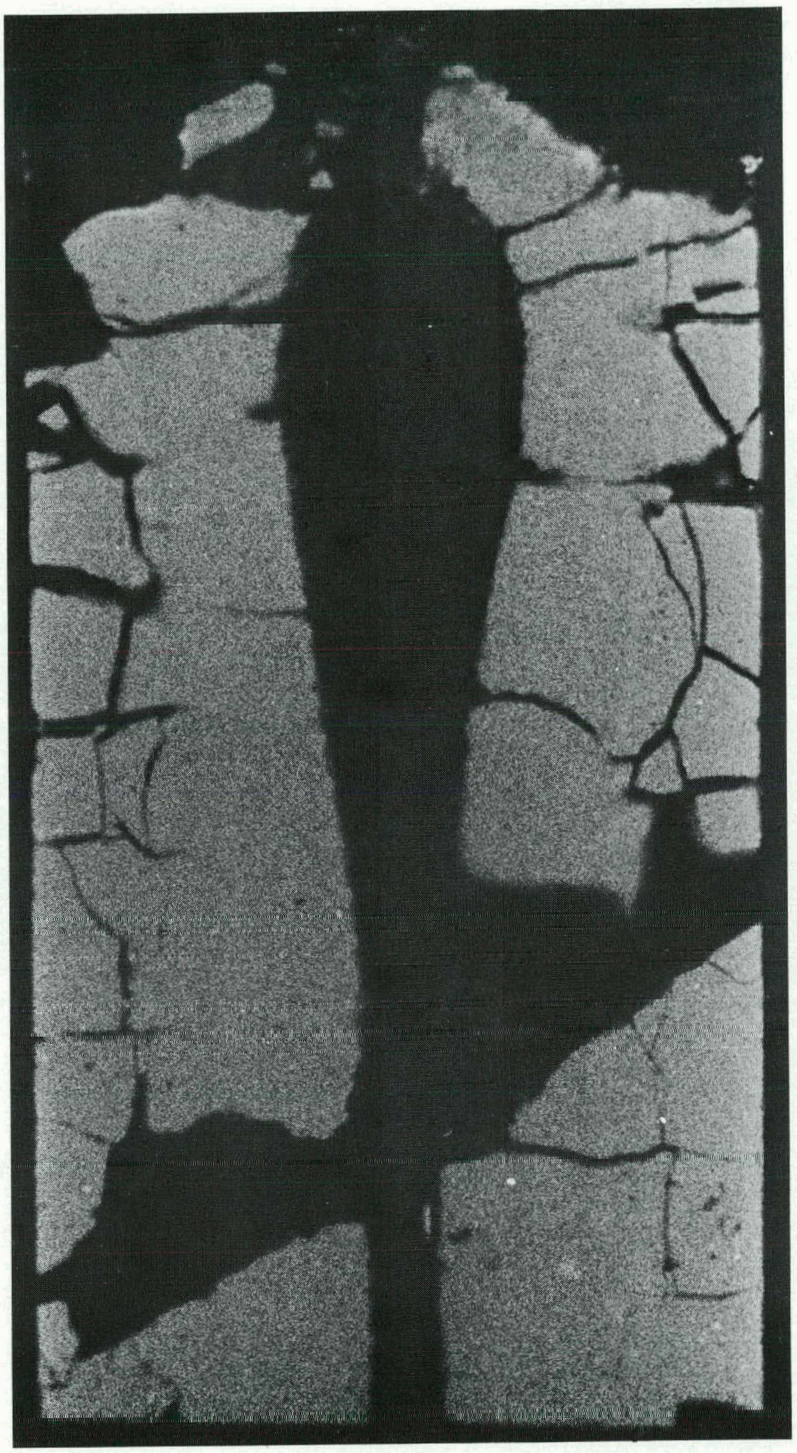

Fig. 119, α-auto., etched X 10

Sample 9-2A

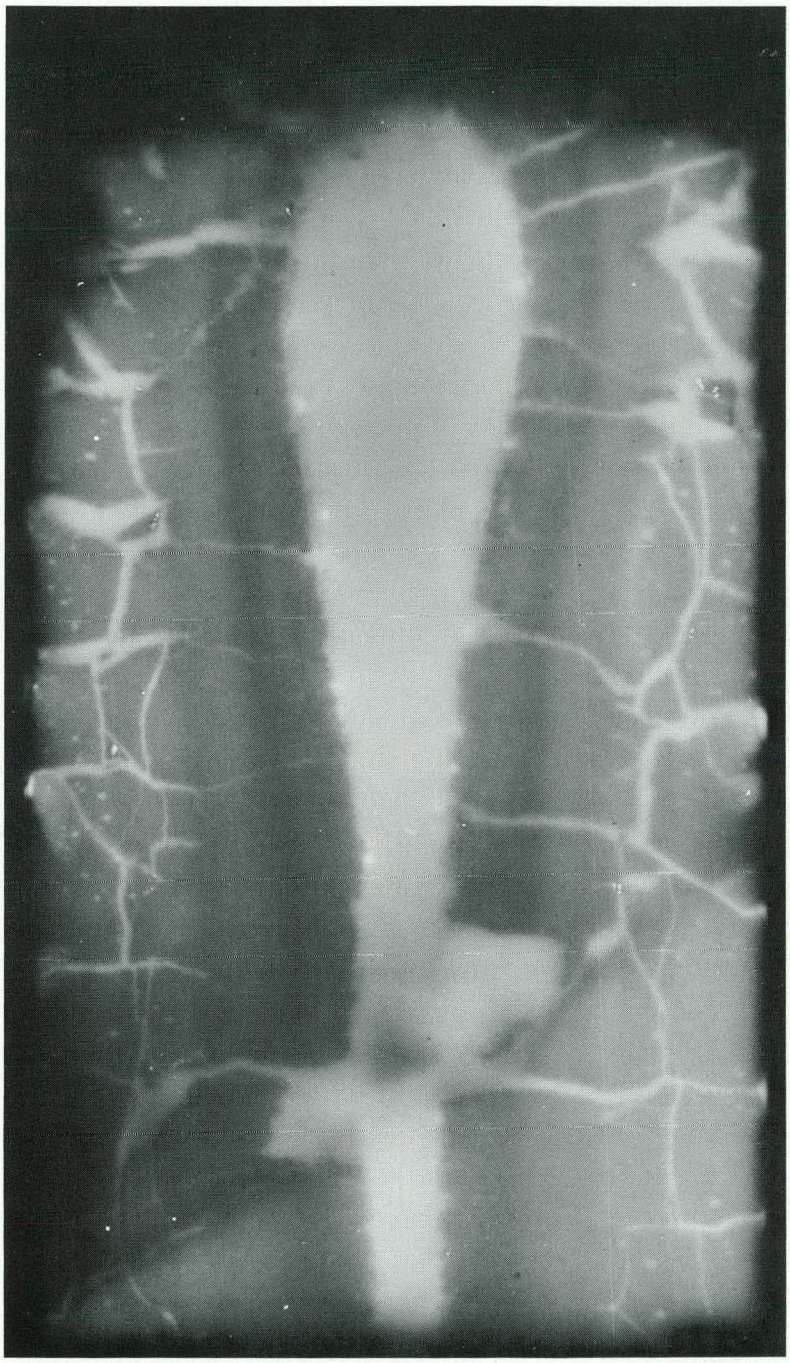

Fig. 120, β/γ-auto., polished X 10

Sample 9-2A

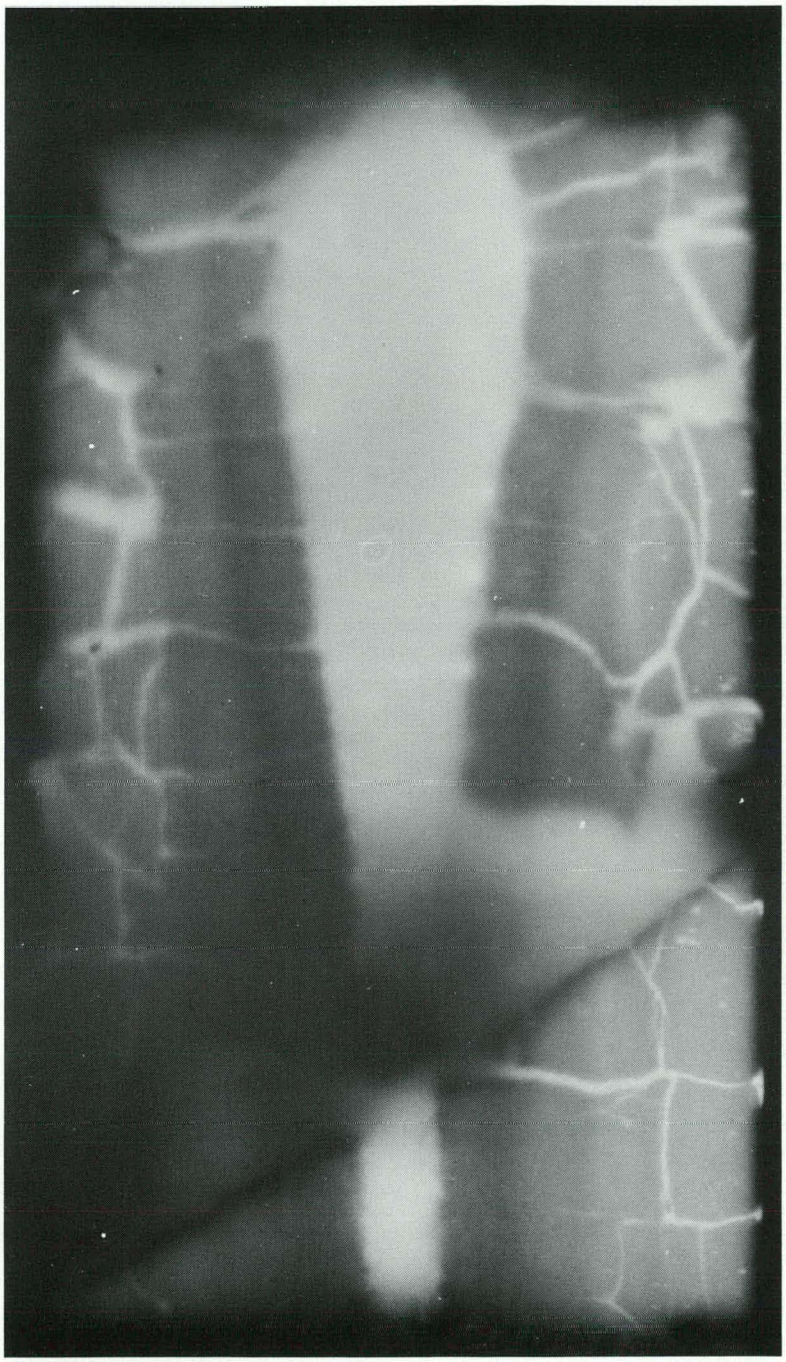

Fig. 121, β/γ-auto., etched X 10

Sample 9-2A

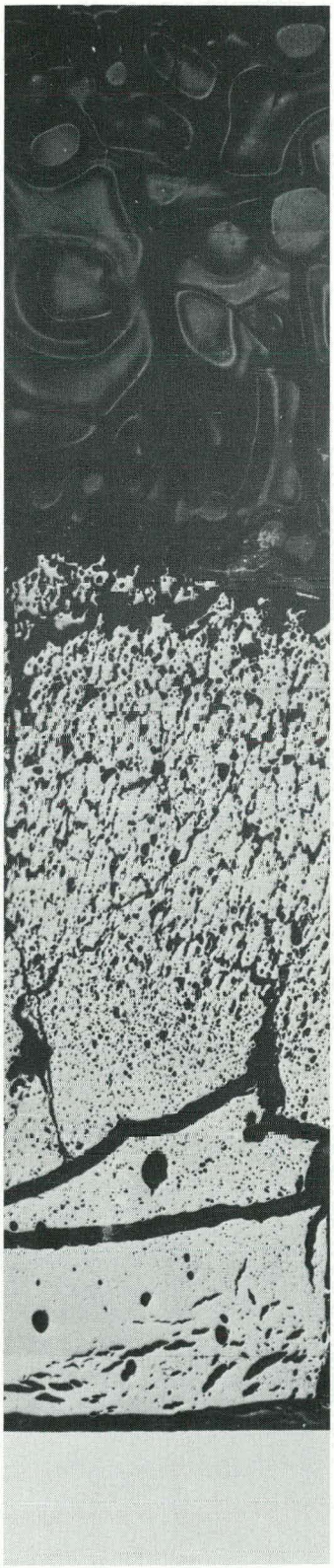

Fig. 122, polished, X 30

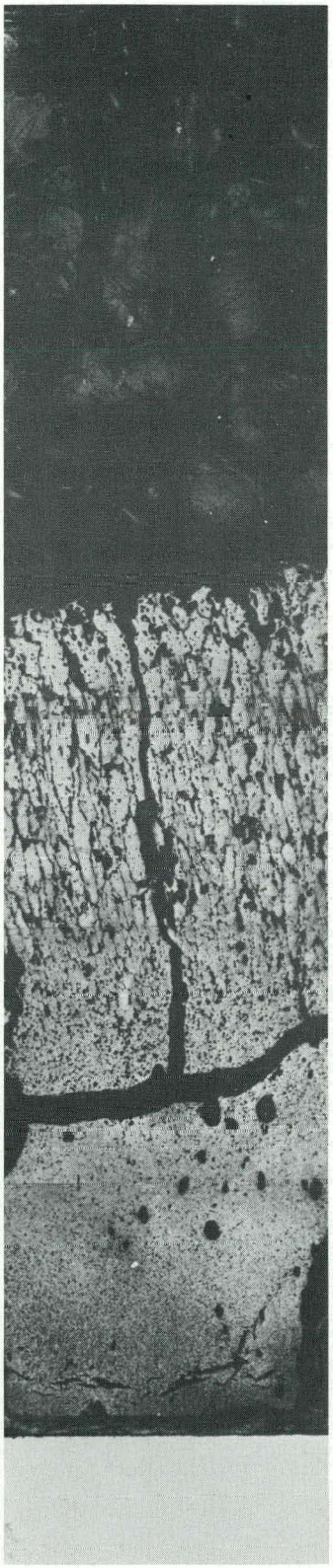

Fig. 123, etched, X 30

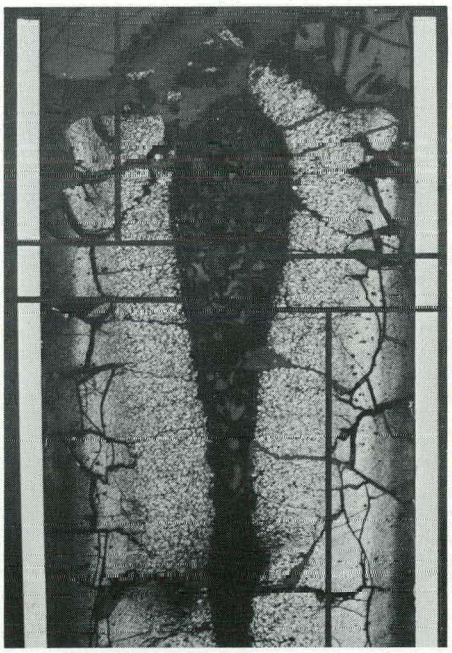

Fig. 123 Fig. 122

Sample 9-2A

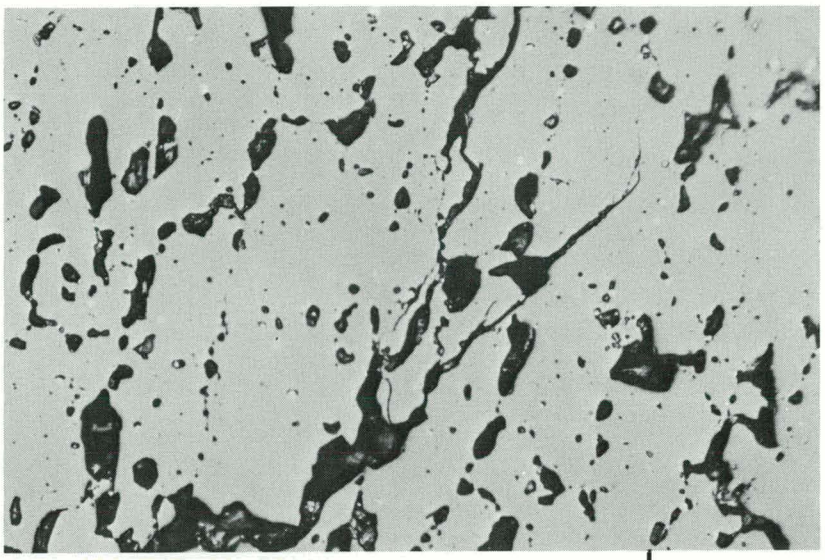

Fig. 124 Polished, X 400

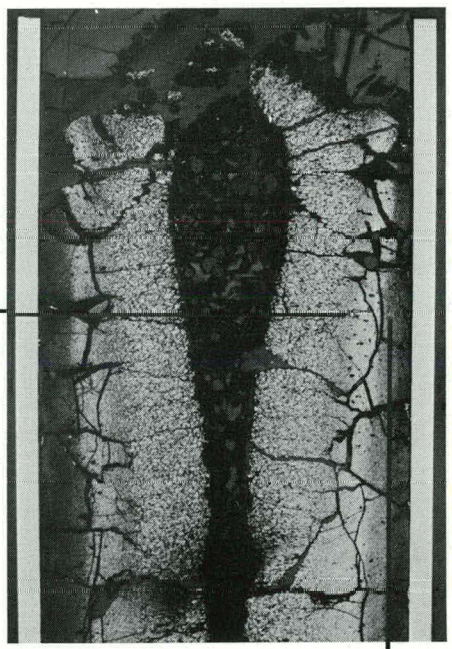

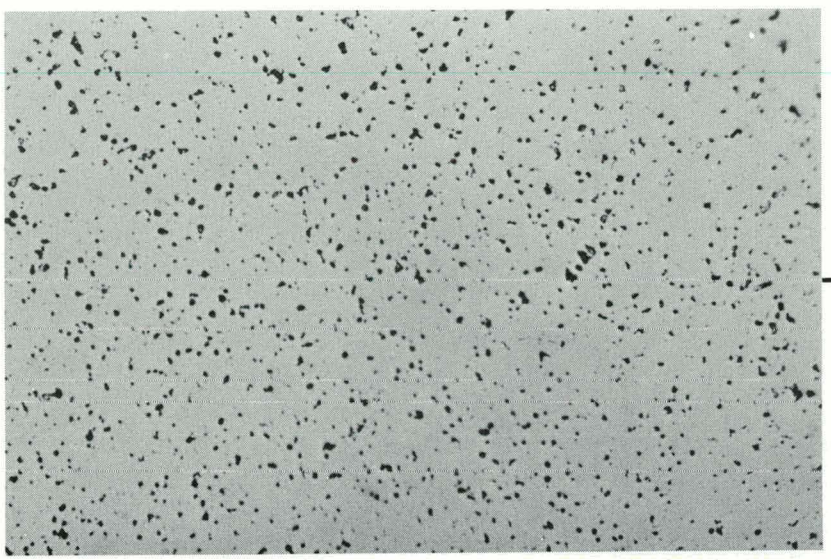

Fig. 125 Polished, X 400

Sample 9-2A

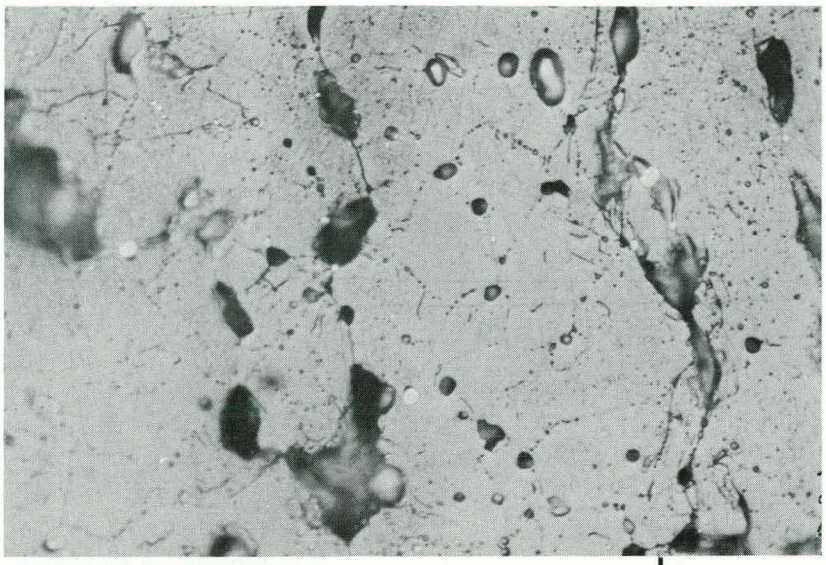

Fig. 126 Etched, X 800

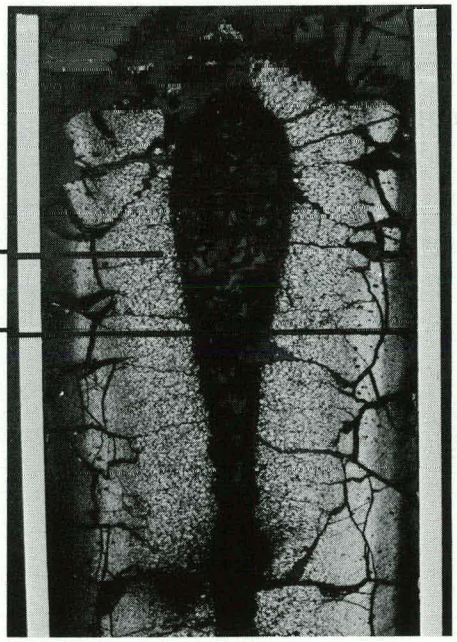

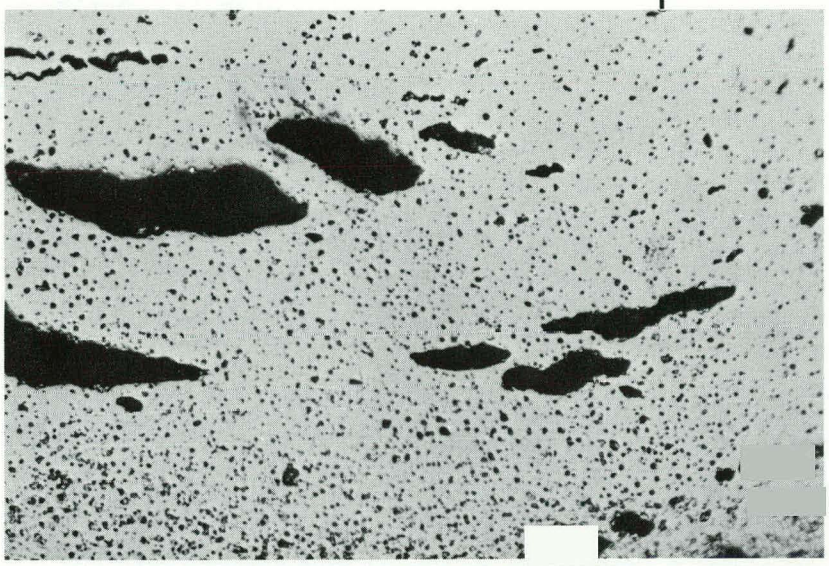

Fig. 127 Polished, X 400

Sample 9-5A

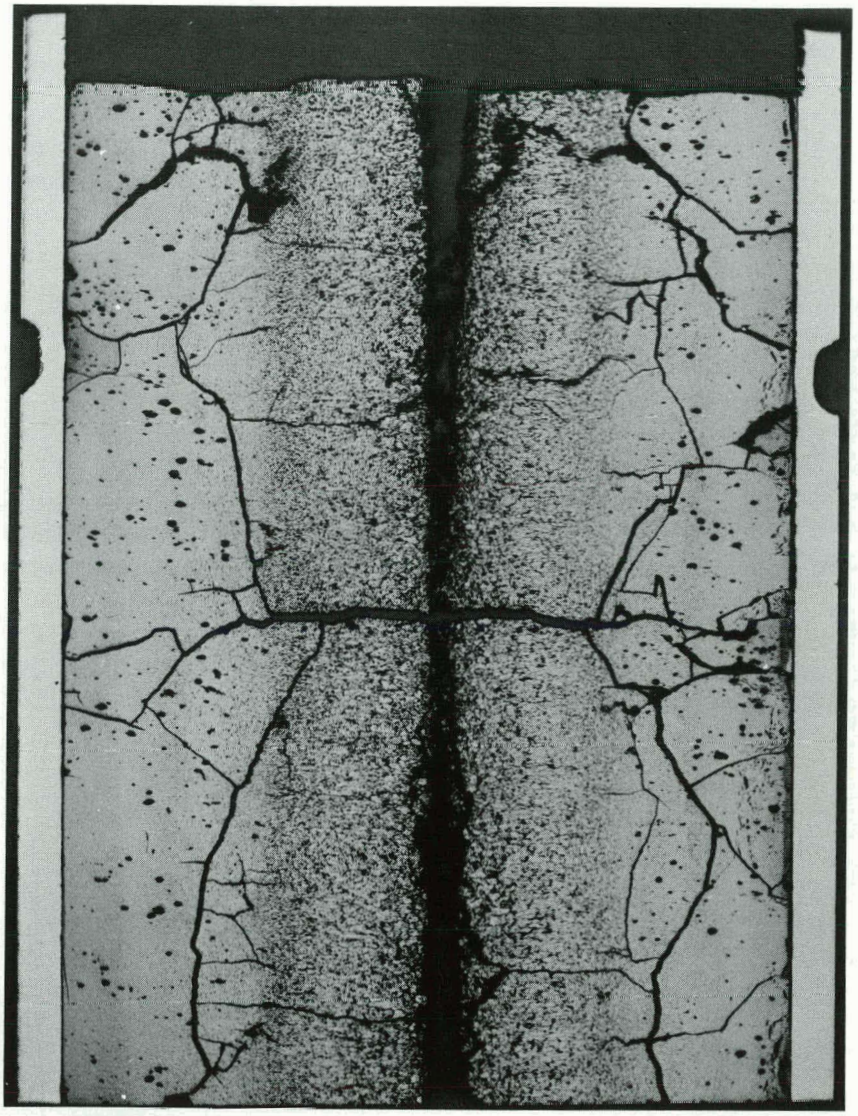

Fig. 128 X 10

Sample 9-5A

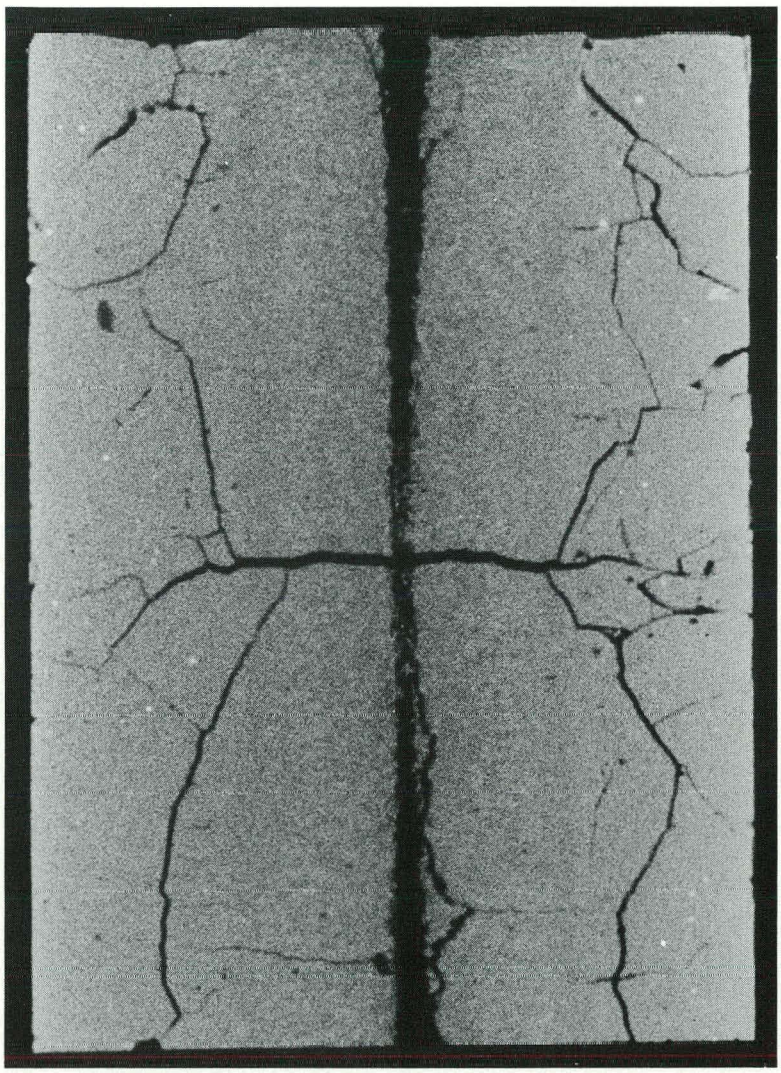

Fig. 129, α-auto., polished X 10

Sample 9-5A

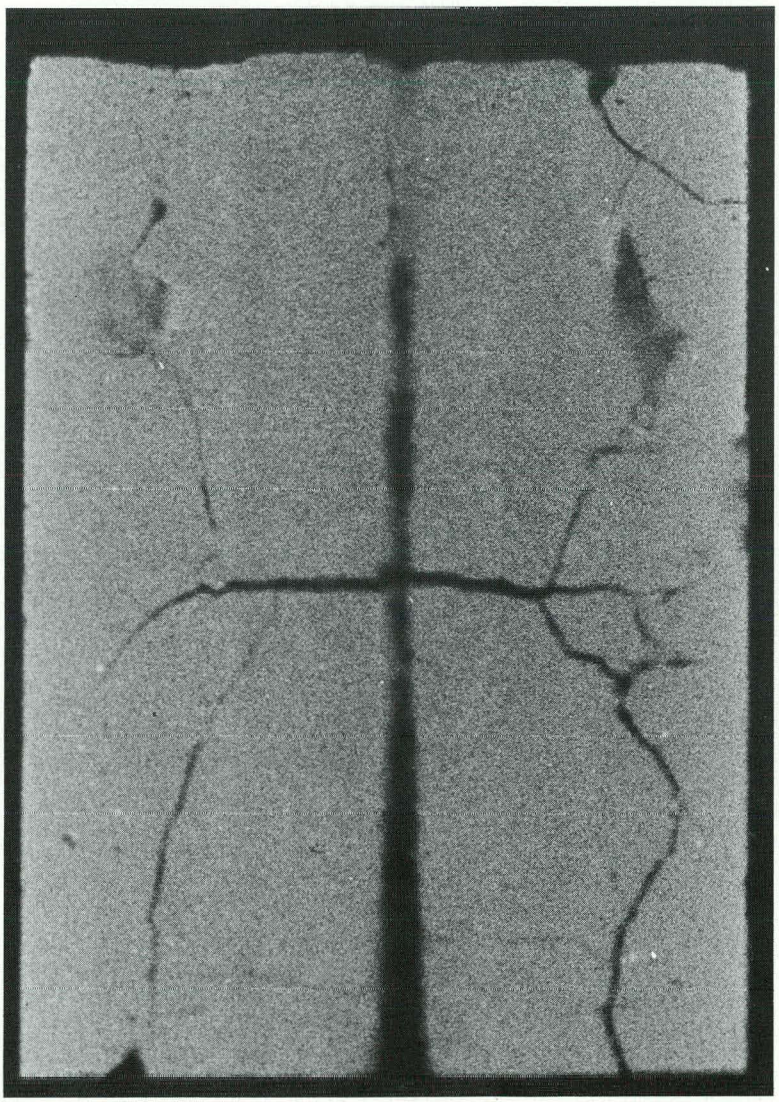

Fig. 130, α-auto., etched X 10

Sample 9-5A

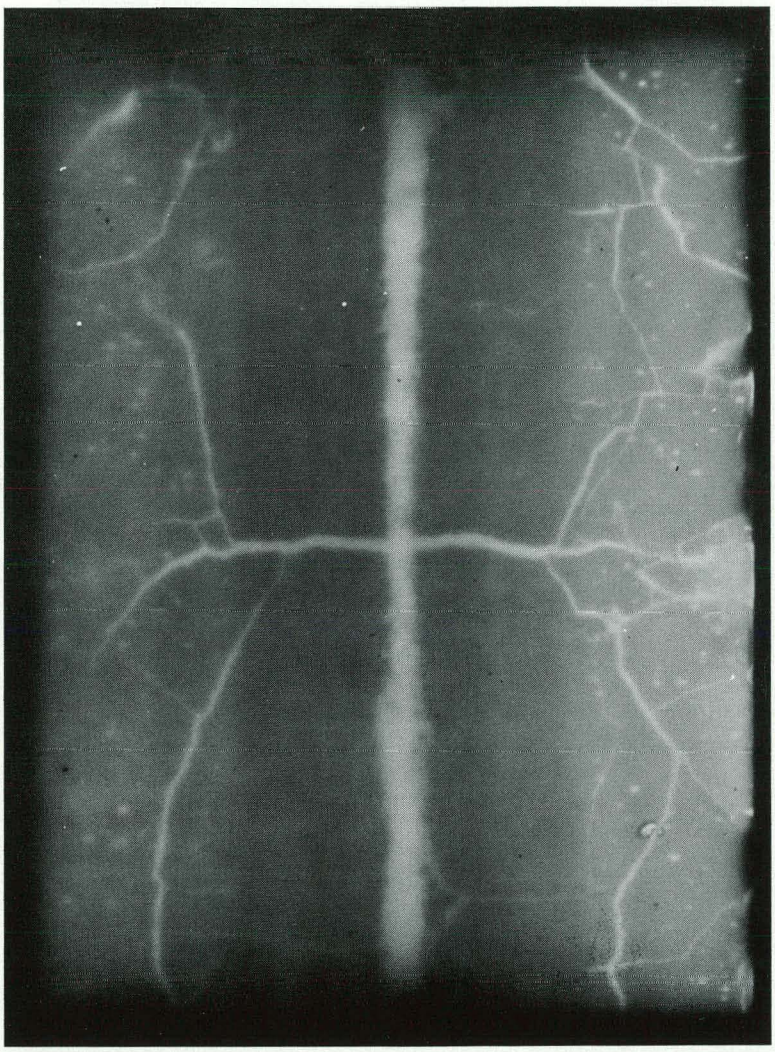

Fig. 131, β/γ-auto., polished X 10

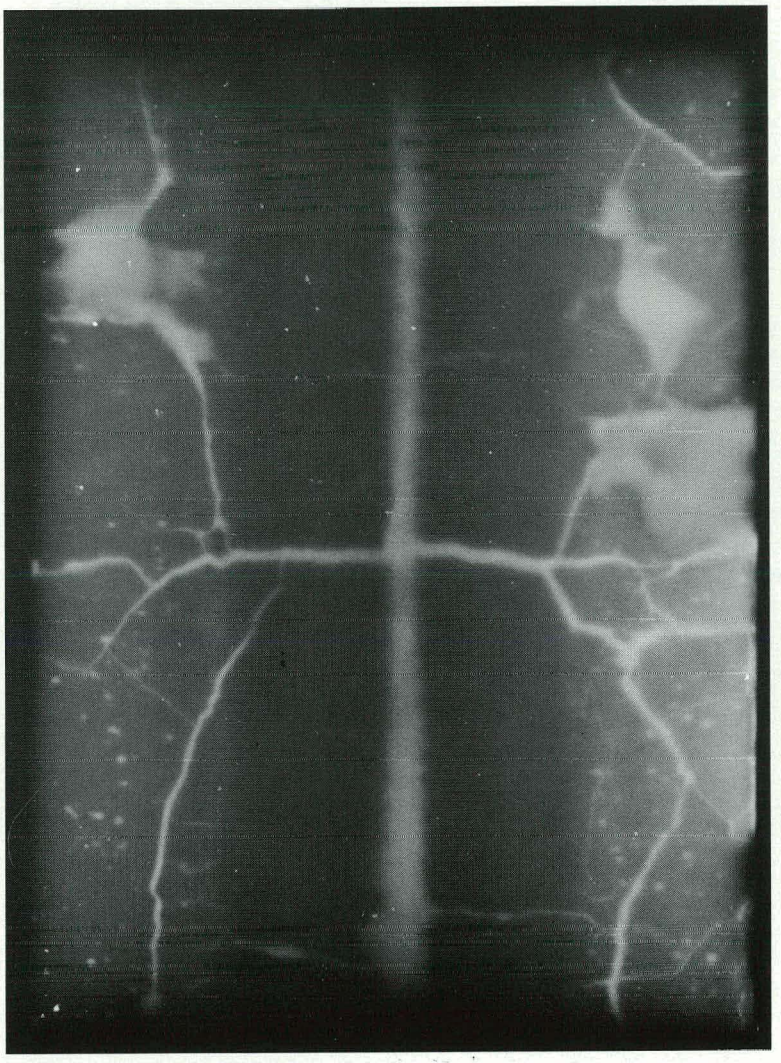

Fig. 132, β/γ-auto, etched X 10

Sample 9-5A

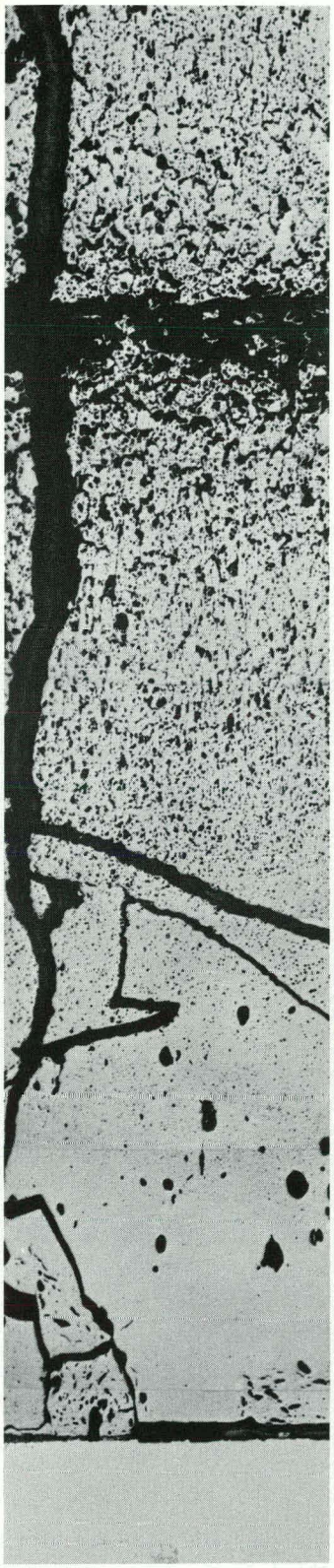

Fig. 133, polished, X 30

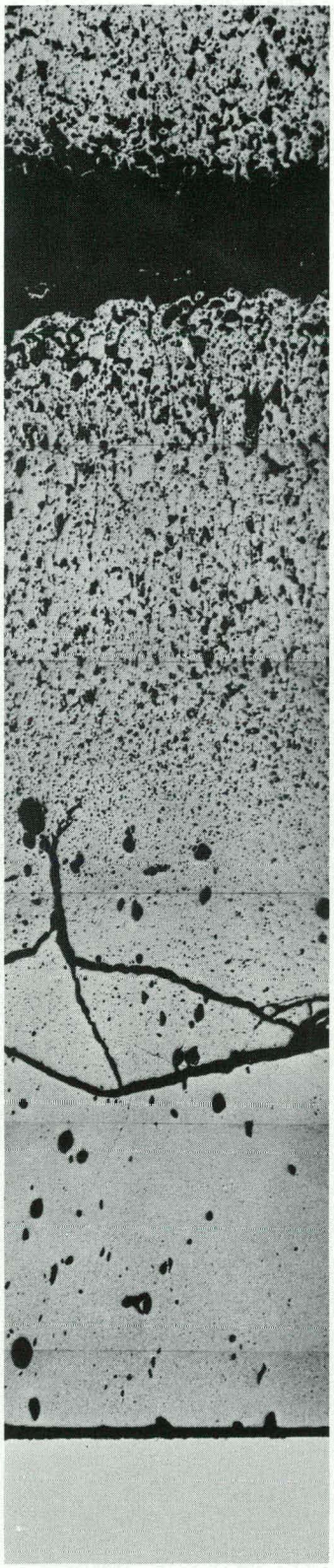

Fig. 134, etched, X 30

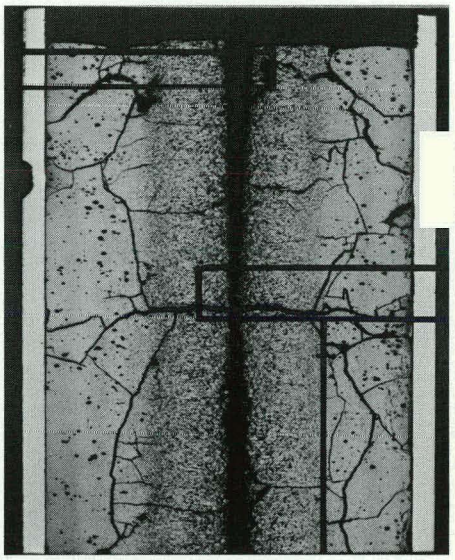

Fig. 133
Fig. 134

Sample 9-5A

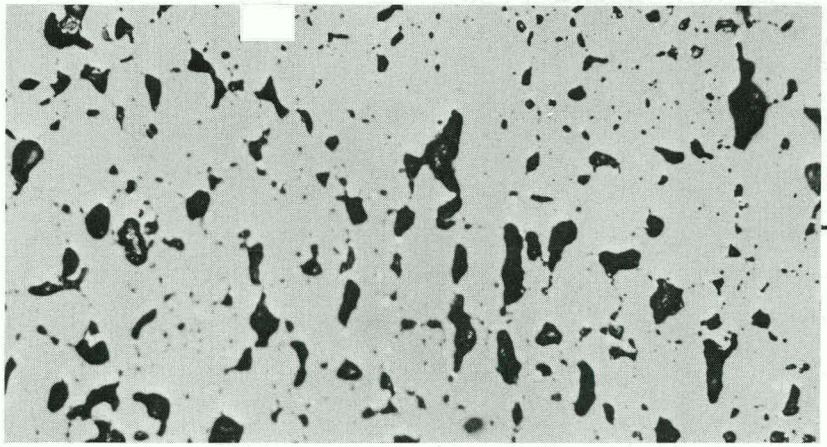

Fig. 135 Polished, X 4oo

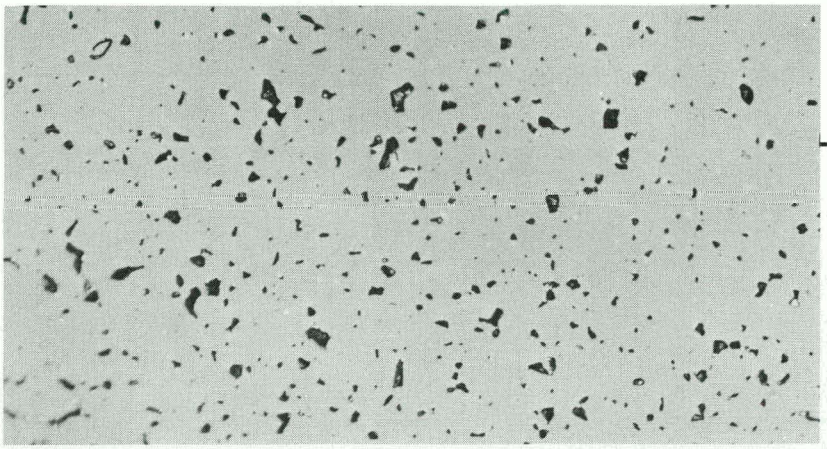

Fig. 136 Polished, X 4oo

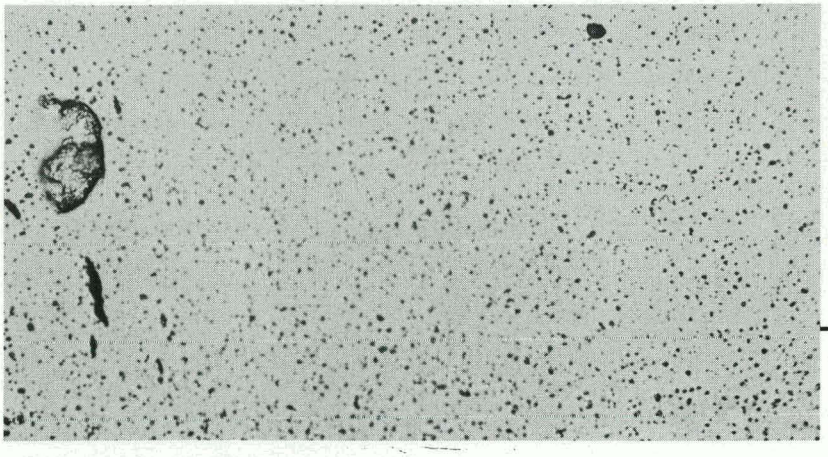

Fig. 137 Polished, X 4oo

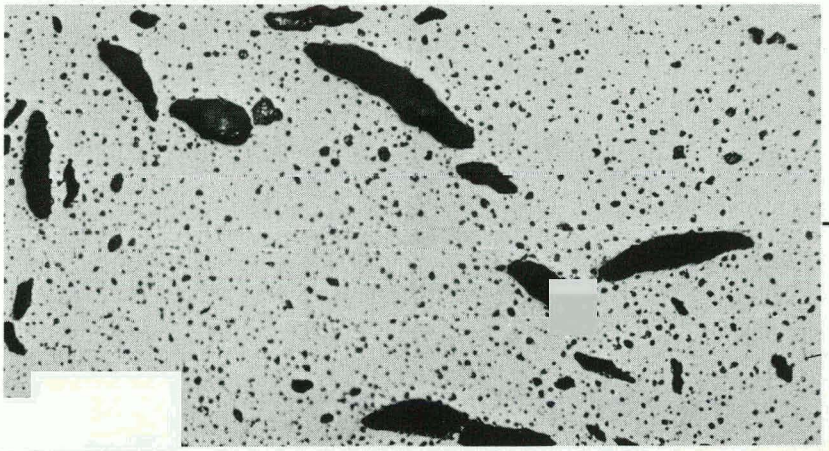

Fig. 138 Polished, X 4oo

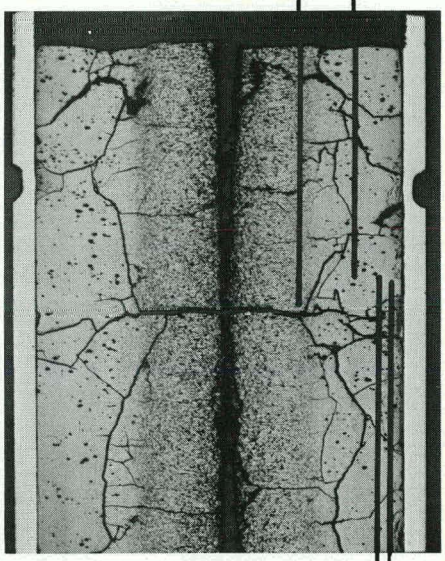

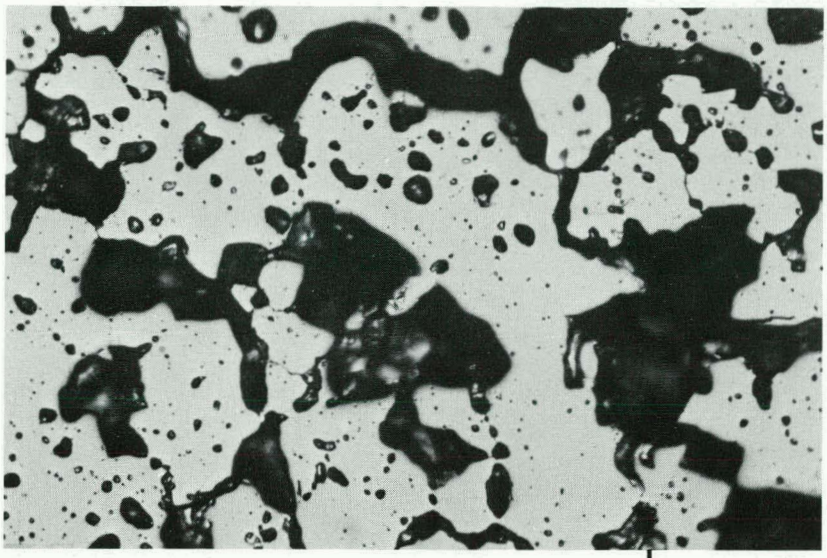

Fig. 139 Polished, X 4oo

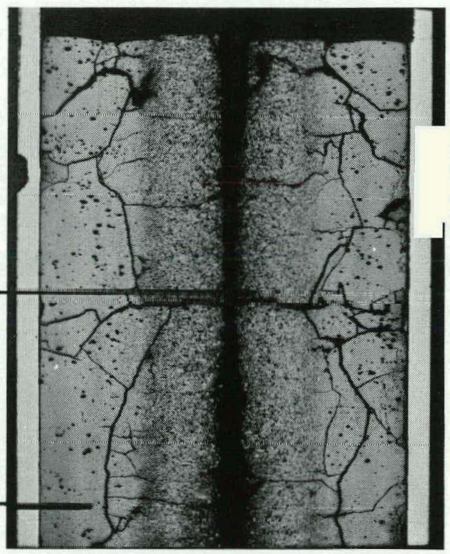

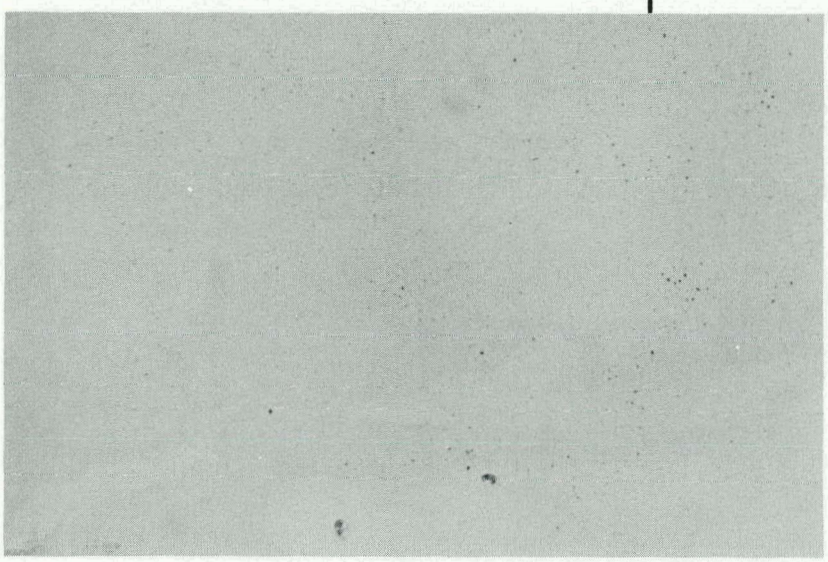

Fig. 14o Polished, X 4oo

Sample 9-5A

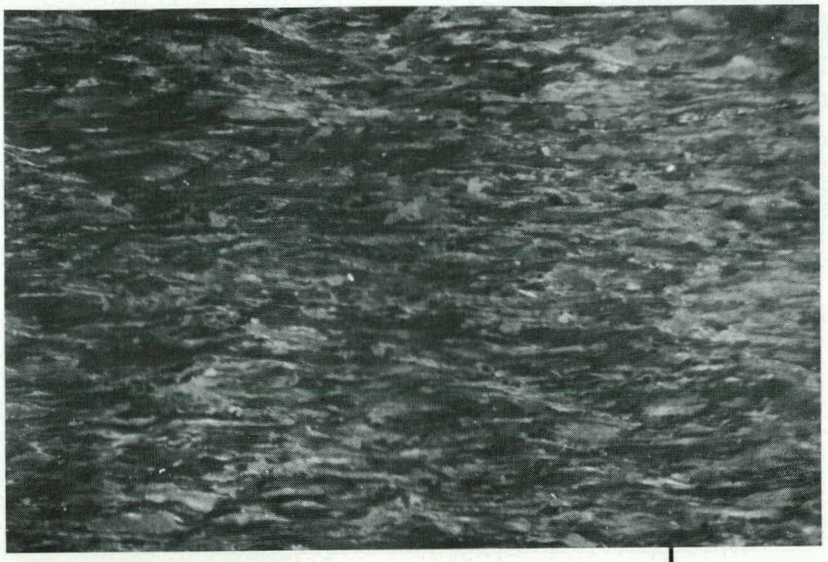

Fig. 141 Polished, pol. light, X 400

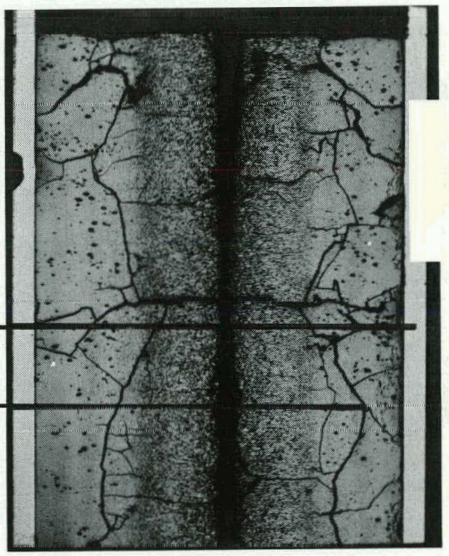

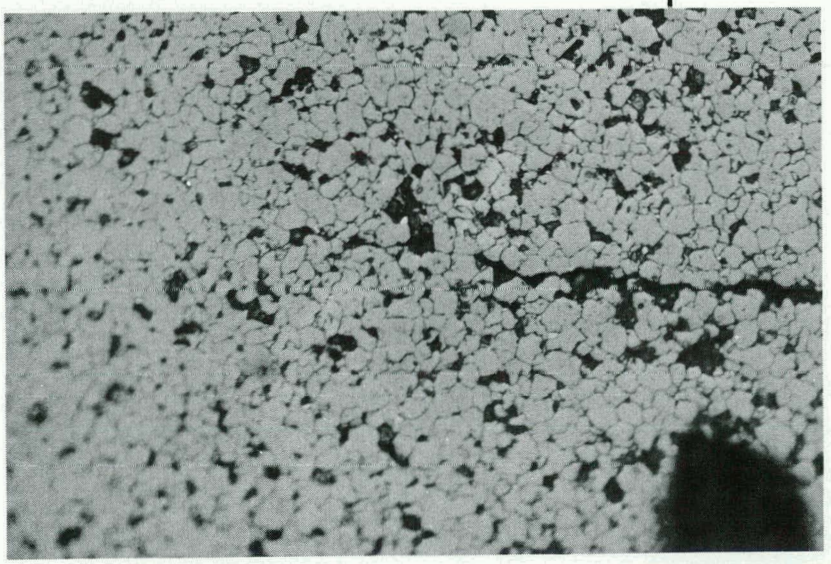

Fig. 142 Etched, X 400

Sample 11-1

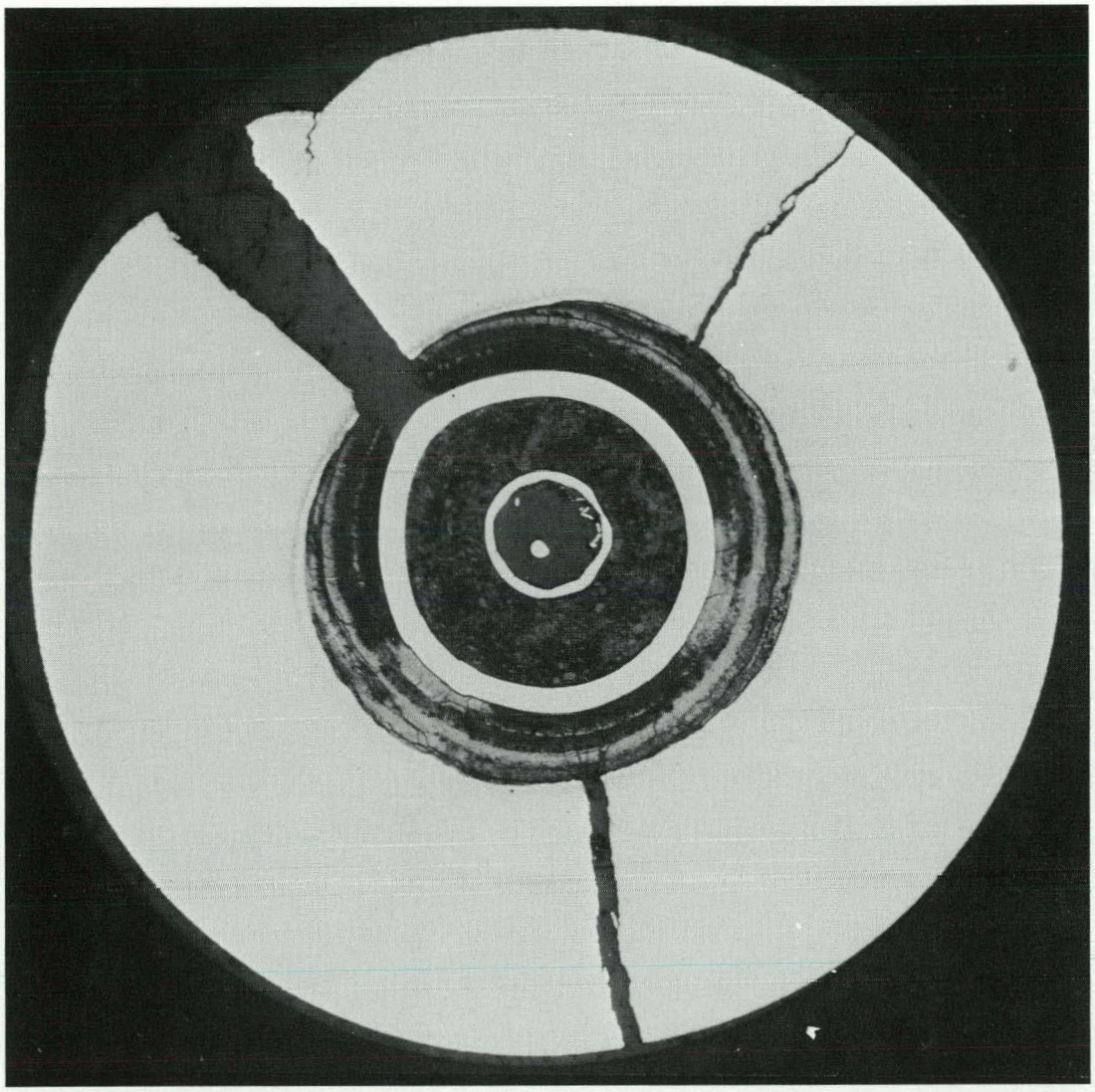

Fig. 143 Macro, polished, X 10

Fig. 144 Etched, X 3o

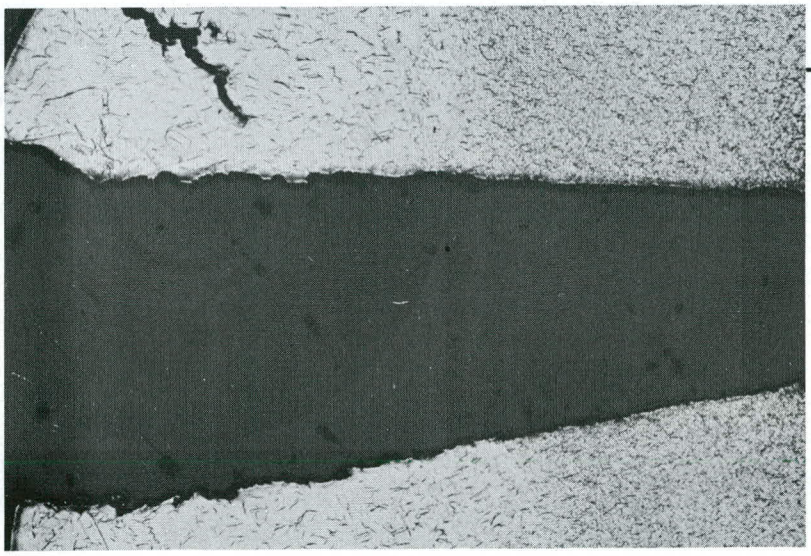

Fig. 145 Etched, X 3o

Fig. 146 Etched, X 3o

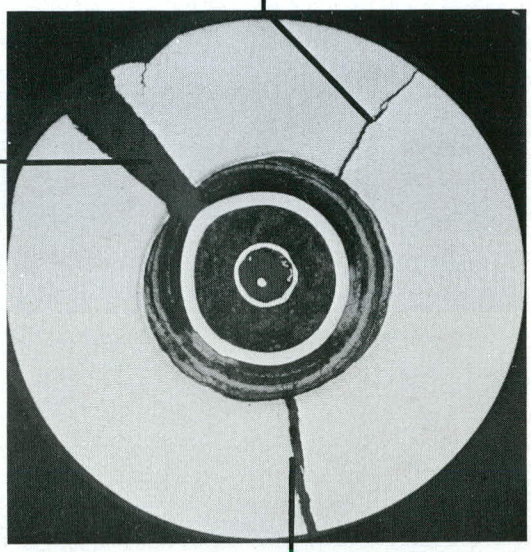

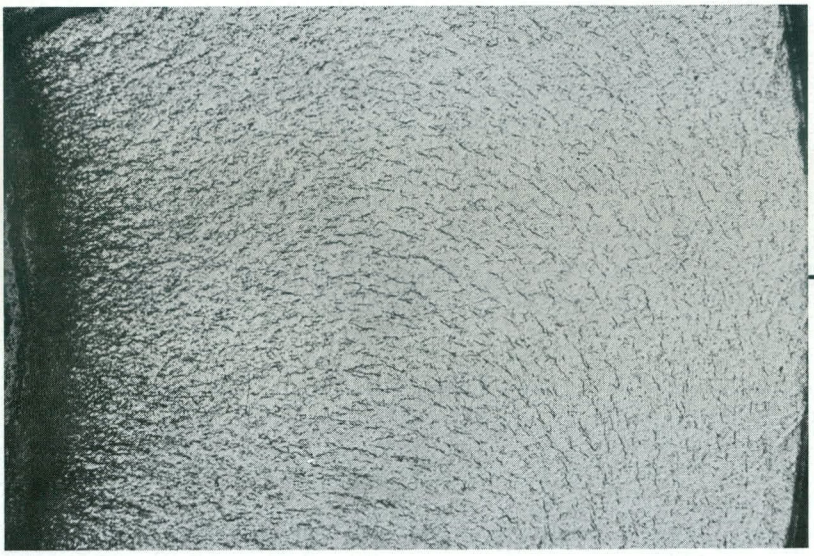

Fig. 147 Etched, X 3o

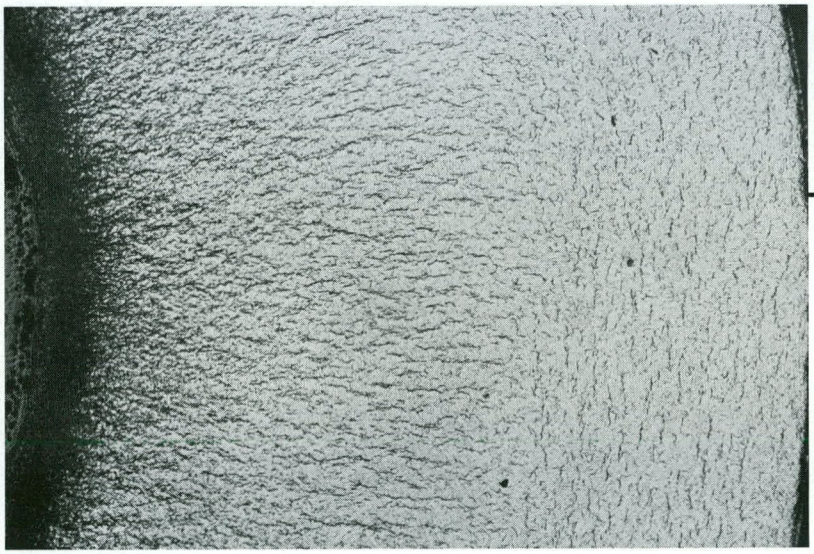

Fig. 148 Etched, X 3o

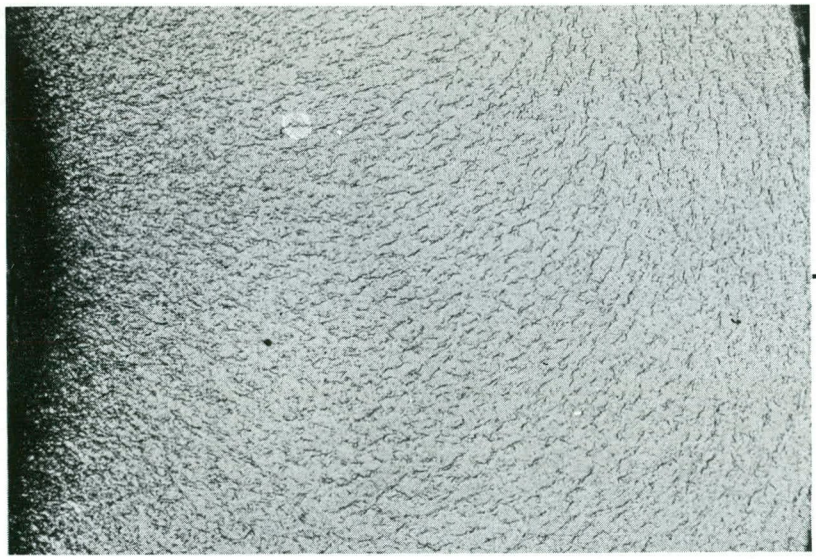

Fig. 149 Etched, X 3o

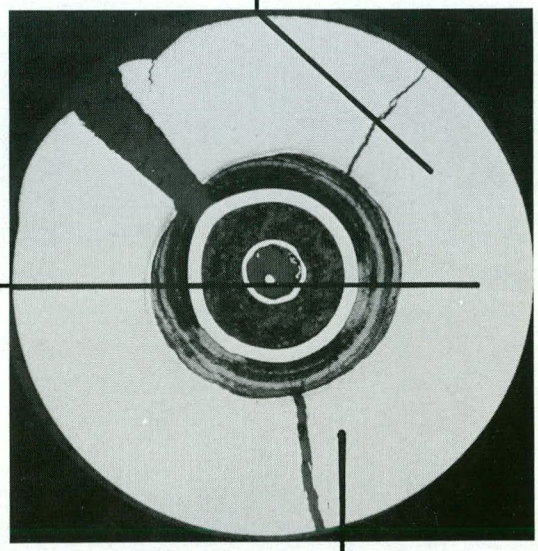

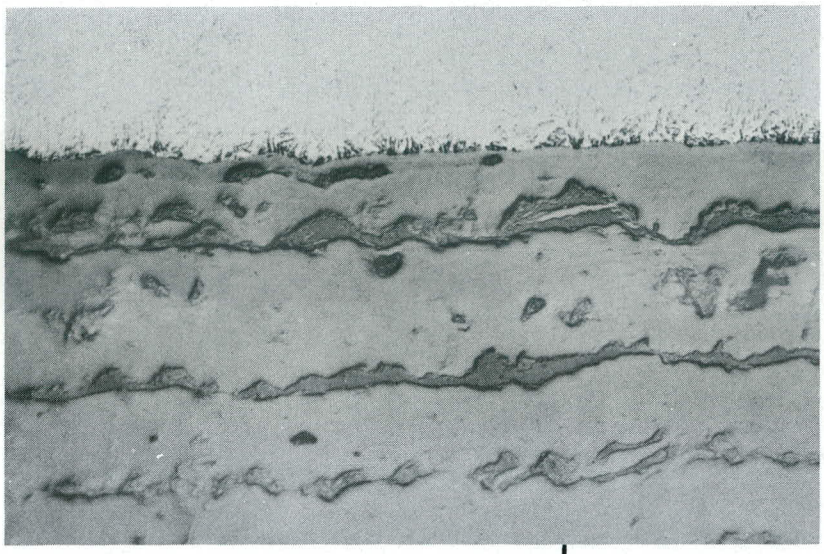

Fig. 15o Polished, X 4oo

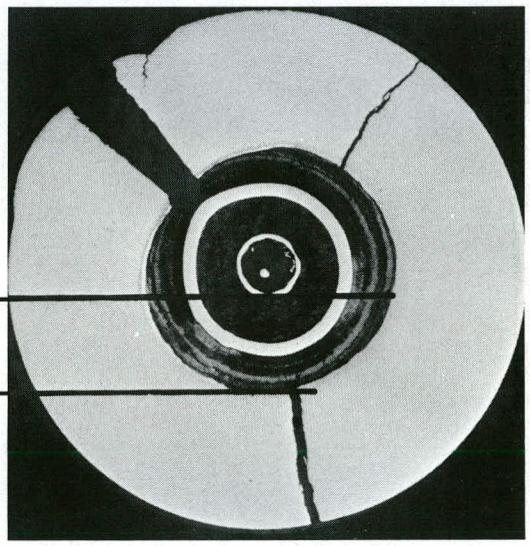

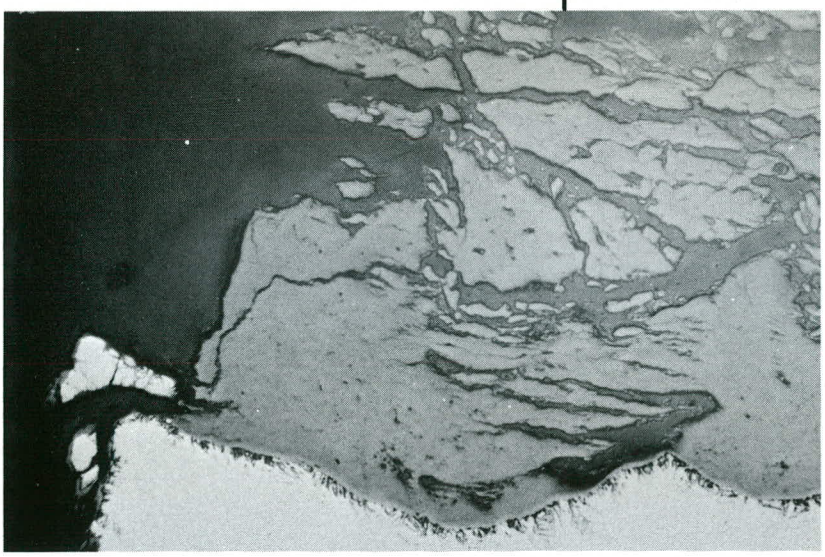

Fig. 151 Polished, X 4oo

Fig. 152 Polished, pol. light, X 400

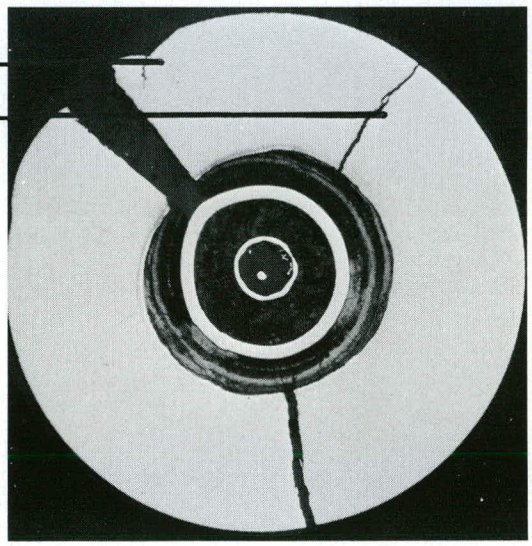

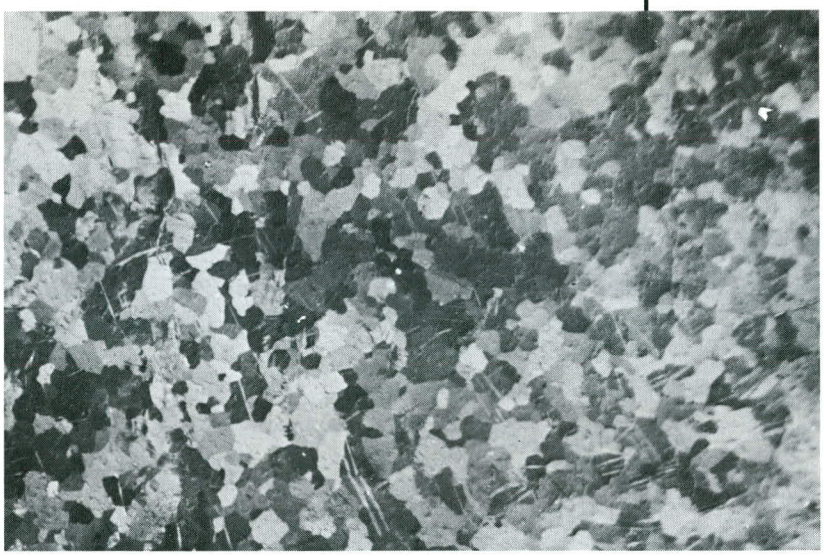

Fig. 153 Polished, pol. light, X 400

Sample 11-1

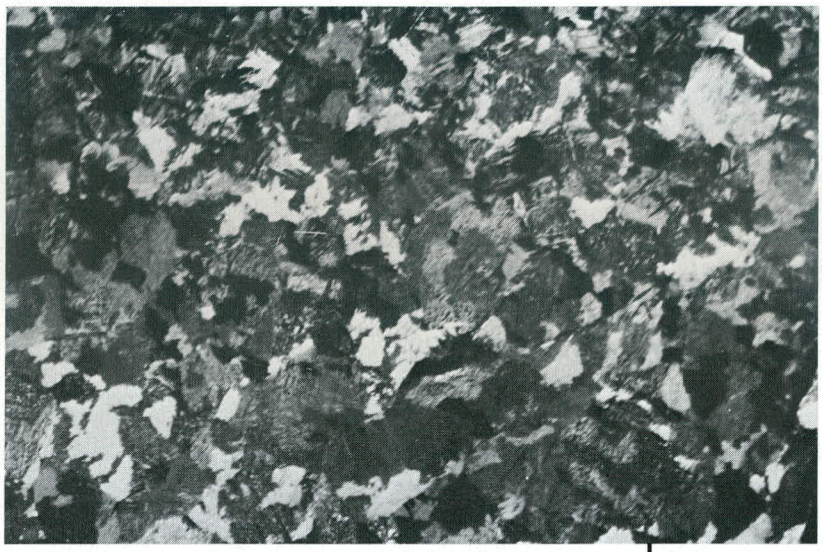

Fig. 154 Polished, pol. light, X 400

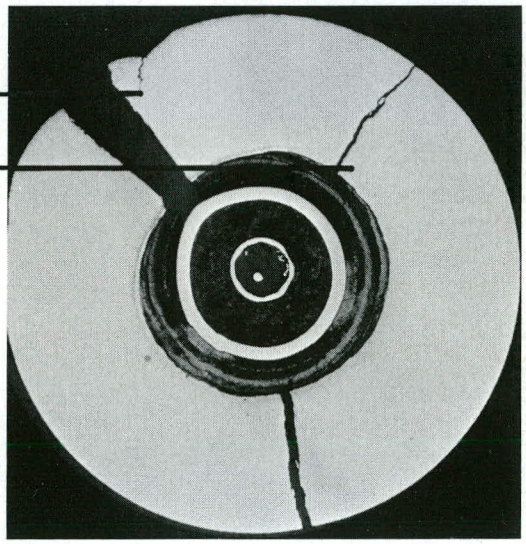

Fig. 155 Polished, pol. light, X 400

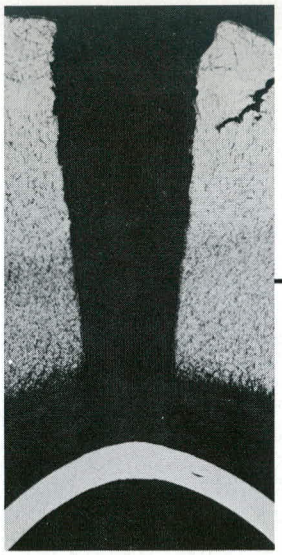

Fig. 156 Etched, X 1o

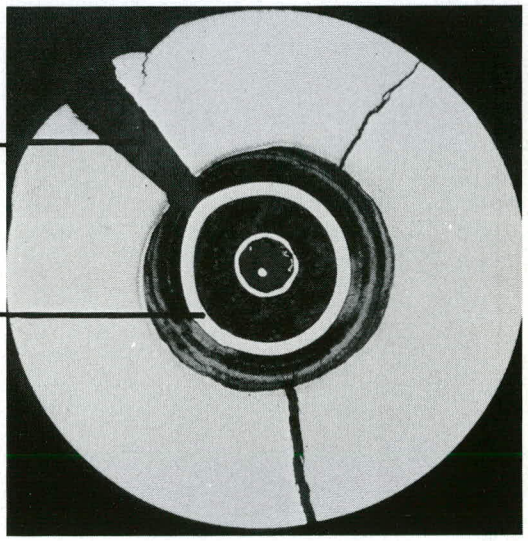

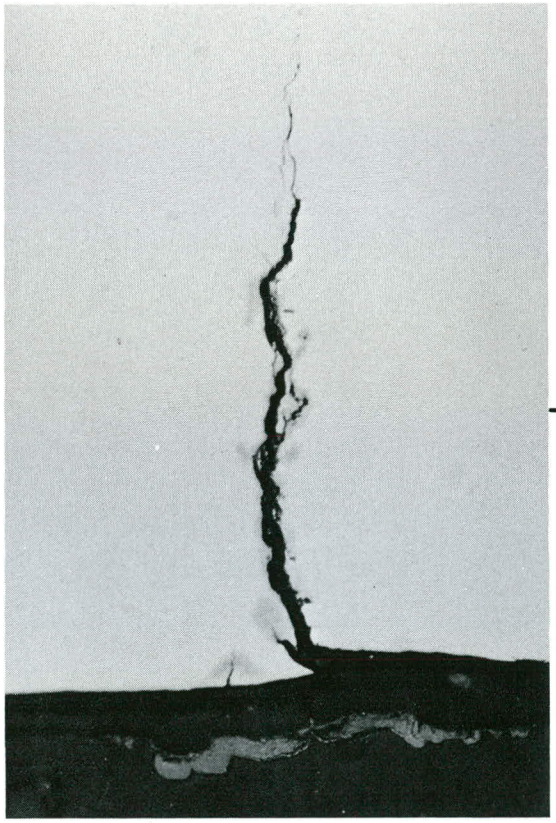

Fig. 157 Polished, X 4oo

Sample 11-2-A

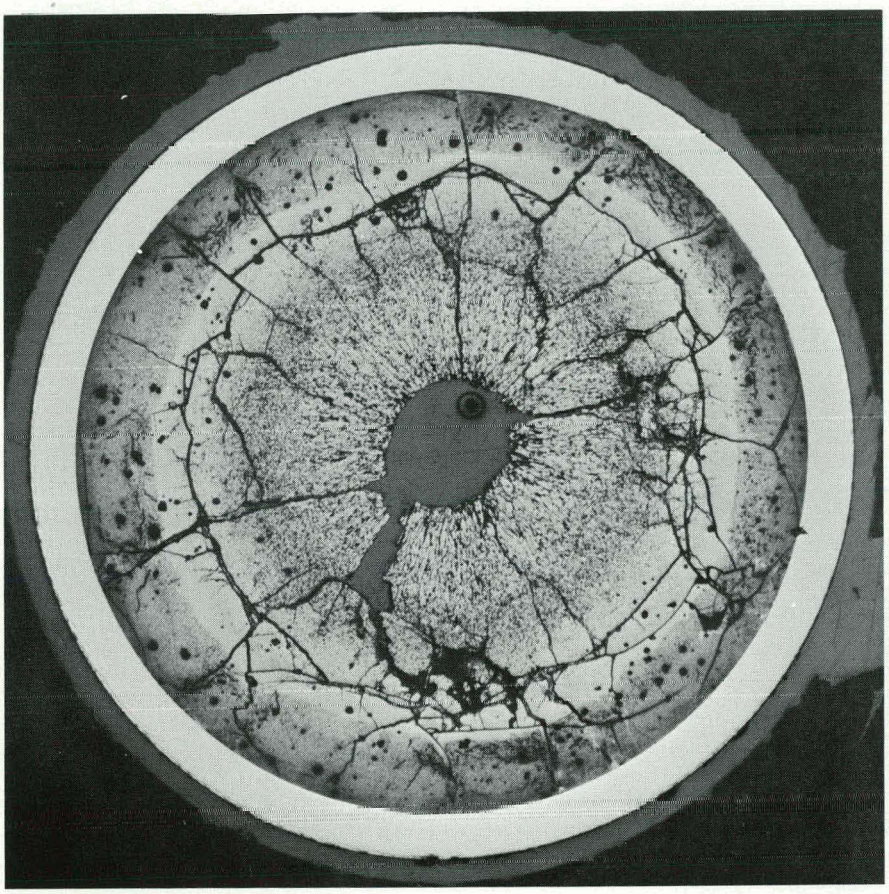

Fig. 158 X 10

Sample 11-2-A

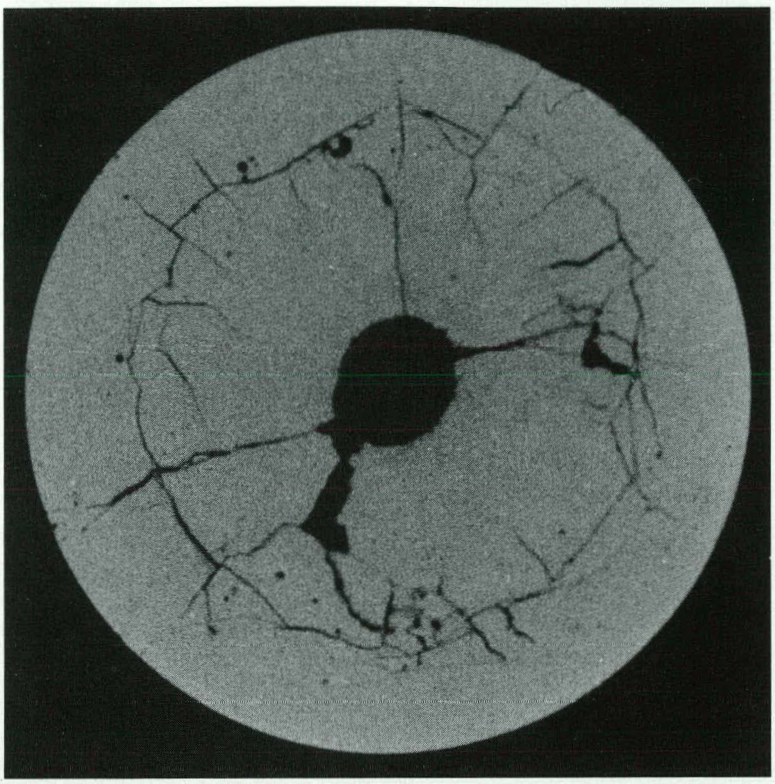

Fig. 159, α-auto., polished X 10

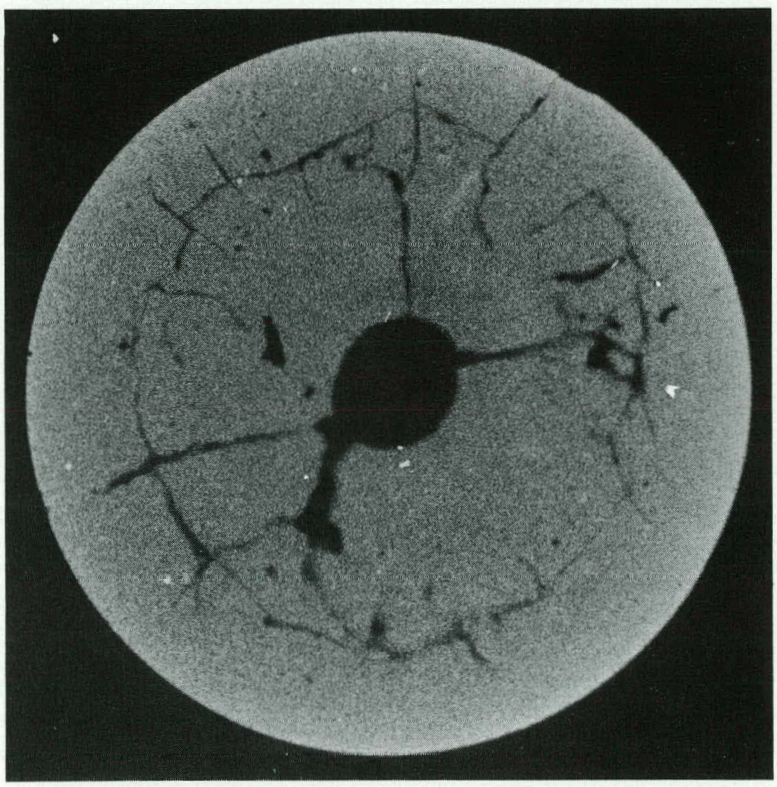

Fig. 160, α-auto., etched X 10

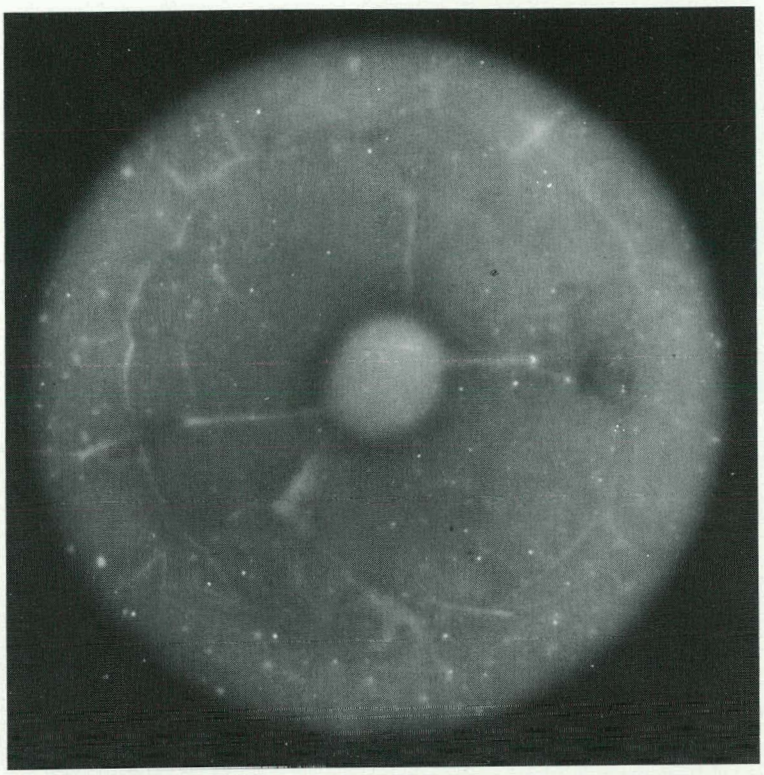

Fig. 161, β/γ-auto., polished X 10

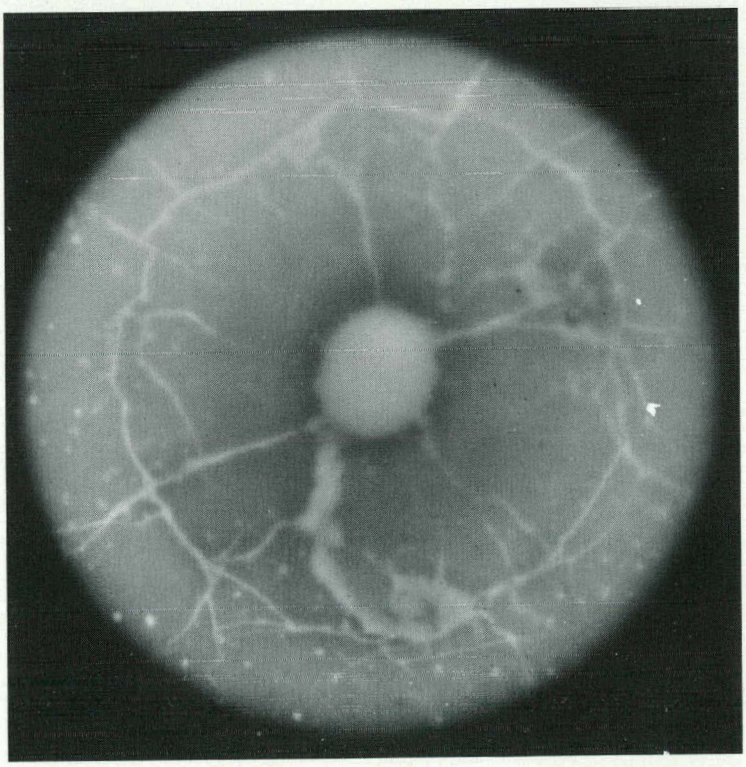

Fig. 162, β/γ-auto., etched X 10

Sample 11-2-A

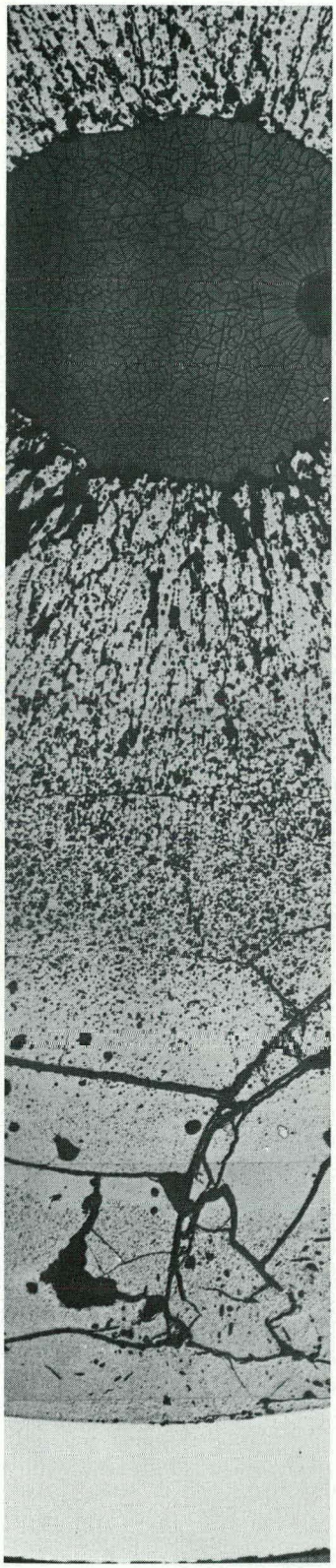

Fig. 163, polished, X 30

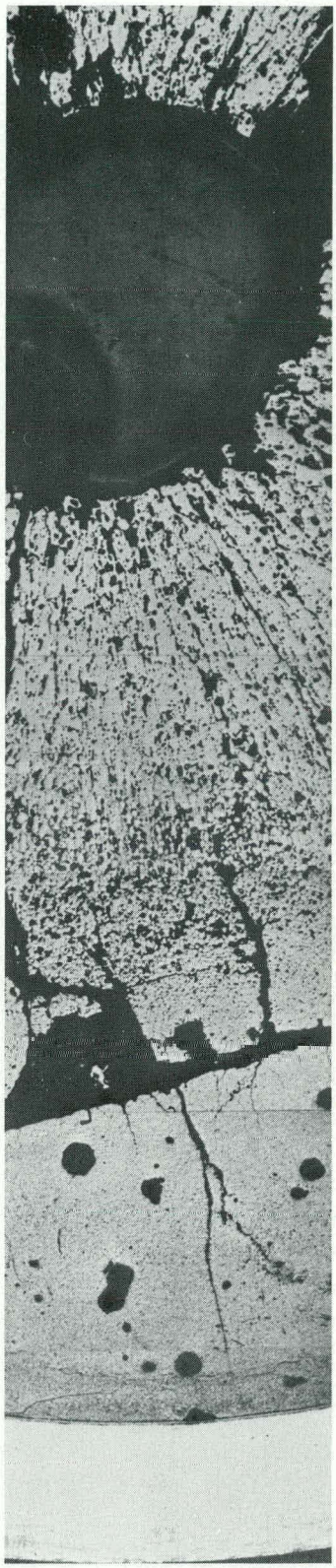

Fig. 164, etched, X 30

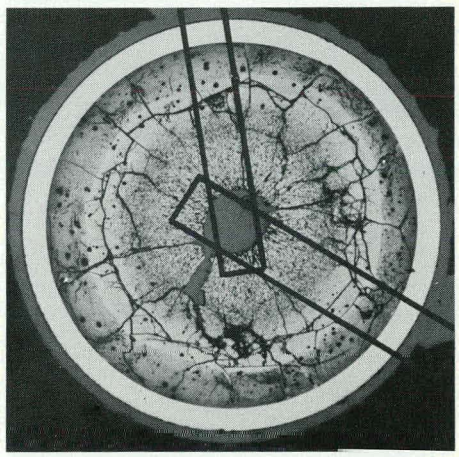

Fig. 164 Fig. 163

Sample 11-2-A

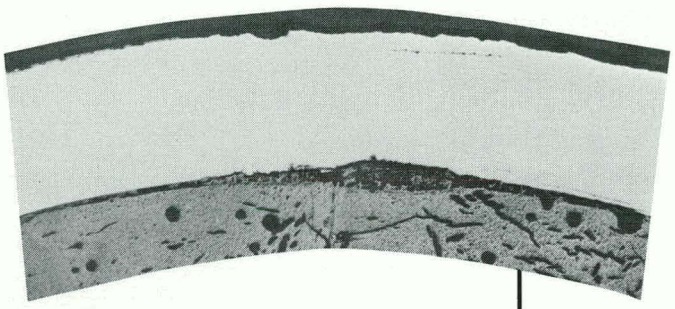

Fig. 165 Polished, X 3o

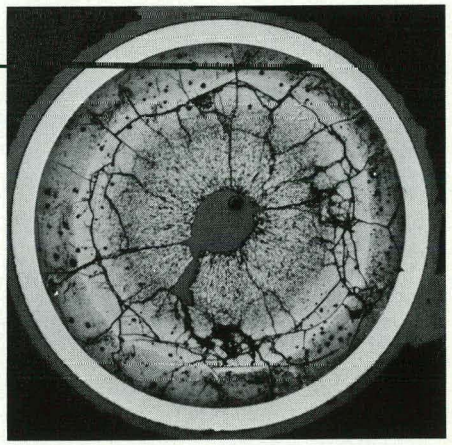

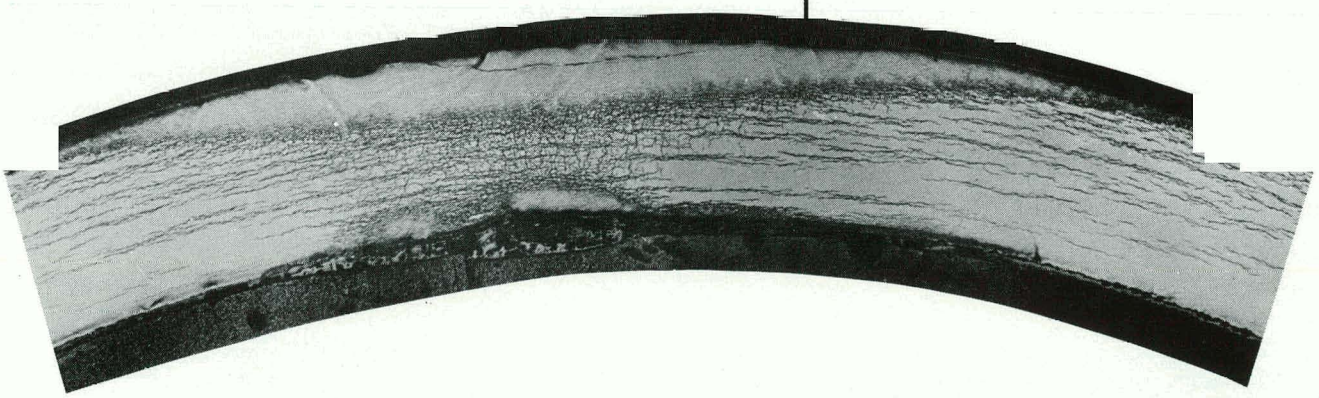

Fig. 166 Etched, X 4o

Sample 11-2-A

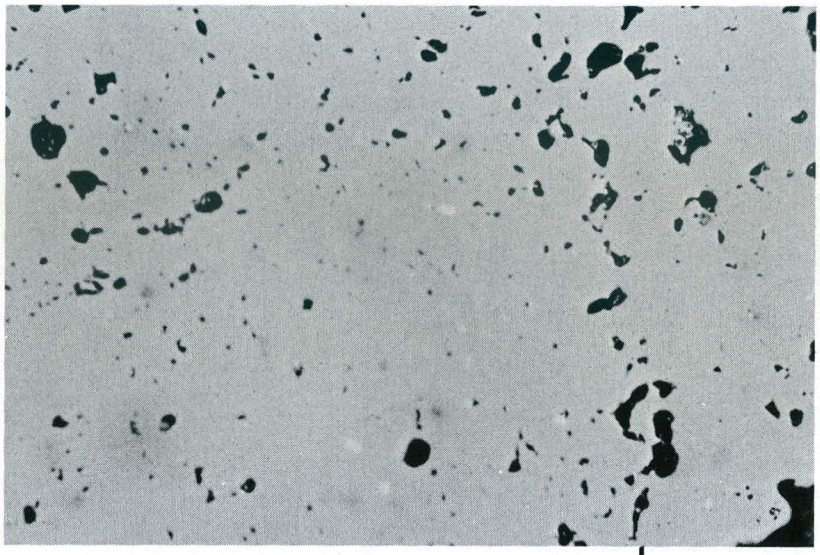

Fig. 167 Polished, X 400

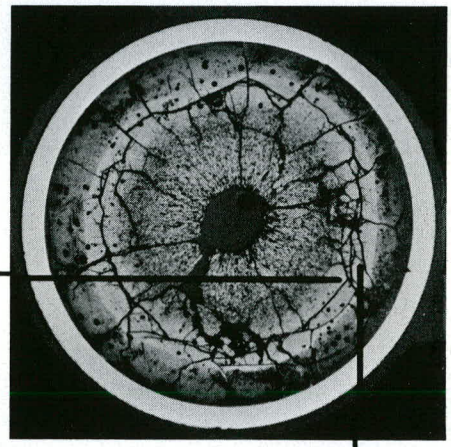

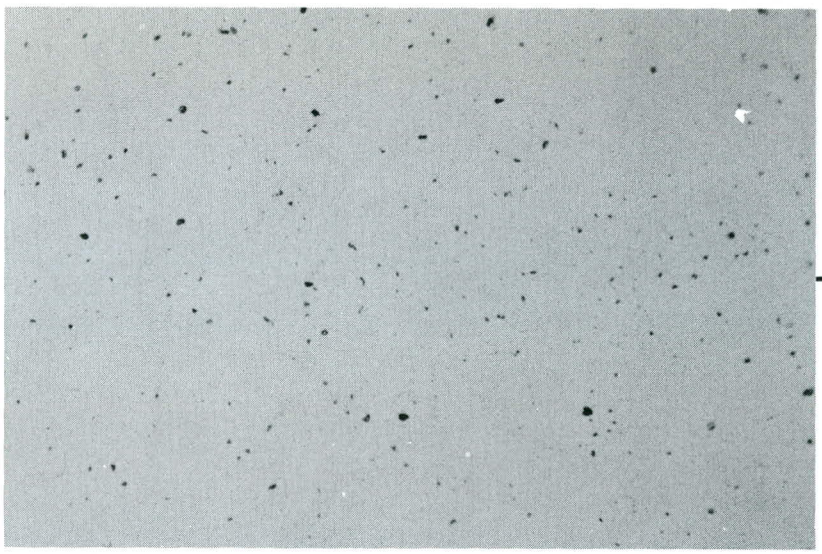

Fig. 168 Polished, X 400

Sample 11-2-A

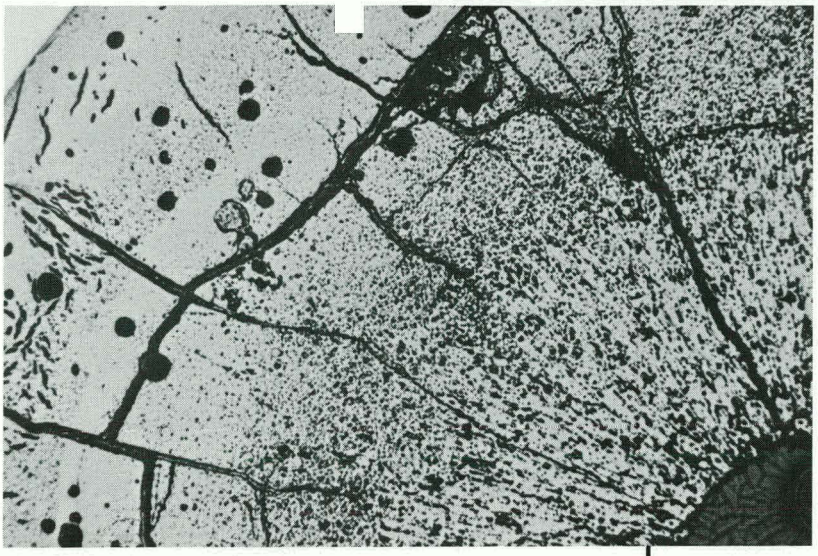

Fig. 169 Polished, X 3o

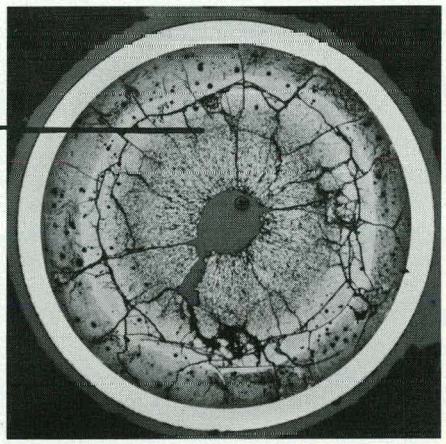

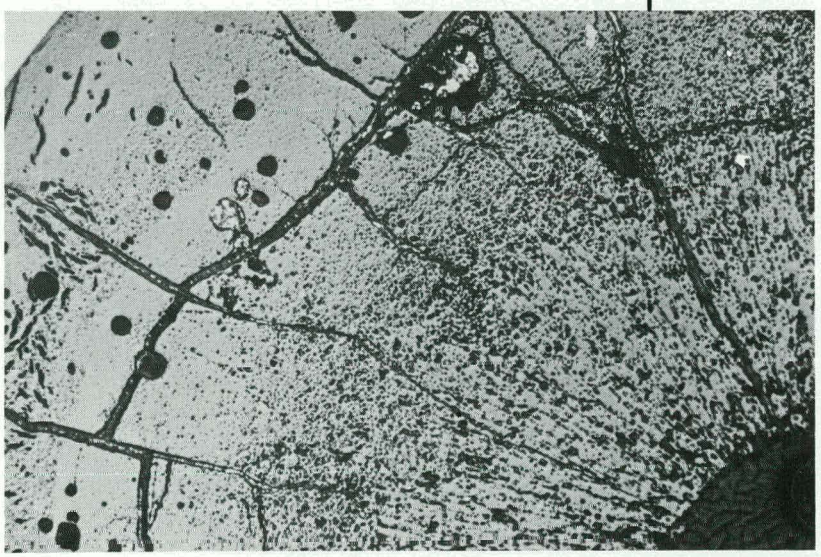

Fig. 17o Polished, pol. light, X 3o
same area as in fig. 169

Sample 11-2-A

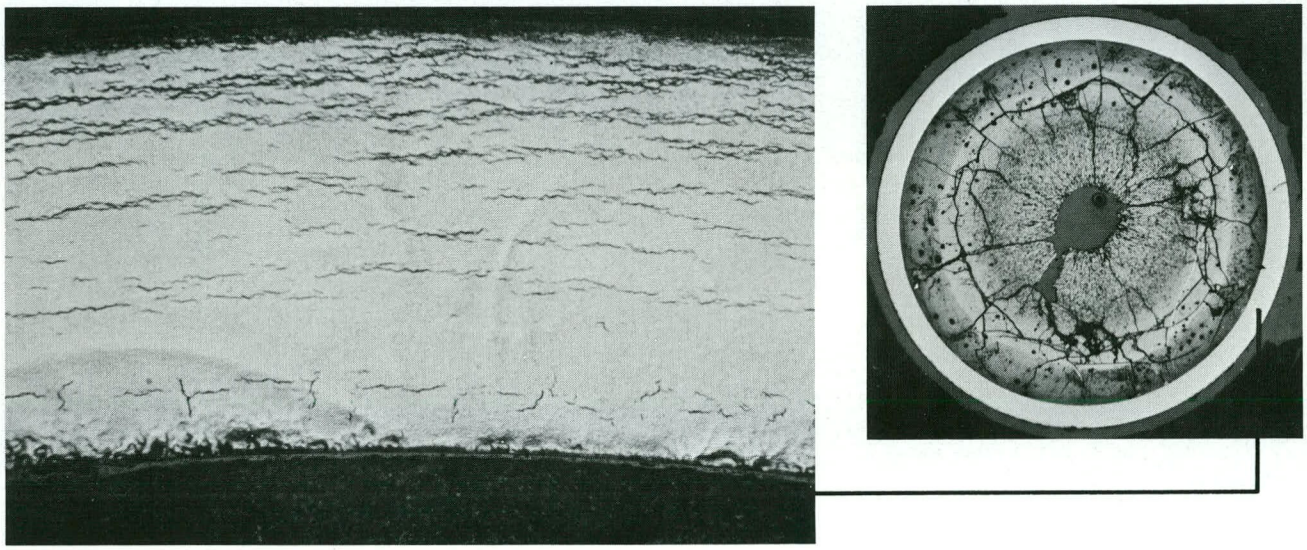

Fig. 171 Etched, X loo

Sample 11-2-A

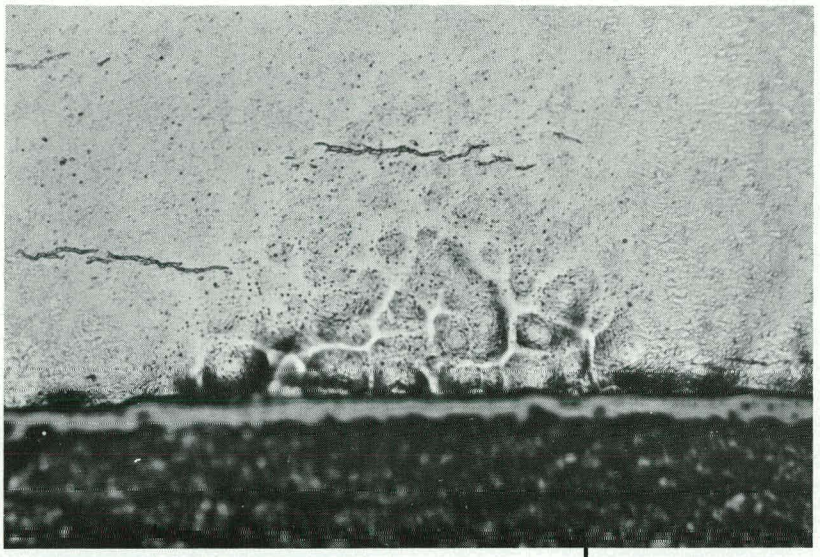

Fig. 172 Etched, X 400

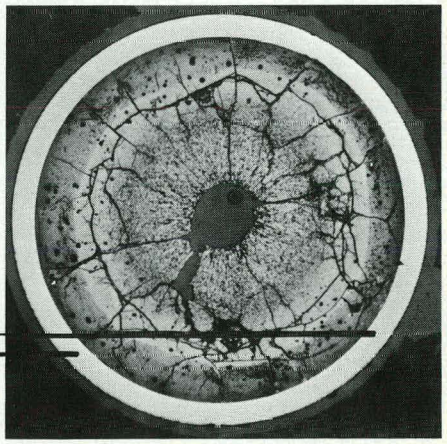

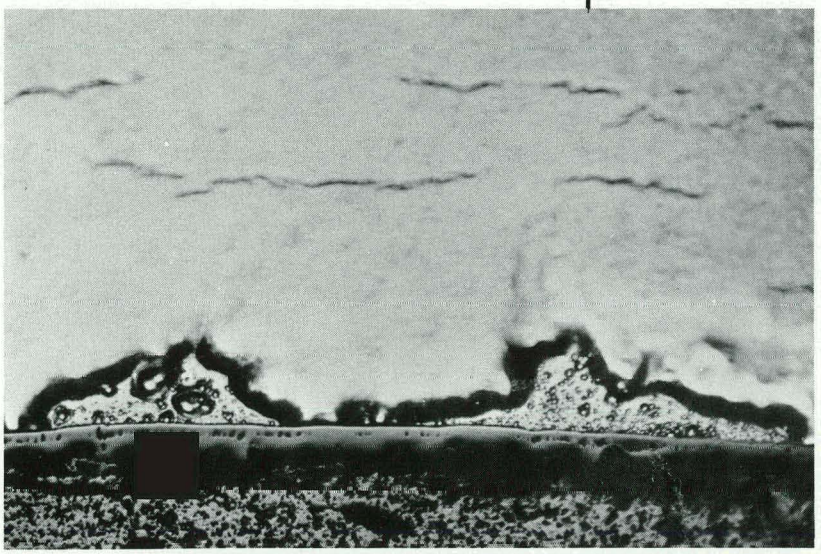

Fig. 173 Etched, X 400

Sample 11-2-A

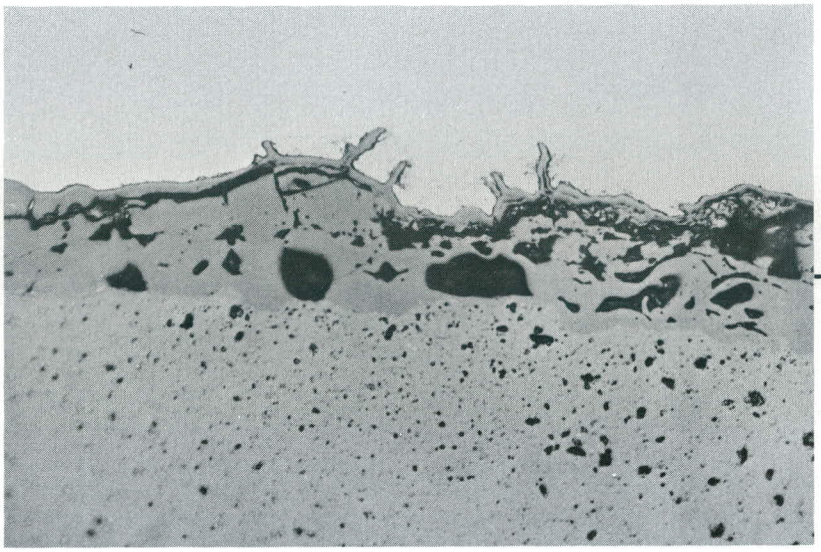

Fig. 174 Polished, X 400

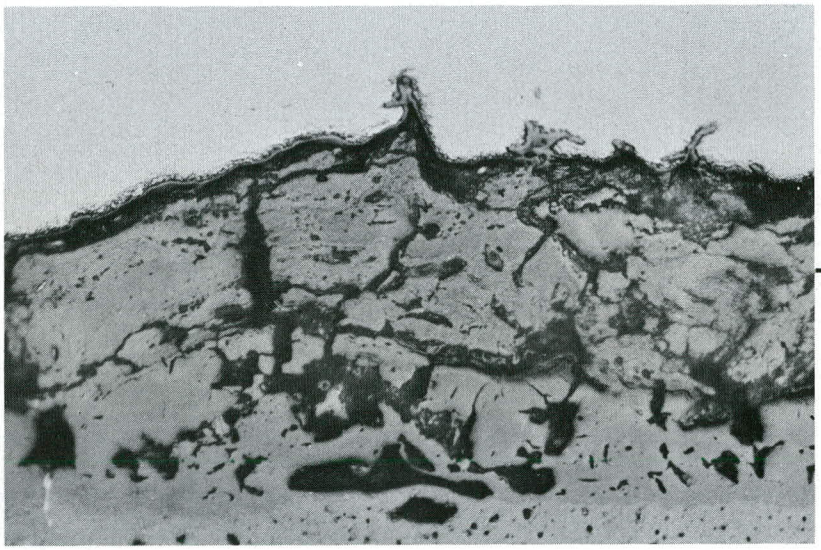

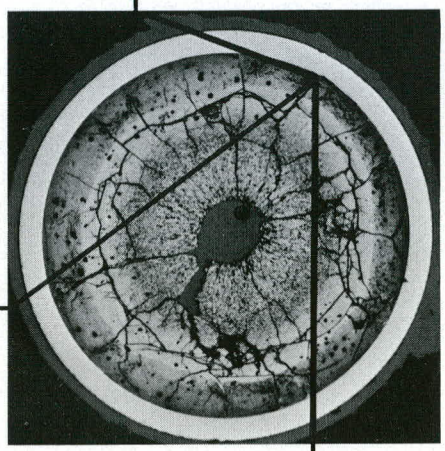

Fig. 175 Polished, X 400

Fig. 176 Polished, X 400

Sample 11-2-A

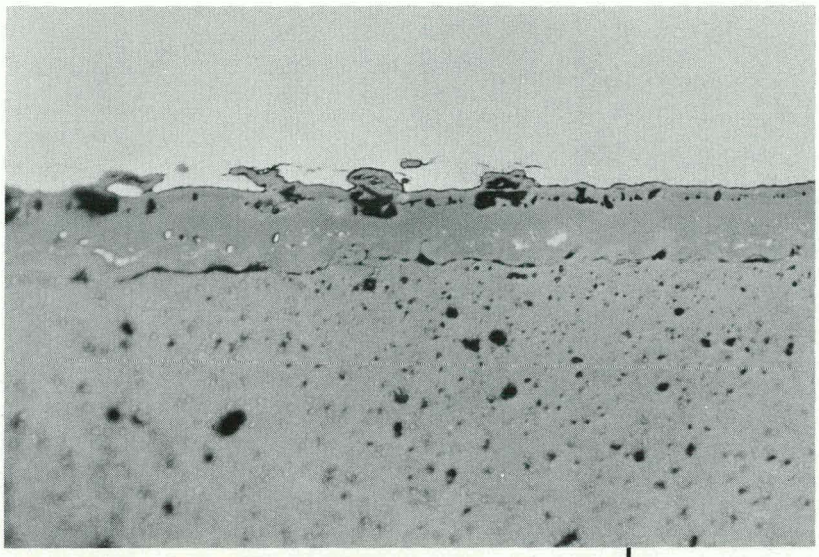

Fig. 177 Polished, X 400

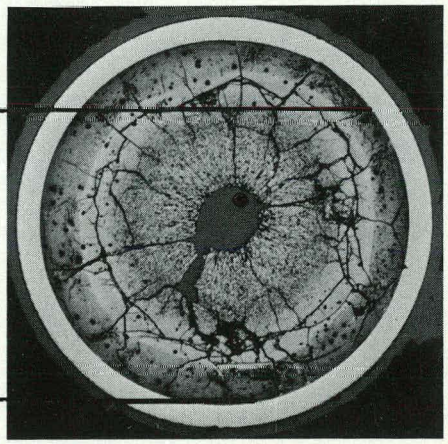

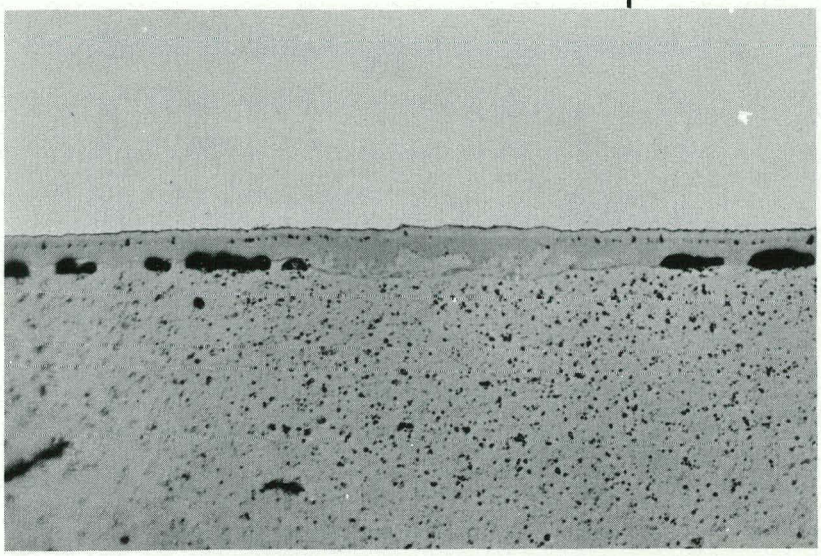

Fig. 178 Polished, X 400

Sample 11-2-1

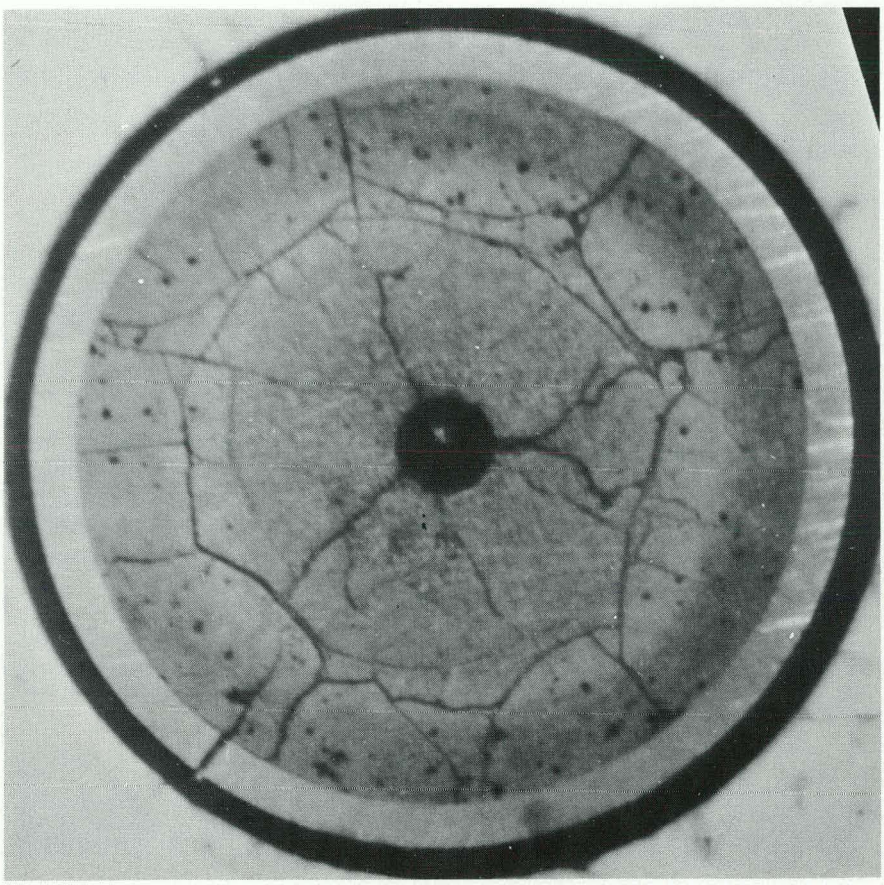

Fig. 179 X 10

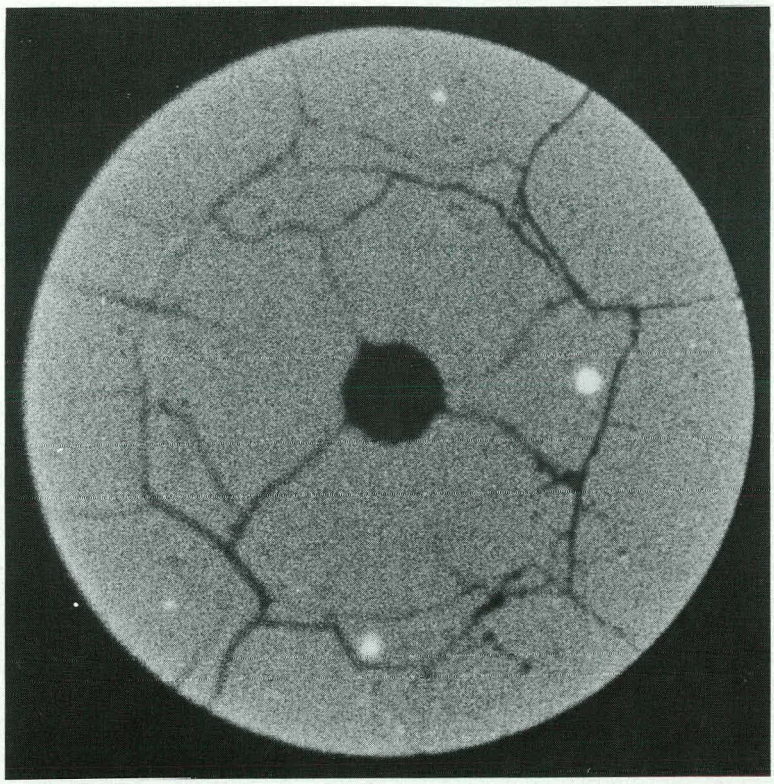

Fig. 180, α-auto., polished X 10

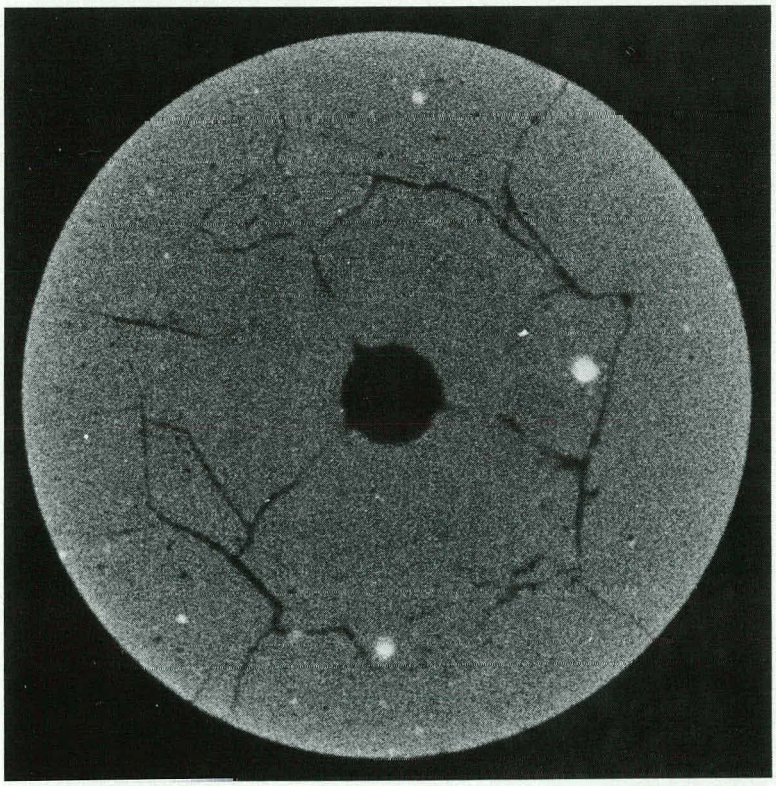

Fig. 181, α-auto., etched X 10

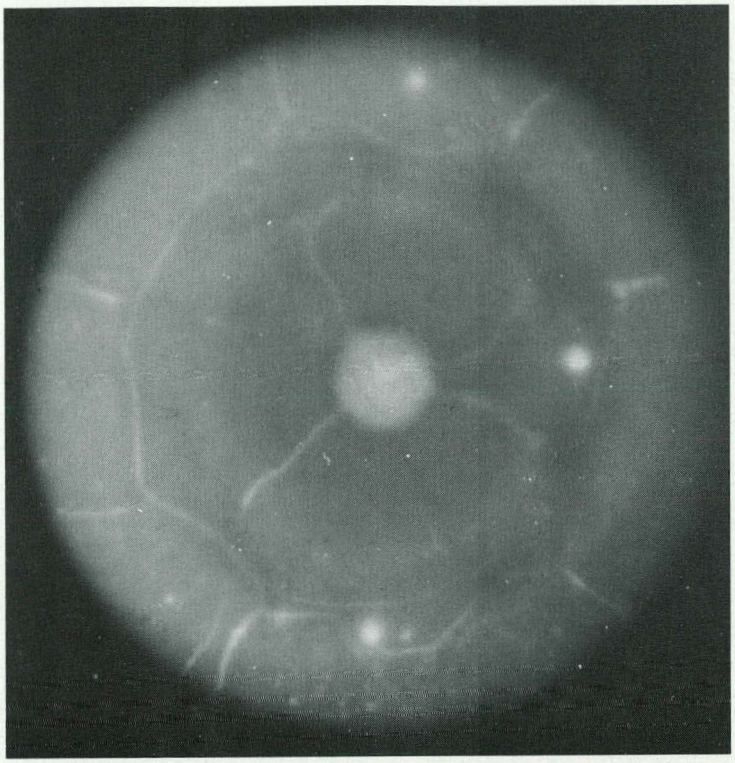

Fig. 182, β/γ-auto., polished X 10

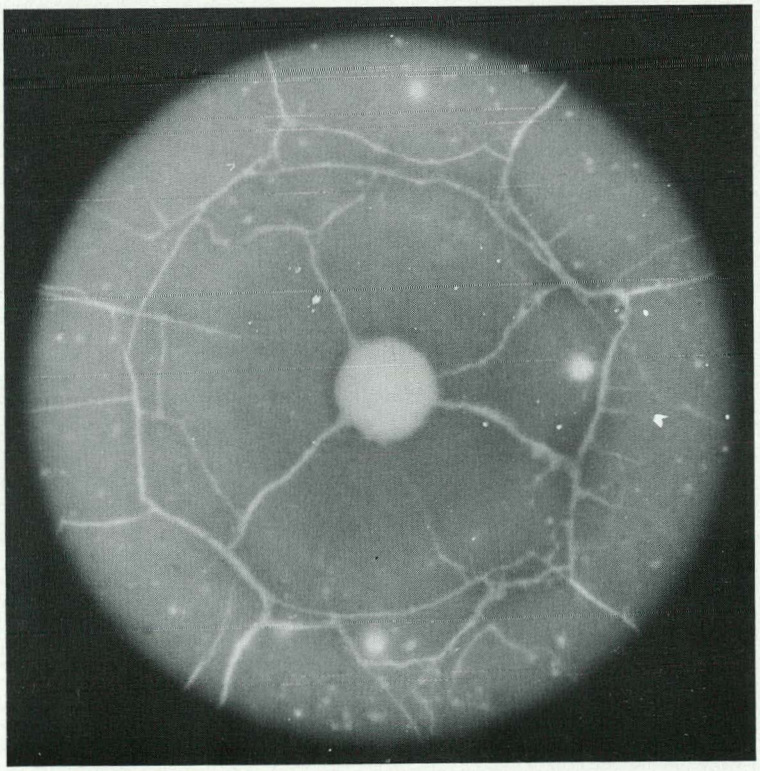

Fig. 183, β/γ-auto., etched X 10

Sample 11-2-1

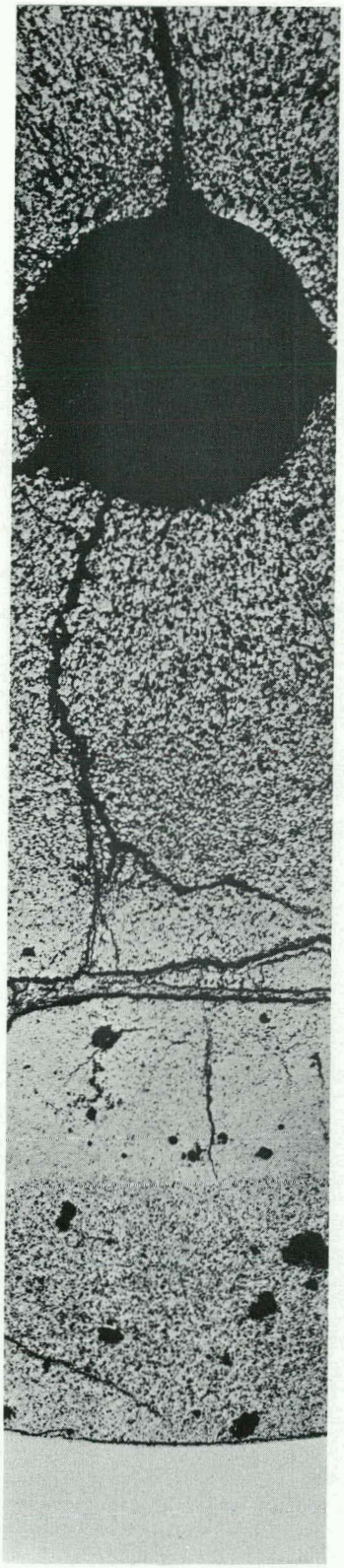

Fig. 184, polished, X 30

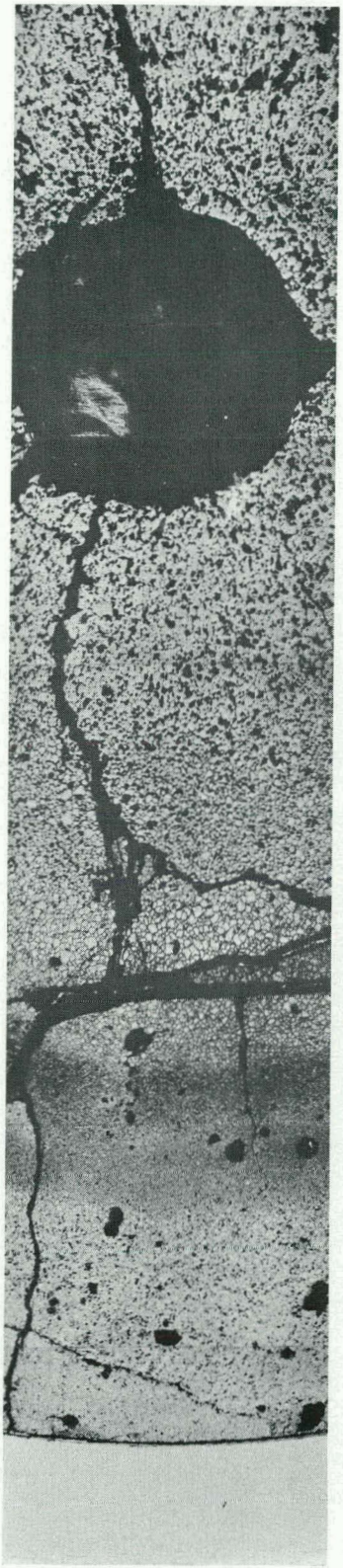

Fig. 185, etched, X 30

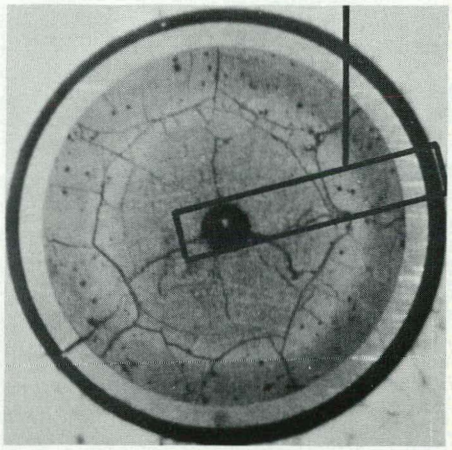

Fig. 184
Fig. 185

Sample 11-2-1

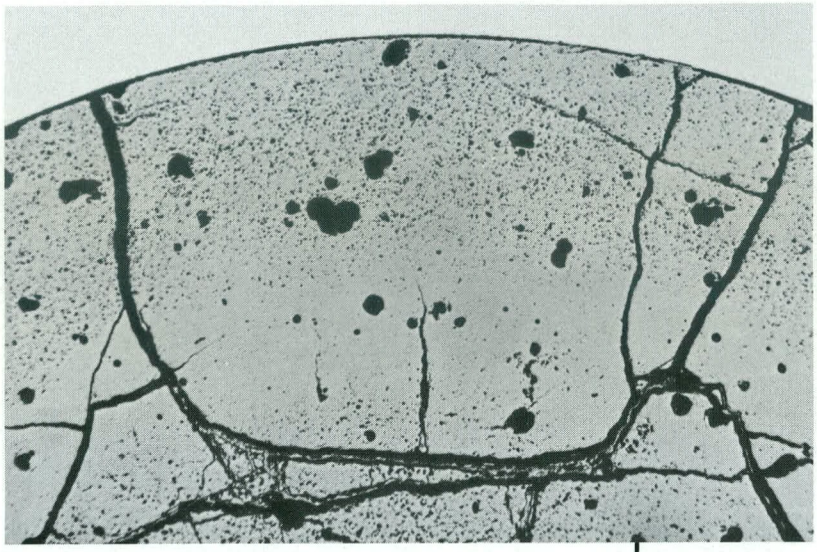

Fig. 186 Polished, X 3o

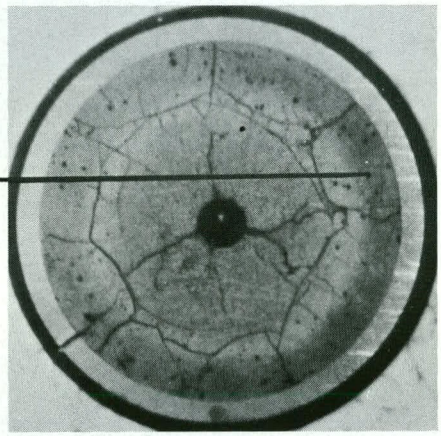

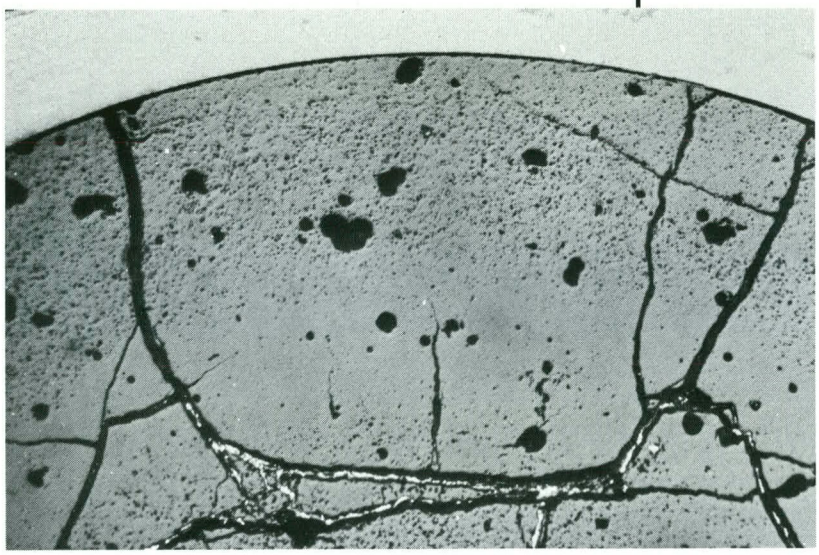

Fig. 187 Polished, pol. light, X 3o

same area as in fig 186

Sample 11-2-1

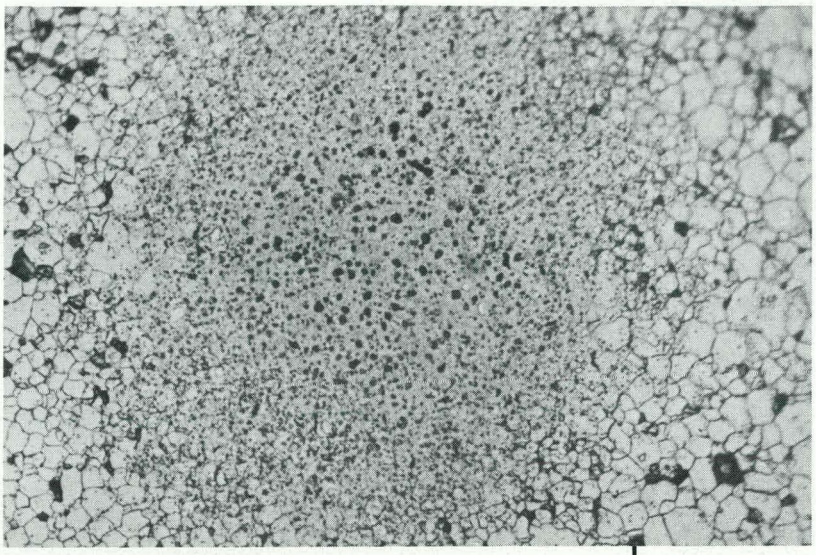

Fig. 188 Etched, X 400

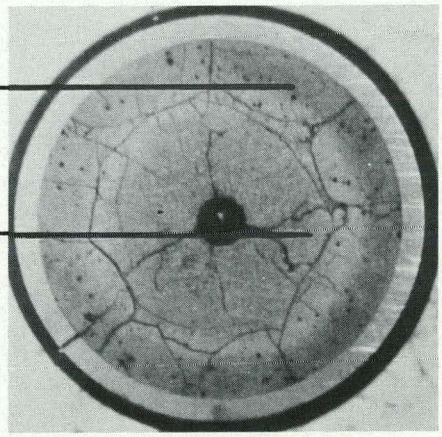

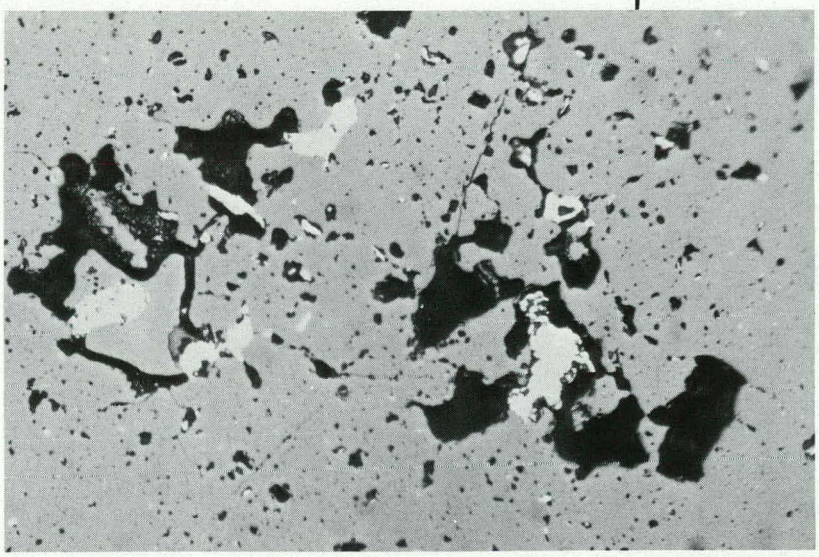

Fig. 189 Polished, X 400

Sample 11-2-1

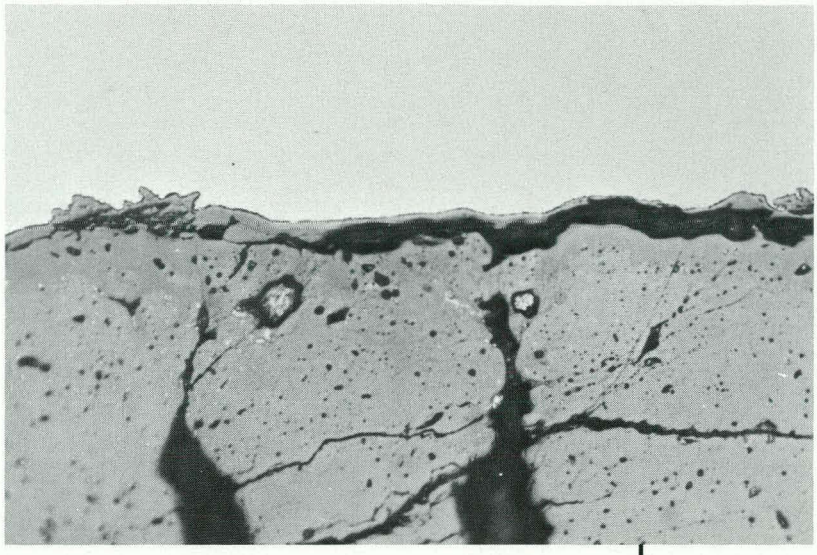

Fig. 190 Polished, X 400

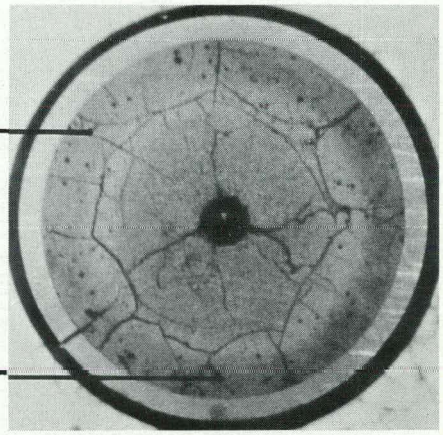

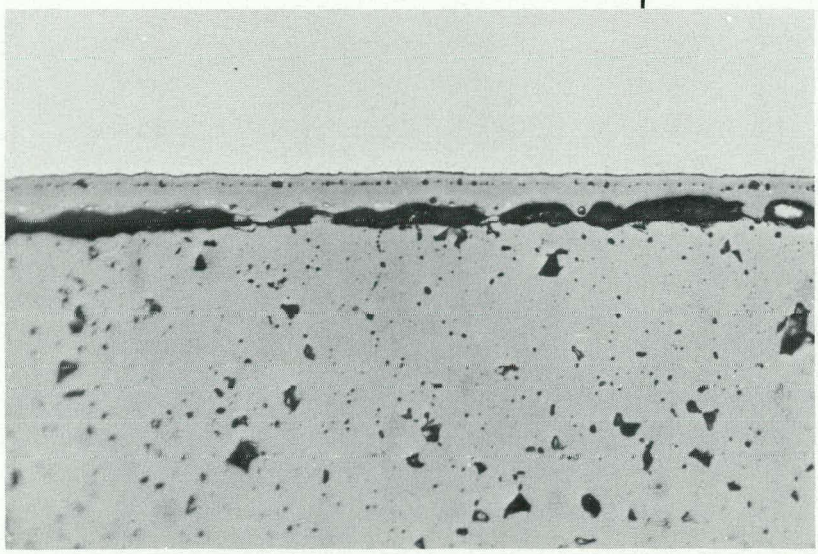

Fig. 191 Polished, X 400

Sample 11-2-1

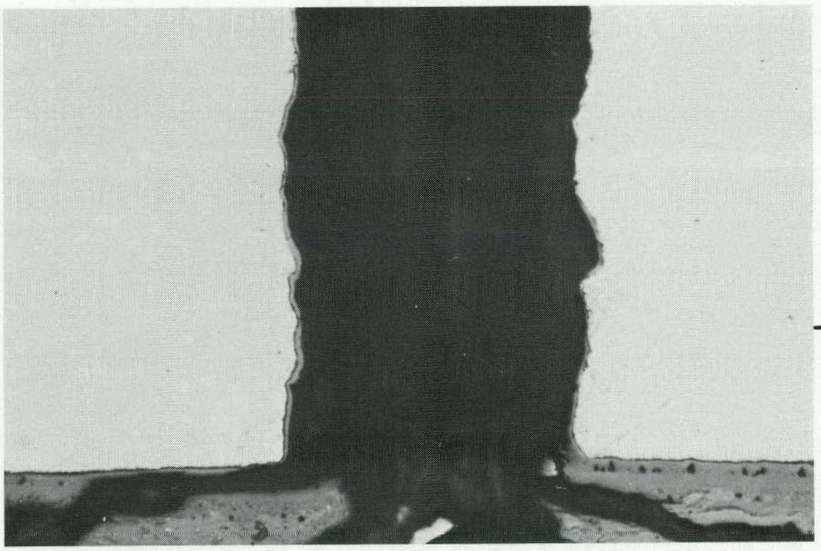

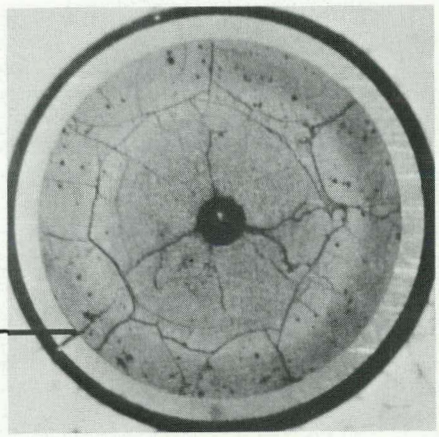

Fig 192 Polished, X 400

Sample 11-2-1

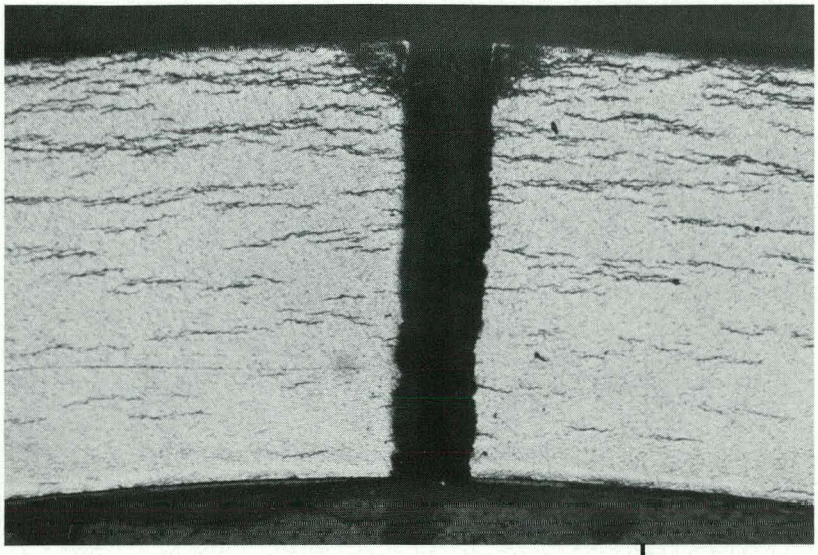

Fig 193 Etched, X 1oo

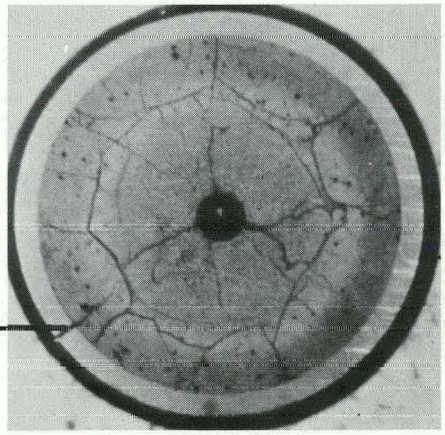

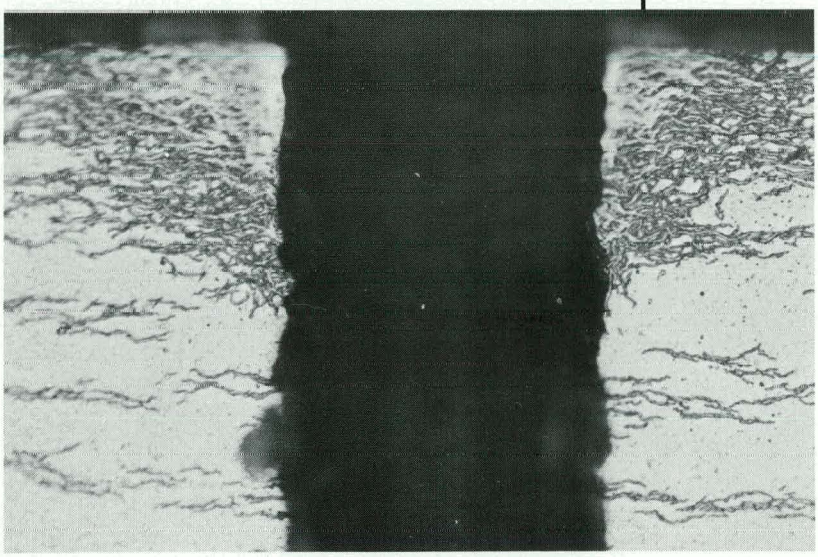

Fig. 194 Etched, X 4oo

Sample 11-3

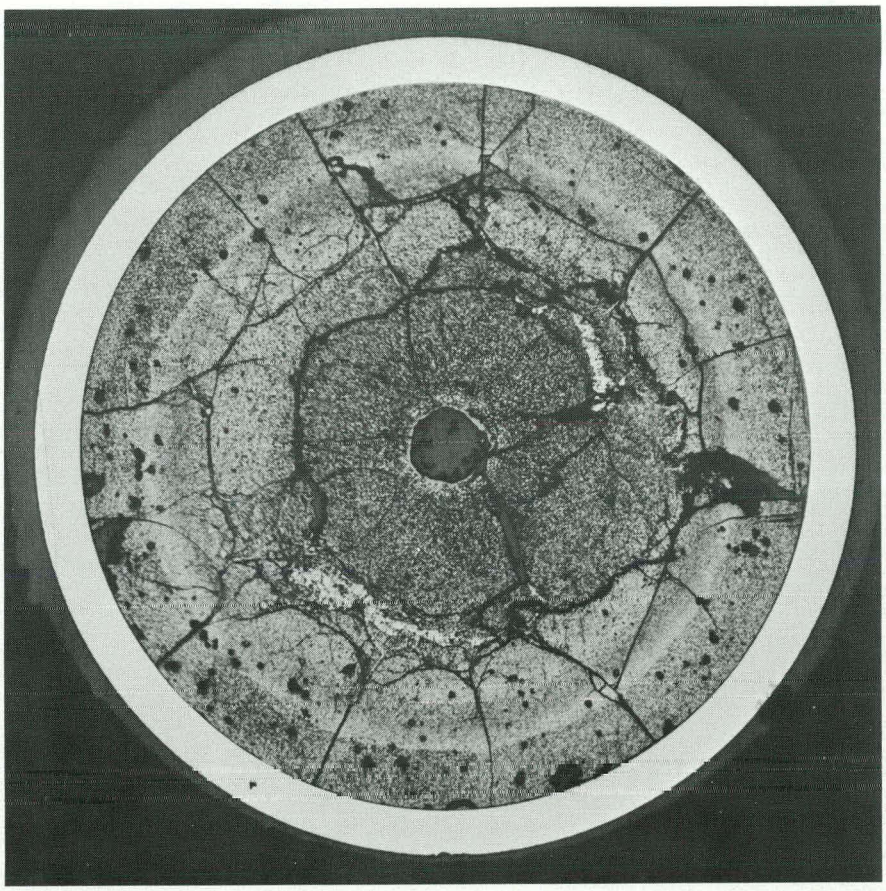

Fig. 195 X 10

Sample 11-3

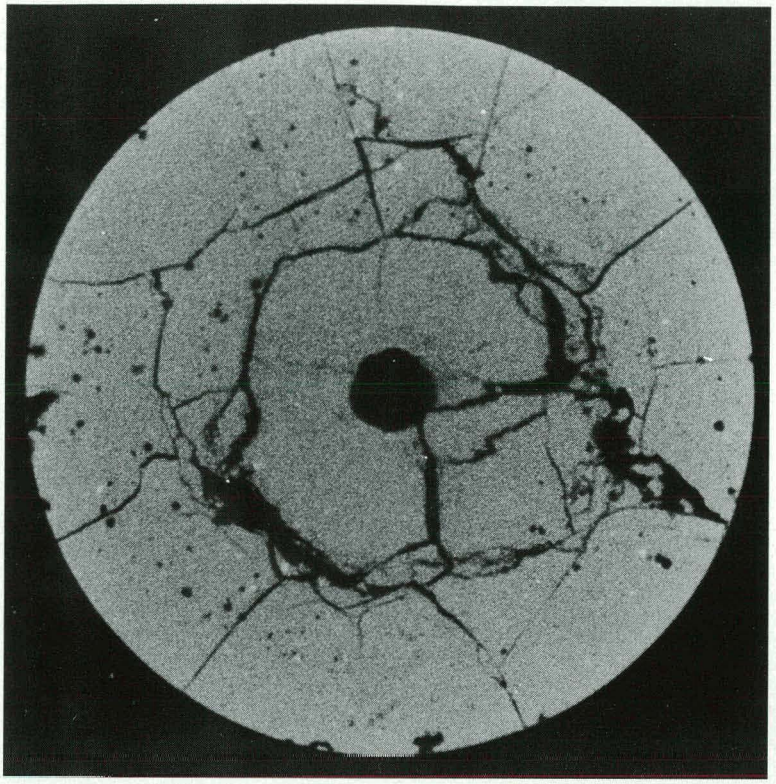

Fig. 196, α-auto., polished X 10

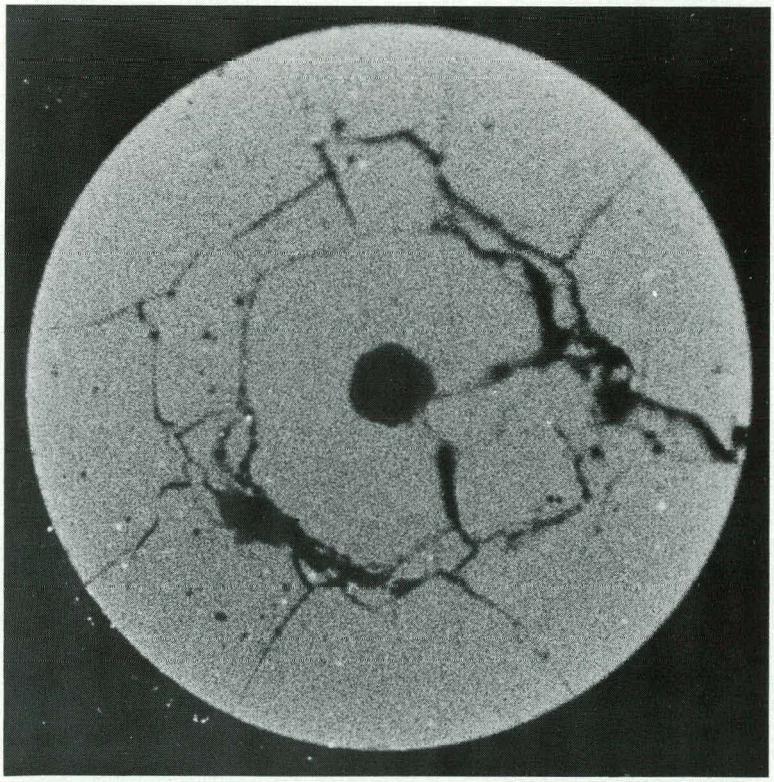

Fig. 197, α-auto., etched X 10

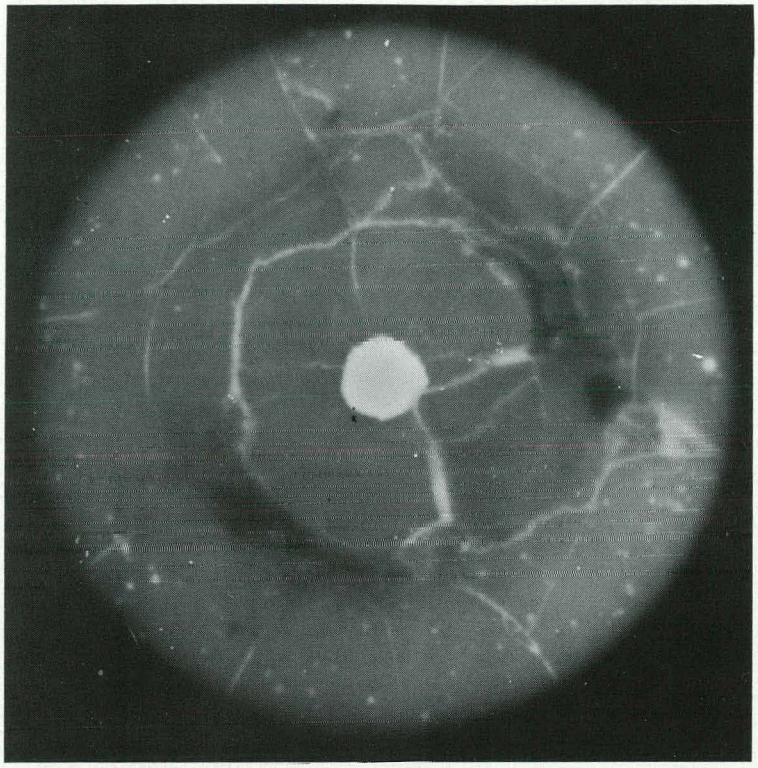

Fig. 198, β/γ-auto., polished X 10

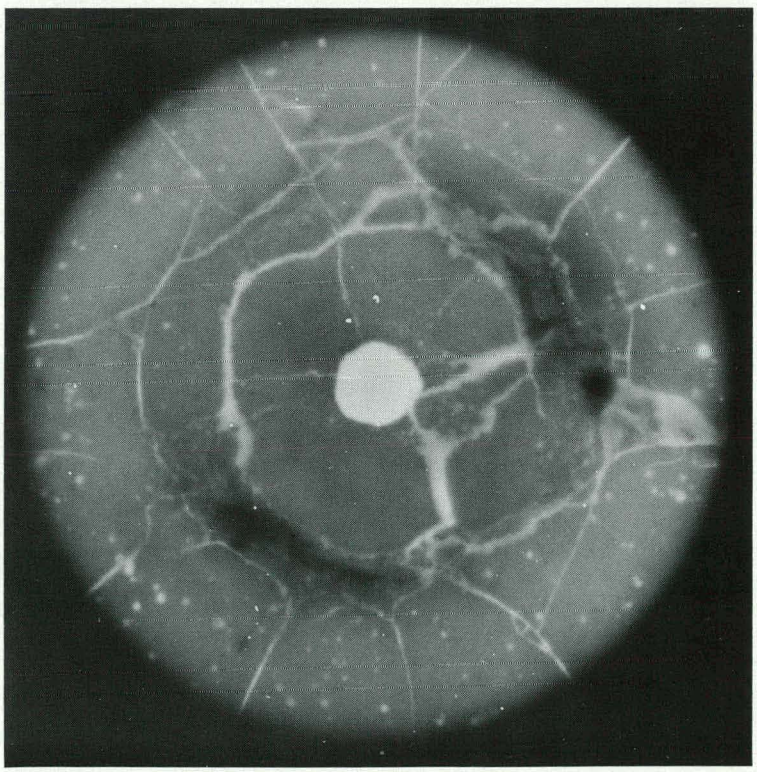

Fig. 199, β/γ-auto., etched X 10

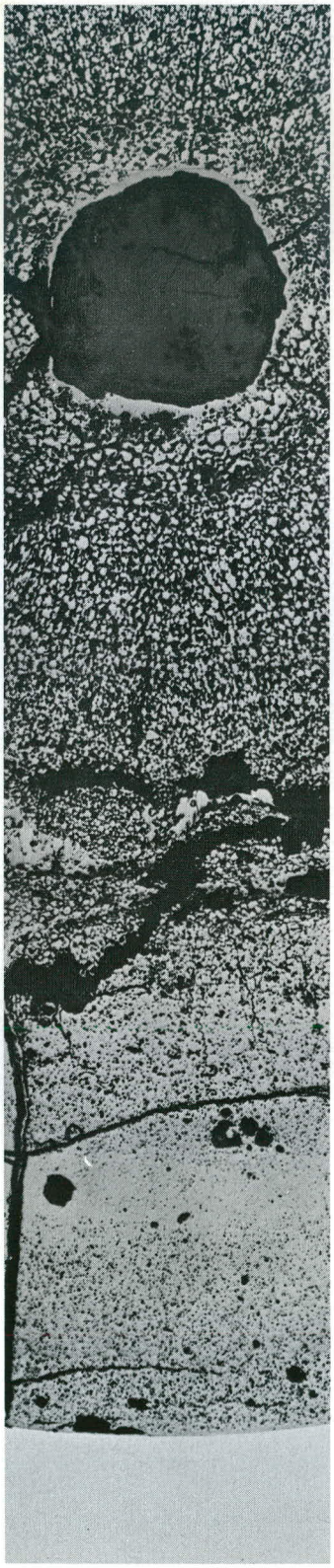

Fig. 200, polished, X 30

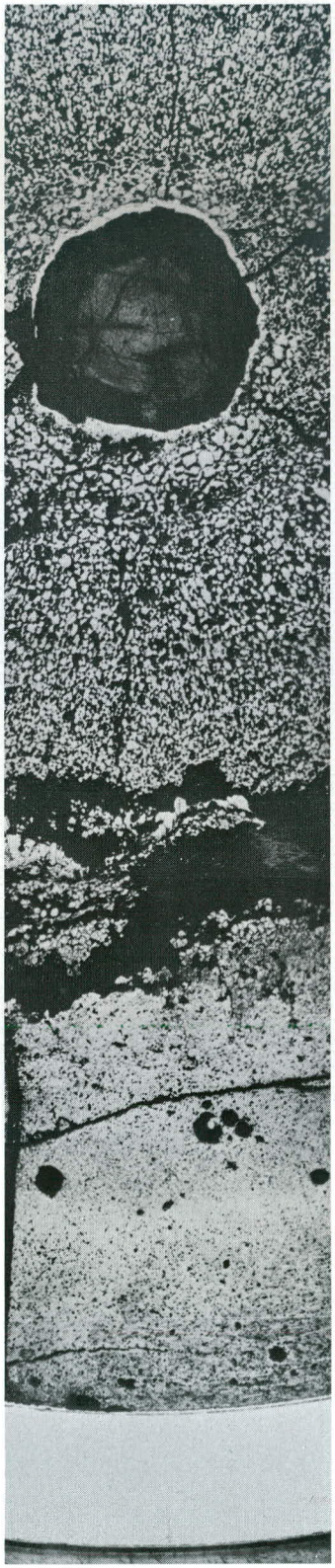

Fig. 201, etched, X 30

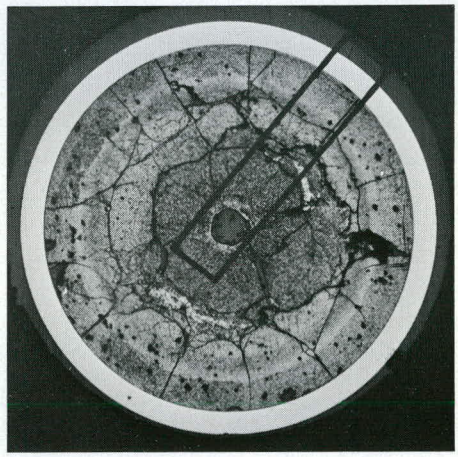

Fig. 200
Fig. 201

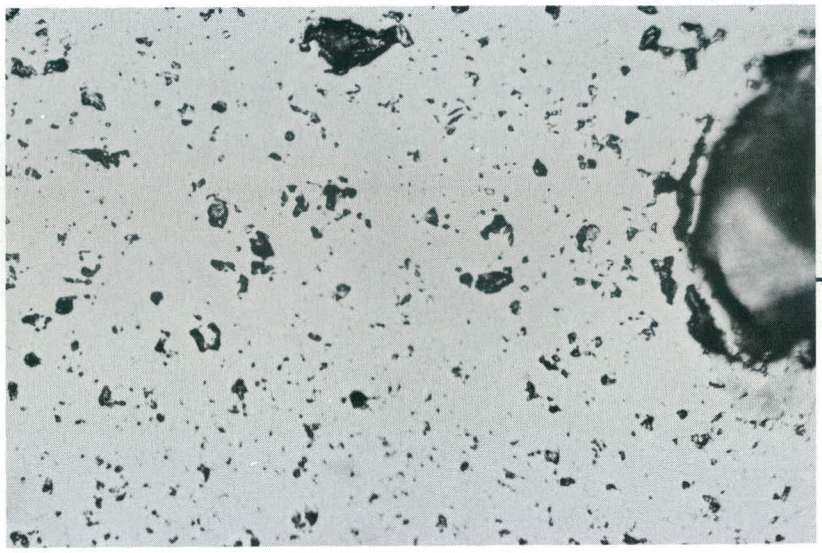

Fig 2o2 Polished, X 4oo

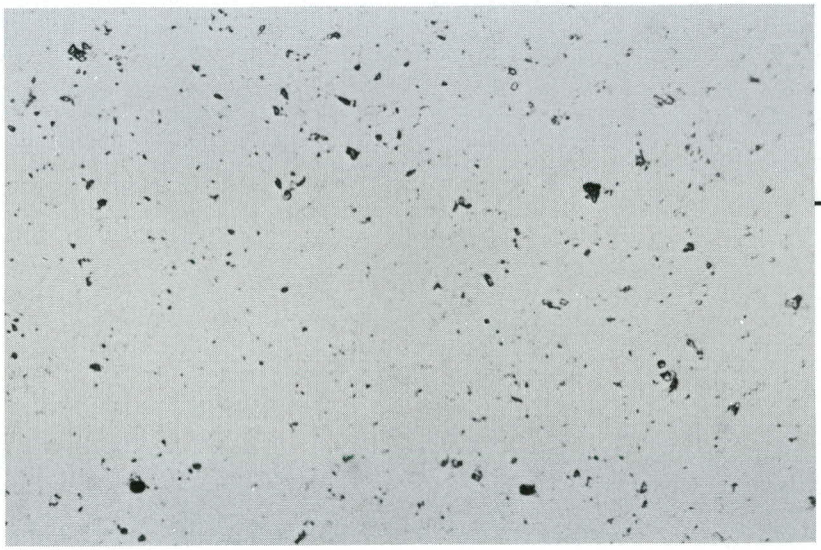

Fig. 2o3 Polished, X 4oo

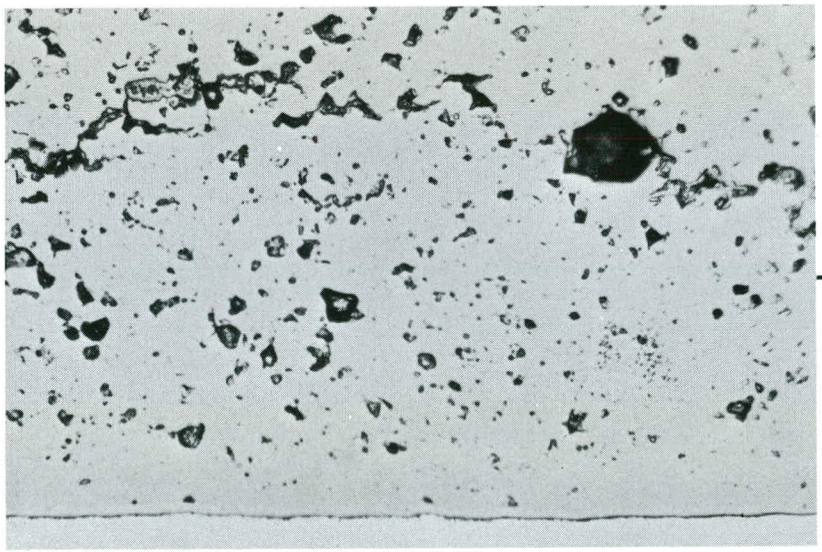

Fig. 2o4 Polished, X 4oo

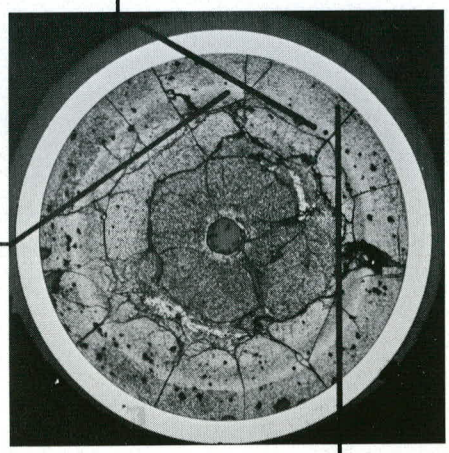

Sample 11-3

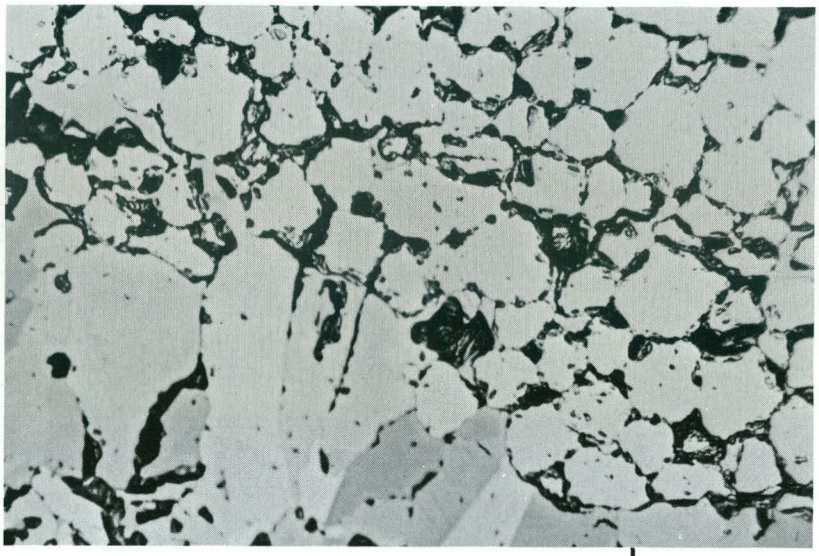

Fig. 2o5 Polished, X 4oo

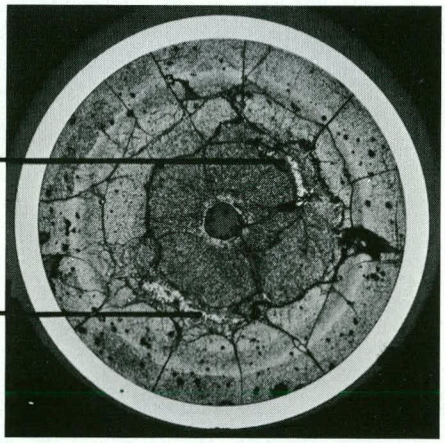

Fig. 2o6 Polished, pol. light, X 4oo

Sample 11-3

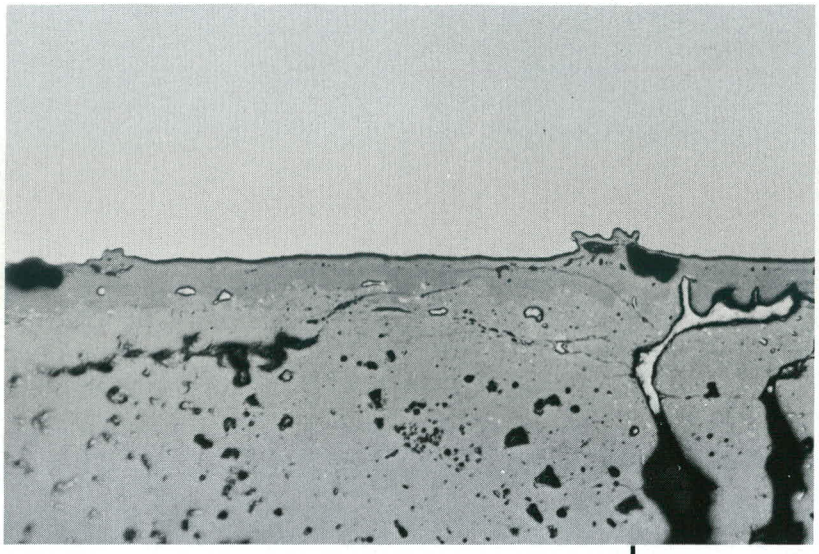

Fig. 2o7 Polished, X 4oo

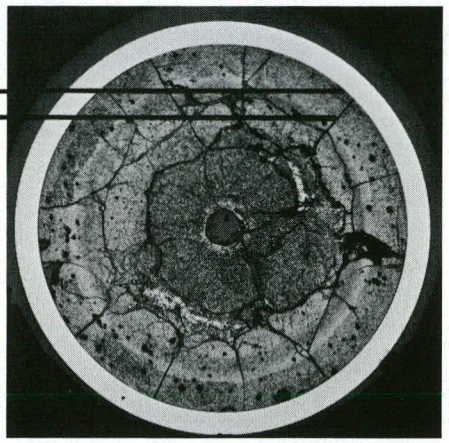

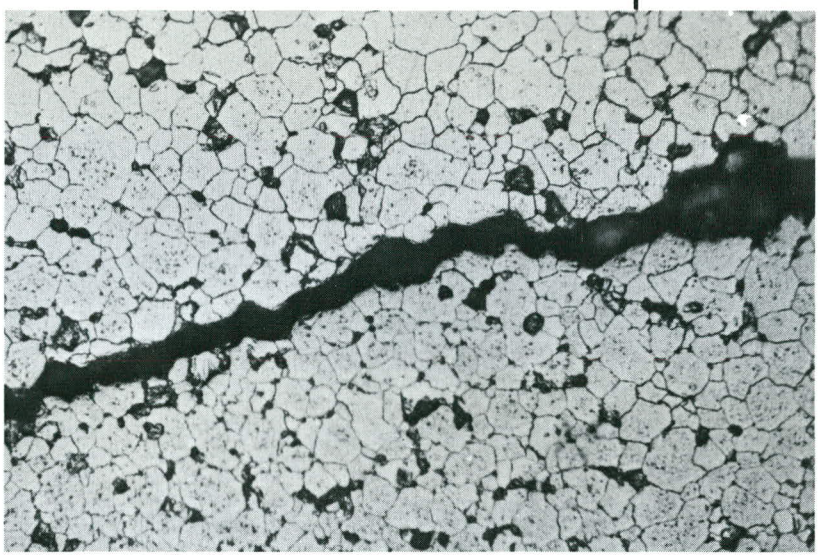

Fig. 2o8 Etched, X 4oo

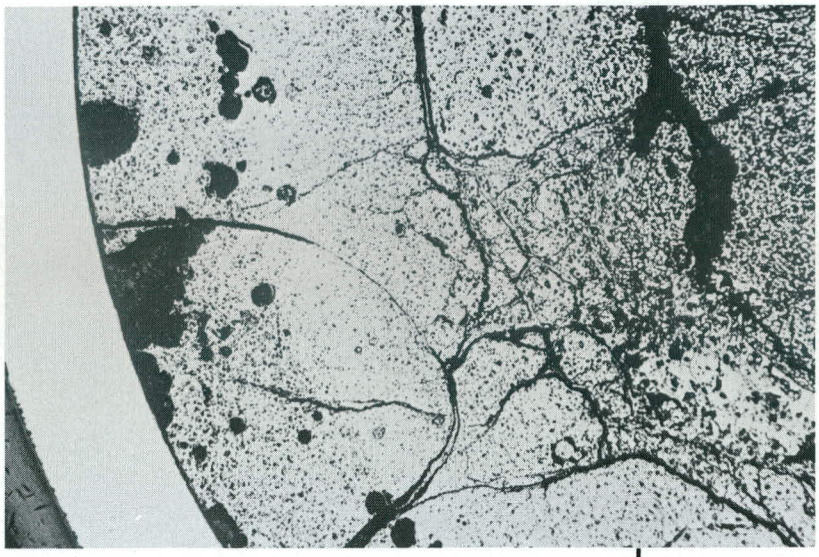

Fig. 2o9 Polished, X 3o

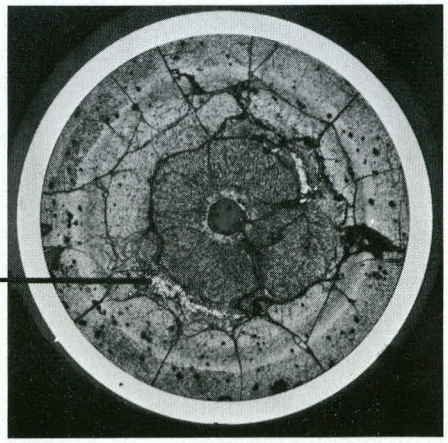

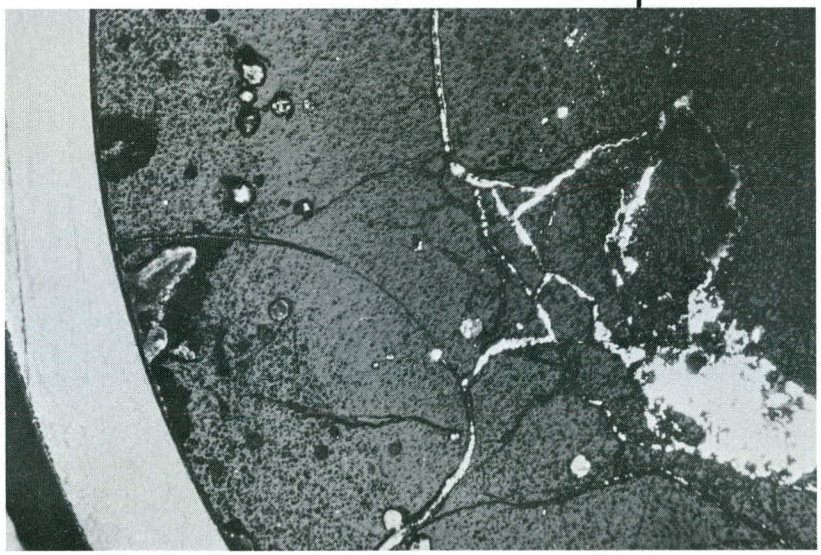

Fig. 21o Polished, pol. light, X 3o
same area as in fig. 2o9.

Sample 11-6-A

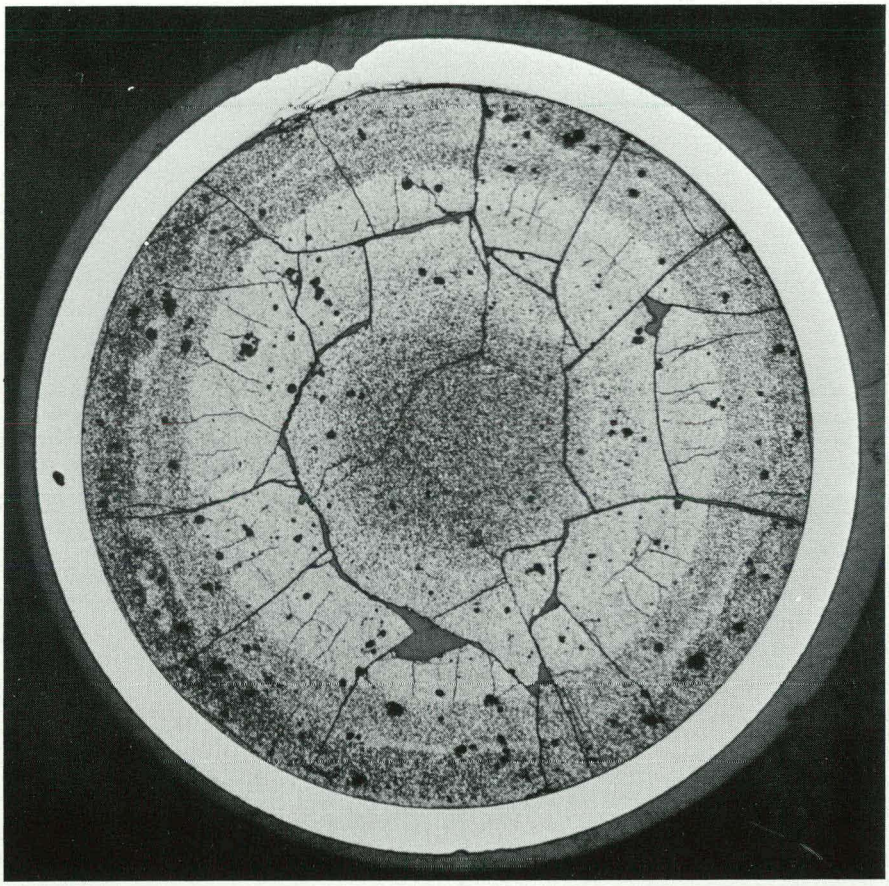

Fig. 211 X 10

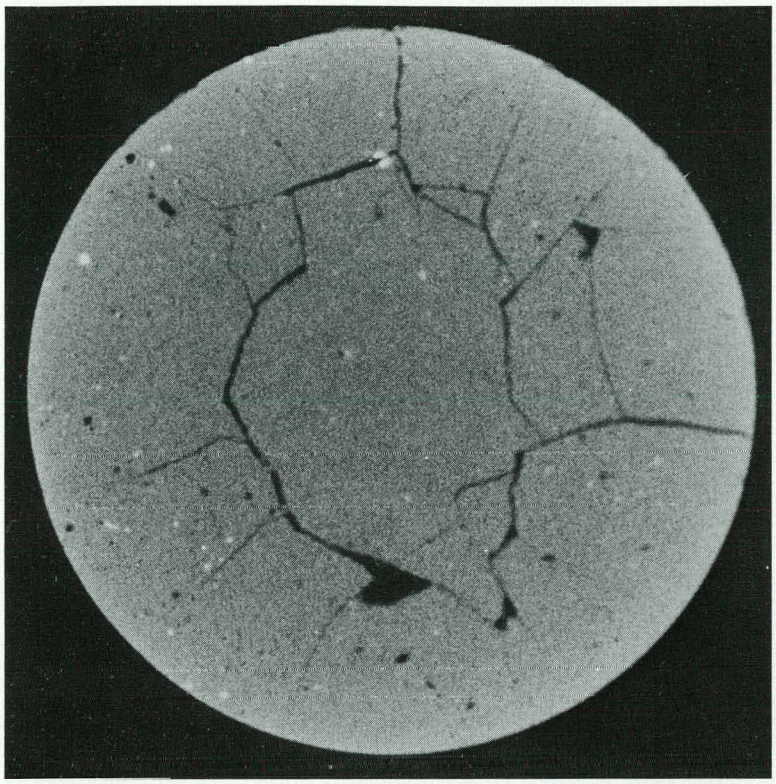

Fig. 212, α-auto., polished X 10

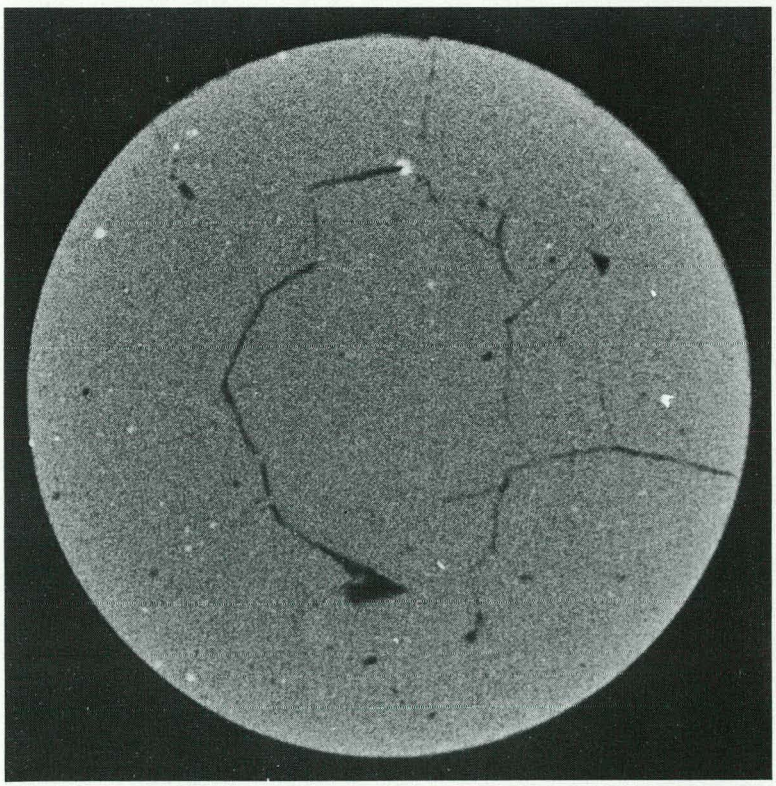

Fig. 213, α-auto, etched X 10

Sample 11-6-A

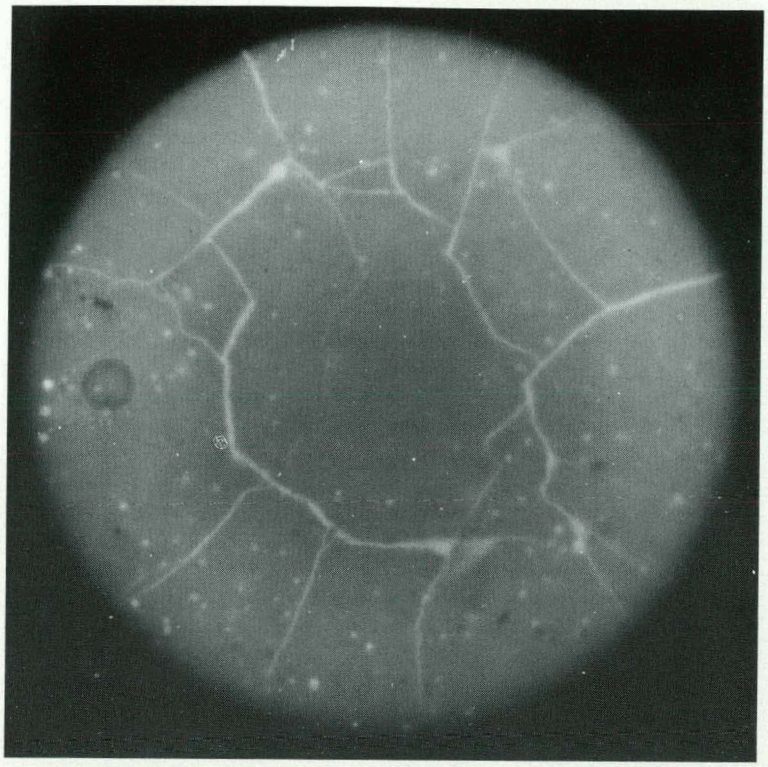

Fig. 214, β/γ-auto., polished X 10

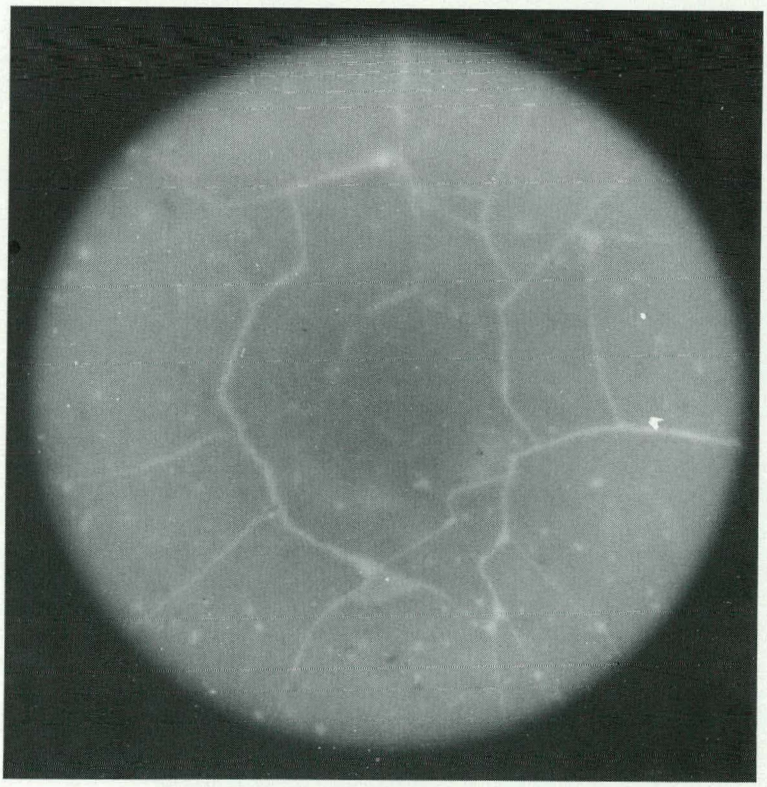

Fig. 215, β/γ-auto., etched X 10

Sample 11-6-A

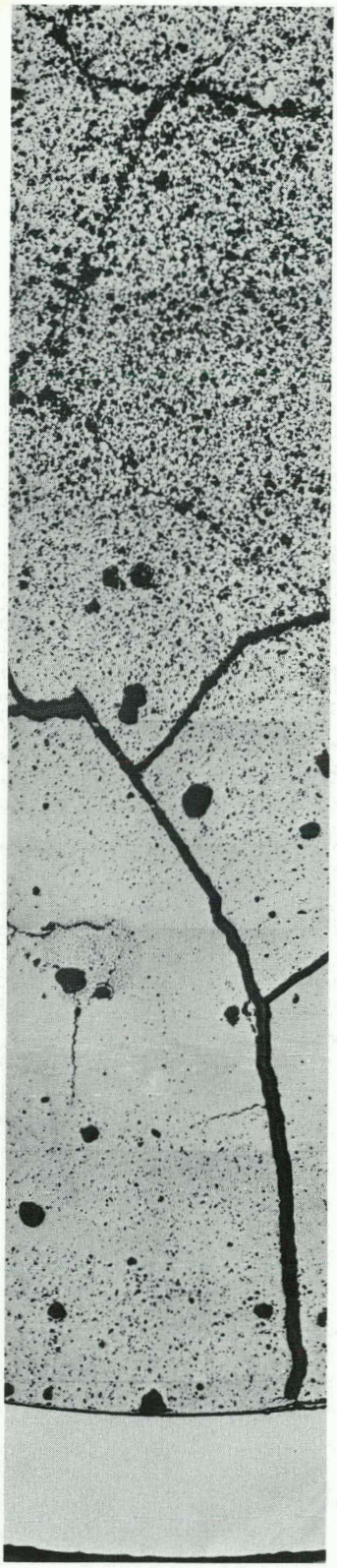

Fig. 216, polished, X 30

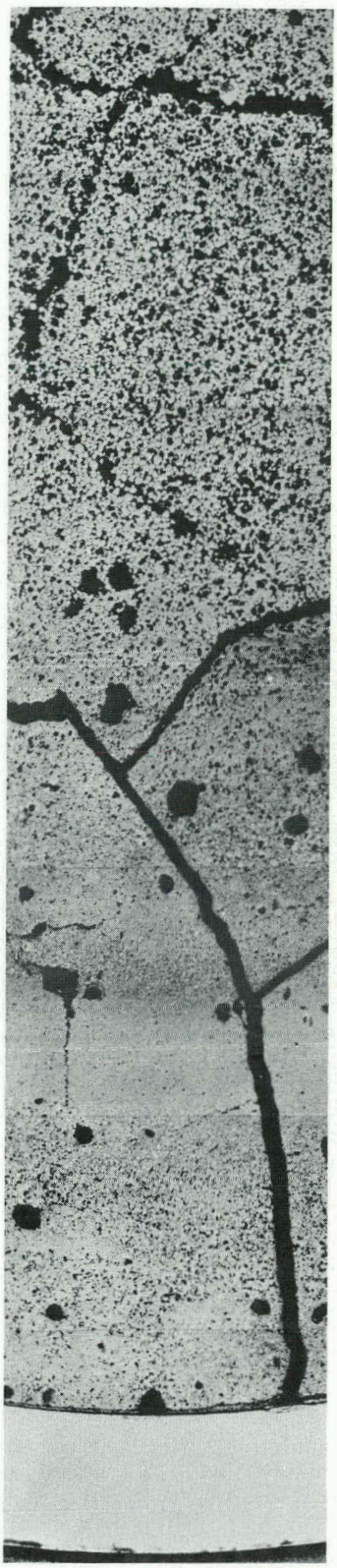

Fig. 217, etched, X 30

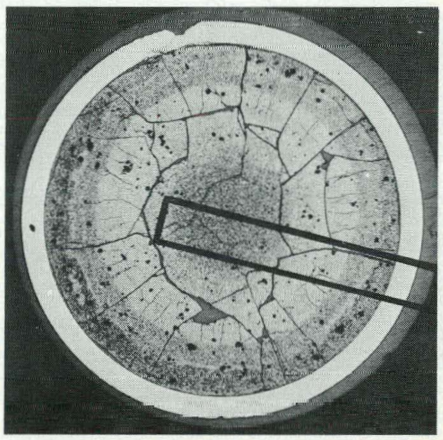

Fig. 216
Fig. 217

Sample 11-6-A

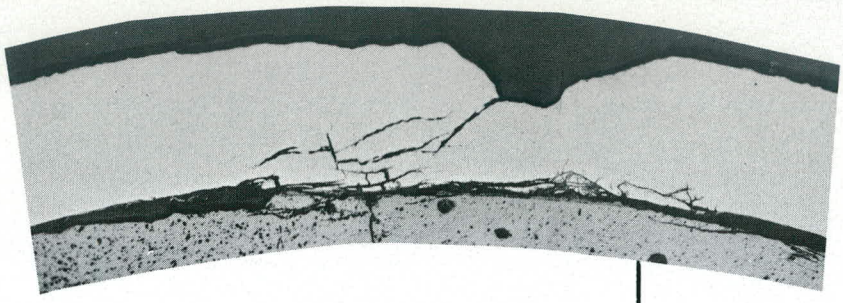

Fig. 218 Polished, X 30

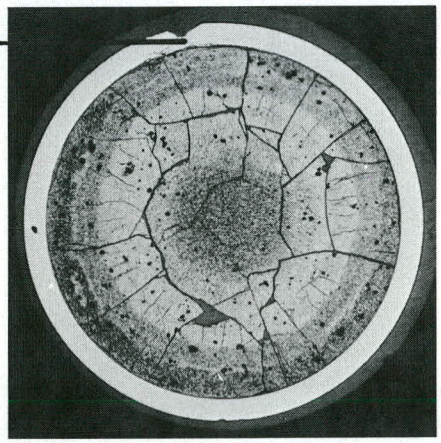

Fig. 219 Etched, X 30

Sample 11-6-A

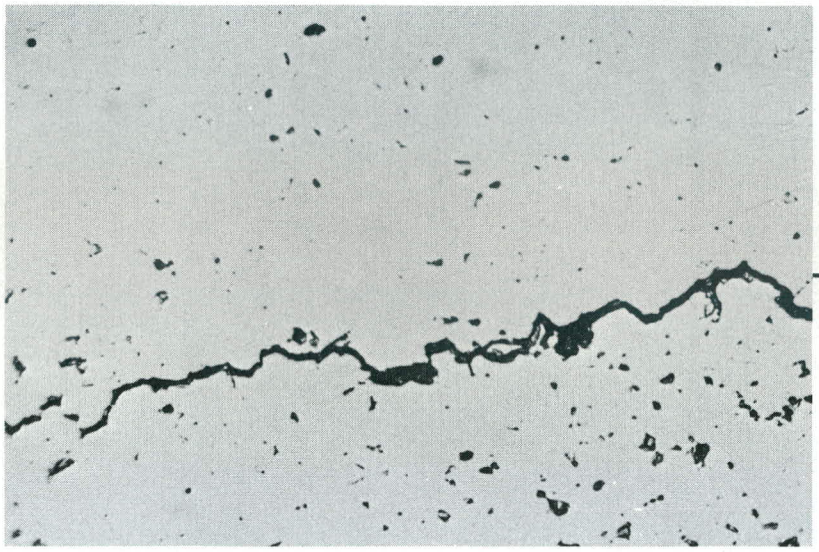

Fig. 220 Polished, X 400

Fig. 221 Polished, X 400

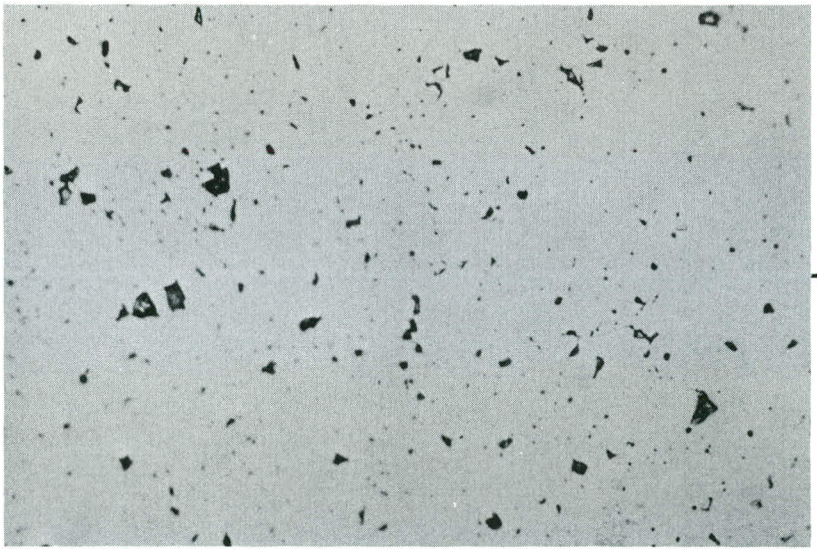

Fig. 222 Polished, X 400

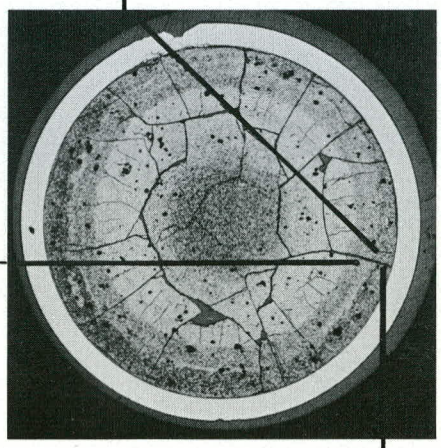

Sample 11-6-A

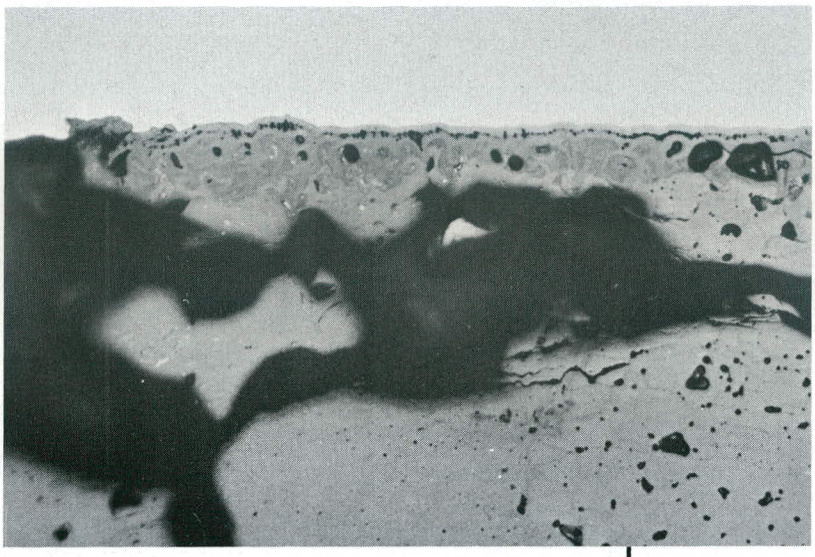

Fig. 223 Polished, X 400

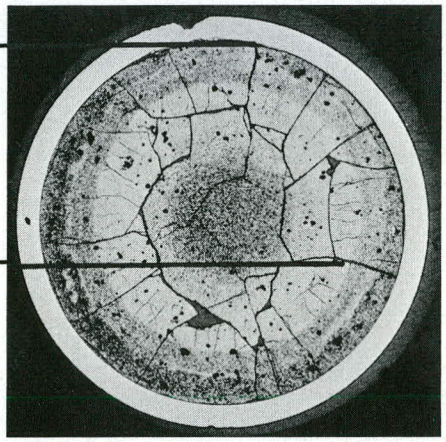

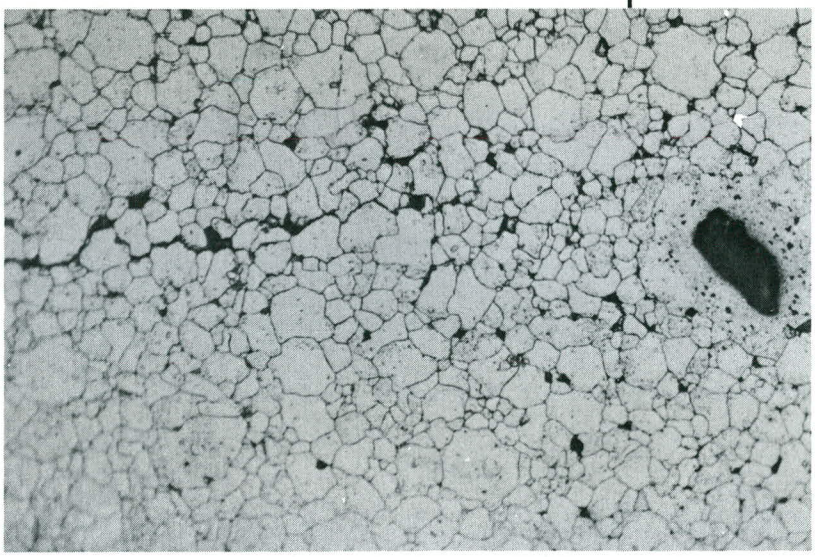

Fig. 224 Etched, X 400

Sample 11-6-A

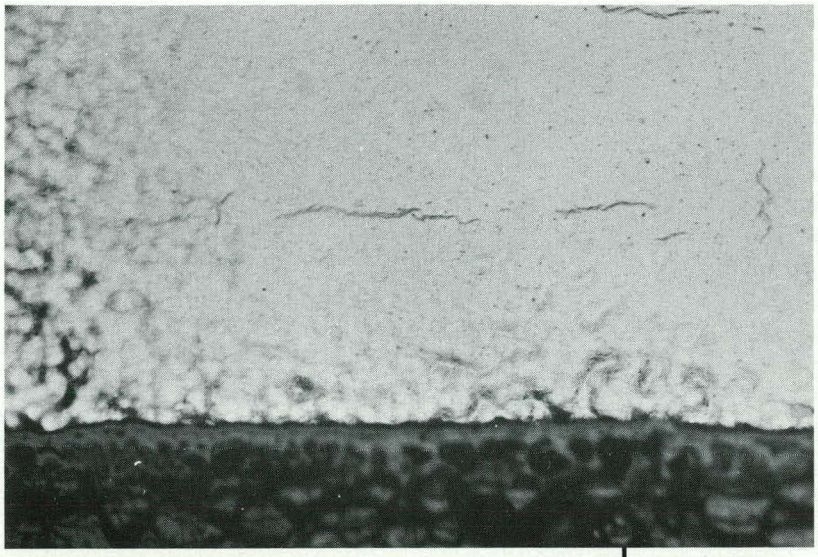

Fig. 225 Etched, X 400

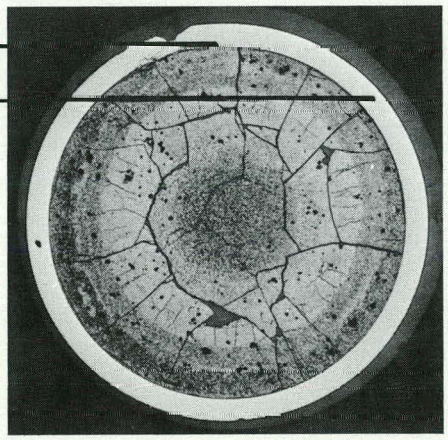

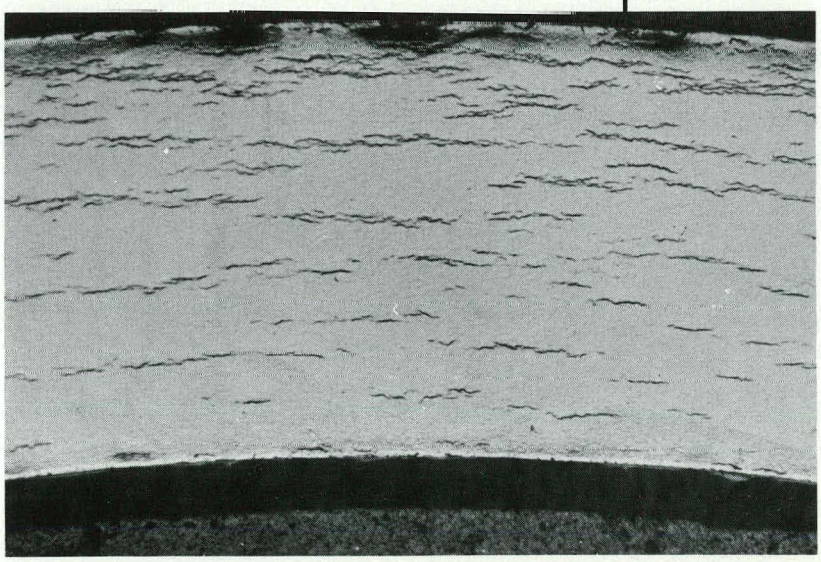

Fig. 226 Etched, X 100

Sample 11-6-A

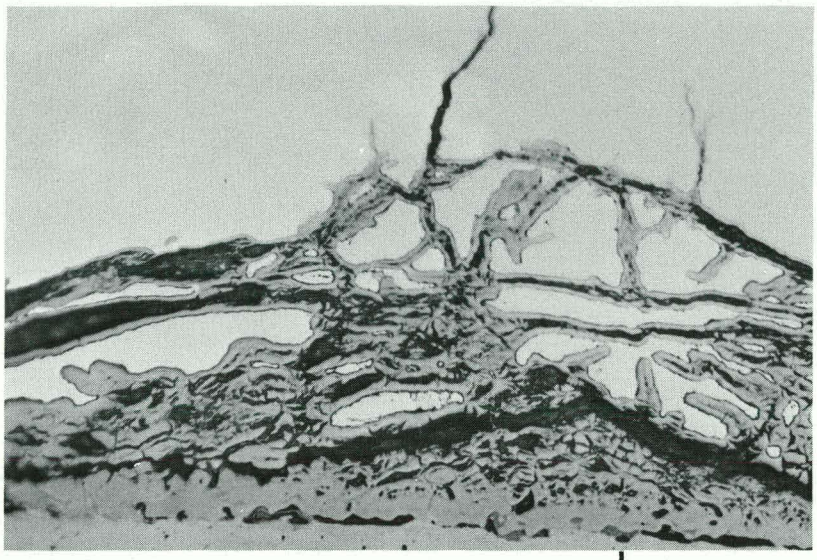

Fig. 227 Polished, X 400

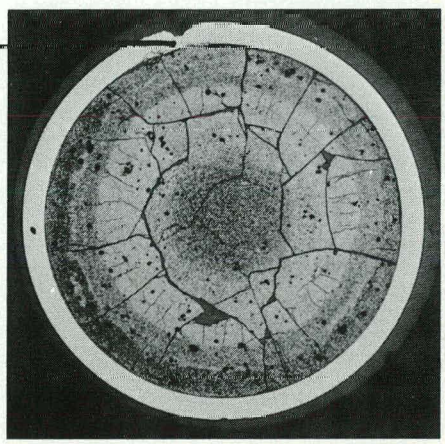

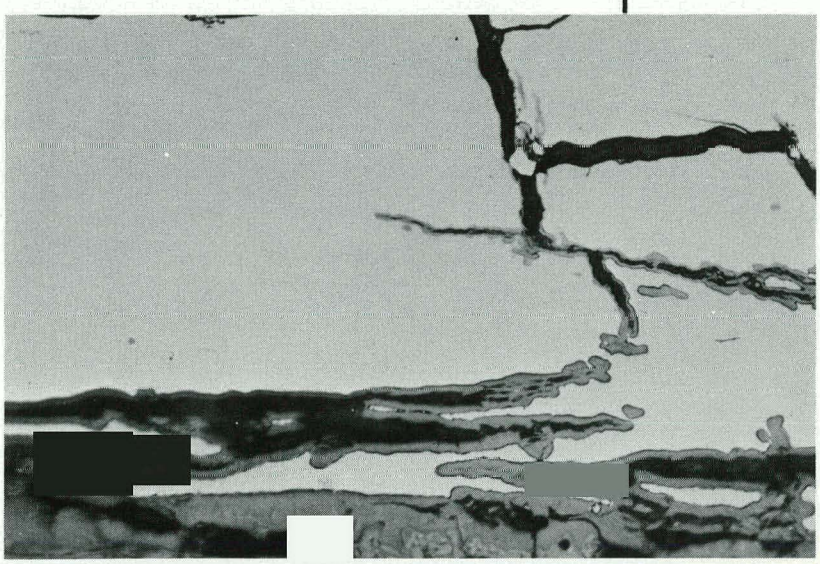

Fig. 228 Polished, X 400

Sample 11-6-1

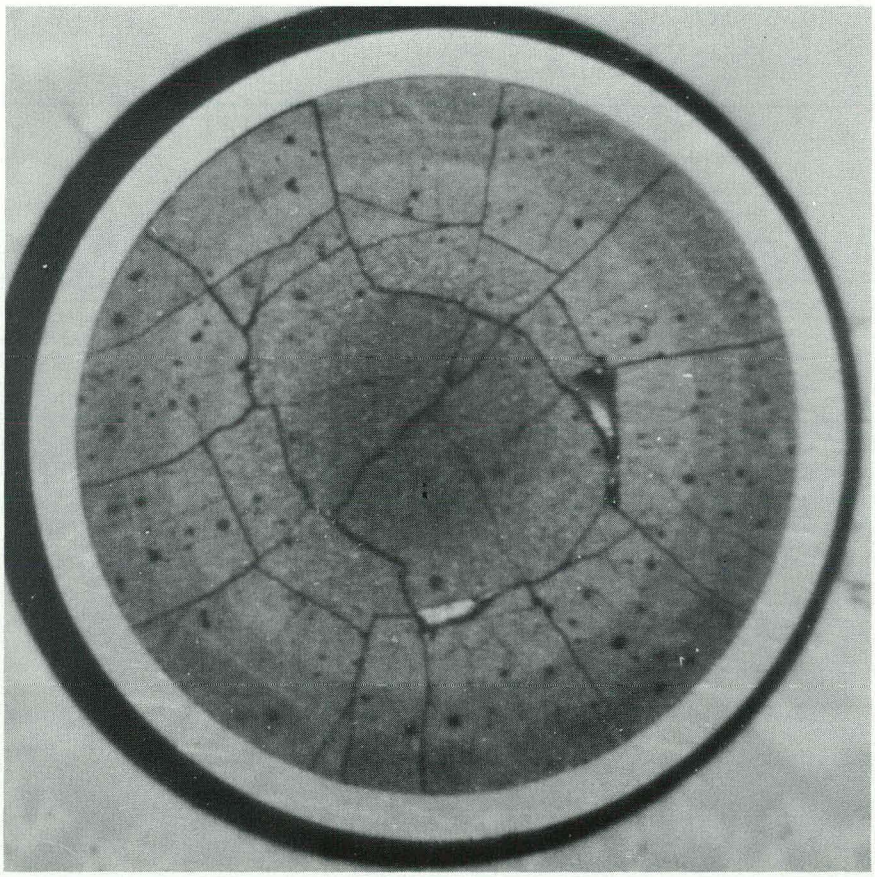

Fig. 229 X 10

Sample 11-6-1

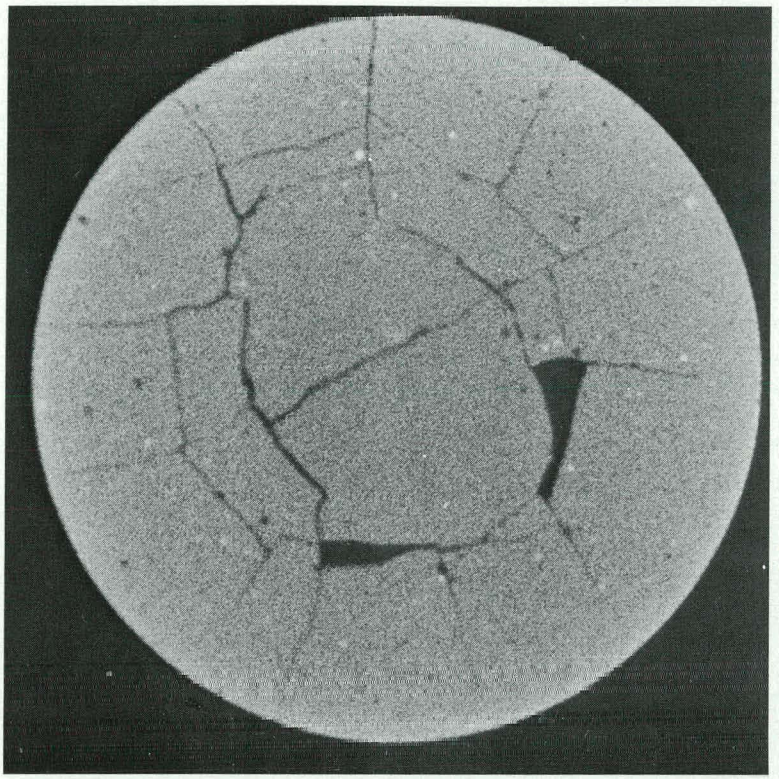

Fig. 230, α-auto., polished X 10

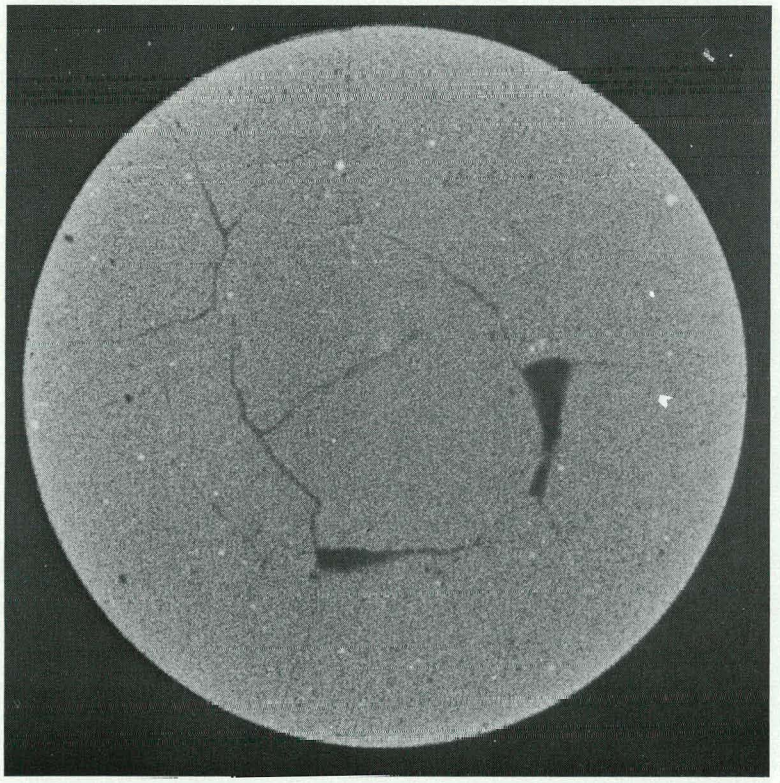

Fig. 231, α auto., etched X 10

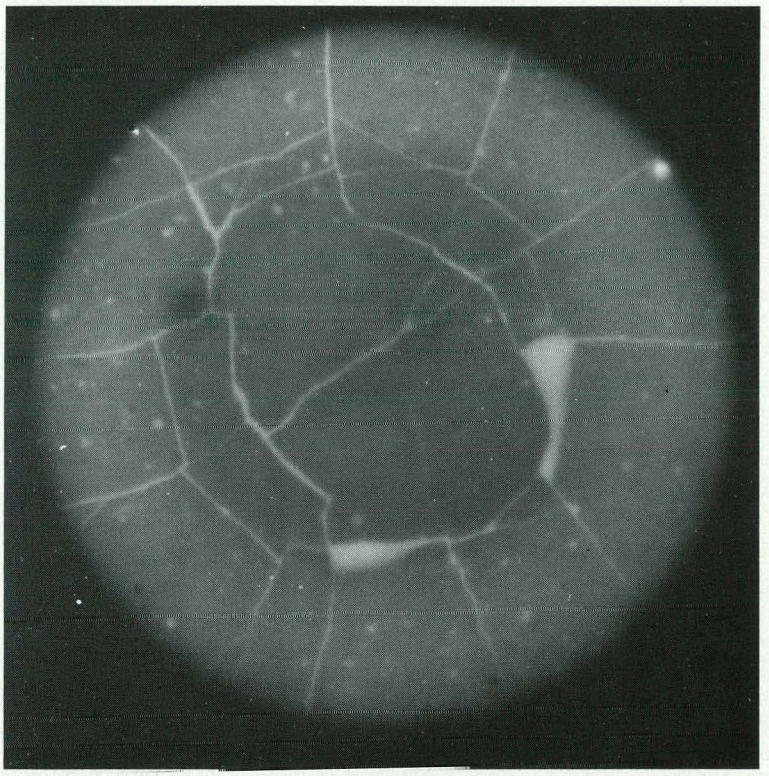

Fig. 232, β/γ-auto., polished X 10

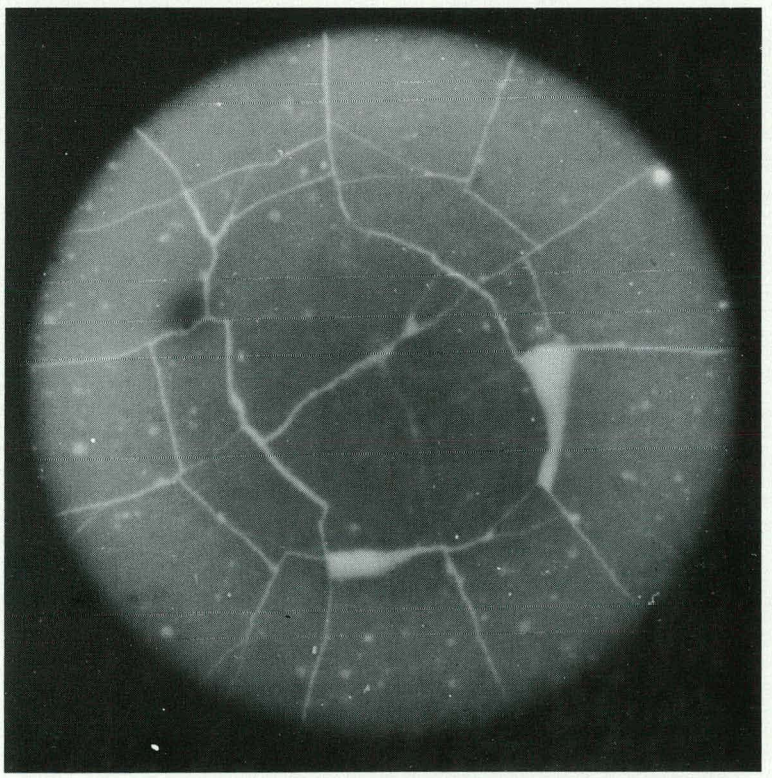

Fig. 233, β/γ-auto., etched X 10

Sample 11-6-1

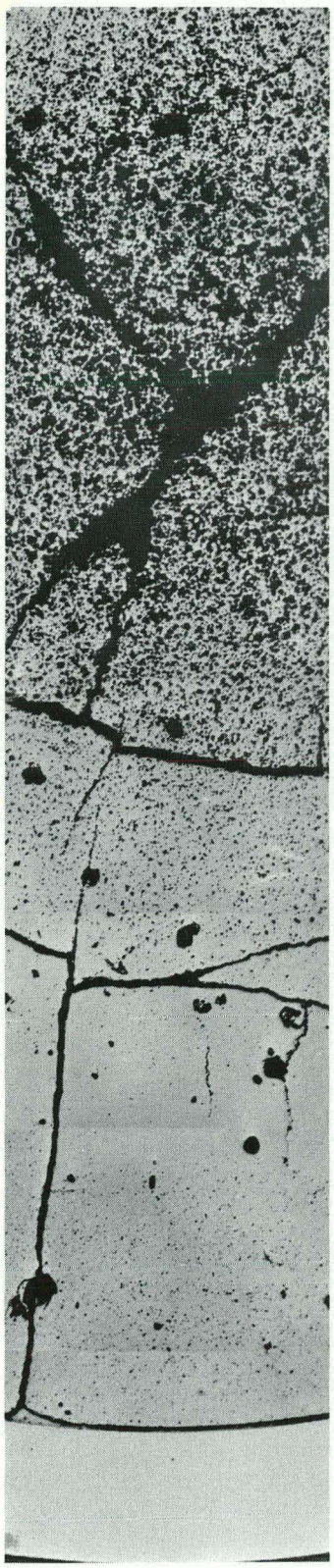

Fig. 234, polished, X 30

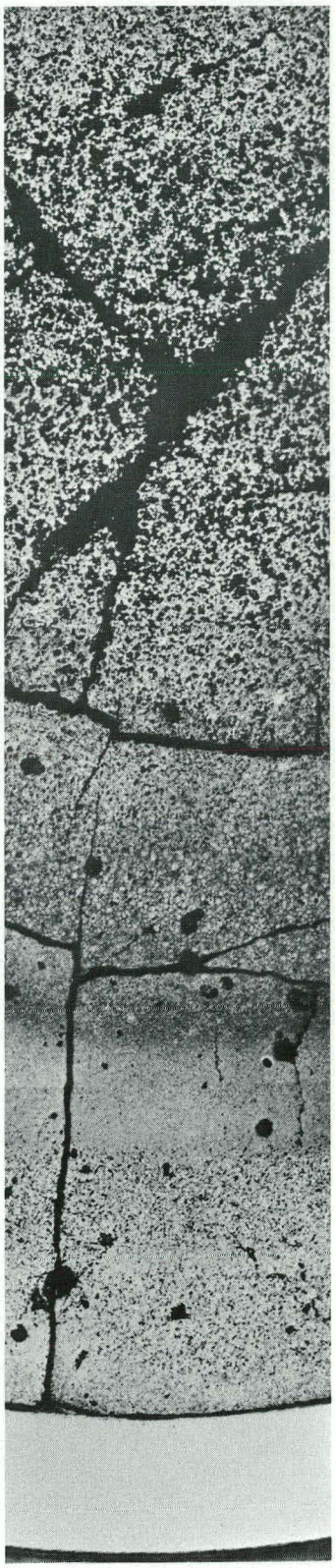

Fig. 235, etched, X 30

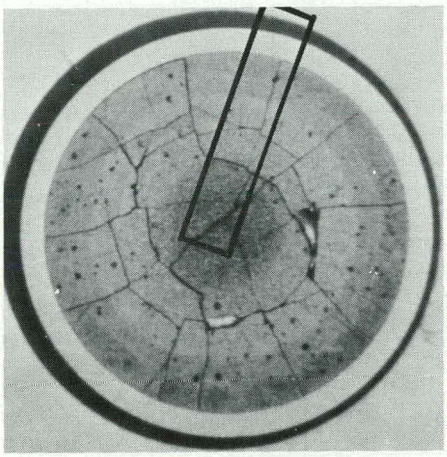

Fig. 234
Fig. 235

Sample 11-6-1

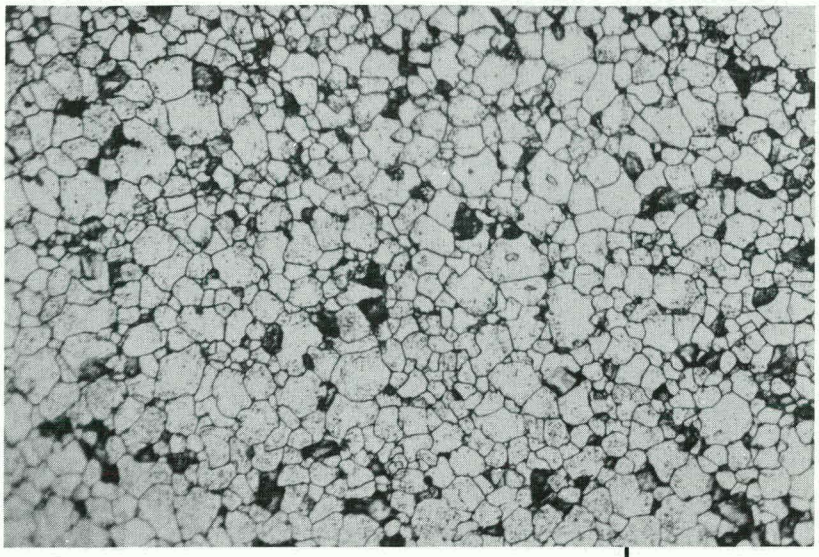

Fig. 236 Etched, X 400

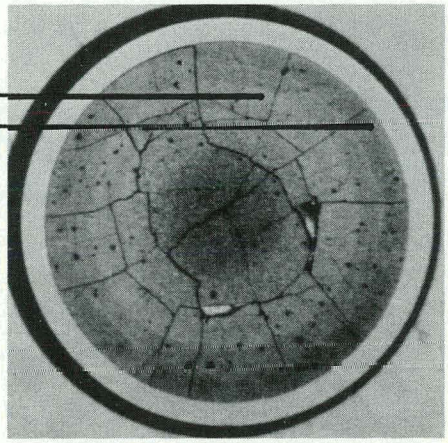

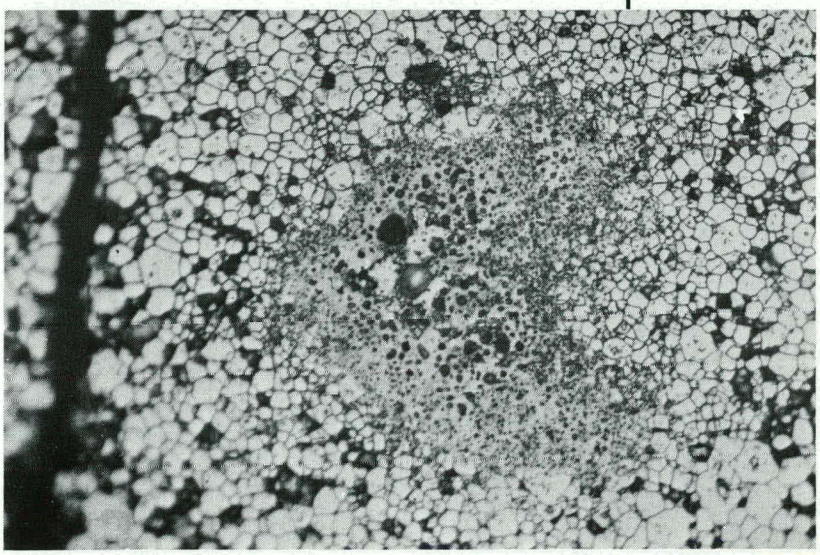

Fig. 237 Etched, X 400

Sample 11-6-1

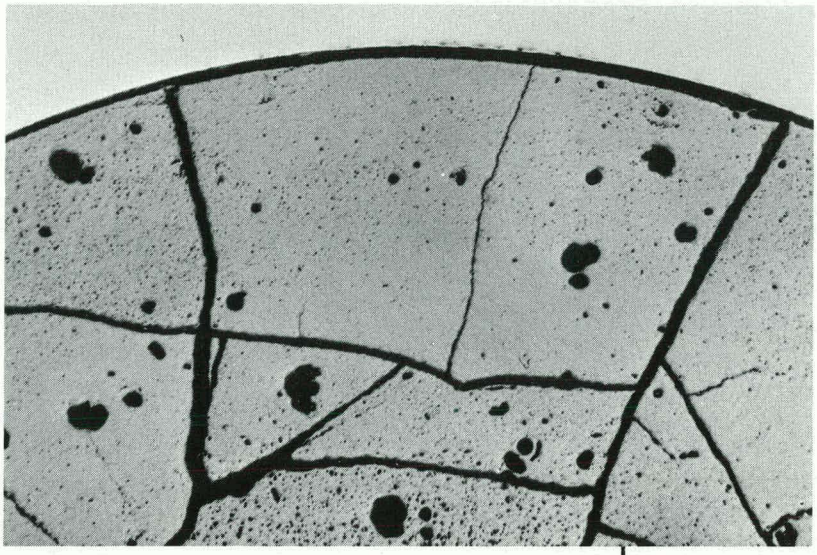

Fig. 238 Polished, X 3o

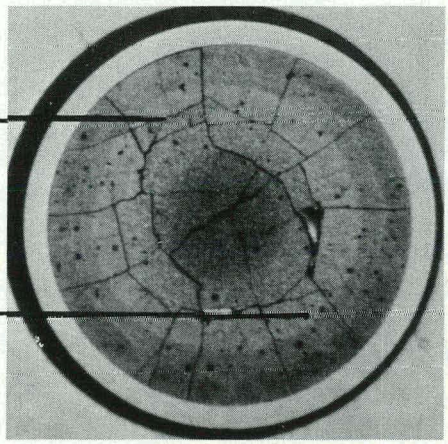

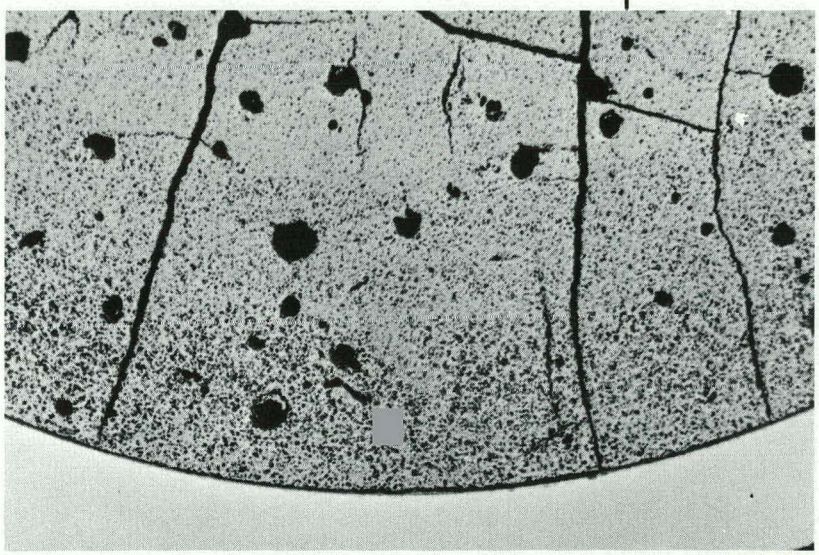

Fig. 239 Polished, X 3o

Sample 11-6-1

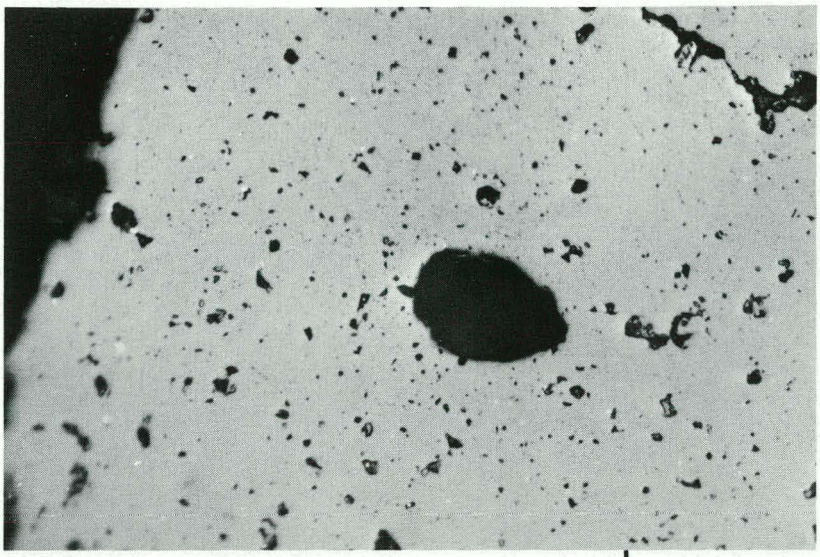

Fig. 24o Polished, X 4oo

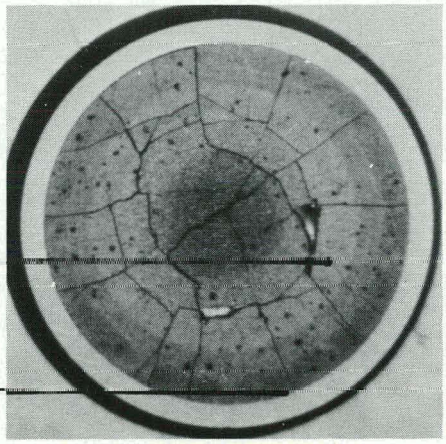

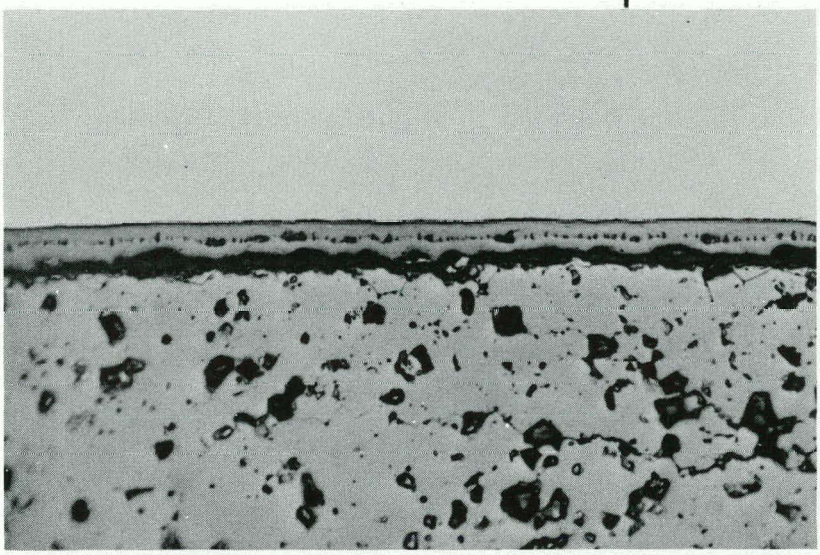

Fig. 241 Polished, X 4oo

Sample 11-7

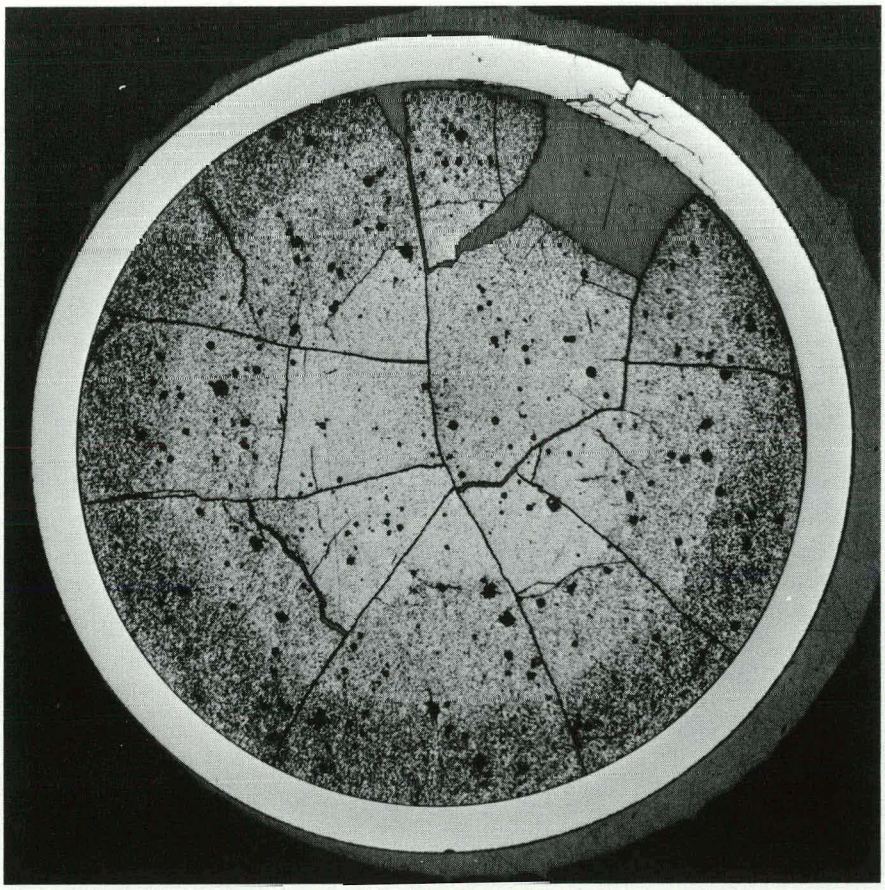

Fig. 242 X 10

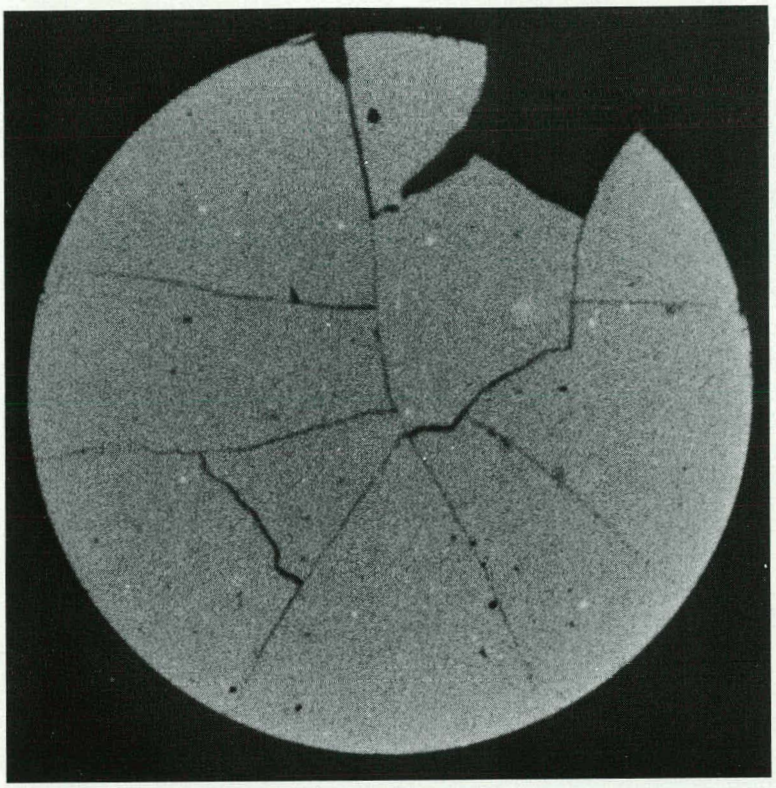

Fig. 243, α-auto., polished X 10

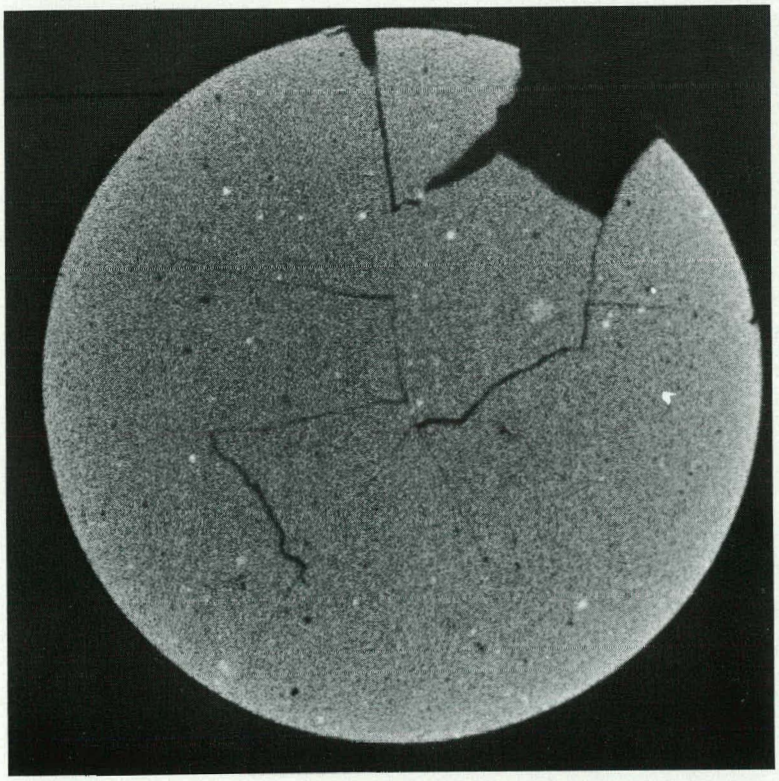

Fig. 244, α-auto., etched X 10

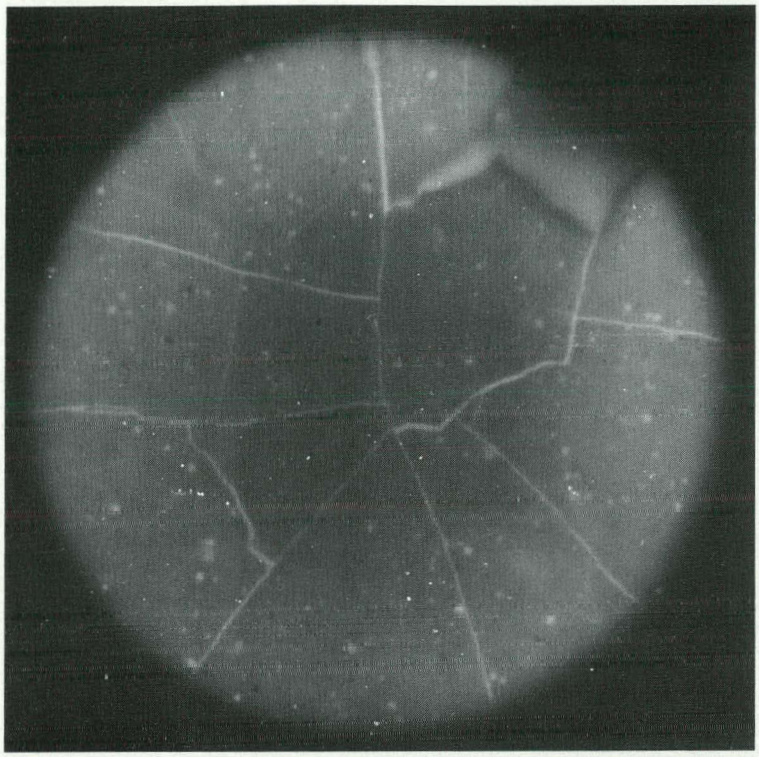

Fig. 245, β/γ-auto., polished X 10

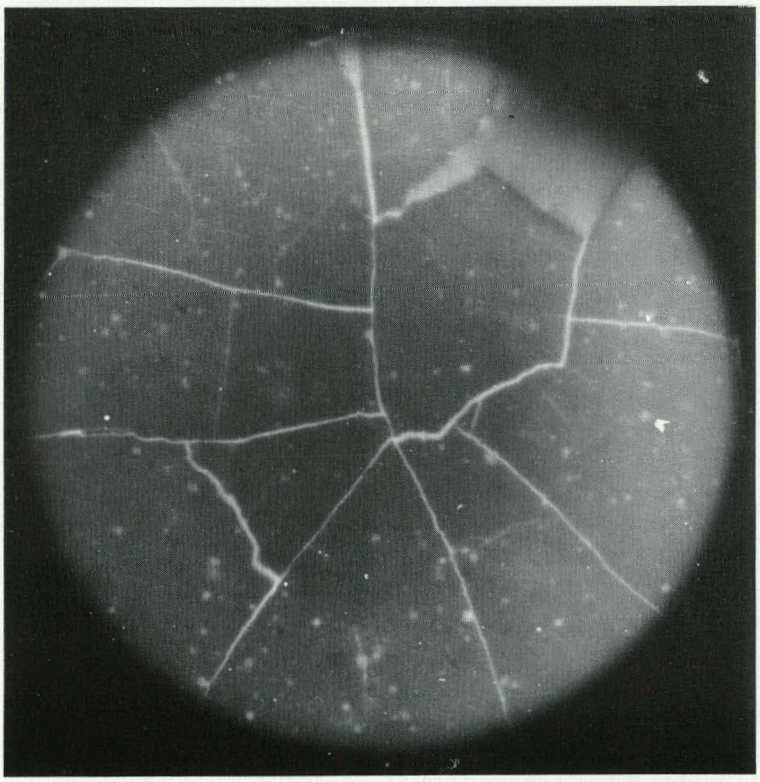

Fig. 246, β/γ-auto., etched X 10

Fig. 247, polished, X 30

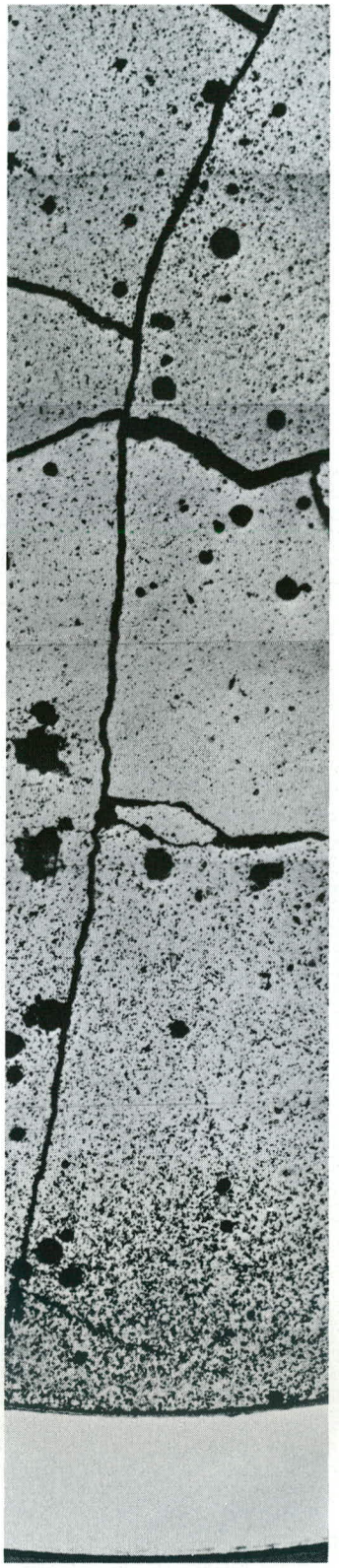

Fig. 248, etched, X 30

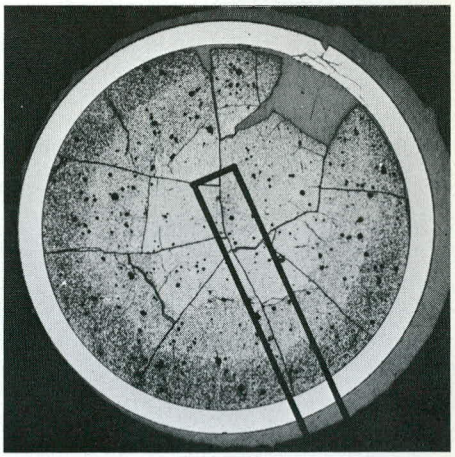

Fig. 247
Fig. 248

Sample 11-7

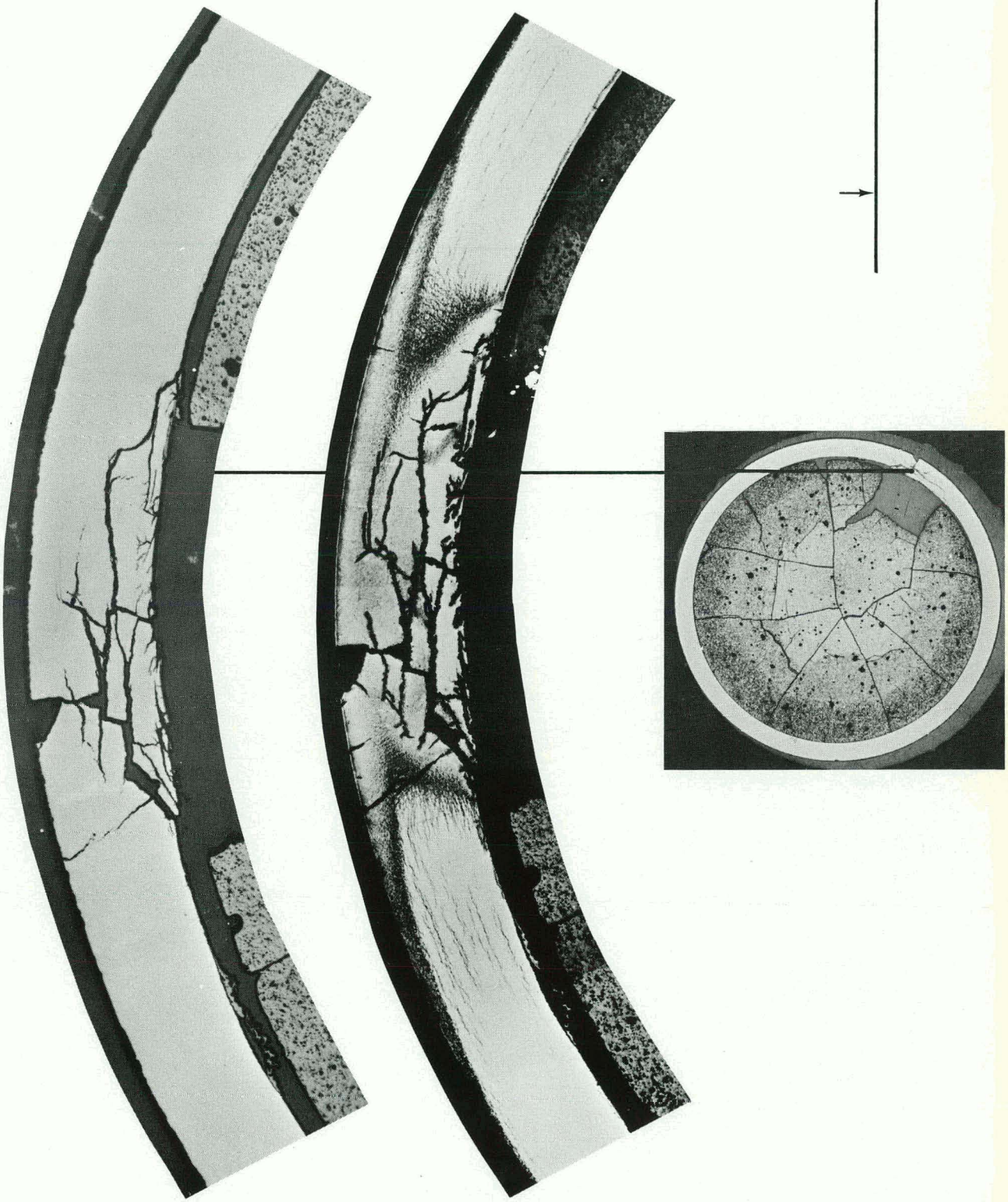

Fig. 249 Polished, X 3o

Fig. 25o Etched, X 3o

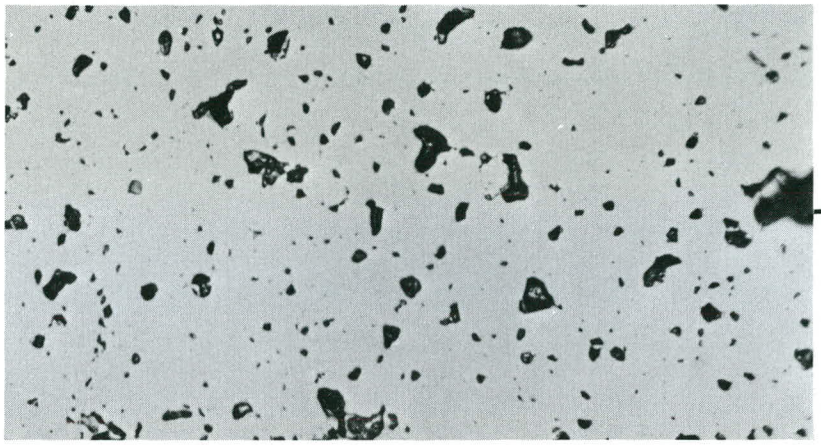

Fig. 251 Polished, X 4oo

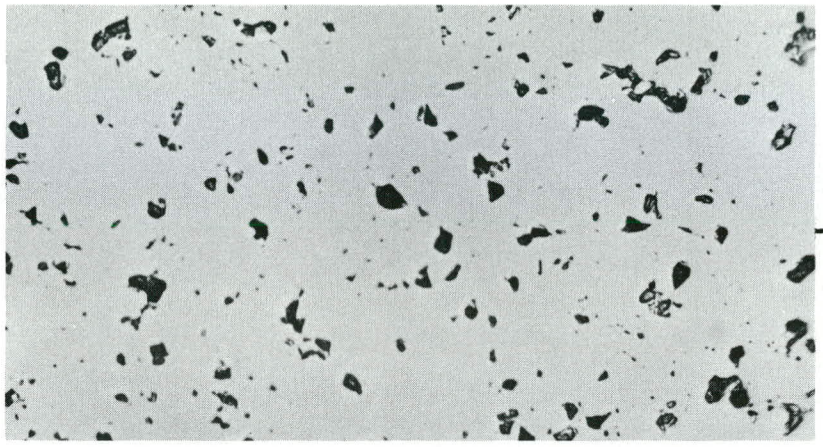

Fig. 252 Polished, X 4oo

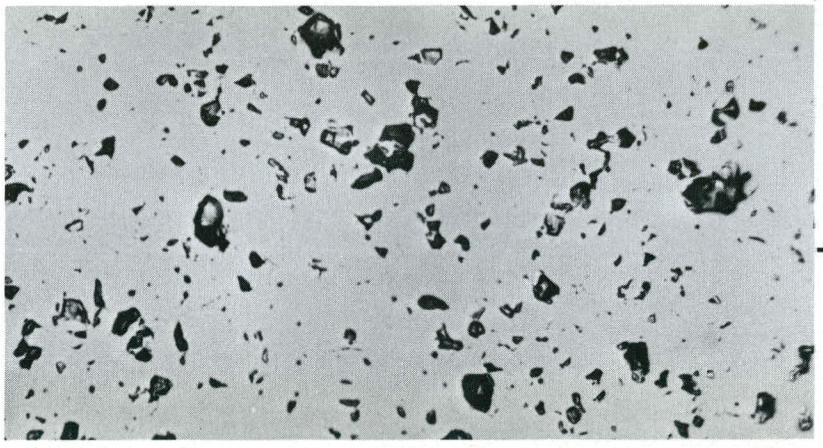

Fig. 253 Polished, X 4oo

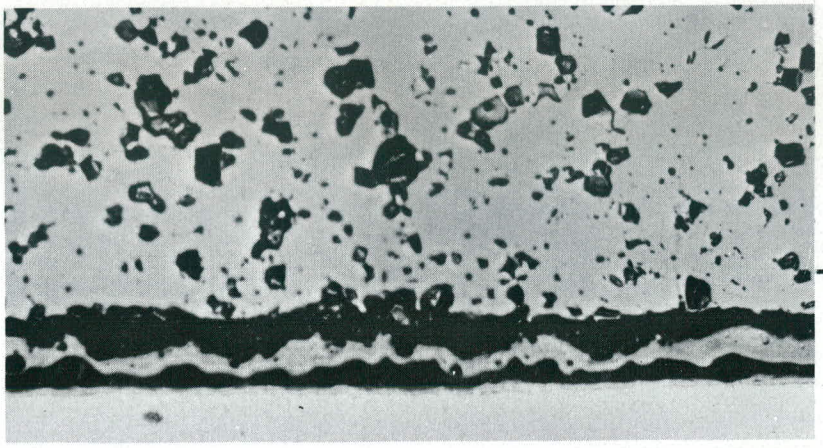

Fig. 254 Polished, X 4oo

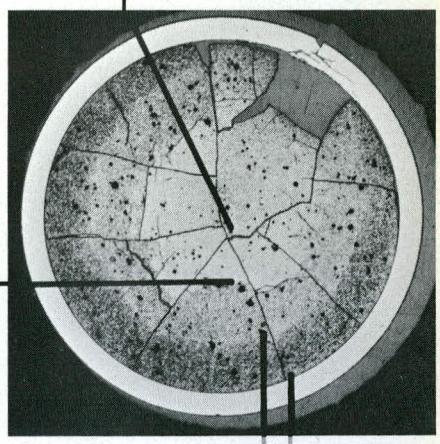

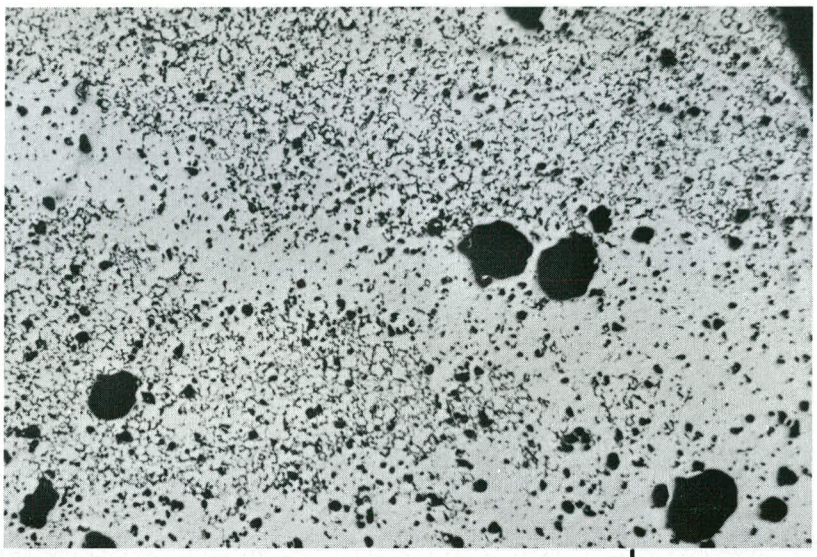

Fig. 255 Polished, X 400

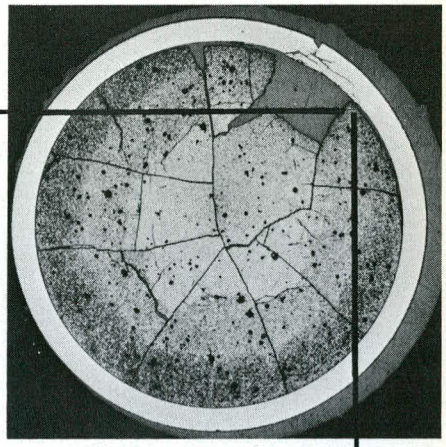

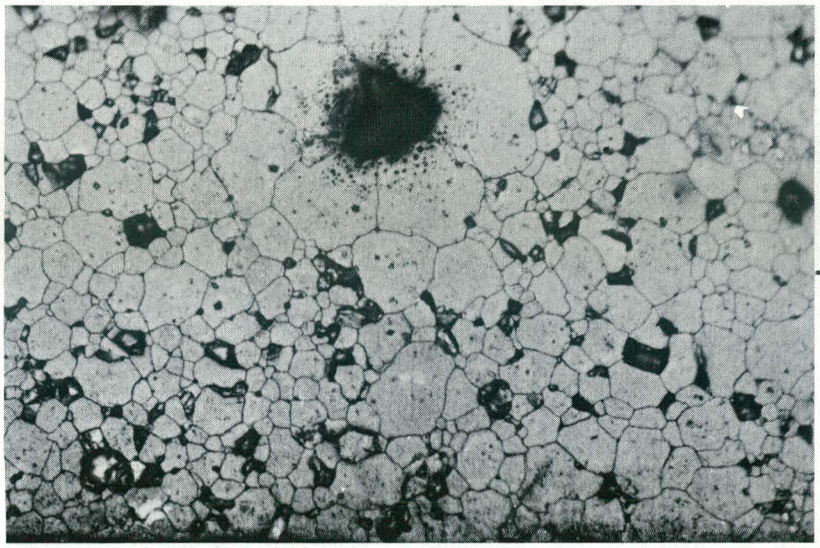

Fig. 256 Etched, X 400

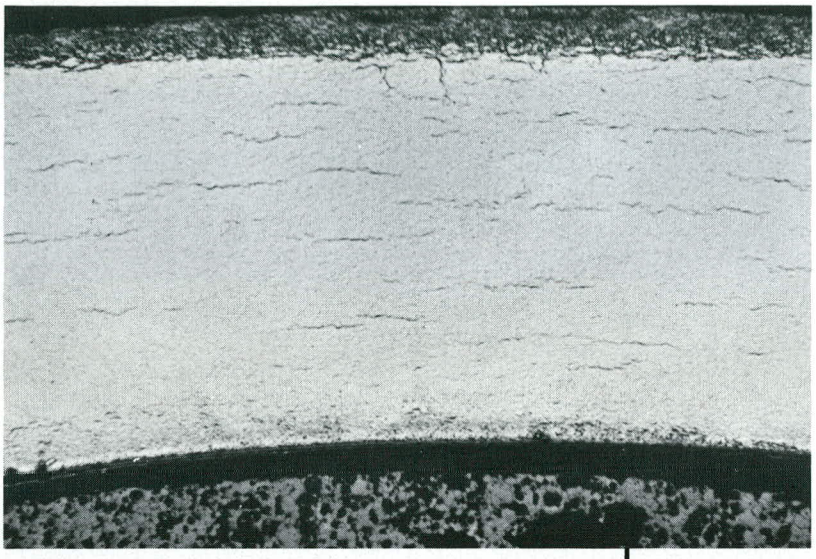

Fig. 257 Etched, X loo

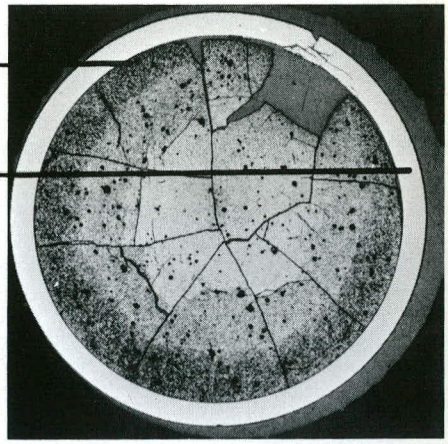

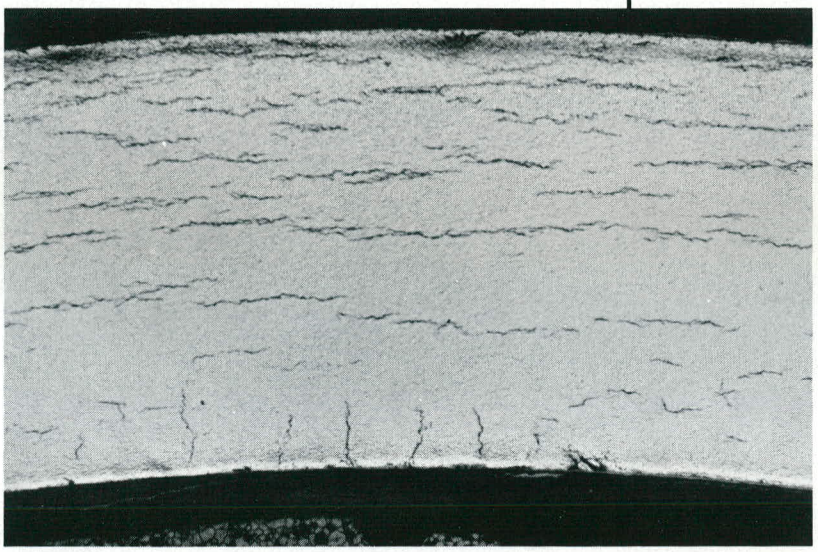

Fig. 258 Etched, X loo

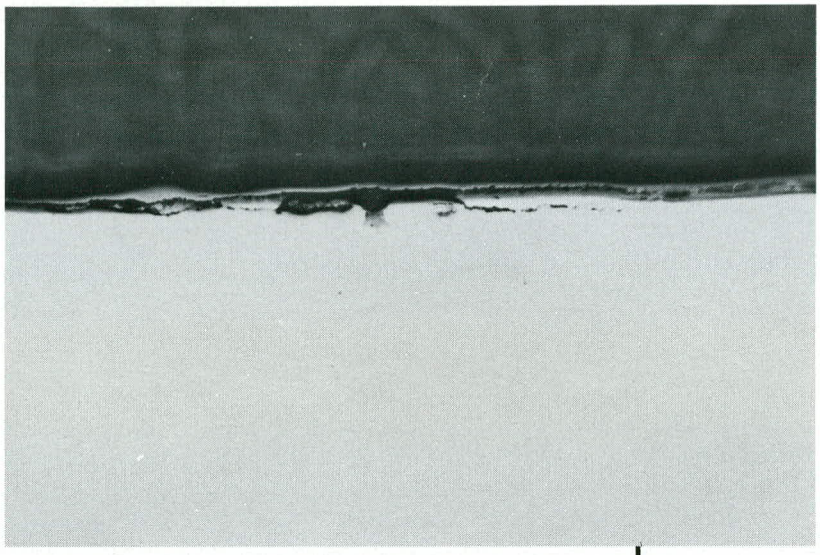

Fig. 259 Outer oxide layer, polished, X 4oo

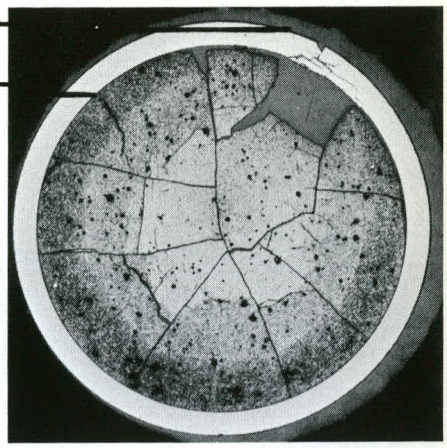

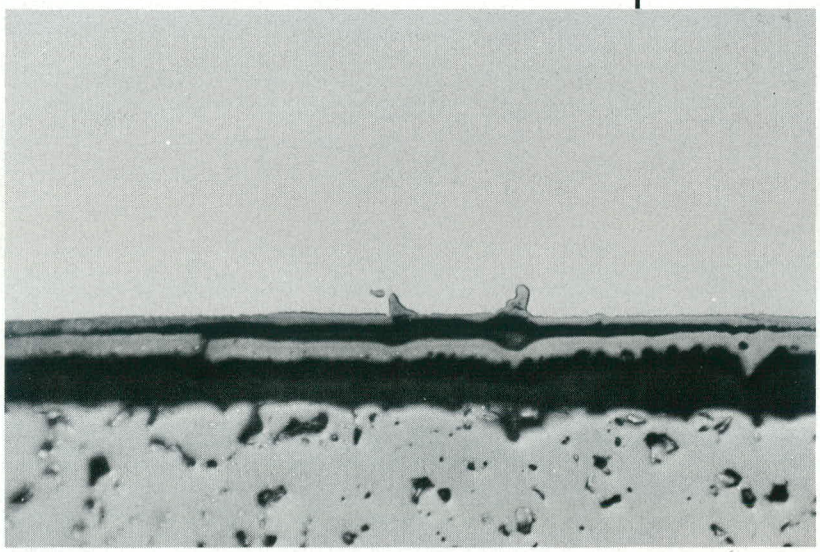

Fig. 26o Inner oxide layer , polished, X 4oo

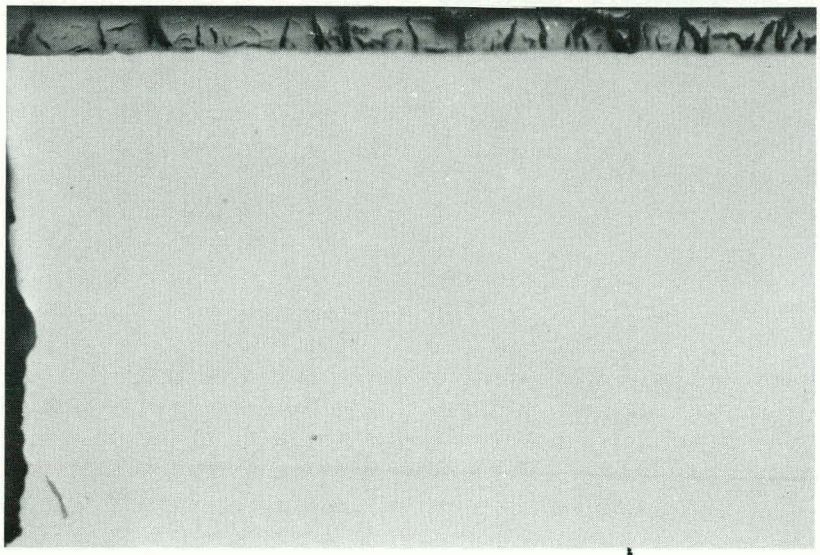

Fig. 261 Polished, X 4oo

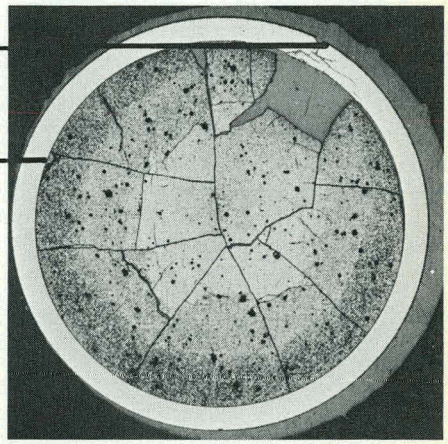

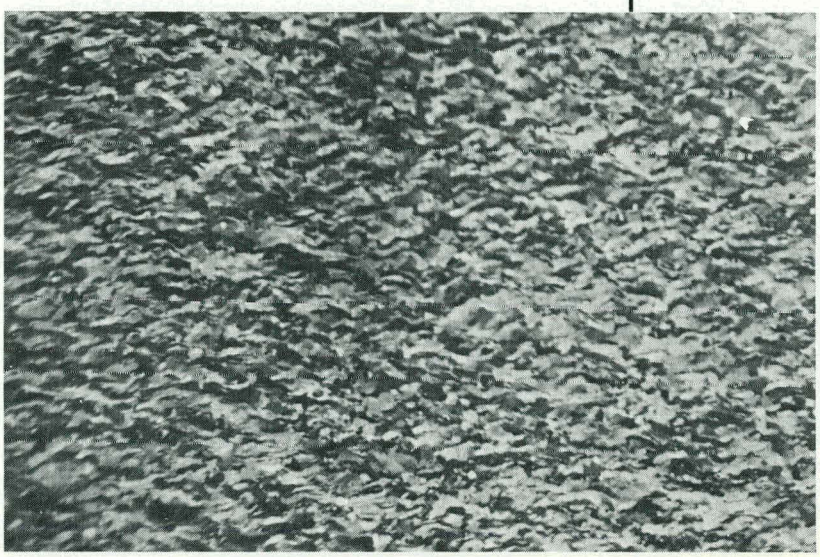

Fig. 262 Polished, pol. light, X 4oo

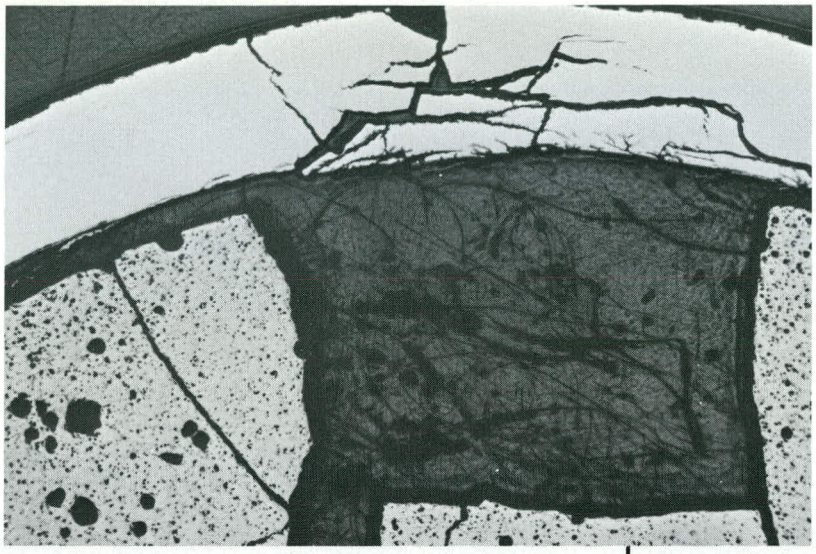

Fig. 263 Polished, X 3o

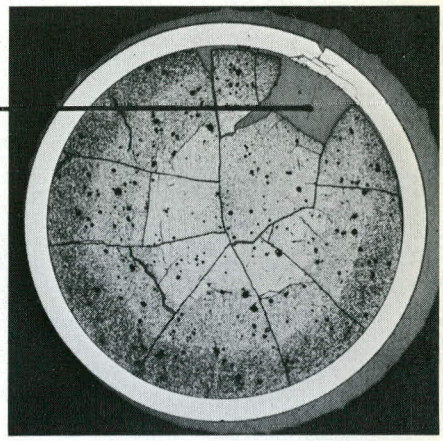

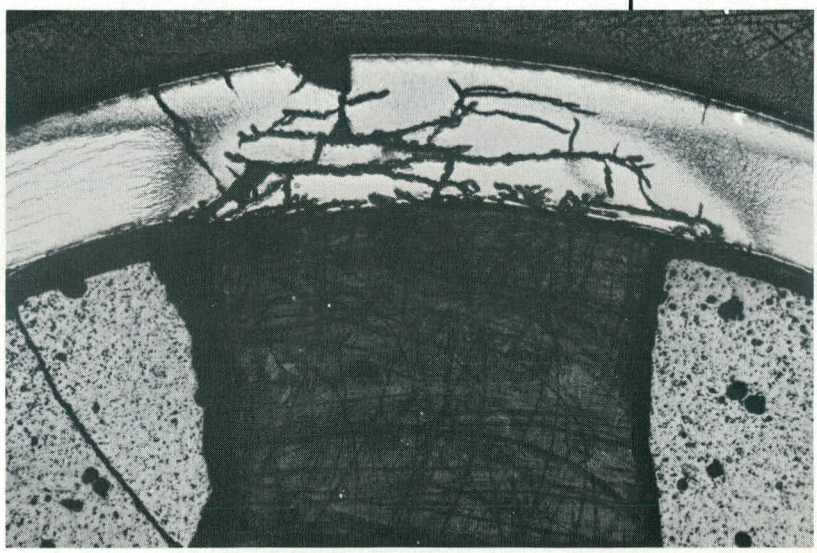

Fig. 264 Etched, X 3o